Lateral Bending Liquid Crystal Elastomer Beams for Microactuators and Microgrippers

Alissa Potekhina

Submitted for the degree of Doctor of Philosophy

Heriot-Watt University

School of Engineering and Physical Sciences

June 2022

Abstract

With the rapid development of microsystems in the last few decades, there is a requirement for high precision tools for micromanipulation and transportation of micro-objects, such as microgrippers, for applications in microassembly, microrobotics, life sciences and biomedicine. Polymer based microgrippers and microrobots executing various tasks have been of significant interest as an alternative to the traditional silicon and metal based counterparts due to the advantages of low cost fabrication, low actuation temperature, biocompatibility, and sensitivity to various stimuli. The exceptional actuation properties of liquid crystal elastomers (LCE) have made these materials highly attractive for various emerging applications in the last two decades. Large programmable deformations and the benefits offered by the elastic, thermal and optical properties of LCEs are suitable for implementing stimuli-responsive microgrippers as well as various biomimetic motion in soft robots.

In this thesis, a method and the associated processes for fabrication and molecular alignment in LCE were developed, which enabled new functionality and improved performance of the LCE based microactuators and microgrippers, providing controlled response by thermal and remote photothermal actuation, and allowing easy integration of the LCE end-effectors into robotic systems for automated operation. Lateral bending actuation has been demonstrated in LCE microbeams of 900 µm of length and 40 µm of thickness, owing to the new monolithic micromolding technique using vertical patterned walls for alignment. The effects of parameters such as the beam width, the size of the microgrooves, and the surface treatment method on the behavior of the microactuators were studied; the internal alignment pattern of liquid crystals in the structure was investigated by different microscopy methods. An efficient method for finite element modeling of the bending LCE actuators was developed and experimentally verified, based on the gradient of equivalent thermal expansion in the multi-layer structure, which was able to predict the bending behavior of the actuators in a large range of thicknesses as well as rolling behavior of the actuators of tapered thickness. The novel LCE microgripper with in-plane operation showed efficient thermal and photothermal actuation, achieving the gripping stroke of 64 µm under the light intensity of 239 mW/cm^2 for the gripper length of 900 µm, which is more efficient than the typical SU-8 polymer based microgrippers of the same dimensions. The LCE gripper was successfully demonstrated for the application in manipulation of the objects of tens to hundreds of micrometers in size. Therefore, the novel LCE microgripper bridges the gap

in the LCE-based gripper technologies for typical object size in applications for systems microassembly, biological and cell micromanipulation. The lateral bending functionality enabled by the proposed method expands design opportunities for thermal and photothermal LCE microactuators, providing an effective route toward realization of new modes of gripping, locomotion, and cargo transportation in soft microrobotics and micromanipulation.

Acknowledgements

Research Thesis Submission
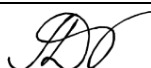
Name*:	Alissa Potekhina		
School:	School of Engineering and Physical Sciences		
Version: *(i.e. First, Resubmission, Final)*	Final	Degree Sought:	PhD

Declaration

In accordance with the appropriate regulations I hereby submit my thesis and I declare that:

1. The thesis embodies the results of my own work and has been composed by myself
2. Where appropriate, I have made acknowledgement of the work of others
3. The thesis is the correct version for submission and is the same version as any electronic versions submitted*.
4. My thesis for the award referred to, deposited in the Heriot-Watt University Library, should be made available for loan or photocopying and be available via the Institutional Repository, subject to such conditions as the Librarian may require
5. I understand that as a student of the University I am required to abide by the Regulations of the University and to conform to its discipline.
6. I confirm that the thesis has been verified against plagiarism via an approved plagiarism detection application e.g. Turnitin.
* *Please note that it is the responsibility of the candidate to ensure that the correct version of the thesis is submitted.*

Signature of Candidate*:		Date:	20 / 6 / 2022

Submission

Submitted By *(name in capitals):*	ALISSA POTEKHINA
Signature of Individual Submitting:	
Date Submitted:	20 / 6 / 2022

For Completion in the Student Service Centre (SSC)

Limited Access	Requested	Yes		No		Approved	Yes		No	
E-thesis Submitted (**mandatory for final theses**)										
Received in the SSC by *(name in capitals):*					Date:					

Table of Contents

List of Figures

List of Tables

List of Publications

The following papers published in peer-reviewed journals contribute to the main part of the thesis:

1. **A. Potekhina** and C. Wang, "Review of Electrothermal Actuators and Applications," *Actuators*, vol. 8, no. 4, p. 69, **2019**. – *Actuators* 2021 Best Paper Award

2. **A. Potekhina**, R.-C. Voicu, R. Muller, M. H. M. Al-Zandi, and C. Wang, "Design and characterization of a polymer electrothermal microgripper with a polynomial flexure for efficient operation and studies of moisture effect on negative deflection," *Microsyst. Technol*., vol. 27, no. 7, pp. 2723–2731, **2021**.

3. **A. Potekhina** and C. Wang, "Numerical simulation and experimental validation of bending and curling behaviors of liquid crystal elastomer beams under thermal actuation," *Appl. Phys. Lett*., vol. 118, no. 24, 241903, **2021**.

   Highlight article: A. McConnon, "Model predicts bending, curling and rolling of liquid crystal elastomer beams," *Appl. Phys. Lett. Scilight*, 251107, **2021**

4. **A. Potekhina** and C. Wang, "Liquid Crystal Elastomer Based Thermal Microactuators and Photothermal Microgrippers Using Lateral Bending Beams," *Adv. Mat. Tech*., **2022** – accepted for publication

Chapter 1   Introduction

1.1 Introduction

In the last few decades, there has been a significant demand for improving the accuracy, speed and reliability of the tools for micromanipulation. In the applications where the size of the objects is as small as few tens of microns, microgripper is an essential tool for micromanipulation and microassembly, which can be integrated in a robotic system for precise and automated operation. A significant interest in research and applications has been toward developing new functionality for the microgrippers and microrobots by researching advanced stimuli-responsive materials and new fabrication techniques. The object transportation capability has also been a crucial subject of research in untethered microrobots and in biomedicine for targeted drug delivery [1]–[3].

Microactuators perform mechanical work by changing their shape in response to the input stimuli, and thus providing the driving force and displacement in various micro-electro-mechanical systems (MEMS), such as in microgrippers. Traditionally, microactuators have been fabricated from silicon or metal. However, the established manufacturing methods using these materials are typically very expensive. Additionally, silicon and metal based microgrippers require large electrical voltage and temperature stimuli in order to produce displacement on actuation, also generating significant electric and magnetic fields, which largely limit their applications for micromanipulation of biological cells and tissues, fragile micro-objects, or sensitive electronic components.

The alternatives to the silicon and metal based transducers are the low-cost polymer transducers. Polymers play a leading role in the research of smart stimuli-responsive systems, because these materials are sensitive to a variety of stimuli, such as heat, light, electric and magnetic field, humidity, pH level, or chemical stimuli; polymers can also respond to multiple stimuli at the same time [4]. Most of the polymers used in microfabrication offer good mechanical and optical properties suitable for designing transducers [5], and also light weight, flexibility, chemical resistivity, biocompatibility and biodegradability, which are the vital characteristics for biomedical applications. By using the state-of-the-art polymer technologies, significant advancements have been achieved in the fields of microrobotics, artificial muscles, wearable devices,

microsurgical devices, drug delivery in biomedicine, microfluidics, adaptive surfaces, and 3D microfabrication [6].

Currently, microrobotics is presented with a number of applications based on rigid mechanisms; however, these structures are often brittle, less adaptable, requiring batteries or bulky external power sources. For small-scale robots, the highly desired characteristics are mobility and robustness, which can both be achieved by using polymers [7]. Soft robots are able to directly convert external stimuli to mechanical work [8]. Smart actuation in the soft robotics is often inspired by the shape change in the biological organisms. For instance, the gripping function in polymeric grippers was demonstrated based on the opening and closing movement similar to that of the flower petals or the leaves of the Venus flytrap [9]. The locomotion of the soft microrobots typically mimics the crawling, inching, leaping and swimming motion of the microorganisms and small animals. Non-reciprocal motion of biological cilia and flagella has been of significant interest for developing microactuators and microrobots with various functions, such as propulsion, object manipulation, and sensing [10].

Stimuli-responsive polymers such as hydrogels, shape memory polymers, and ionic conducting polymers have become highly attractive for the novel applications in actuation in the recent years. However, these materials have certain limitations in terms of processing, the specific deformation modes, and actuation methods. In the last two decades, the remarkable performance of the actuators based on liquid crystal elastomer (LCE) materials has been of interest for various applications, including soft robotics [11], [12], origami-like folding structures [13]–[15], artificial muscles and biomimetic devices [16]–[22]. One of the key advantages of LCE over other common polymers for actuators is the possibility of spatially controlling the pattern of alignment, and therefore, implementing the versatile programmed deformation in the structure [23]–[25]. The large strain gradients occurring under different stimuli (heat, light, humidity, or electric field) induce bending and curling of the initially flat LCE films, due to reorientation of the liquid crystal (LC) mesogens bound to the polymer network.

Actuators can be broadly classified in two categories according to their deformation function: out-of-plane actuators and in-plane actuators. Out-of-plane actuation refers to the direction of displacement outside of the fabrication plane in the LCE flat films, whereas in-plane deformation occurs within the same fabrication plane, for instance, lateral bending. As opposed to the common out-of-plane bending in flat films, the traditional microgrippers and other systems typically operate based on the lateral

movement of the functional parts [26]. However, despite the versatility of programming the out-of-plane deformation shapes, the in-plane actuation of the LCE beams and structures has been limited to simple uniaxial contraction. There is a lot of value in developing a new method to achieve programmed lateral bending actuation, as it would not only allow implementing the simple LCE microgrippers, but also open up a significant opportunity for various LCE applications in planar MEMS and microfluidic systems. The challenges of implementing the in-plane bending of LCE microactuators are often associated with the limited capability for miniaturization of the existing techniques, along with the requirement for post-fabrication assembly. It is necessary to develop an effective technique for monolithic, assembly-free fabrication of the microstructured LCE actuators.

On the other hand, due to the complex physics behind the strain formation in LCE materials, the relationship between the molecular arrangement and the macroscopic shape morphing is not fully understood in the current material science. Therefore, there is no single universal finite element based method for simulation of the behaviors of LCE actuators. Although, a number of models based on different equivalent physics have been demonstrated for the individual examples and applications of LCE actuators, there is still a critical need for a simple, flexible and efficient simulation approach suitable for predicting the shape change of various LCE actuators with good accuracy and for designing the new actuators for practical applications.

LCE technologies are a new and rapidly developing area, and there is a high demand for developing and testing new designs, fabrication and actuation strategies for LCE structures. Unique material properties of LCEs can be used to realize controllable deformations in the structures, which may be impossible to achieve with other polymer materials. The main motivation for the work presented in this thesis was to develop new actuation functionality and to expand the area for practical applications of LCE actuators, particularly, for enabling effective object transportation and motion freedom in the soft robots and systems in micromanipulation.

1.2 Aims and Objectives

The thesis study aims to develop novel polymer-based microactuators with new functionality and improved actuation properties, as well as the appropriate fabrication

techniques, for applications in micromanipulation and microrobotics. Towards these, the main objectives are outlined as follows:

- Review of the recent progress in the area of polymer-based actuators and microgripper technologies; identifying opportunities and challenges.

- In-depth study and comparison of the liquid crystal elastomer-based microfabrication methods, methods for alignment of LC mesogens for programmable shape change on actuation.

- Establishing the procedures for preparation of the LCE precursor and fabrication of the flat LCE films based on the existing methods from the literature; characterization of the out-of-plane bending behavior of the LCE actuators (LCE beams).

- Design of LCE microactuators with new lateral bending functionality (LCE microbeams), modeling of the bending behavior.

- Development and optimization of the fabrication method that enables the new functionality for the LCE microbeams; characterization of the actuation behavior for the in-plane LCE microbeams.

- Development of a finite element simulation method for thermally actuated LCE beams and microbeams.

- Design, fabrication, testing and demonstration of the LCE microgrippers for applications in micromanipulation and microrobotics.
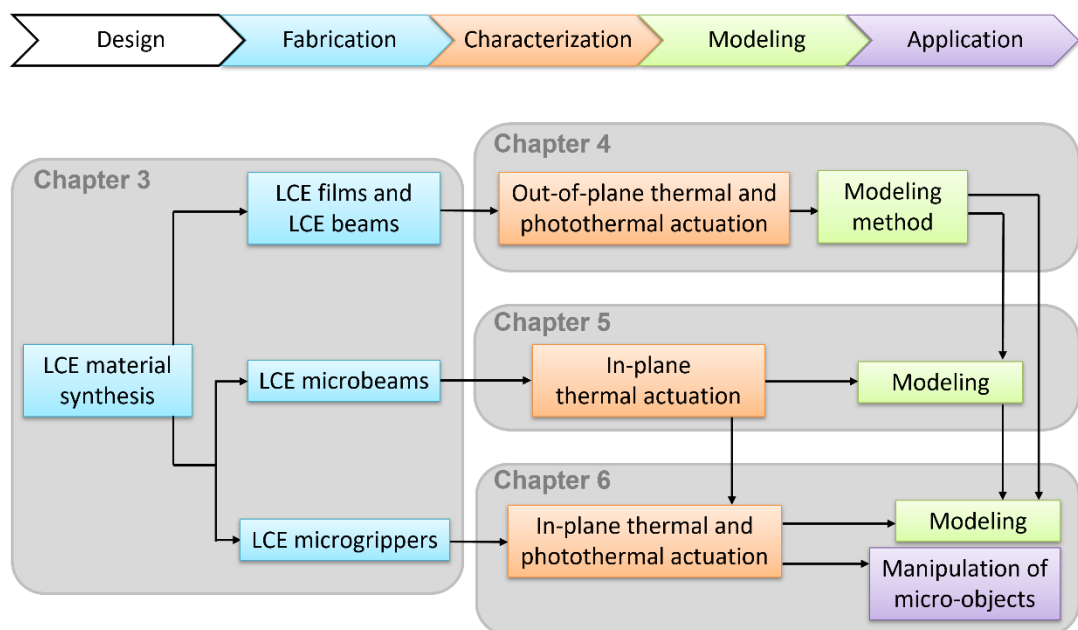
Figure 1.1 Outline of the research work

4

The flow chart in Figure 1.1 shows the general outline of the work, in alignment with the research objectives. It is shown that the research outcomes are used in the following steps for development and optimization, such as in characterization and modeling.

1.3 Originality and Main Findings

Micropatterned surfaces have been widely used for alignment of LC mesogens on planar substrates previously in the literature; however, this was only used to produce LCE actuators for out-of-plane bending. The main novelty of this thesis work lies in the unconventional way of using patterned sidewall surface of the mold for creating the in-plane variation of LC alignment, and thus, achieving a new spatially controlled in-plane bending functionality in the LCE microactuators without post-fabrication assembly. The methods of fabrication, characterization, and modeling for the novel in-plane bending LCE microbeams and microgrippers have been developed respectively. A wide range of potential applications has been identified for the new method, such as in micromanipulation, microfluidic and lab-on-a-ship systems, biomimetic technologies, and soft microrobotics.

The main findings of the thesis study can be described as follows:

- A new combination of alignment and fabrication techniques, including direct laser writing, replica molding, chemical treatment and LCE micromolding, has been developed and optimized for spatial modification of the LC alignment for fabrication of the monolithic LCE microactuators and microgrippers.

- The effect of the surface treatment of the mold on the alignment of LC and the actuation behavior of the LCE microbeams was investigated.

- A simple finite element model for thermal bending LCE actuators was developed, which is capable of predicting the behavior of the beams with good accuracy in a wide range of thicknesses, and also the beams with more complex geometry, such as tapered thickness.

- A novel LCE microgripper demonstrated a significantly higher in-plane gripping stroke at lower stimuli, as compared with existing SU-8 microgrippers, and a monolithic, assembly-free structure, as compared to existing LCE microgrippers, bridging the gap in the LCE-based applications for untethered manipulation of the objects in the size range from tens to hundreds of microns.

5

1.4 Thesis Layout

Firstly, a review of the recent progress in the polymer-based actuator technologies for microgrippers and microrobotics was carried out as given in Chapter 2. The literature review focuses on SU-8 and LCE based actuators, their properties, fabrication methods, and applications. Microgripper devices demonstrated in the literature based on these materials have been compared in terms of the structural design, actuation strategies and general performance.

Experimental work was carried out as outlined in the flow chart in Figure 1.1. It starts with the development of the fabrication methods for LCE actuators in Chapter 3. The same LCE material was used to fabricate the out-of-plane bending LCE beams of several millimeters of length from the LCE films based on existing methods using flat cells, and also to fabricate the novel lateral bending LCE microbeams on micrometer scale based on the combination of direct laser writing and micromolding techniques.

The out-of-plane bending behavior of the fabricated LCE beams was characterized, and the results of measurements were used to develop a new method of modeling and numerical simulation for the LCE actuators in Chapter 4. The model was experimentally validated and used to predict the bending and rolling behavior of the LCE beams of different thicknesses and of tapered thickness upon thermal actuation. The developed modeling method is further used for numerical simulation for lateral bending LCE microbeams in Chapter 5 and LCE microgrippers in Chapter 6.

As opposed to the out-of-plane bending in typical LCE beams, Chapter 5 investigates the new lateral bending behavior in the LCE microbeams enabled by the novel combination of techniques for LCE alignment and fabrication. The impact of different fabrication parameters on the actuation behavior have been studied. Furthermore, this chapter shows using various methods of material characterization to investigate the alignment of LC mesogens and the glass transition temperature of LCE with and without dye doping. Based on the results of the development and characterization of the in-plane LCE microbeams, the novel LCE microgrippers for thermal and photothermal actuation were developed and characterized in Chapter 6, for practical applications in micromanipulation. The LCE microgrippers with in-plane operation were used to perform pick-and-place operation using glass micro-beads.

Finally, Chapter 7 provides the conclusion on the work presented in this thesis, together with a discussion of possible directions for the future work.

Chapter 2 Literature Review

2.1 Materials for Microactuators and Microgrippers

Microgripper is a typical tool for pick-and-place operations with various objects in the size range from several millimeters down to sub-micrometer dimensions, where traditional tools and techniques relying on human dexterity cannot offer the required level of precision and throughput. Typical applications for microgrippers are manipulation and microassembly in MEMS and semiconductor industry [27], cell manipulation in life sciences [28], biological samples, tissues and blood vessels manipulation in biomedicine and microsurgery [29], material characterization [30]. In the last few decades, a significant research effort has been focused on the development of microgripper designs, actuation mechanisms, improved functionality, sensing and feedback schemes. Additionally, there is a growing interest in developing autonomous, untethered, stimuli-responsive systems that could execute tasks on microscale, such as in microrobotics. Smart microscopic robots with untethered locomotion and micromanipulation functionality will find an extensive use in microassembly applications in the areas inaccessible for large instruments in microsurgery, targeted drug delivery, biomimetic technologies.

Several detailed literature reviews have been published recently on actuation and sensing strategies in microgrippers [31], [32], which are typically based on one of the five operation principles: electrothermal, electrostatic, piezoelectric, electromagnetic, or shape memory based mechanisms. Less conventional principles, such as photothermal actuation, have also been previously demonstrated in the literature. A comprehensive survey has been presented recently on the mechanical structures of the microgrippers [26], which has given a detailed comparison for a large number of gripper designs allowing effective translation of the small driving displacements of the actuator into large gripping strokes at the gripper tips. Previously, most of the research in microactuators and microgripper applications has been demonstrated traditionally using materials such as silicon and metals. The established manufacturing methods for these materials can provide high resolution of the fabricated microstructures. Moreover, the driving electrodes and controlling circuits can be easily integrated in the silicon and metal microactuators, and these can be directly integrated into larger systems for practical applications, such as in micromanipulation. However, the cost of silicon

micromachining is high. Also, the electrical voltage stimulus for driving of the silicon and metal-based microactuators is usually high (up to tens and hundreds of volts); however, the displacements achievable on actuation in the structures are very limited due to the large stiffness of these materials. On the other hand, polymer-based actuators have been of significant interest in the recent years. Polymers allow relatively low cost of fabrication by photolithography, soft lithography or other methods; therefore, polymers can be used to make cheap, disposable or interchangeable components for systems. Complex electrical integration is not required when remote actuation is implemented, for instance, using light.

This literature review will focus on the recent advances in polymer-based actuators, aspects of microfabrication, stimuli-responsive material properties and the applications for object micromanipulation.

2.1.1 Polymer Based Actuators

Young's modulus of different polymers varies in the range from kPa to few GPa, from the soft "viscoelastic" to the hard "glassy" state [4], [6]. At present, one of the most widely used polymers in microfabrication is SU-8, a UV-crosslinkable epoxy resist, which can be processed via standard photolithography. In recent years, a lot of attention is attracted to the new polymers with high performance and advanced properties, such as hydrogels, shape memory polymers, ionic conducting polymers, and liquid crystal polymers. Shape-shift and generation of the output force and displacement in these polymer materials are based on several fundamentally different physical mechanisms.

A recent review [6] has classified polymeric actuators into four groups based on the actuation principle: a) volume change; b) elastic relaxation; c) change in order; and d) surface tension-driven actuation. Compared to the traditional silicon and metals, many polymers possess a relatively large coefficient of thermal expansion (CTE), such as the SU-8 photoresist with the CTE of 52 ppm/°C [33]. This advantage is therefore effectively used for thermal actuation. Volume change in the polymers can be induced by swelling and deswelling in an aqueous medium, an example is the hydrogel. The swelling behavior can be controlled with heat, chemical, pH and other stimuli. Large volume change and biocompatibility are the main advantages of hydrogels, which make these actuators highly attractive for biomedical applications [34]. However, hydrogels

8

require liquid medium for operation. Another principle is where the elastic restoring force returns the structure to the initial shape after deformation. For instance, the shape memory effect is the ability of materials to recover the initial (permanent) shape under various stimuli, once the material was "frozen" in a temporary deformed state. This is the characteristic of the shape memory polymers (SMPs) [6], rubber is the most common example. These materials are able to deliver a significant amount of deflection; however, the actuation of most SMPs is irreversible. In the ionic conducting polymers (ICP), an example of electroactive polymers, the clusters of ions are migrating inside the polymer under the electric stimuli; actuation is induced via mass transfer [35]. Surface tension has been used in polymeric structures for irreversible self-folding [36]. Finally, actuation by change in the molecular order is a unique characteristic to the materials such as liquid crystal elastomers (LCEs), liquid crystal networks (LCNs), or liquid crystal polymers (LCPs). The reorientation of the liquid crystals incorporated in the polymer system induces large macroscopic deformations.

Fabrication and assembly of the stimuli-responsive soft actuators may be challenging, it can be based on manual assembly, printing, molding, top-down lithography and bottom-up synthesis [9]. Fabrication of stimuli-responsive untethered soft grippers and robots usually require multiple steps, combining photolithographic and self-folding techniques to construct a 3D structure from a 2D patterned film. From the design point of view, a particular challenge is that actuation, sensing, and other functions are often integrated in the soft compliant structure [4]. Novel LCE materials are particularly suited for implementing complex actuation due to the local control of the internal molecular orientation.

2.1.2 SU-8 Photoresist in Microfabrication

SU-8 is a photo-cross-linkable epoxy from the commercial vendor MicroChem, which is widely used for wafer patterning via photolithography in microelectronic applications, and also as a structural material in MEMS and other applications due to its chemical stability and good mechanical properties. A series of SU-8 products with different viscosities allow fabrication of the photoresist layers in a wide range of thicknesses from 0.5 µm to >200 µm in a single coat [33]. Optical transparency and high contrast of SU-8 allows producing structures with high aspect ratio and nearly

vertical walls, which also show good chemical and thermal stability. The cured photoresist possesses excellent mechanical properties for a structural material in many MEMS applications, such as the Young's modulus of 2 GPa, the glass transition temperature of 200°C, the coefficient of thermal expansion of 52 ppm/°C, the thermal conductivity of 0.2 W/mK, and the tensile strength of 73 MPa [37].

SU-8 is a negative photoresist, which consists of the three key components – Novolac epoxy, organic solvent, and photoacid generator. The typical SU-8 based photolithography cycle is the following: spin-coating, soft bake, UV exposure, post-exposure bake, development, and hard bake. Firstly, the viscous liquid SU-8 is coated onto the substrate by spinning at a suitable speed, where the thickness of the resulting layer is controlled with spinning speed and acceleration. Soft baking is performed in order to evaporate the solvent from the photoresist. It is usually performed in two steps, first at a lower temperature, followed by higher temperature in order to reduce stress formation. It was demonstrated previously in the literature, that soft baking is the crucial step in formation of stress; therefore, it is recommended to use short as possible time and low temperature for soft baking in order to prevent crack formation in the structures, as well as for better pattern fidelity [38]. After the substrate cools down to room temperature, the photoresist solidifies.

Next, the SU-8 layer is cross-linked by UV exposure, the pattern can be created using a photolithographic mask. A strong photo-acid is formed upon UV-exposure, which catalyzes the cross-linking reaction in the material during the subsequent post-exposure baking. The first step of baking at the lower temperature helps promote diffusion of the photo-acid and reduces stress, while the second step at a higher temperature completes the thermally-driven photoacid-aided polymerization process. It was demonstrated in the literature that the post-exposure baking temperature which is too high may adversely affect the resolution of small features in the cross-linked structures, which results in widening of the lines in the pattern [38]. Finally, the non-cross-linked resist is dissolved in the developer solution, leaving the polymerized patterns on the substrate. Hard baking can be performed at a high temperature to further cross-link the material in preparation of the device for application, however, this step is optional.

The properties of SU-8 have been well-researched in the last several decades, as the photoresist has been extensively used as a structural material for MEMS. The relatively new area is the study of SU-8 composites, particularly the graphene and graphene oxide composites. It has been shown that incorporation of graphene improves some of the

characteristics of SU-8, such as: increased glass transition temperature, thermal conductivity, electrical conductivity [39], increased microhardness [40], and increased Young's modulus [41]. With all the advantages, however, the increasing content of graphene oxide in the composite negatively affects the photopolymerization rate, and significantly reduces the total conversion of SU-8 groups. The quality of the micropatterned structures is also significantly limited due to the size of graphene/graphene oxide platelets incorporated into the material [42].

The SU-8 resist is best suited for applications where a layer of the material is patterned and left on the substrate, i.e. permanent structures, for example, master templates for molding, microfluidics, lab-on-a-chip systems, or integrated systems such as integrated spectrometers [38]. Soft lithographic methods of fabrication [43], such as replica molding, are typically used in microfluidics and other applications. The replica molding technique uses the molding templates with microstructures and microchannels patterned on the master wafer, which can be fabricated from SU-8, allowing a wide range of structural thicknesses of up to 200 µm with well-defined vertical walls. The cured photoresist is very hard to remove from the substrate, however, the free-standing structures can be obtained by using a sacrificial layer under the SU-8 layer. For instance, this was used to release the fully patterned SU-8 microgrippers from the substrate [44]. The smallest feature that is possible to fabricate in SU-8 is only limited with the exposure technique and the divergence of the light beam due to the diffraction effect; in traditional masked photolithography the smallest feature is limited to a few microns [38]. However, using advanced high-resolution techniques such as Direct Laser Writing (DLW), multiphoton polymerization or X-ray lithography, SU-8 structures of sub-micrometer size have been demonstrated [45].

The SU-8 is an important structural polymer in applications for actuators. The relatively large CTE of the photoresist allows achieving significant displacements in the structure upon thermal actuation. The next section contains a review of SU-8 based actuators and microgrippers, which operate based on the thermal expansion effect.

2.1.3 SU-8 based Electrothermal Microgrippers

Electrothermal actuation is based on the conversion of electrical energy into thermal energy through the Joule heating effect in the resistive element and the resultant of

thermal expansion of the actuation structure. In electrothermal SU-8 based actuators, a conductive thin layer of metal, such as gold or copper embedded in the polymer layers can be used to create the microheaters. The actuator reaches a stable state when the generated thermal energy is balanced with the heat dissipation through the surface or the anchors. The advantages of the thermal/electrothermal actuation over other common actuation methods (piezoelectric, electrostatic, electromagnetic) are lower operational voltages, which are typically in the standard IC (Integrated Circuits) range of up to a few volts, large displacements [31], easy control, scalability and compact structure. Electrothermal actuators can operate in air, vacuum, dusty environment, liquid medium; the absence of electrostatic and magnetic fields allows operation with biological samples and electronic chips. The drawback of electrothermal actuators is relatively slow operation.

One of the key applications for the SU-8 actuators is in microgrippers for micromanipulation in MEMS microassembly and cell manipulation in life sciences. A summary of a number of SU-8 based electrothermal microgrippers from the literature is given in Table 2.1. These are classified according to the design of the actuators, which is based on several conventional actuator types, such as: hot-and-cold-arm actuators, chevrons, bimorphs, and simple uniaxial expansion beams. These actuator types are shown in Figure 2.1. Table 2.1 also shows a comparison of the maximum displacement of the gripper tips and the corresponding driving voltage. Although the voltage values required for actuation can be less than 1 V, the temperature generated in the actuator often exceeds 100°C. It is crucial that the temperature at the gripper tips should be low enough to ensure safe manipulation without damaging the sensitive microscopic objects; for instance, the maximum temperature limit is about 40°C for handling of biological specimens.
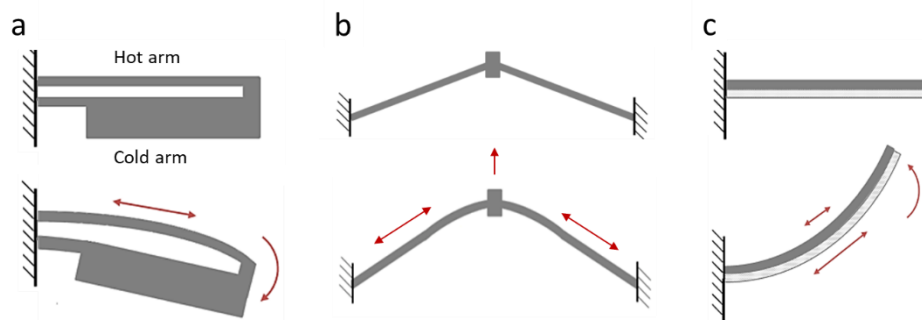
Figure 2.1 Types of thermal actuators and their operation: a) hot-and-cold-arm actuator, b) chevron actuator, c) bimorph actuator.

Table 2.1 Summary of SU-8 based electrothermal microgrippers. Based on Publication (1).

Actuator type	Structure	Materials	Displacement of the tips, μm	Voltage, V	Reference
Hot-and-cold arm	U-shape	SU-8, Cr, Au	11	2	[46], [47]
	Folded heater	SU-8, Au	262	1.94	[48]
	Meander heater	SU-8, Cr, Au	~9.6	~0.25	[49]
	Inclined arm	SU-8, Cr, Au	~14.3	~0.25	[50]
	Curved arm	SU-8, Cr, Au	8	0.7	[51], [52]
	'Skeletal'	SU-8, Cr, Au	17-20	0.65	[53], [54]
	Three-beam	SU-8, Pt, Ti	100	10	[55]
Chevron	V-shape	SU-8, Au	10	<1	[28]
		SU-8, Cu	71.5	0.195	[29], [56]
		SU-8, Cr, Au	40	- (25 mA)	[57]
		SU-8, Au	70.5	0.74	[58]
	Z-shape	SU-8, Au	80	0.54	[59]
		SU-8, Au	80	0.4	Publication (2)
	Cascaded	SU-8, Cr, Au	50	- (26 mA)	[60]
Expansion beams		SU-8, Cr, Cu	~100	0.5	[61]
		SU-8, Cr, Au	11	0.65	[52], [62]
Bimorph	Microcage	SU-8, Al, DLC	~80° arc	3.2	[63]

The actuation principle in the hot-and-cold-arm actuators is that the resistive heating of the structure is generated by electrical current passing across two serially connected arms. The arm with a smaller cross-section has higher electrical resistance than the arm with a larger cross-section; consequently, a larger thermal energy is generated in the thin "hot" arm. The asymmetric thermal expansion creates a bending moment, resulting in the deflection of the actuator towards the "cold" arm. Such an SU-8 microgripper of the U-shape actuator type is shown in Figure 2.2a, the inset shows the metallic heater structure [46]. The conduction tracks are only embedded in the actuator part. The bending displacement is effectively amplified at the tips of the long non-conductive gripper arms, which also helps reduce the temperature at the tips in order to perform cell manipulation. The actuation displacement in the U-shape actuator is a function of geometric parameters such as lengths and widths of the arms, length of the flexure, and the gap between the arms. Further, the heater and the arms can have various designs. For instance, the folded microheater track may only be embedded in the "hot" arm, therefore, heating is localized within only one beam [48]. The meandering heater was

13

shown to produce a large heating effect in the SU-8 microgripper [49]. Apart from the traditional U-shape, the actuator shape can be modified for better efficiency, such as designs using curved and inclined beams [50], [51]. Finally, the actuator can have three and more beams instead of two in order to realize specific modes of actuation and bi-directional actuation [53], [55]. The disadvantages of the hot-and-cold-arm actuators are non-rectilinear motion, generally low output force, limited reliability and life-time due to the effect of localized heating in the thin beams.
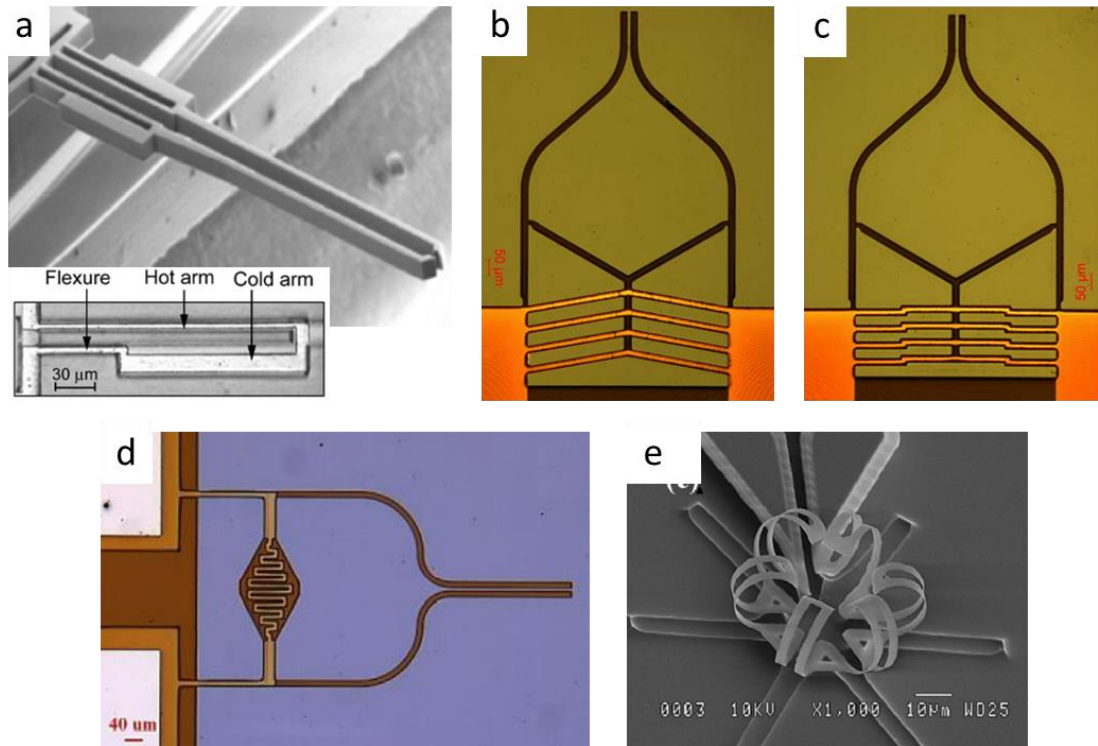
Figure 2.2 SU-8 based electrothermal microgrippers with different types of actuators: a) Hot-and-cold-arm actuator [46], b) V-shape chevron [59], c) Z-shape chevron [59], d) expanding beam actuator [52], e) bimorph actuator [63].

Another type of electrothermal actuator is the chevron actuator, such as the V-shape and Z-shape chevron designs, which were used in SU-8 microgrippers shown in Figure 2.2b and Figure 2.2c, respectively [59]. The symmetric beams push the central shuttle upon thermal expansion generated by the current running across the chevron, the parallel conductive tracks embedded in the chevron beams can be seen in Figure 2.2b and Figure 2.2c in a bright color. The driving displacement is translated into the opening movement of the tips of the microgripper. The total displacement of the chevron depends on two critical parameters: beam length and inclination angle or offset. Z-

chevron has multiple design parameters, which allow optimizing the design for a wide range of beam stiffness. It was shown that the Z-actuator produces larger displacements at smaller footprint size than the V-actuator [64]. However, a common drawback of chevron actuators is the risk of out-of-plane buckling due to the low stiffness of the beams. A common approach to increase the stiffness and the output force of the actuators is parallel stacking of chevrons, such as shown in Figure. It can be seen from Table 2.1 that the SU-8 microgrippers based on chevron actuators can provide large tip openings with low actuation voltage of less than 1 V, using a compliant "tweezers" design for amplification of the displacement. An electrothermal SU-8 microgripper based on Z-shape chevron actuator and polynomial-shape arm flexures was developed in Publication (2); which also includes a study of the moisture effect on the negative displacement of the gripper arms during the first cycle of actuation.

Figure 2.2d shows an SU-8 microgripper with the microheater embedded in the actuator beam placed between the gripper arms [62]. The axial elongation of the actuator beam upon electrothermal heating generates a pushing force acting on the gripper arms, which controls the opening of the gripper tips. The serpentine-shape microheater effectively generates resistive heating. This type of actuator based on uniaxial expansion of the beams is different from the conventional U-type based on bending due to the asymmetric expansion, and from the chevron type with rectilinear tip motion. Nevertheless, it was shown that some SU-8 microgrippers actuated by expanding "hot" beams can provide large tip displacements of ~100 µm under low voltages [61].

Finally, the well established bimorph actuators consisting of two or more dissimilar materials utilize the difference in the CTE values of the layers to produce thermal bending in the structure. Most commonly, the layers are deposited on top of each other in a planar fabrication process; therefore, bimorph actuators exhibit out-of-plane displacement, unlike the actuator types discussed previously, which exhibit in-plane displacement. Electrothermal bimorph actuators have been used in application for micromanipulation previously in the literature. An SU-8 microcage based on bimorph structures is shown in Figure 2.2e. The structure has six "fingers", which consist of an SU-8 layer with high CTE, a diamond like carbon (DLC) layer with extremely small CTE, and the embedded metal layer for electrothermal actuation [63]. The fingers curl after fabrication due to the release of compressive strain in the DLC layer, forming a normally-closed structure. The microcage opens upon heating and securely captures the object when the stimulus is removed.

In summary, this overview shows that electrothermally-driven SU-8 based microgrippers have been actively used for applications in micromanipulation in the literature. The SU-8 microgrippers are based on well-established actuation strategies and structural types, such as those demonstrated in traditional silicon and metal-based electrothermal actuators [26], [32]. The key advantages of the SU-8 as a structural material in actuators is the large CTE value and low stiffness of the polymer, which allow large displacements in the structure achievable upon actuation with low thermal stimulus. The small driving displacement of the actuator can be effectively amplified several times by appropriate design of the compliant gripper arms. Low cost and relatively easy fabrication of SU-8 grippers by photolithography make it a preferred candidate for fabrication of disposable, exchangeable end-effectors for manipulation systems. Biocompatibility of SU-8 allows the microgrippers to be used for handling of the living cells and tissues.

2.1.4 Liquid Crystal Elastomers for Actuators

Liquid crystal elastomers (LCEs) are a class of materials, which have recently attracted a significant interest for advanced applications in actuators and sensors due to the materials' remarkable mechanical and actuation properties. LCE materials possess a unique combination of elasticity typical for polymers, and self-ordering properties such as that of liquid crystalline materials. The principle of shape change in LCE is illustrated in Figure 2.3. An LCE material consists of three main components: liquid crystal mesogens, polymer backbone and crosslinker. The rigid rod-like thermotropic LC mesogens (grey ovals) are attached to a flexible backbone (black solid lines); the network is formed using cross linkers (green double lines) between the polymer chains. In the liquid crystalline phase (for example, nematic), the mesogens can be aligned along one vector, called 'the LC director', forming a monodomain LCE. The material which was crosslinked in the anisotropic state will retain its shape when no actuation stimulus is applied. When the temperature increases and approaches the phase transition temperature of the material, LC mesogens lose their formation and shift to isotropic phase with no directional order. Loosely crosslinked and flexible polymeric chains conform to the changes in the LC order. Hence, phase transition induces large macroscopic deformation: the elongated nematic LCE in Figure 2.3 exhibits rapid

shrinking along the LC director, and expansion in the perpendicular directions upon heating above the phase transition point. After the actuation stimulus is removed, elastic restoring forces return the original shape to the elastomer. Therefore, the actuation is fully reversible and repeatable.
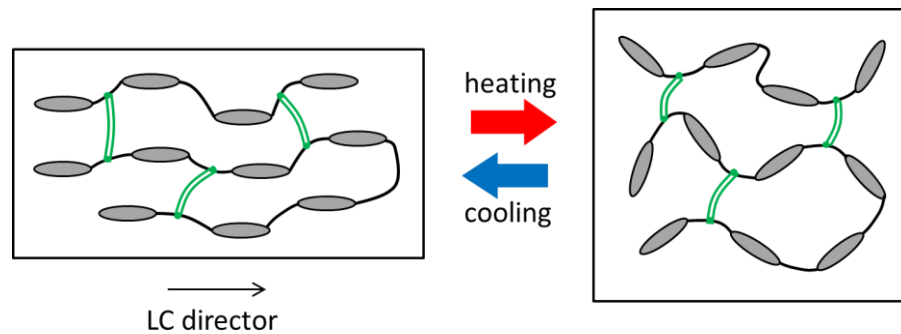
Figure 2.3 Stimuli-induced reversible shape change in LCE

LC mesogens are chemically bound to the polymeric chain in LCE. According to the form of the link, LCEs are classified into three main types, these are shown schematically in Figure 2.4. The "main-chain" LCE is formed if the mesogens are directly incorporated into the polymer backbone. If the mesogens are located in the side pendant chains linked to the backbone with a spacer, this forms the "side-chain" LCE of one of the two types: the "end-on" type when rod-like mesogens are attached to the backbone by their ends, or the "side-on" type when they are attached to the backbone in the middle of their structures [65].
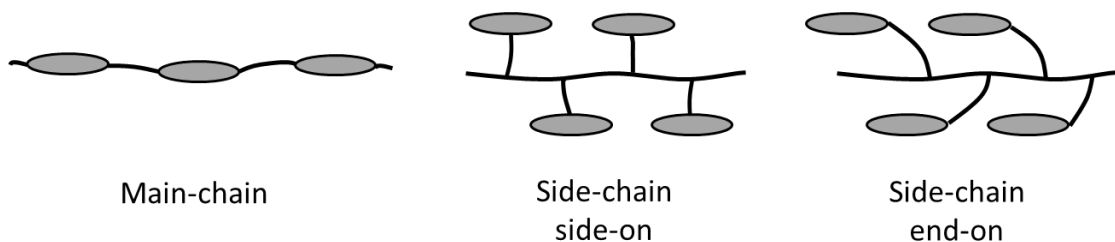
Figure 2.4 Types of LCE based on the link between the mesogens and the backbone chain

The degree of orientational order of mesogens in the liquid crystal elastomers is typically described with the scalar order parameter, Q, given with equation (2.1) [66]

$$Q = \frac{1}{2}(3\cos^2\varphi - 1) \tag{2.1}$$

where φ is the average angle between the mesogen axis and the overall LC director. In case of the ideal anisotropic alignment of mesogens, the order parameter would be $Q = 1$, while in case of complete isotropy with random LC orientation, $Q = 0$. Another parameter is also taken into account, which is the orientational order parameter of the backbone, Q_B. In the main-chain LCE, the Q coincides with Q_B, however, in the side-chain LCE, the two parameters could be linked via a coupling coefficient. It has been established that the macroscopic shape in LCE is related to the molecular order as expressed with equation (2.2) [66]:

$$\lambda_m = \left(\frac{1+2Q_B}{1-Q_B}\right)^{\frac{1}{3}} \tag{2.2}$$

where λ_m is the spontaneous uniaxial elongation, which can be measured experimentally. The scalar order parameter and the spontaneous distortion are typically used in theoretical modeling for the LCE materials. However, the fundamental nature of strain formation in LCE is not very well understood to the present day due to a variety of interconnected physical phenomena leading to deformations in the materials [8].

In practice, the ability to locally control the orientation of mesogens in photo-crosslinkable LCEs has opened a significant path for microstructured actuation and applications in the last two decades [67]–[69]. Compared to the other materials and polymers, which normally exhibit uniform expansion under the thermal stimulus, LCE offers a unique advantage of implementing complex deformation shapes with a monolithic structure composed of a single layer. The traditional surface effect-induced alignment methods for LC used in displays and other applications [70], as well as multiple novel methods of alignment, have been demonstrated for patterned LCE actuation [71]. Not only the anisotropic actuation properties, but also the mechanical properties of the material can be spatially programmed [72], [73]. LCE materials are responsive to various stimuli, including heat, light, humidity, chemicals and solvents; doped LCEs can be made responsive to electric and magnetic stimulation.

The first idea of a material possessing this unique combination of properties and capable of actuation based on LC order change was discussed in 1975 [74]. A significant rise of interest for using LCE materials in actuation and sensing applications was noticed in the last two decades due to the development of a flexible synthesis procedure. Subsequently, it was demonstrated that advanced modern microfabrication techniques such as photolithography, molding, and 3D printing can be used to produce complex miniaturized LCE structures [75]. The LCE possesses all advantages of polymer

materials such as flexible low-cost fabrication methods, high processability, light weight, and it can produce very large deformations with relatively low stimulus. Unlike hydrogels, LCE actuators perform both in dry and liquid media. Actuation in LCE is achieved using various stimuli. LCE actuators are capable of generating contraction force comparable to that of human muscles (~300 kPa) [76]. In terms of the specific work capacity, some LCE materials may offer an alternative to piezoelectric stacks (~2.6 J/kg) [23], [65]. In the recent years, LCE based actuators have been demonstrated for a wide range of applications, such as the following:

- Soft robots: crawling/walking [77]–[79], swimming [80], [81] microrobots;
- Responsive surfaces: surfaces with switchable adhesive, self-cleaning, wetting properties [82]–[85], photo-switchable topology [86];
- Haptic devices: Braille display [87];
- Adaptive optics: tunable iris-like apertures [22], [88], variable light transmission, variable focus lens [89];
- Artificial muscles [16], [17], [20], [21], [90];
- Biomedical: stents, tissue scaffolds etc. [75];
- Microfluidics: microvalve [91], micropump [92];
- Object manipulation: grippers, autonomous flytrap [19], and microhand [93];
- Shape-changing micro-particles [94], [95] and fibers [96];
- Light-driven motors [97];
- Self-folding structures [13]–[15], [98].

Molecular architecture has a strong influence on the properties of the LCE. The main-chain and side-chain types exhibit different degrees of coupling between the mesogenic units and the backbone. The main-chain LCEs have the strongest coupling, while the end-on LCEs have the weakest coupling [74]. In the result, the macroscopic deformation induced by phase transition is typically the largest in the main-chain LCEs, with the strain values reaching as large as 400% [82]. Besides, within each type, there is a variety of LCE materials with unique properties that can be obtained based on using different mesogen units and different synthesis chemistries. For instance, it has been shown that the length of the flexible spacer that links the LC unit to the backbone has a significant influence on the network anisotropy [99], and even the phase transition temperature [100]. The smaller spacer length in the side-chain LCEs provides the stronger coupling between the LC and the polymer chain, hence a larger degree of anisotropy.

The stress-strain response of liquid crystal elastomers is usually described as soft or semi-soft elasticity due to reorientation of the mesogens under the strain [69]. It has been shown that the Young's modulus of LCEs is anisotropic, depending on the direction of stretch during measurement, with relatively larger modulus along the LC director, and smaller modulus perpendicular to the director due to LC reorientation [101]. The LCE may be treated as nearly incompressible materials, such as in finite element modeling, because their volume tend to remain constant under variable strain conditions [102]. The Poisson's ratio of LCE is often assumed to be close to 0.5 in modeling; however, the recent in-depth research of some LCE materials demonstrated, for example, a possible emergence of auxetic behavior and a negative Poisson's ratio in the materials [103]. New research results continue to show unusual stress-strain relationships and mechanical responses in LCE materials [104].

The crosslinking density is another parameter that has a major impact on the mechanical properties of the LCE networks. The elastic modulus of the material can be tailored in a wide range from rubbery elastomers to glassy, nearly temperature-independent LC polymers [65]. The Young's modulus of the LC networks is typically demonstrated within the range from ~0.1 MPa to few GPa [4], [105]. As an example, thermal actuation of the bending LCE cantilevers with various concentrations of the crosslinker was demonstrated in the literature [17]. By increasing the crosslinker content in the mixture from 12 wt% to 75 wt%, the Young's modulus was increased from 30 MPa to 1.5 GPa. At the same time, the bending curvature of the actuators was reduced significantly with the increasing crosslinker concentration.

The unique characteristic of the LCE materials, as compared with other common polymers used in MEMS applications, is the self-ordering property due to the constituent LC mesogens. Thermotropic liquid crystals switch between several phases, ordered and disordered; the transition occurs at a certain temperature (phase transition temperature) for each particular LC molecule. Firstly, at the glass transition temperature, T_g, the LCE material switches from a glassy state to a soft state with liquid crystalline properties. Below the T_g the elastomer may be rigid and brittle, with low mobility of the molecular network. A significant benefit is that most LCE materials with low crosslinking density have low glass transition temperature, often below the room temperature, which allows for effective actuation in LCE upon relatively low thermal stimuli. Above the glass transition temperature, LCE material exists in the ordered liquid crystalline phases: nematic, smectic, or cholesteric phase. In the nematic phase,

all mesogens in the monodomain structure tend to align with the single LC director but without any local order of the mesogens (as in the schematic in Figure 2.3). Nematic LCEs are the most common for applications in actuators. In the smectic phase, apart from uniform alignment, specific local molecular order exists: organized rows of mesogens in the Smectic A phase, or tilted rows in the Smectic C phase. Cholesteric phase, also named chiral, is characterized with a helicoid twist of the LC director with periodicity across the material layer. Smectic and chiral LCEs are less frequently used for applications in actuators, but a number of examples have been demonstrated previously in the literature [100], [106]–[108].

Upon temperature increase to a phase transition point, LC mesogens switch from the liquid crystalline to isotropic phase, where the anisotropic order is lost, and the mesogens obtain random orientation, which causes large macroscopic deformations in the elastomer network. Glass transition and phase transition temperatures of LCEs can be experimentally determined via differential scanning calorimetry (DSC) method. Large actuation due to the change in the LC order can only be achieved within the nematic range and the nematic-isotropic transition point; with further increase in the actuation temperature the deformations are much less significant, which is evident from the measurements of the material elongation upon increasing temperature demonstrated previously in the literature [109].

Apart from the anisotropic expansion related to the mesogen reorientation, the LCE materials exhibit volume expansion under elevated temperatures, similar to other polymers, which is characterized with a coefficient of thermal expansion (CTE). The anisotropic CTE have different values for parallel and orthogonal directions to the LC orientation: the orthogonal CTE is relatively large (>100 ppm/°C) as compared with that of the typical crosslinked acrylates, and it increases rapidly with temperature [110]. The thermal expansion in LCE have been utilized previously in numerous actuator applications, not only to induce deformation upon thermal stimulus in the initially flat structures, but also, interestingly, to create the initial deformation in the structure by carrying out the LCE polymerization at elevated temperatures [88].

Liquid crystals have been extensively used in the display applications for many decades due to their switchable optical properties. LC elastomers, similar to the low-molar-mass liquid crystals, possess the property of birefringence – the existence of two different refractive indices for the incident light with different polarizations. The alignment of mesogens in LCE may be observed using polarized light microscopy (POM). In case the

aligned LCE material is placed between two parallel polarizers, the maximum light is transmitted through when the light polarization direction coincides with the LC director; while in the case of two cross polarizers, the maximum light passes through when the LC mesogens are directed at 45° to the polarizers. If the LC director is twisted across the thickness, the polarization of the transmitted light would be altered by the LCE layer. Unidirectional alignment, as well as circular, radial, and more complex patterned LC alignment can be identified by POM [24]. X-ray diffraction (XRD) technique is also widely used to investigate the degree of order in LCE materials. Scattering of X-rays in the LCE depends on the alignment of mesogens. Irregular molecular arrangement in the isotropic phase results in the typical symmetric ring-shape XRD patterns, whereas the presence of liquid crystalline order results in some distinctive XRD patterns, which contain information of the LC phase, direction of alignment, and even quantitative information of the lateral distances between the mesogens, such as in smectic LCEs [111].

Some LCE materials with certain synthesis chemistries have shown switchable transparency. It has been demonstrated that under mechanical stretching, the opaque polydomain LCE, which strongly scatters light, obtains unidirectional monodomain alignment and becomes transparent [66], [112]. The variable transparency reveals the regions with different alignment in the cross-linked LCE layer [113]. The opaque LCE also transforms into transparent isotropic state above the 'clearing' temperature. Temperature-induced transparency change is associated with LC phase transition, while stretch-induced transparency change is associated with polydomain-monodomain transition [114].

In order to enhance material properties, LCE composites with various nanomaterials have also been investigated in the literature. A comprehensive summary of LCE-based composites can be found in [115], [116]. Carbon nanomaterials (carbon nanotubes, graphene and carbon nanoparticles) are usually incorporated with the purpose to enable photoabsorption in the IR spectrum, to improve mechanical strength, electrical and thermal conductivity. Metallic nanoparticles can enhance photothermal effect (gold) or induce magneto-mechanical response (iron oxide). Incorporation of photoluminescent dyes in thermoresponsive LCE allows controlling the intensity of luminescent emission under actuation [117], [118]; such materials have significant potential for applications in sensors. To enable light absorption in the near-IR, visible and UV spectrum, various absorbing agents can be dispersed in the LCE material. An overview of frequently used

photothermal agents in the overall wavelength range of 320-980 nm has been presented recently in [119]. Chemical dyes based on azobenzene derivatives are a common choice for the photothermal LCE actuators operated in the visible and near-UV range, carbon derivatives, and recently, polydopamine (PDA) [120], [121] have been used in LCEs for photothermal actuation in near-IR range.

2.2 Chemical Synthesis of the LCE Materials

2.2.1 Overview of Synthesis Methods

Liquid crystal elastomers are a large class of materials with versatile chemical compositions, different forms of coupling between the mesogens and the polymer chain. Hence, different LCE materials require different synthesis routes. Several methods of chemical synthesis have been developed previously in the literature; the principal difference is whether the procedure starts with polymeric or monomeric precursors. The methods have been previously classified in terms of the starting materials [16], [115], [122], or in terms of the chemical reaction [75]. From the viewpoint of the starting materials, below the four conventional LCE synthesis techniques are summarized, according to [65], [122]:

a) LCE synthesis from Poly(hydrosiloxane)

The "one-pot" reaction developed by Finkelmann [123] has been a widely used LCE synthesis procedure. The poly(hydrosiloxane) backbone chain, functionalized LC monomers, and crosslinker, are mixed together in the presence of a platinum catalyst. After formation of the weakly crosslinked gel in the first stage, the material can be stretched to induce anisotropic LC orientation, and then the second step of crosslinking fixes the LC alignment. Various mesogens can be used within this method; however, only side-chain LCEs can be produced [115].

b) LCE synthesis from LC polymers

This procedure uses pre-formed LC polymers or oligomers with additional functional groups. These are mixed with a multifunctional crosslinking agent, which reacts with these groups selectively at certain conditions. A partially

crosslinked material can be aligned uniaxially and further crosslinked. Various starting materials can be used in this procedure.

c) LCE synthesis from LC polymers containing crosslinking moiety

In this method, pre-formed LC polymers contain crosslinkable groups, which are enough to form a network. Crosslinking can be initiated by UV irradiation or thermal treatment.

d) LCE synthesis from LC monomers

This method is different from other approaches as it uses monomeric precursors. Functionalized LC monomers, crosslinkers, and radical initiators are mixed together; and the reaction is triggered by UV light or thermal curing. Polymerization and crosslinking are performed simultaneously within the one-step procedure. As opposed to LC oligomers with high molar mass used in the previous synthesis routes, the LC monomers have low molar mass. A variety of acrylate-functionalized LC monomers have been used within this method.

The latter approach using LC monomers has been of significant interest especially for the development of microsystems. The increasing interest in LCE materials for applications in microactuators and microrobots in recent years is largely due to the high degree of control over polymerization and crosslinking offered through this procedure. A significant advantage of this synthesis method is that the mixture of low-molar-mass monomers possesses low viscosity, allowing a variety of fabrication methods (capillary-filled cells, micromolding) and alignment methods (patterned surfaces, photoalignment, magnetic field etc.). Fast in-situ polymerization is enabled by photo-initiation, both at high temperatures or room temperature. These advantages make the one-step synthesis technique for polyacrylate-based LCE suitable for microfabrication and nanofabrication, which cannot be achieved via other synthetic routes [16]. The potential challenge is that the chemical reaction involving free radicals may be inhibited by oxygen from ambient air, leading to uneven crosslinking or altered alignment; therefore, the environment should be controlled [75], [124], [125]. Also, such reaction is non-selective, and propagates without further stimulus after it has been triggered, therefore, it cannot be stopped [75].

2.2.2 LCE Material System Using Acrylate-Functionalized LC Monomers

The chemical structure and mechanism of LCE polymerization from acrylate-functionalized LC monomers are discussed based on the example of the LCE precursors used in the experimental part of this thesis. Since the aim of this work was to study new fabrication methods and the performance of LCE-based actuators for applications in microsystems, the preparation of the LCE material follows the established chemical synthesis method based on the system of LC monomers demonstrated previously in the literature [88], [126]. The advantages are the easy one-step synthesis procedure, effective actuation performance, and control over the alignment pattern. The resulting material is a liquid crystal elastomer with polyacrylate backbones, with end-on LC mesogens in the side-chains, and with LC-containing cross linkers. The chemical components of the LCE precursor are described as follows: two reactive LC monomers, the photoinitiator, and in addition, the light-absorbing dye. The chemical structures of the components are shown in Figure 2.5.

The nematic reactive mesogen 4-methoxybenzoic acid 4-(6-acryloyloxy-hexyloxy)phenyl ester with the sum formula $C_{23}H_{26}O_6$, has a molecular weight of 398.45 g/mol. The mesophase behavior of the mesogen is the following: the temperature of the crystalline-nematic transition is 54.9°C, the temperature of the nematic-isotropic transition is 43.6°C. The rigid LC mesogenic unit, highlighted with a grey oval in Figure 2.5, is linked end-on to a flexible aliphatic tail (spacer) with a polymerizable acrylate end-group. The acrylate-functionalized monomers form pendant LC groups in the side-chains of the polyacrylate backbone in LCE. The nematic reactive mesogen 1,4-Bis[4-(3-acryloyloxypropyloxy)benzoyloxy]-2-methylbenzene with the sum formula $C_{33}H_{32}O_{10}$ has a molecular weight of 588.60 g/mol. The mesophase behavior of the mesogen is the following: the temperature of the crystalline-nematic transition is 59.4°C, the temperature of the nematic-isotropic transition is 128.2°C. The rigid LC mesogen, highlighted with a grey oval in Figure 2.4, is linked at both ends to the flexible spacers with polymerizable acrylate end-groups. Therefore, it acts as a liquid crystalline crosslinker, anchored at both ends to the polymer network in the LCE. The photoinitiator 2,2-Dimethoxy-2-phenylacetophenone with the sum formula $C_{16}H_{16}O_3$ has a molecular weight of 256.30 g/mol. This component is used to initiate the photo-polymerization of prepolymers, such as unsaturated polyesters and acrylates. The melting temperature of the crystalline substance is about 67°C.

4-methoxybenzoic acid 4-(6-acryloyloxy-hexyloxy)phenyl ester
(LC monomer)

1,4-Bis[4-(3-acryloyloxypropyloxy)benzoyloxy]-2-methylbenzene
(LC crosslinker)

2,2-Dimethoxy-2-phenylacetophenone
(Photoinitiator)

4-(4-Nitrophenylazo)aniline
(Azo-dye Disperse Orange 3)
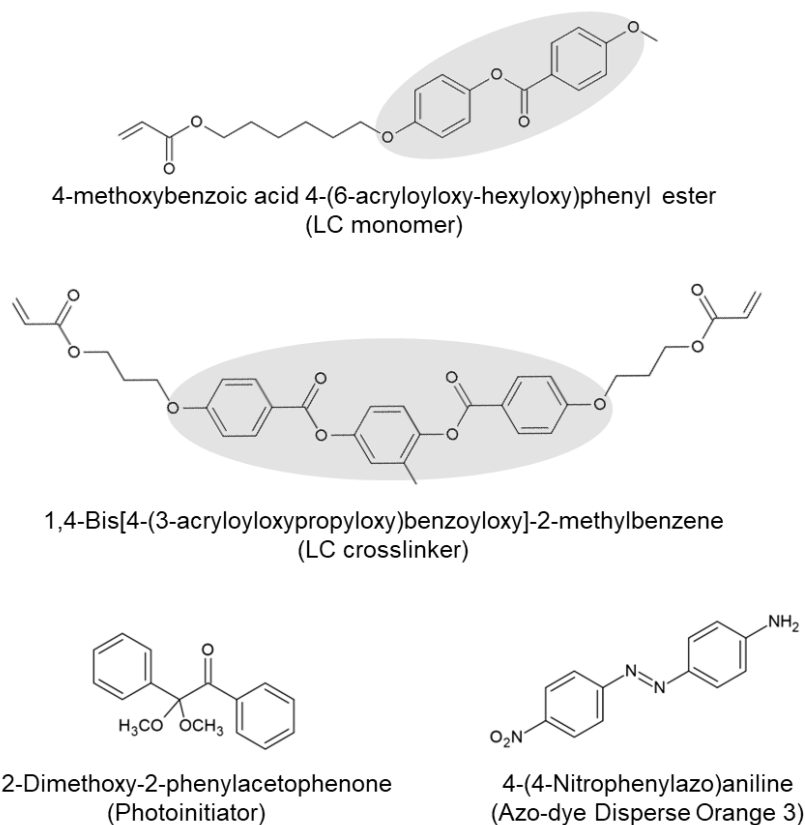
Figure 2.5 Chemical structures of the LCE components used in the work
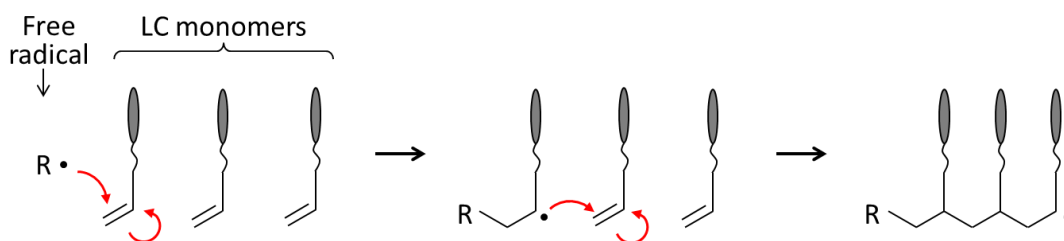
Figure 2.6 Reaction of polymerization in acrylate-based backbone LCE

The one-step synthesis of the LCE is carried out by radical polymerization, the principle has been thoroughly reviewed in the literature [16], [75], [115]. The essential components: LC monomers, crosslinker and photoinitiator; are melted and mixed together homogeneously. The mesogen alignment must be established at this stage. Then, under exposure with UV light, the photoinitiator molecule breaks down to form a radical with an unpaired electron, which triggers the process of polymerization. The polymerization reaction is shown schematically in Figure 2.6. The reaction is performed in the nematic state. The radical reacts with the C=C double bond, forming a new bond

and a new unpaired electron. Thus, once initiated, the reaction propagates further, forming a long polymer chain (polyacrylate backbone) with mesogenic side chains. The diacrylate LC crosslinker forms links between the polymer chains. Hence, the processes of polymerization, crosslinking and alignment occur simultaneously.

Finally, in order to enable light absorption for photothermal actuation, a chemical dye can be embedded into the LCE material. The dye used in this work is 4-(4-Nitrophenylazo)aniline (also known as Disperse Orange 3), an azo-dye with the sum formula $C_{12}H_{10}N_4O_2$ and the molecular weight of 242.23 g/mol; the structure was shown in Figure 2.5. It is a crystalline powder substance with the melting temperature of about 200°C. The light absorption spectrum of the dye is shown in Figure 2.7 [127]. The light absorption peaks are at the wavelength regions of 440-446 nm (with the extinction coefficient ≥22000) and 272-278 nm (extinction coefficient ≥9000). Upon illumination, the azo molecule releases a significant amount of heat and triggers a photothermal actuation response in the elastomer. The dye molecules do not form covalent bonds with the polymer, the dye is simply dispersed homogeneously in the material [78].
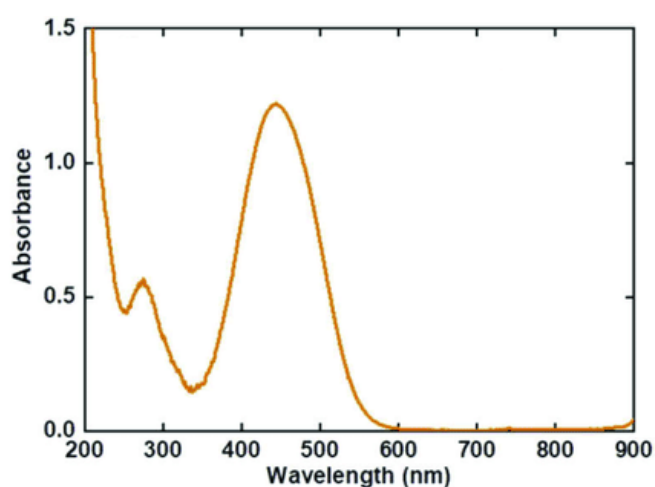
Figure 2.7 Light absorption spectrum of the azo-dye Disperse Orange 3. Reproduced from [127]

2.3 Alignment Methods for LCE

The actuation function in LCE materials is dictated by the internal alignment of LC mesogens, which must be formed prior to the final cross-linking stage. The advancement of the LCE actuators and applications is associated with the ability to locally control the alignment to achieve complex shape change in the LCE structures.

Alignment methods for LCEs can be categorized according to the physical principle used for alignment inducement [71]: mechanical stress-induced alignment, surface-induced alignment, and external field-induced alignment. Based on these general principles, versatile techniques have been developed and demonstrated previously in the literature. A summary of popular LCE alignment techniques is given in Table 2.2, where the methods are compared in terms of versatility of the alignment patterns, and quantitative measures of spatial control.

Table 2.2 Summary of methods for LCE alignment

Alignment principle	Alignment technique	Spatial control	Versatility of alignment patterns	Examples
Mechanical stress	Stretching (films)	can be patterned by selective crosslinking	Uniaxial, multiaxial	[14], [113], [128]
	Fiber drawing	-	Uniaxial	[76], [81], [129]
	Stamping/embossing	<1 mm	Programmable	[87], [130]
	3D printing	~100 µm	Programmable	[25], [89], [131], [132]
	External fluid flow (microfluidic)	~200 µm (particle size)	Bipolar (particles), uniaxial (fibers)	[92], [94], [96], [133]
	Molding in capillaries	<50 µm (channel size)	Uniaxial (along the channel)	[134]
Surface topology	Rubbing	~mm	Uniaxial, multiaxial, twisted	[78], [90], [110], [135]–[139]
	Oriented CNT	-	Uniaxial	[140]
	Patterned microgrooves	≤2 µm	Programmable	[24], [141], [142]
Surface effect	Surface properties	-	Homeotropic, tilted, planar	[19], [88], [137], [142], [143]
	Surface photoalignment	~100 µm	Programmable	[23], [88], [144]–[146]
External fields	Magnetic field	-	Uniaxial (direction of the field), radial	[22], [82]–[84], [124], [147]
	Electric field	electrode can be patterned (~100 µm)	Uniaxial (direction of the field)	[86]
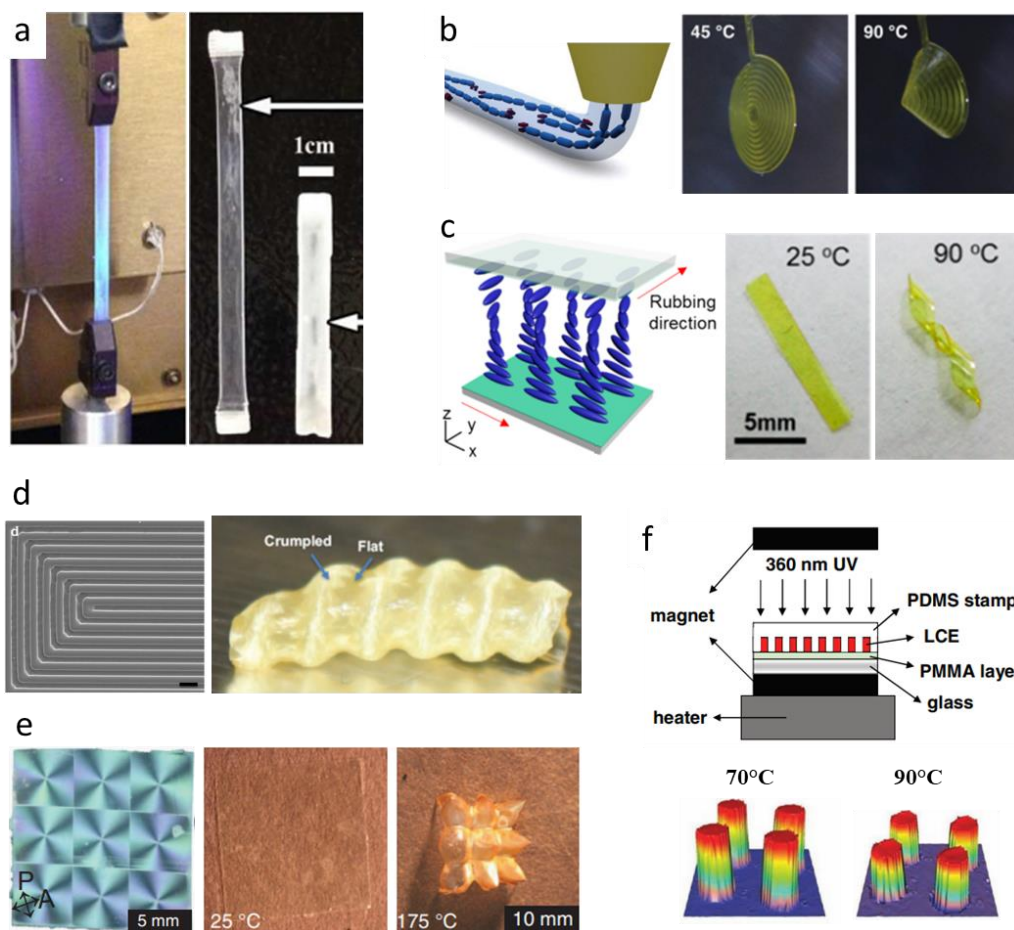
Figure 2.8 Examples of LCE alignment principles and shape change: a) alignment by mechanical stretching [113], b) extrusion printing [89], c) surface rubbing [139], d) patterned surfaces [142], e) photoalignment [23], f) magnetic field [83].

Figure 2.8 shows examples of different alignment principles and versatile actuation shapes that were achieved with each method. The mechanical stress methods are usually used to induce LC reorientation by uniform stretching (Figure 2.8a) [113]; recently, programmed alignment was enabled by extrusion printing (Figure 2.8b) [89]. Surface alignment methods rely on the LC interaction with the surface material, where both the surface shape and the material properties play a significant role. Unidirectional alignment near the surface is induced across a large area simply by rubbing (Figure 2.8c) [139]; whereas complex patterned deformation can be configured with high spatial precision using pre-patterned grooves (Figure 2.8d) [142], or photoalignment layers (Figure 2.8e) [23]. Finally, when using external fields for alignment, such as magnetic field, the orientation of LC mesogens is controlled with the direction of the field intensity (Figure 2.8f) [83]. Further in this section, the key methods of LCE alignment and recent progress is discussed in more details.

2.3.1 Stress-Induced Alignment

Stresses induced by mechanical forces have been widely used for alignment in some LCE materials, such as the polysiloxane-based and thiol-acrylate LCEs. The first polymerization step allows obtaining a partially crosslinked, gelated material, where a simple mechanical stretching can then be used to orient the rigid LC mesogens along the stretch direction [123]. A fully crosslinked system is obtained through the second polymerization stage. Stretching load can be applied along one or multiple axes; it has also been shown that a certain degree of control over the pattern can be achieved with selective UV curing [113], [128]. The mechanical stretching method is used for the alignment of the LCE films; while thin LCE fibers can be produced by pulling the molten LCE mixture with a tweezer [76], [129]. This alignment technique can be effective for macroscopic artificial muscle-like actuators, however, it has a very limited use on smaller scale. Apart from tensile stress, shear stress can be effectively used to create programmed alignment shapes in LCE structures by using templates for stamping and embossing [87], [130].

Recently, the 3D printing techniques become inexpensive and increasingly popular in microfabrication, since it has been shown that alignment of the LCE occurs due to shear and extensional forces while the polymer mixture is extruded through the narrow nozzle. The effect depends on the printing speed, ink composition, and rheology factors [25], [89], [131]. A programmed printing process enables high spatial and parametric control, complex 3D alignment patterns can be realized in printed LCE structures.

Alignment of LCE can also be achieved by coupling with the adjacent fluid flow, through the microfluidic fabrication method. LCE microparticles and fibers are formed by injecting the pre-polymer in a fluid stream. The shear flow of the fluid interacts with the polymer surface and introduces a field director [92], [94], [96], [133]. In the result, fabricated LCE particles, shells or fibers are capable of shape changing under actuation. Additionally, the alignment effect has been demonstrated through the capillary micromolding method [134]. When the LCE precursor fills the long and narrow molding channels via capillary motion, the LCs tend to align along the channel due to the fluid shear force and due to the symmetry of the confined channels. This method is effective in producing LCE microwires with uniform alignment, when the channel width is less than 50 μm.

2.3.2 Surface-Induced Alignment

Surface alignment effect comes from two factors: the surface topology, where microscopic grooves are capable of inducing preferential directional alignment of LCs, and the surface chemistry, i.e. interaction of the LC molecules with the surface molecules of the alignment materials [71]. LC orientation propagates into the bulk material, but to a limited thickness, typically estimated as ≤100 μm, due to decay in the molecular order further away from the surface [115]. Surface alignment methods are very effective for creating versatile alignment patterns in the thin flat LCE sheets using instantly polymerizable acrylate-based LCE materials.

The standard technique of surface rubbing has been used for alignment in LC displays for several decades [148], and currently it is extensively used in LCE devices [90], [110], [135]–[137]. In this method, a substrate coated with an alignment layer (e.g. polyimide) is mechanically rubbed in one direction, for instance, with a synthetic cloth, which produces unidirectional micro- and nano-grooves on the surface. LC mesogens adopt the monodomain alignment parallel to the grooves near the surface. This method is simple and efficient for uniform orientation over a large area. When the liquid LCE precursor is filled into a cell between two substrates with different direction of alignment, this creates a twisted alignment across the thickness of the LCE layer. Also, it is possible to create a spatially modulated pattern with alternating rubbed and non-rubbed areas by applying mask with about 1 mm wide openings during rubbing [78]. The drawbacks of rubbing technique are lack of spatial control, unsuitability for irregular surfaces [149], as well as electrostatic charge and contamination caused by rubbing [142]. Soft imprinting of the alignment layer through PDMS replica have been also demonstrated in practice [150], [151]. LCE alignment assisted by nanomaterials have been demonstrated, such as using a sheet of highly aligned carbon nanotubes (CNT) of 10 nm diameter, which promotes uniform orientation of LC molecules, additionally enhancing mechanical strength of the composite, providing electrical conductivity and increased light absorption [140].

Surface topology assists in the alignment of LC; however, an adaptable non-contact method with high spatial control is essential for micro-scale fabrication. This is achieved by using pre-patterned microgrooves [24], [141]. Microchannels can be patterned on the substrate from a UV-curable material by conventional photolithography. Microgrooves can be patterned on both upper and lower cell surfaces;

therefore, homogeneous, twisted, splayed architectures are possible. The reorientation of LC molecules is mainly due to the elasticity effect in nematic LC [152], the liquid crystals reorient to minimize the angle between the mesogen axis and the direction of the groove. Analytically, the surface anchoring strength of microchannels is expressed in equation (2.3) [142], [152]:

$$\rho_{max} = \frac{\pi^2 K A^2}{\lambda^3} \tag{2.3}$$

where ρ_{max} is anchoring energy density, K is average elastic constant of LCs, A and λ are amplitude and wavelength of microgrooves, respectively. Therefore, deeper and narrower grooves have a stronger alignment effect, however, the microgrooves of up to 2 µm in size were demonstrated for successfully control of the LC alignment [142]. This alignment method is highly efficient in realizing complex spatially controlled alignment on microscale: parallel, circular and radial microgrooves [24], miniaturized topological defects [142]. Non-trivial modes of LCE actuation are achievable with this approach.

Not only surface topology, but also the surface chemistry plays an important role in LC orientation. Surfaces from different materials can induce planar, tilted, or perpendicular (homeotropic) orientation of LCs. For instance, untreated polyimide produces a strong homeotropic LC anchoring, which becomes planar after rubbing. Splay alignment in LCE films (homeotropic at one surface, planar at the opposite surface) is used in numerous applications for bending actuators. A clean polydimethylsiloxane (PDMS) surface, the material used for replica molding, also induces homeotropic alignment due to the low surface energy [143], [153]; transforming to planar alignment is possible by using chemical treatment and coatings [153].

Another widely used technique is photoalignment. This principle implies interaction of LCs with photosensitive alignment layers on the substrate, where the surface alignment properties are configured using polarized light. This technique is non-contact and contamination-free. A significant advantage is the ability to perform alignment in mechanically inaccessible areas, such as in a closed cell [149]. The alignment layer is produced from materials capable of molecular orientation under linearly polarized illumination; reviews of typical photoaligning materials can be found in [149], [154]. Certain mechanisms are irreversible, while some materials allow optical rewriting [149]. Local control over alignment pattern is achieved by using photomasks. Compared to the other alignment methods, this method is most effective in producing azimuthal, radial [88], spiral [144] orientation. For this purpose, samples can be illuminated with linearly polarized light through a narrow wedge mask, while the substrate is rotated. Azimuthal

LCE films demonstrate cone-shape deformation upon actuation. A significant contribution was made recently with the development of a computer-controlled point-by-point exposure method [23]. Programmed alignment of individual "voxels" as small as 0.0005 mm^3 allows creating arbitrary patterns with high local resolution.

2.3.3 Field-Induced Alignment

Under the influence of magnetic field, LC mesogens align along the field lines [155], due to diamagnetic nature of organic molecules. Magnetic field can induce current in the aromatic ring; therefore, the LC molecule tends to orient towards the minimum energy position to reduce the flux, i.e. parallel to the field [156]. To achieve alignment, the material must be cross-linked at the moment when magnetic field is applied. A common approach is to use rare earth permanent magnets which provide sufficient field strength. Apart from vertical alignment [82], [83], [124], also planar [147] and radial [22] alignment have also been demonstrated using custom-made setups. This method is particularly effective for the widespread LCE applications such as surfaces with switchable properties containing vertical micropillars [82]–[84]. The micropillars of aligned main-chain LCE are capable of large reversible contraction of 300-400% [82]. The magnetic field-assisted alignment method is efficient in providing nearly perfect homeotropic orientation [155], however, it lacks spatial control. Magnetic field induces strong anisotropic alignment of LC mesogens in large volumes of the material. This method is most suitable for thick LCE films (several hundred μm), or for the structures with embedded elements which might cause scattering of light [22].

The effect of external electric field on liquid crystals arises from the dielectric anisotropy of LC molecules in the mixture [157]. This property was utilized to achieve homeotropic alignment in LCE under electric field for the responsive surface application [86]. The areas with LC alignment were locally patterned by patterning the shape of the electrode.

2.4 Fabrication Methods for LCE Actuators

The choice of a fabrication method for LCE actuators is based mainly on the size and shape of the structure in a particular application. Several different fabrication techniques

have been demonstrated previously in the literature. A comparison of the popular LCE fabrication methods is given in Table 2.3; each method is suitable for fabrication of a particular type of the structures and is capable of providing a limited feature size. For example, the usual method of fabricating flat LCE films of various thicknesses is inside a flat cell between two glass slides. Patterned surfaces with switchable adhesion properties, which have the most popular applications of LCE, are typically produced by molding using a soft replica from pre-fabricated templates. A flexible and versatile 3D printing method using LCE materials has recently become increasingly popular for various applications.

Table 2.3 Summary of methods for LCE fabrication

Fabrication method		Minimum feature size	Versatility of structural shapes	Examples
Planar glass cells	Manual or laser-assisted cutting	~ mm	Flat films, stripes, and various cut shapes	[77], [78], [88], [126], [144]
	Photo-patterning	~ µm	Patterned flat structures	[19], [81]
	Multi-phase photo-patterning	~ µm	Patterned flat films with selectively aligned areas	[138], [158]
	DLW / TPA	<1 µm	2D and 3D structures	[79], [93], [159]–[161]
Soft lithography	Replica molding / embossing	<1 µm	Micropillars; structures replicated from templates; LCE with embedded elements	[22], [82], [84], [124], [162]–[164]
	Microtransfer molding	15 µm	Isolated or interconnected structures from templates	[20], [83]
	Microcontact printing	8 µm	Stamped 2D patterns	[165], [166]
	Capillary micromolding	5 µm	Microwires, gratings	[134]
Printing	3D- and 4D-printing	100-150 µm	3D structures (multi-material structures possible)	[25], [89]
	Ink-jet printing	150 µm	2D structures (multi-material structures possible)	[137]
MEMS-analogous micro-patterning		1.5 µm	MEMS-integrated LCE layers	[146]
Microfluidic		Ø 20 µm (fibers)	Particles, shells and fibers	[92], [94], [96]

A standard procedure to prepare LCE films is by using flat glass cells. Two glass substrates, which may be coated with an additional layer of material for surface-induced

alignment, are fixed together with a spacer of a certain thickness in the middle. The molten LCE mixture is infiltrated into the cell by capillary action, and cooled down to the nematic phase. At this stage, LCs must obtain pre-designed alignment, and afterwards the material is finally polymerized and cross-linked by UV exposure. The cell can then be manually opened, and the cured LCE film can be detached from the substrate. For macro-scale applications, the film can be cut into stripes or other shapes. Manual cutting with a blade or scissors provides limited control and feature size, but it has been used to demonstrate simple structures, such as caterpillar-inspired crawling soft robots [77], [78]. More detailed pre-designed structures are made using a blade with robotic control for cutting [88] or laser-assisted cutting [126].

Pre-designed LCE structures can be made by selective UV exposure using a photomask placed on top of the glass cell. The non-polymerized material can be removed with solvents. The mask based exposure method provides flexibility of the pattern; for instance, to produce free-standing LCE disk actuators in [81] or to configure transparent regions in [19]. A multi-phase photo-patterning method was suggested for LCE films with selectively aligned areas [158]. After the first mask exposure, the exposed regions preserve LC alignment. Instead of dissolving the rest, the material is brought to the isotropic phase at an elevated temperature, where the second "flood" exposure is performed in order to polymerize the remaining areas of the film. This method enables various 3D actuation in flat LCE films, such as bending, folding, curling and buckling [138].

LCE structures with sub-micron resolution and 3D shape have been demonstrated by fabrication through direct laser writing (DLW) and two-photon absorption (TPA) techniques [79], [159], [160]. A two-step DLW process has been used to fabricate non-reciprocal actuators with different alignment and material properties [93], [161]. These are powerful techniques leading to versatile, truly 3D, high-resolution LCE microactuators and applications.

A different method of fabrication of the LCE structures is soft lithography, i.e. molding. Molding is a well-established method widely used for polymer-based fabrication in microfluidics and other applications. A master template is replicated into a soft mold, usually made of polydimethylsiloxane (PDMS), which is then used to fabricate LCE-based structures. Several soft lithography techniques exist, such as replica molding, microtransfer molding, microcontact printing, and micromolding in capillaries [167], [168]. Molding methods are of significant interest for LCE-based microfabrication due

to their scalability, versatility of structural shape, high resolution and surface quality [124]. Moreover, using silicon templates with nano-structures, features of the size of <1 µm can be replicated in an LCE [162], [164].

The replica molding technique uses the PDMS mold with inverted structures. A molten LCE material is either filled in the mold cavities, or casted on the substrate and pressed with the mold (embossing technique). Then, the LCE is cooled down and crosslinked by UV curing. Simultaneously, LC alignment is induced by magnetic field or other technique. Replica molding is commonly used to fabricate stimuli-responsive surfaces with micropillars [82], [84], [124], and also for structures with embedded elements [22], [163]. In microtransfer molding, LCE is filled into the recess of the PDMS mold; the mold is then pressed onto the substrate, the material is UV-polymerized, and the mold is detached. Unlike the previous technique, this method allows producing both isolated and interconnected structures, as well as multi-layered structures [43]. This technique was used to transfer LCE pillars onto a separately prepared and pre-coated substrate [20], [83]. Microcontact printing, or stamping, uses a soft stamp to transfer the LCE-based "ink" onto the substrate, and cure the resulting pattern with UV light. The LCE structures have demonstrated change in the height by thermal actuation [166]; however, the method suffers from lack of thickness control and uniformity [165]. In the capillary micromolding method, the PDMS mold is attached to the substrate, and the molten mixture is filled in the microchannels by capillary motion. This approach was used to fabricate LCE gratings and microwires [134].

Recently, 3D printing of LCE structures has emerged as a powerful method for fabrication of versatile LCE actuators due to the capability of producing structures of arbitrary shape and thickness; combination of different materials is also possible. The LCE ink is dispensed through the nozzle at the elevated temperature, and this is followed by UV crosslinking [25], [89]. 3D-printed structures with programmed LC alignment are capable of complex 3D actuation, and they have shown relatively high work capacity. The fabrication technique has vast potential for state-of-the-art applications such as soft robotics, haptic surfaces, adaptive optics and other applications [89]. However, the minimum feature size is limited with the diameter of the nozzle, typically about 100-150 µm. Another printing method, ink-jet printing, was also demonstrated for LCE fabrication using a commercial ink-jet printer [137]. Artificial LCE cilia actuators produced by ink-jet printing can potentially be used in lab-on-a-chip systems. This method also allows combining multiple materials in a printed structure.

Although versatile structural shapes of LCE actuators are possible using photo-patterning, molding and printing fabrication techniques, practical applications are often limited due to integration of the LCE parts into larger systems. In many MEMS applications, it may be required to be able to pattern the structure locally, avoiding mechanical processing and post-assembly. Therefore, a MEMS-like fabrication method for LCE has been demonstrated recently [146]. It is based on conventional processes used for MEMS fabrication such as spin-coating, photolithography, plasma-assisted etching; however, the critical factor is the choice of materials and solvents with high selectivity. Deformable LCE actuators of various shapes can be fabricated with 1.5 μm resolution.

The microfluidic method has been used to produce freely suspended LCE microparticles capable of shape changing under actuation stimuli [94], and LCE fibers [96]. Droplets of LCE mixture are injected into a microfluidic stream, which also assists the LC alignment, and polymerized by UV exposure. The diameter of the particle/fiber is controlled with flow velocity. More recently, LCE shells with a liquid core have been prepared by this method for application as active one-piece micropumps [92]. The microfluidic fabrication technique is limited to microparticle and fiber-type structures, but it provides continuous, automated fabrication with high throughput.

2.5 Actuation Methods for LCE

The LCE actuation mechanism is not limited to the temperature-induced phase change. Several actuation methods based on different stimuli have been demonstrated [116], [169], such as thermal, photothermal, photo-mechanical actuation, solvent/pH/humidity-induced actuation and electro-mechanical actuation.

Thermal actuation is related to the liquid crystalline-to-isotropic phase transition at the elevated temperatures, and thermal expansion. Thermal energy can be brought to the LCE structure by several ways: a) by raising the temperature of the environment, such as in a liquid medium; b) by resistive heating of a conductive path attached/embedded in the structure; or 3) by photo-thermal conversion using the light-absorbing agent incorporated in the LCE. For electrothermal actuation, it may be challenging to integrate conductive tracks into dielectric LCE. Electrical "wires" must be flexible in order to allow large deformations in the elastomer; moreover, LCE has poor adhesion to metals

and silicon. Several methods have been proposed in the literature, such as using conductive ink [14], wrapped [170] or sandwiched [171] metallic wires, dispersed conductive particles [116], embedded metal-polyimide heaters [22], [163], encapsulated liquid metal heaters [128], or microheaters placed at the base of the LCE pillar [172].

Remote actuation using light is a significant advantage for many applications, which require actuation performed in a mechanically inaccessible area (for microrobotics, drug delivery applications), or if electrical connection is impossible. Commercial light-absorbing chemical dyes and carbon-based nanoparticles are widely used to enable photothermal actuation in LCE [119]. Azobenzene-based dyes undergo cycling photo-isomerization under illumination within the absorption band in visible or UV range, releasing a significant amount of heat. Photothermal actuation is performed with high speed, high control and local resolution. Lasers or focused LEDs are commonly used for controlled actuation of LCE structures. Structured light has been used to perform selective or propagating actuation, such as for directional robotic locomotion [78], [81]. Actuation with sunlight has been demonstrated in autonomous LCE actuators [173].

Photo-mechanical actuation mechanism [105] arises from photo-isomerization of the light-sensitive azobenzene compounds in the LCE material. Azobenzene is a UV-responsive molecule that undergoes shape change from trans-isomer to cis-isomer form under illumination, where cis-isomer requires larger volume. Upon molecular shape change, the internal order is disturbed, leading to macroscopic shape change. The amount of the absorbed light is larger near the LCE film surface, and is usually attenuated further into the material layer. Depending on whether AZ molecule is located in the crosslinker part or side-chain part, the actuator will bend towards or away from light source, respectively. This actuation method allows spatio-temporal control and reversible 3D motion in different directions under polarized light illumination [174].

The thermal/photothermal and photo-mechanical actuation described above are the most widely used methods for LCE actuation in various applications. Additionally, actuation based on LCE response to solvents, moisture, or pH level has been demonstrated in the literature, which potentially gives rise to LCE-based sensor applications [23], [136], [145], [175]. The actuation arises from anisotropic swelling, causing disturbance in the molecular order. Also, electro-mechanical actuation was observed in ferroelectric LCEs, LCE composites, LCE with increased dielectric constant and other LCE materials [116], [176]–[178].

2.6 Finite Element Simulation Methods for LCE Actuators

Due to the complex physics behind the spontaneous deformation in nematic liquid crystal elastomers, modeling of the LCE actuators remains a challenge. There is no single universal method for numerical simulation of the behaviors of LCE actuators. For finite element method (FEM) based analysis using commercial software, various behavioral models have been proposed in the literature. These models are often based on the equivalent actuation effects, in order to represent the collective effect of strains arising in the material upon actuation and leading to deformation of the initially flat LCE structures.

A common approach to modeling the thermal actuation in LCE is by modifying the thermal expansion coefficients in the model. Firstly, in the uniaxial aligned LCE materials which shrink along the LC director upon heating, the shrinking strain can be calculated from measurements of the length of the LCE actuator at various temperatures. The temperature-dependent shrinking strain is usually presented with a complex nonlinear curve [14], [109], [179]. The shrinking deformation of LCE can then be modeled using temperature-dependent anisotropic coefficients of thermal expansion. The CTE values in this case have been modeled as a piecewise fitting function derived from the measurements of strain [128], [180]. The monodomain LCE films are used in combination with other materials to form bimorph structures, large curling deformation of the LCE-based bimorphs was simulated using the temperature-dependent anisotropic CTE in [180]. The same principle was also used in modeling the deformations of the patterned LCE actuators in [128].

To simulate bending and rolling deformation observed in splay aligned LCE films, the functionally graded model has to incorporate the variation of LC alignment across the thickness of the layer. The model demonstrated in the literature based on anisotropic thermal expansion was built in three layers, representing areas with homeotropic, tilted (45°), and planar LC alignment [181], [182]. The CTE was given in a tensor form, based on the anisotropic thermal strain measured in orthogonal directions. Although in practice the LC orientation has a continuous variation through the thickness of the splay film, the three-layered model showed a good approximation of the actuation behavior [181]. A similar three-layered model was used to simulate the unique rolling behavior of the film with tapered thickness along the actuator [182], however, the simulation could only provide accurate prediction for the temperatures below 65°C (glass transition

39

temperature). The simulation approach using layered models is convenient for representing the internal gradient of properties, and it has been demonstrated previously for other non-polymeric materials, such as for structures which bend due to residual stresses after fabrication. To simulate the presence of a stress gradient in these materials, each layer must be assigned with a local stress value [183], [184], or a calculated CTE value [185].

Another computational method for LCE actuators demonstrated in the literature was based on anisotropic stretch factors [186], obtained from the measured thermoelastic curve. A model based on anisotropic stretch factors has also been used to simulate the bending behavior of a LCE film with splay alignment, assuming a continuous gradient of material properties throughout the thickness [187].

In LCE structures with locally patterned alignment leading to complex 3D actuation behaviors, finite element modeling may require dividing the geometry into a large number of small domains, followed by detailed configuration of the local properties in the individual domains. For instance, folding of the LCE hinges was modeled in [13] through introducing local spontaneous strain tensors based on anisotropic expansion coefficients. In each small domain, the tensor was transformed according to the actual LC orientation rotated with respect to the reference direction. The model was capable of predicting various complex deformation shapes. In photothermal LCE actuators, controlled local actuation can be induced using spatially modulated laser beam. Numerical modeling for such systems was performed by introducing a local photo-strain tensor [188], [189]. LCE-based photothermal microrobots with a patterned LC director in the given examples from the literature performed controlled movement (crawling, rotating) under the traveling light stimulus; the dynamic simulation model was used effectively to study deformation propagating across the LCE structure in time. Another effective simulation technique for predicting the mechanical response as function of strain in patterned LCE films is based on elastodynamics. A finite element elastodynamics model was demonstrated in [98], [145], [190], [191] for LCE films with twisted alignment, where the LC director varied smoothly across the thickness. The model was based on the coupling between the strain and the nematic order in small volume elements. The Hamiltonian-based model included kinetic energy, elastic energy, and coupling between strain and nematic order. The strain was presented with a piecewise constant function. To represent the effect of an external thermal stimulus in the simulation, the nematic order parameter was changed. The relationship between the

temperature and the order parameter could be obtained by fitting experimental and analytical data of the elongation of a uniformly oriented LCE. As the temperature increases, the nematic order decreases. The 3D simulation model was capable of predicting programmed shape evolution with various topological defects in LCE actuators.

Numerical simulation is a valuable design tool in research and applications of LCE-based actuators due to complex locally programmed actuation response of the material. However, it remains challenging to characterize the mechanical performance of actuators with non-trivial design. It has been shown that various equivalent effects can be used to mimic the behavior of the programmed LCE layers under various stimuli, which allow using commercial finite element software for LCE modeling. Still, simulation usually relies on using the reference experimental data for the material's highly non-linear, anisotropic properties. With the growing interest in developing LCE actuators for practical applications, there is a great demand for more efficient, more accurate, more flexible methods for simulation of the LCE-based systems.

2.7 LCE for Applications in Microgrippers and Microrobotics

LCE materials can be used for applications in soft stimuli-responsive microgrippers in microassembly, biomedical and microsurgical devices [9], [192]. In the thermally actuated microgrippers fabricated from traditional materials such as silicon, metals, or SU-8, the functionality is determined by the structural design, which must efficiently transform the thermal expansion of the beams into lateral movement of the gripper tips. In comparison, grippers based on LCE materials could be realized with a simple robust structure, which bends due to the internal variation of the LC director in the structure, and could provide large deflection at relatively low actuation temperatures and a soft grip without damaging the object. Fast remote micromanipulation can be achieved through photothermal actuation. A number of studies have demonstrated grippers produced from a splay-aligned LCE with out-of-plane bending [19], [93], [193], [194]. Usually, the LCE films are manually cut and attached to the tip of the holder (wire, probe) in order to perform gripping of an object. Figure 2.9a shows example of such LCE photothermal gripper (artificial flytrap) capturing an object of few millimeters in size; Figure 2.9b shows a LCE microhand picking a micro-size particle. The assembling

41

process of the microgripper increases the cost and complexity of fabrication and may limit integration of the device into larger systems. This factor becomes crucial, taking into account the small size of the objects in the typical micromanipulation tasks, for instance, manipulation of biological cells and objects of tens to hundreds of microns in size.

Some examples of LCE grippers fabricated by 3D printing have been demonstrated [131], [132], such as an electrothermal gripper shown in Figure 2.9c, where the orientation of the LC mesogens could be controlled by extrusion. Although it is an efficient rapid prototyping technique, but the minimum feature size of the structure is limited by the size of the printing nozzle, and hence, these grippers can only be used for relatively large centimeter-scale objects. An electrothermally-driven gripper with a Si-based frame and LCE actuator, shown in Figure 2.9d, had in-plane operation, unlike the other LCE-based grippers, however, the LCE actuator itself was operated by a simple longitudinal contraction [170]. The main drawback of this system was the multi-material structure that required complex assembling.
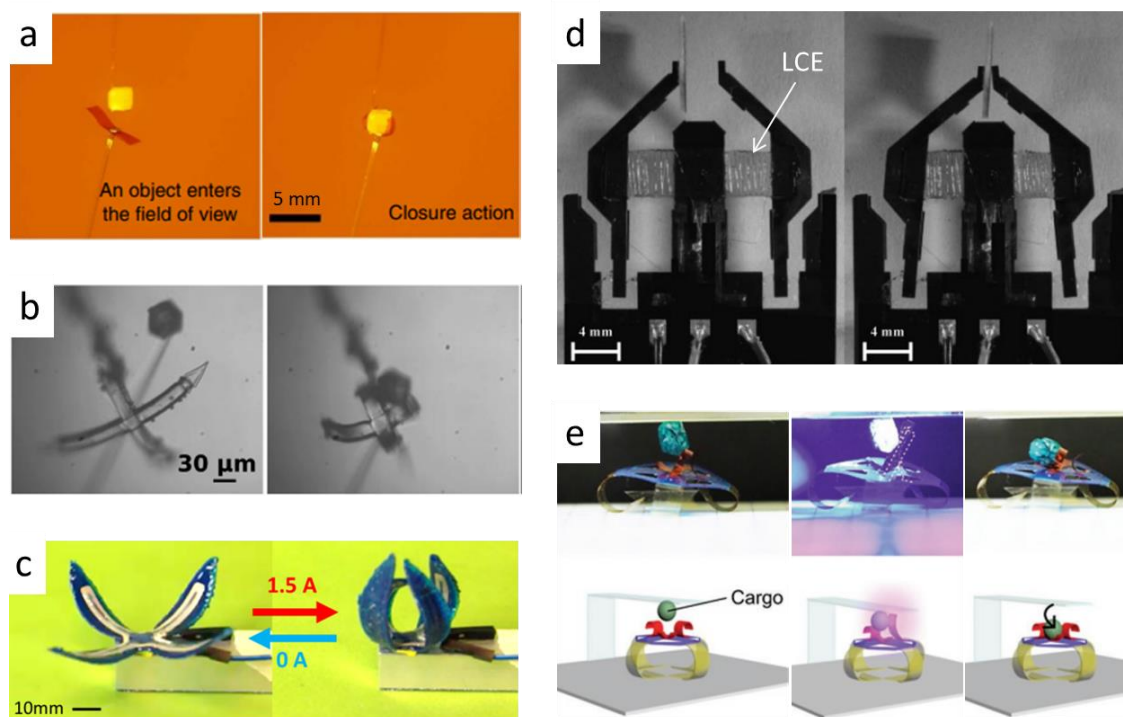
Figure 2.9 LCE-based applications for object manipulation: a) LCE artificial flytrap [19], b) LCE photonic microhand [93], c) soft robotic LCE gripper [132], d) gripper based on the LCE actuator [170], e) cargo-transporting LCE microrobot [195].

In the last couple of decades, LCE materials have emerged as a key candidate for applications in soft robotics [4], [11], [12], [196]. The remarkable properties of LCE for spatially controlled actuation have been utilized to mimic motion of living organisms: inching, crawling, leaping or swimming. However, the majority of the soft LCE-based robots demonstrated to date can only perform unidirectional locomotion [18], [78], [188], [197]–[200]. Sometimes, the walking direction is determined externally by the grated surface [77], [79]. Recently, it has been shown that the motion of LCE soft robots and actuators can be modulated by asymmetric light irradiation [126], [201], selective actuation of LCE doped with different dyes [202], precise spatiotemporal control of the laser beam [81], [189]. In-plane bending of the LCE actuators can be programmed through selective crosslinking of different LCE sections [128], [203]. However, these methods have limited potential for miniaturization, and can be rather complex in operation. Moreover, the existing LCE-based soft robots are largely limited to a single task of locomotion. The first miniature photothermal LCE robot with 2D locomotion freedom and object transportation ability was constructed from splay-aligned LCE layers, it could pick a hanging object, transport and offload it [195]. The robot is shown in Figure 2.9e. The motion and cargo pickup functions were separated due to different sensitivities of the chromophore in different parts of the robot.

Many microorganisms, which inspire the modern microrobotic technologies, use cilia and flagella parts for propulsion, sensing, gripping and autonomous operations [10]. Artificial cilia-like actuators are also used in microfluidics and lab-on-a-chip systems for active fluid mixing and other functions [204], [205]. A light-driven artificial LCE cilia with splay alignment has been demonstrated in the literature exhibiting out-of-plane curling [137]. It has also been shown that in the photo-mechanical LCE actuators containing azobenzene compounds, the bending of LCE cilia can be guided by the direction of the light stimulus and relies on the depth of penetration of the light [129], [206], [207]. But at the same time, low versatility in patterning may be a limiting factor for some advanced robotic applications. To date, no example of thermally actuated in-plane bending LCE cilia has been reported. Development of the in-plane bending LCE actuators could enable new modes of gripping and locomotion in LCE microrobots and systems for micromanipulation which was the aim of the thesis work.

2.8 Summary

In the last couple of decades, a growing interest has been demonstrated for developing smart soft microrobots and microgrippers for micromanipulation, which would be responsive to various stimuli and allow untethered actuation, such as light, humidity, pH-induced actuation, alongside with the traditional thermal, electrothermal, electrostatic, or electromagnetic actuation approaches.

Extensive research on microgrippers based on SU-8 polymer has been demonstrated previously in the literature. The electrothermal SU-8 microgrippers offer large gripping strokes under relatively low actuation voltages (below 1 V), which is several times more efficient than the traditional silicon and metal-based microgrippers. However, generally, SU-8 based fabrication is a well-established process based on standard photo-lithographic techniques. The current prospects in the field of SU-8 microgrippers are limited to studies of reliability, investigation of SU-8 composites with nanomaterials for enhanced material properties, and novel device designs with improved performance. Other than actuators, SU-8 is traditionally used in a wide range of applications, such as fabrication of the master templates for subsequent molding, which is of interest in the current work.

Liquid crystal elastomers have been at the forefront of the field of smart materials and soft actuator technologies in the last two decades. This is due to the main advantages such as complex programmable deformation, sensitivity to multiple stimuli, and large work capacity. LCE materials offer unprecedented level of spatial control over the deformation pattern, as compared to other polymers, using various methods of alignment of LC mesogens. Therefore, LCE based technologies open up significant possibilities in the development and programming the response of soft microrobots, soft grippers with low actuation stimuli, and biomimetic applications. A significant research has already been presented on LCE actuators, however, there is a high demand for further developments in several key areas, such as: methods for monolithic fabrication of the microgrippers and actuators, integration of the LCE parts into larger systems, cargo transportation capability for microrobots, new functionalities and new applications for microstructured LCE, and efficient finite element simulation techniques.

Chapter 3   A Fabrication Method for Lateral Bending LCE Microbeams

3.1 Introduction

The use of micropatterned surfaces has been one of the most popular and effective methods to control the orientation of LC mesogens [142]. Microgrooves on the planar substrate are able to induce alignment of LCs with a high degree of order over large areas, such as in the flat LCE films with uniform, twisted or splayed director. But despite the flexibility of local patterning, microgrooved surfaces have only been used to produce LCE structures for out-of-plane bending. However, many planar micro-electro-mechanical systems typically operate based on the lateral bending of the functional parts. One key application of lateral microactuators is a microgripper for manipulation of the objects on sub-millimeter scale. With the existing fabrication methods, such LCE actuator systems require further assembly in order to be used for practical applications for in-plane actuation. The work described in this chapter focuses on developing the monolithic microfabrication technique to realize the new in-plane bending function in LCE microactuators and microgrippers by controlling the LC orientation gradient across the width of the narrow microbeams using microgrooved vertical surfaces.

Considering the small dimensions in sub-millimeter range of the actuators for typical applications in micromanipulation, the method suitable for implementing the LCE actuators is micromolding. In the last two decades, molding techniques have been widely used in LCE-based fabrication, such as for creating surfaces with switchable properties using micropillars [20], [83], [84]. Such micropillars have a simple structure, and the LCs are usually aligned uniformly. In contrast, in the present work the fabrication by capillary micromolding was combined with local patterning of the mold for alignment purpose to realize complex free-standing LCE structures. The fabrication process was developed, which enables the new actuation functionality and monolithic fabrication for LCE actuators on microscale. This chapter discusses various steps of the process for fabrication of the LCE actuators: both the out-of-plane actuators based of the flat LCE films, and the in-plane microactuators based on the new combination of methods.

This chapter is partly based on the results from the Publication (4).

3.2 Preparation of the Liquid Crystal Elastomer Precursor

This section discusses the preparation of the liquid LCE precursor mixture, which is used for fabrication of both the flat LCE films and the more complex patterned LCE microactuators. The materials and equipment required for preparation of the molten LCE precursor mixture are as follows:

- LCE components: 4-methoxybenzoic acid 4-(6-acryloyloxy-hexyloxy)phenyl ester (LC monomer), 1,4-Bis[4-(3-acryloyloxypropyloxy)benzoyloxy]-2-methylbenzene (LC crosslinker), 2,2-Dimethoxy-2-phenylacetophenone (photoinitiator), Disperse Orange 3 (azo-dye)
- Materials and instruments: glass vial, spoon for dry chemicals, paper, tissues
- Equipment: laboratory scales, hotplate, vortex mixer
- Personal protective equipment (PPE): protective eye glasses, nitrile gloves, lab coat

The LCE precursor was prepared using two reactive liquid crystalline components, both purchased from Synthon Chemicals; which will be further referred to as 'LC monomer' and 'LC crosslinker' for simplicity. The precursor also contained the photoinitiator and the light-absorbing azo-dye, both purchased from Sigma Aldrich. All components were used as received. The chemical structure and properties of the materials were discussed in Section 2.6.2. In this work, three different LCE material recipes were used with different concentrations of the light-absorbing dye (LCE Precursors 1, 2 and 3). The dye was added in the LCE material to enable remote photothermal actuation, whereas the undoped LCE was used for thermal actuation. The molar ratios of the components in the mixture are listed in Table 3.1. The proportion of the LC monomer to the LC crosslinker in all mixtures remained the same.

Table 3.1 Components of the LCE precursors used in the work

LCE recipe	Molar fractions of the parts			
	LC monomer	LC crosslinker	Photoinitiator	Azo-dye
LCE Precursor 1	79 mol%	20 mol%	1 mol%	–
LCE Precursor 2	78.2 mol%	19.8 mol%	1 mol%	1 mol%
LCE Precursor 3	77.4 mol%	19.6 mol%	1 mol%	2 mol%

The molar fraction of each component in the mixture is expressed with equation (3.1):

$$x_i = \frac{n_i}{n_{total}}, \tag{3.1}$$

where x_i is the molar fraction of the ith substance in mol%, n_i is the amount of the substance in the mixture expressed in moles, and n_{total} is the total number of moles of all substances in the mixture. The mass of each dry component in the mixture can be calculated with equation (3.2):

$$m_i = n_i \times M_i, \tag{3.2}$$

where m_i is the mass of each substance in grams, and M_i is the molar mass of each substance in g/mol. The molar mass of the LC monomer is $M_1 = 398.45$ g/mol, for the LC crosslinker $M_2 = 588.60$ g/mol, for the photoinitiator $M_3 = 256.30$ g/mol, and for the azo-dye $M_4 = 242.23$ g/mol.

For preparation of the LCE Precursor 1 without dye doping, the molar fractions of the LC monomer, crosslinker, and photoinitiator were $x_1 = 0.79$, $x_2 = 0.20$, and $x_3 = 0.01$ respectively. In the fabrication process, the total amount of only about 0.7×10^{-3} mol was typically enough to fill at least 4 glass cells. Therefore, assuming a basis $n_{total} = 0.7 \times 10^{-3}$ mol, the mass of each component could be calculated using equations (3.1) and (3.2) as follows:

$$m_1 = 0.79 \times (0.7 \times 10^{-3} \, mol) \times 398.45 \, g/mol = 220.34 \, mg,$$
$$m_2 = 0.20 \times (0.7 \times 10^{-3} \, mol) \times 588.60 \, g/mol = 82.40 \, mg, \tag{3.3}$$
$$m_3 = 0.01 \times (0.7 \times 10^{-3} \, mol) \times 256.30 \, g/mol = 1.79 \, mg,$$

Therefore, to prepare the LCE Precursor 1 for one cycle of fabrication, 220.34 mg of the LC monomer, 82.40 mg of the LC crosslinker, and 1.79 mg of the photoinitiator were used. The total mass of the mixture was 304.53 mg.

Following the same principle, the mass of each component can be calculated in the LCE mixture containing the azo-dye. If the same masses of the LC monomer and LC crosslinker are used to prepare the mixture, since their proportion remains the same, the basis n_{total} can be re-calculated to determine the mass m_4 of the azo-dye that needs to be added to the given mixture:

- for the LCE Precursor 2 (with 1 mol% of the dye): $m_1 = 220.34$ mg, $m_2 = 82.40$ mg, $m_3 = 1.81$ mg, and $m_4 = 1.71$ mg;
- for the LCE Precursor 3 (with 2 mol% of the dye): $m_1 = 220.34$ mg, $m_2 = 82.40$ mg, $m_3 = 1.83$ mg, and $m_4 = 3.46$ mg.

In case a different amount of liquid LCE precursor is required, such as for using more than 4 fabrication cells at once, the mass of the components can be re-calculated using a different basis n_{total}. Figure 3.1 shows the process of preparation of the molten LCE precursor.
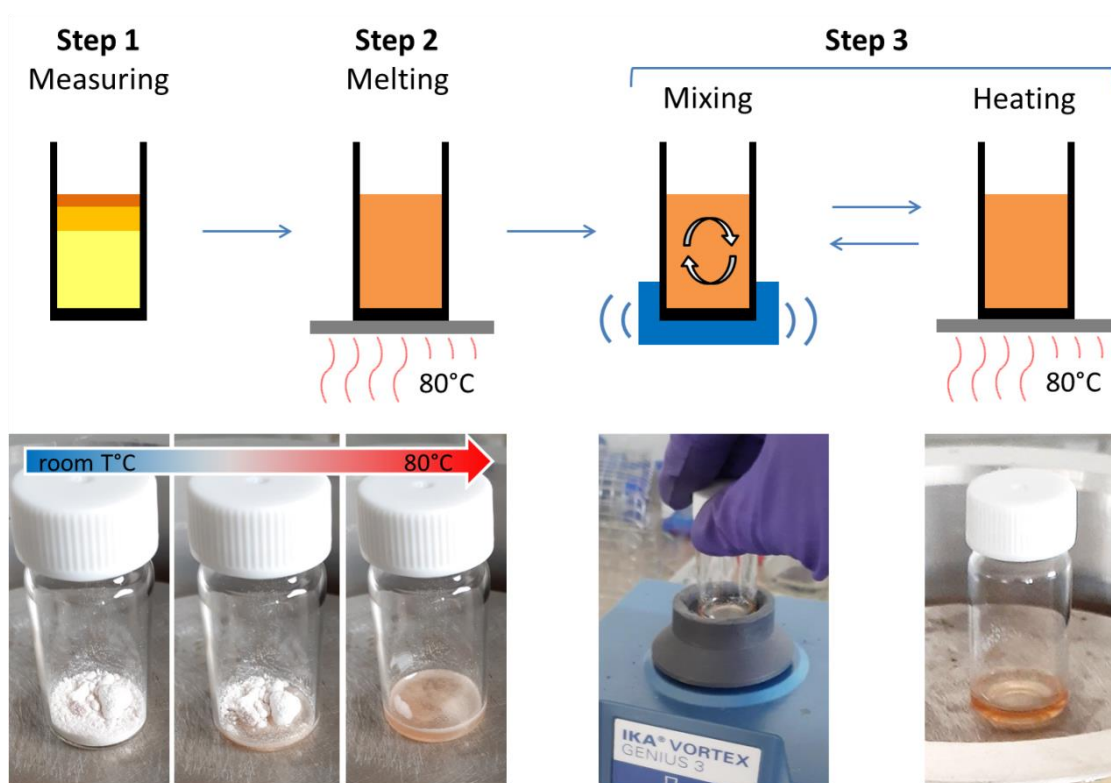
Figure 3.1 Process steps for preparation of the molten LCE precursor

In Step 1, the required mass of each part was measured using the laboratory scales (Denver Instrument) within about ±0.1 mg of accuracy, and all dry components were put together into a small glass vial. In the Step 2, the vial was placed on the hotplate at room temperature, and the temperature was ramped to 80°C, which is above the melting point of the dry parts (54.9°C for the LC monomer, 59.4°C for the LC crosslinker, and 67-70°C for the photoinitiator). The photographs showing the melting process of the LCE precursors are shown in the Figure 3.1. The off-white powder mixture melted completely before reaching the temperature of 80°C. In Step 3, the molten precursor was mixed; maintaining the high temperature is required to ensure that the LC components are in isotropic state. Mixing was performed by vortexing (SciQuip Vortex VariMix) at the maximum speed of 2500 rpm for a few seconds, after which the vial was quickly put back onto the hotplate. The mixing and heating cycle was repeated for

at least 7 times to produce a uniform mixture. The LCE precursor obtains a clear brown color, whereas before mixing it may be slightly opaque and non-uniform.

It is crucial for the LCE mixture to be kept at isotropic, molten state until the mixture is infiltrated into a cell or mold and ready for polymerization. A cool, crystallized mixture cannot be stored and reused for another fabrication process, as was observed in the experiments. If the temperature falls below LC phase transition temperature in an uncontrolled fashion, it may compromise the alignment of LC mesogens during fabrication, and such LCE device cannot be used for applications in actuation. Therefore, the glass cells or molds were always prepared beforehand, the LCE precursor was prepared at 80°C and used immediately, and any leftovers were disposed.

3.3 Fabrication of the LCE Films

The common method of fabrication of the LCE films requires using two glass slides with a spacer between them, which forms a flat cell, where the molten LCE precursor is infiltrated by capillary motion. Alignment layers, such as the unidirectionally rubbed polyimide (PI) layers, are used for controlling of the LC alignment. Therefore, the difference in LC orientation across the thickness of the layer induces bending of the initially flat films upon thermal actuation. In this work, the LCE films were aligned using the rubbed PI at one side against the untreated glass surface on the other side. The behavior was investigates for the LCE films of the uniform as well as tapered thickness. The fabrication process is discussed below in details.

Materials required for preparation of the glass cell and fabrication of the LCE film:

- LCE materials: molten LCE precursor
- Materials and instruments: standard microscope glass slides, borosilicate cover glass slides, polyimide (Kapton) film (50 and 125 µm of thickness), synthetic cloth, metallic spatula, razor blade, scissors, adhesive tape, liquid glue, tissues
- Equipment: hotplate, Hg lamp or UV LED (Thorlabs M365L2-C1)
- Personal protective equipment (PPE): protective eye glasses, UV-blocking protective goggles, nitrile gloves, lab coat

Figure 3.2 shows the preparation steps of the glass cell used in fabrication of the thermally-actuated LCE films. The cell was prepared using two glass substrates. For the bottom substrate, the standard microscope glass slide (Fisher Scientific) of 1.0-1.2 mm

of thickness was used. For the top substrate, a thinner 22*26 mm borosilicate cover glass (VWR International, 0.13-0.17 mm of thickness) was used. For the alignment layer on the bottom substrate, a polyimide (Kapton) film of 125 µm of thickness was used.
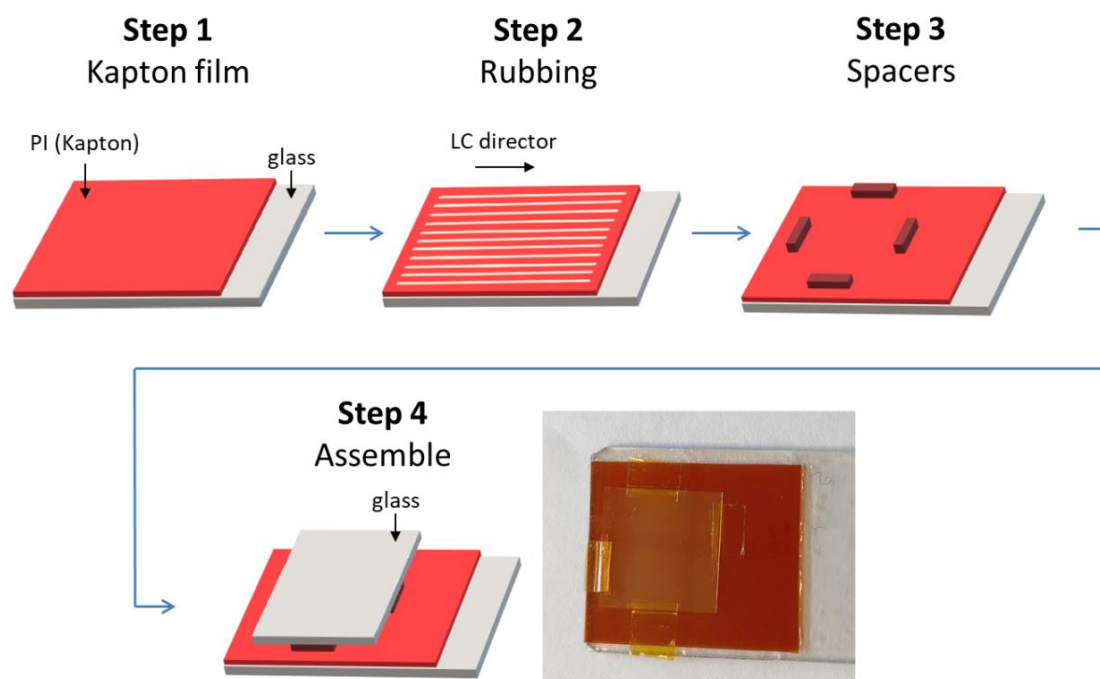
Figure 3.2 Process steps for preparation of the glass cell for fabrication of the LCE films

In the Step 1, a piece of the PI film was attached to the glass slide with an adhesive (glue or double sided adhesive tape). The area of PI should be slightly larger than that of the top glass substrate for easy assembling of the cell. The surface of the untreated PI film must be flat and clean to ensure effective alignment of the LC molecules. In the Step 2, PI surface was rubbed unidirectionally with a synthetic cloth several times to create nano-grooves. Though, a liquid PI which is spin coated onto the glass substrate and dried was more commonly used for the purpose of LC alignment previously in the literature, due to the strong alignment effect [78]. As compared with the high-quality spin-coated PI, the 125 µm thick Kapton film used in the work is expected to provide a slightly weaker alignment effect due to its rigidity and arbitrary roughness of the surface. On the other hand, Kapton film is readily available and does not require special processing conditions or additional equipment for deposition, unlike the liquid PI solution. Easy handling was an important factor in the choice of the alignment layer.

In the Step 3, the small pieces of Kapton film were used as spacers of two different thicknesses – 50 µm and 125 µm, as well as a combination of these stacked onto each other to achieve the total thickness of 100 µm or 175 µm. Several spacers were placed onto the bottom substrate near the edges of the top substrate. In order to prepare the cells with tapered thickness variation, the spacers of different thicknesses were placed at the opposite edges of the cell. In the Step 4, the top glass slide with a clean untreated surface was placed on top and fixed using either small pieces of adhesive tape, such as Kapton tape, or a small amount of glue. The assembled glass cell is shown in Figure 3.2.

Once the glass cells and the LCE precursor mixture have been prepared, the LCE films were fabricated by infiltrating the molten precursor into the cell, as shown in Figure 3.3.
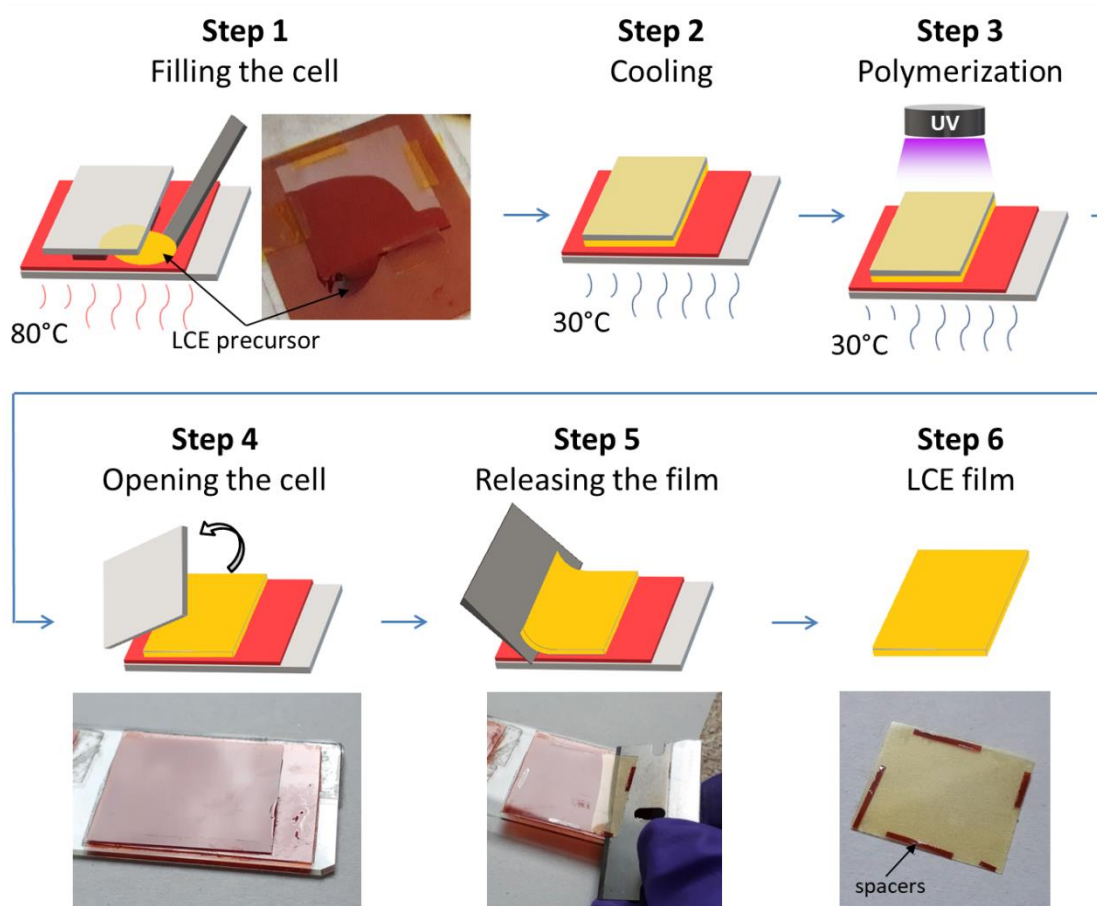
Figure 3.3 Process steps for fabrication of the LCE films

In the Step 1, the glass cell was heated to 80°C on top of the hotplate. A small amount of the mixture stored at 80°C was picked up and placed on the PI surface near the edge

51

of the cell, as shown in Figure 3.3. The liquid mixture started filling the cavity by capillary motion; the cell was filled completely within a minute. A small metallic spatula was used to pick up the molten LCE, the end of the spatula was firstly heated on the hotplate before manipulation to not allow the LCE to cool down in contact with the tool. It was observed that a plastic pipette cannot be used for this purpose, because the molten LCE mixture cools quickly in contact with the pipette. At this stage, if multiple cells/molds were intended to be used in fabrication, all the cells were filled with the LCE precursor, any unused mixture was safely disposed.

In the Step 2, the LCE was cooled down to nematic state, and the LC mesogens obtained the predefined alignment. The temperature of the hotplate was lowered to 30°C, so that the cells cooled naturally from 80°C to 30°C at the rate of about 2°C/min. The slow cooling rate ensured effective reorientation of the LC. Upon reaching the phase transition temperature of the mixture (~64°C [88]), the LC monomers align along the nano-grooves on the bottom PI surface, i.e. in the direction of rubbing. At the top untreated glass surface, it is expected that the LCs adopt nearly homeotropic alignment [142]. Another crucial factor was sensitivity of the photoinitiator in the LCE mixture to the ambient UV light. Therefore, at the sensitive stage of phase transition during cooling, the filled cells were always shielded from light with a non-transparent cardboard placed on top of the hotplate during this step of fabrication. It was also important to shield the cells from ambient light as much as possible at the stages of filling in the cell (Step 1) and the following cross-linking process (Step 3). The LCE material affected by direct light during the fabrication showed poor or no actuation behavior. However, it was demonstrated that shielding from the ambient light ensured successful fabrication of the LCE actuators.

In the Step 3, the LCE was polymerized by UV exposure. Mercury lamp (Ushio USH-205DP) with the peak output at the wavelength of around ~365 nm was used as the source of UV light. The lamp was integrated into the exposure system equipped with a automatic shutter. The output power at the wavelength of 365 nm was measured with a power meter (Model 840-C Handheld Optical Power Meter, Newport). For this, a non-transparent card with a round hole of 4 mm in diameter was placed over the detector chip of the power meter. The average value of the power was measured 199 μW, which translates to the average light intensity of ~1.58 mW/cm^2. Additionally, the light intensity transmitted through the borosilicate glass cover was measured to be ~1.42 mW/cm^2, meaning that nearly 90% of the total incident light intensity is transmitted

through the top glass and delivered to the LCE layer. The cells were illuminated with UV light for 3 hours on the hotplate at the constant temperature of $T_p = 30°C$. The controlled temperature provides better uniformity of the process, as opposed to the ambient temperature conditions which may fluctuate over the course of the 3 hours. A large UV dose was required to ensure complete cross-linking of the material. After finishing this step, the glass cells were removed from the hotplate.

In Step 4, the top glass slide was carefully removed using a razor blade. In Step 5, the LCE film was slowly and carefully peeled from the bottom substrate using a razor blade. A fully polymerized LCE material was slightly flexible with elastic properties typical of polymers; however, it could be subjected to tearing if the release was not performed with sufficient care. A photograph taken during this procedure is shown in the Figure 3.3. The blade was used to pick up the edge of the LCE film, and was slowly slid under the film to peel it off the surface. In Step 6, the fabricated LCE film was released. The small PI spacers were embedded in the film, which were easily cut off with scissors or a blade. The film exhibited bending actuation under thermal stimulus. Further, the films could be manually cut using scissors into long strips of ≤1 mm in width for inspection under the microscope and quantitative characterization of the actuation behavior.

3.4 Design and Fabrication of the In-plane LCE Microactuators

The general design and operation of the in-plane bending LCE microactuators are shown in Figure 3.4. The long actuator microbeams with rectangular cross-section are patterned with vertical microgrooves on one sidewall, while the opposite sidewall is flat. Different topology of the two surfaces would change the orientation of the LC mesogens, and therefore create the in-plane gradient in the LC director across the width of the microbeam, which is necessary to induce different anisotropic expansion effect under the actuation stimulus, resulting in the lateral movement of the tip.

The sawtooth-shape features for creating the vertical grooves are integrated in the design of the digital mask, providing full spatial control of patterning. When the molten LCE precursor is filled in the molding channels, LC alignment mechanism relies on the topology and anchoring properties of the surrounding surfaces, the geometry of the channels, and the shear flow forces acting during filling of the mold. In the vicinity of

the surface with microgrooves, the LC mesogens can reorient to minimize the surface energy, as was discussed in the Section 2.7.2. Grooved surfaces are commonly used to promote a strong uniform LC alignment along the groove direction, however, for this purpose, the surface materials such as polyimide (PI), polyvinyl alcohol (PVA), or epoxies are typically used, which provide strong planar anchoring effect. On the other hand, it is known that in contact with PDMS, LC mesogens normally align homeotropically to the surface due to the low surface energy of PDMS [143], [153]. However, several factors can contribute to the orientation of LCs confined in the PDMS channels, for instance, the ratio of the sides of the channel [208], the symmetry of the narrow channel, the strong shear flow [134], or the chemical treatment that modifies the surface properties [153]. An example of the LCE molding in microchannels from the literature, is the capillary micomolding method used for fabrication of the LCE fibers [134]. Uniform alignment of LCs along the narrow capillary channels was demonstrated in the literature, and a similar effect could be expected in the current work using the molding method.
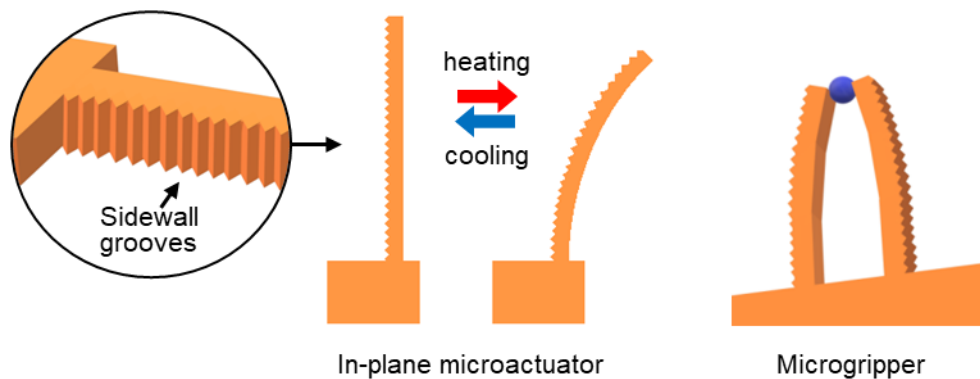
Figure 3.4 Proposed design and operation of LCE-based in-plane bending microactuators and a microgripper with microgrooves on the sidewall

In the absence of other external alignment sources, such as magnetic or electric fields, it is expected that the liquid crystals would preserve a more homogeneous nematic orientation near the flat channel wall, but would be disturbed near the patterned wall. Given the highly anisotropic thermal shrinking properties of LCE, the variation of alignment across the width of a beam after molding would result in the lateral bending of the microbeam. Thus, LCE microgrippers can also be realized using two microbeams with microgrooves, which bend towards or away from each other (Figure 3.4).

54

The overall process flow for fabrication of the LCE microactuators is shown in Figure 3.5. The key steps are the following: fabrication of the master structures; replica molding; cutting the inlets; surface treatment; assembling the molds; filling the molds with the LCE precursor by capillary effect; alignment and UV polymerization of LCE; and finally, de-molding to release LCE structures. Each step presents certain challenges and limitations, the parameters have to be carefully optimized to achieve the desired in-plane bending actuation of the LCE structure. The optimized procedures for each step and the results are discussed in the following sections.
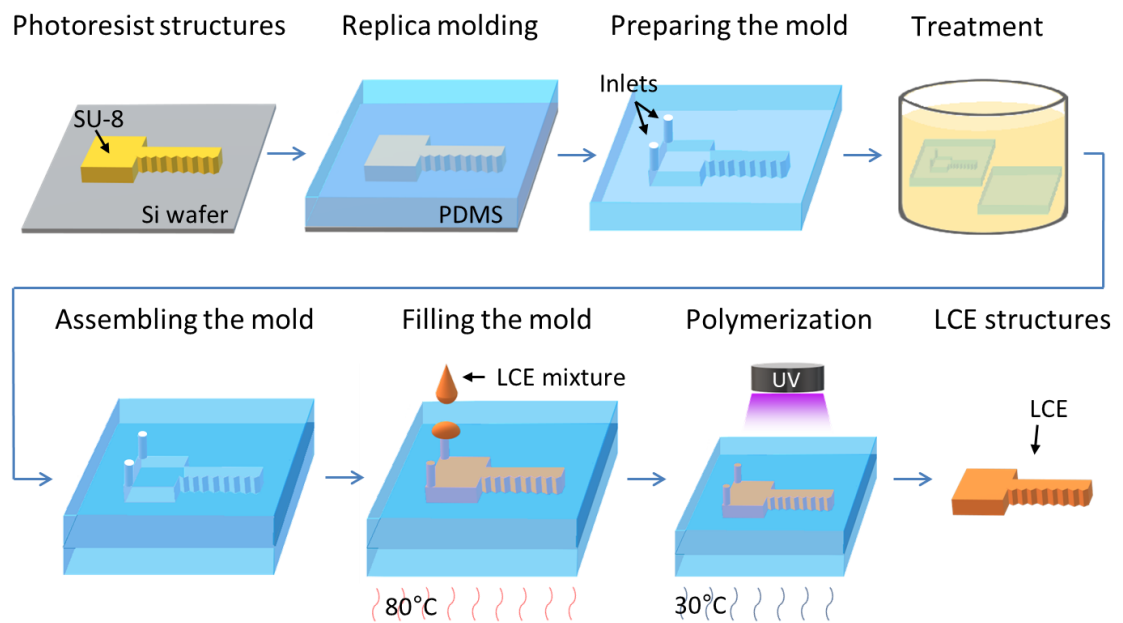
Figure 3.5 Fabrication steps for the LCE-based in-plane bending microactuators

3.5 Fabrication of the Photoresist Based Master Structures

The first step of the process was fabrication of the master structures. This task becomes critical due to the high aspect ratio of the vertical grooves, and it required the development of a suitable micro-manufacturing technique. For the relatively thick planar microstructures of the target thickness of 40 µm, the resolution of the grooves must approach to values as small as 1-2 µm. Multiple conventional microfabrication methods had been previously used to create structures with corrugated sidewalls for various applications with resolution down to sub-micron size, including deep reactive ion etching (DRIE) [209], inductively coupled plasma (ICP) etching [210], masked

photolithography [38], direct laser writing (DLW) [211], or via the photolithographic standing wave effect [212]. For our application, the DLW technique was employed. In DLW photolothography, a scanning UV laser beam is used to create a pattern in the layer of a photoresist using a predesigned digital mask. The absence of a physical mask opens possibility for rapid change of the design in the data driven method. DLW-based UV lithography can provide spatial resolution in sub-micron range in thin photoresist layers (~2.9 µm) [213]. On the other hand, thicker polymer structures (~90 µm) [214] have also been fabricated by DLW and used for subsequent replica molding. A good example of a structure with a sawtooth-shape wall produced by DLW is an integrated spectrometer demonstrated in the literature [211], where the structural details of 1 µm were obtained by laser writing in the photoresist layer of 10 µm in thickness.

Before designing the final shape of the LCE microactuators for testing and application, the DLW parameters must be carefully optimized. A good quality of the profile of the photoresist structures is crucial for obtaining the preferred internal alignment of the LC mesogens and achieving successful fabrication of LCE through molding.

The materials and equipment required for fabrication of the SU-8 structures are as follows:

- Materials and chemicals: silicon wafer/diced wafer piece, SU-8 3025, SU-8 developer, Isopropyl Alcohol, acetone, deionized water
- Equipment: spin coater, hotplate, Heidelberg DWL 66+ exposure system, software for digital mask design (KLayout); for inspection and measurements – optical microscope, surface profiler, scanning electron microscope
- Other instruments: glass Petri dishes, tweezers for wafer, nitrogen gun, 3 ml pipette, tissues
- Personal protective equipment (PPE): cleanroom suit, protective eye glasses, nitrile gloves

3.5.1 Design of the Test Structures for Direct Laser Writing

SU-8 polymer would be used for fabrication of the master structures in this work. SU-8 is a high-contrast epoxy-based negative photoresist commonly used in conventional near-UV photolithography. In a relatively thick photoresist layer of a few tens of microns, the sidewall of the structure is required to be strictly vertical. The resulting

LCE structures intended for application in actuation must have a symmetrical rectangular or square cross-section in order to achieve the desired pure in-plane mode of bending. A vertical profile of the master without overcuts or undercuts is also a crucial requirement for the subsequent steps of replica molding and structure release. When performing UV exposure with a scanning laser, it is important to choose appropriate parameters that would ensure a nearly vertical beam distribution through the layer of the material. Another implication is that the SU-8 master structures are required to have sufficient structural strength to allow replica molding with the PDMS resin. It was shown in the literature that the exposure dose can affect the structural profile during the DLW process [214]. This is associated with the distribution of light within the exposed layer. A model was created in the literature and verified experimentally, which represented the normalized dose distribution within the photoresist layer generated by a direct writing laser. This model takes into account the reflection of UV light from the substrate, such as a silicon wafer. The negative photoresist material, such as SU-8, has a threshold value for the absorbed UV dose which is sufficient to make the polymer insoluble. Thus, when the exposure dose is too low, it results in an undercut shape of the fabricated structure, because the UV dose is only sufficient to reach the threshold within the top parts of the thick layer. With the increasing UV dose, the profile turns from an undercut to nearly vertical, and then to an overcut shape. However, if the dose is too high, the reflection of the light from the substrate becomes significant, and an undercut structure is formed. One possible method to diminish this effect is by using anti-reflective coatings. Because no additional anti-reflective layers were used in our process, it was important to determine the optimal UV dose for direct laser writing which would provide both sufficient structural strength and a stable vertical wall profile. Fabrication of the smallest features such as sidewall grooves requires high spatial resolution of laser writing. However, there is a tradeoff between small feature size and large thickness of the structure. It is also highly important that the grooves are well resolved throughout the whole height of the wall and do not merge together towards the bottom of the layer. This is typically observed in a standard masked photolithography due to the effect of diffraction, whereas, in the DLW process it can be controlled by the position of the focal point and the depth of focus of the writing lens.

The initial layout of the test mask was designed for optimization of the fabrication procedure using the widely available KLayout software. The design contained test structures with sidewall grooves in a range of sizes. The purpose of the test mask was to

experimentally optimize the processing parameters for the SU-8 material (such as spin coating, baking, development) and the parameters of direct laser writing (intensity, focus, number of scanning cycles) in order to obtain fully resolved master structures with the desired wall profile. By testing a wide range of sizes of the sidewall grooves, it was possible to determine the fabrication limit for the smallest features, and to observe the overall quality of the pattern transfer before designing the functional structures and actuators. Figure 3.6 shows the design of one unit of the test mask. The overall size of the test unit was 1110x694 µm. The pattern in filled color is the area that would be polymerized by UV laser scanning. The grooves of rectangular shape were described with two key parameters as shown in the examples in Figure 3.6: *L* is the length or depth of the groove and *P* is the period of the groove. According to equation (2.3), the grooves with a smaller period and larger depth produce stronger anchoring effect for alignment of LCs. Practically, the smallest feature would be limited by the resolution limit of the fabrication method. It was previously demonstrated in the literature that the channels of 2 µm in width successfully induced a unidirectional LC orientation [142]. In the optimization process, the test mask contained an array of structures with the sidewall groves in different combinations of *L* and *P*. The value of *L* was varied in the range from 500 nm to 4 µm, with the step of 500 nm; the *P* was varied in the range from 1 µm to 8 µm, with the step of 1 µm. Due to the finite diameter of the UV laser spot, it was expected that some of the smallest ridge patterns may not be resolved.
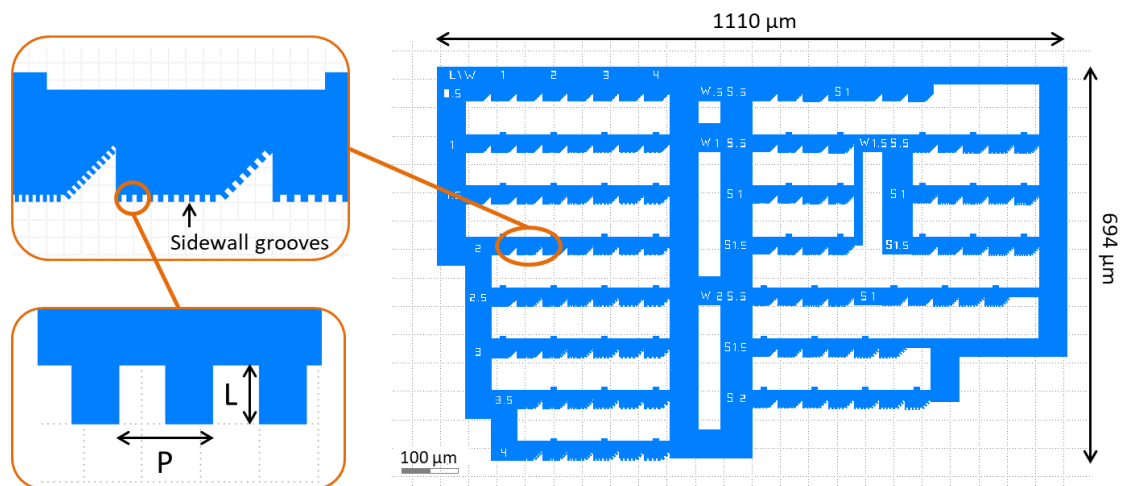
Figure 3.6 Test structure design for optimization of the direct laser writing and material processing parameters

58

3.5.2 Optimization of SU-8 Processing Parameters

For fabrication of the master structures, the SU-8 3025 photoresist (MicroChem) was chosen. Photoresists from the 3000 series offer improved adhesion, clear vertical sidewalls, and reduced coating stress, as compared with the 2000 series [37]. Good adhesion to the substrate was essential for the structures which were intended to be used for the subsequent replica molding. A clean vertical sidewall profile was crucial for the application which uses high-aspect ratio sidewall grooves. For the intended thickness of the structures of about 40 µm, the SU-8 3025 formulation was selected.

The standard photolithography process flow with SU-8 includes the following steps: spin-coating, soft bake, UV exposure, post-exposure bake, and development. The choice of processing parameters was based on the recommended parameters from the manufacturer's guideline [37]. All parameters used in fabrication of the SU-8 master structures are listed in Table 3.2.

Table 3.2 Parameters used in fabrication of the SU-8 master structures

Processing step	Parameters and values
Spin coating	
- Spreading cycle	Speed 500 rpm, acceleration 200 rpm/sec, duration 5 sec
- Thinning cycle	Speed 2500 rpm, acceleration 200 rpm/sec, duration 30 sec
Soft bake	
- Step 1	Temperature 65°C, duration 3 min
- Ramp	Duration 3 min
- Step 2	Temperature 95°C, duration 10 min
UV exposure by Direct Laser Writing	Laser wavelength 375 nm, write head "10 mm", laser power 70 mW, laser intensity 100%, transmission filter value 100%, focus +70%, number of scanning cycles - 6
Post-exposure bake	
- Step 1	Temperature 65°C, duration 1 min
- Ramp	Duration 1 min
- Step 2	Temperature 95°C, duration 3 min
Development	Duration 6 min (+1 min optionally)
Rinse and dry	
- Isopropyl alcohol	Rinse thoroughly 1-3 times until clear
- Deionized water	Rinse thoroughly 1-3 times
- N_2 stream	Blow gently until dry

The substrates used in fabrication of the test structures for the optimization task were the diced square pieces of a silicon wafer, 4×4 cm in size. Firstly, the silicon substrates were cleaned by rinsing in acetone and DI water, and dried on a hotplate for about 3 minutes to dehydrate the surface. After being cooled to the room temperature, the substrate was fixed on the chuck of the spin coater. A small amount of SU-8 of approximately 2 ml was dispensed in the center of the square substrate. Spin coating was performed in two steps: low-speed spread cycle, where the viscous SU-8 is distributed over the whole surface of the substrate, followed by high-speed thinning cycle, where the photoresist layer obtains the thickness defined by the spinning speed, evenly across the substrate area. The chosen parameters of spin coating are given in Table 3.2. The target thickness of the layer was about 40 µm. A higher spinning speed had to be used in fabrication rather than that recommended by manufacturer to obtain the given layer thickness. It was related to the possible increase of viscosity of SU-8 after some time of storage at low temperature in a refrigerator. The SU-8 layer had uniform thickness in the central area of the substrate, and a small edge bead near the edges of the substrate; thus, the patterns for UV exposure had to be placed near the center.

Next, the wafers were soft baked on a hotplate in two steps. To minimize the effect of thermal shock, it is recommended to ramp the temperature gradually at this stage instead of moving the substrate from one hotplate to another surface with a large temperature difference. The minimum time of 10 minutes is required for soft baking of the SU-8 3025 photoresist layer at 95°C, as per the manufacturer's guideline.

Next, UV exposure was performed by direct laser writing with a Heidelberg DWL 66+ exposure system using the predesigned digital mask. Although it is known that the exposure energy for polymerization of SU-8 3025 is recommended to be 150-250 mJ/cm^2, this parameter is usually easy to control in the traditional masked photolithography using a collimated UV light source and a shutter. However, it was challenging to determine the total UV energy delivered to the material through laser writing method. This depends on a number of characteristics, such as laser power, exposure mode, the size of the laser spot, writing speed and the separation of the scanning lines. Therefore the parameters of UV exposure were determined experimentally. The optimized parameters of DLW are listed in Table 3.2. Investigation and optimization of each parameter is described separately in details in Section 4.3.3.

The post-exposure baking was carried out on a hotplate shortly after exposure. Controlled ramping of the temperature was preferred instead of the fast switching between two hotplates, similarly to that during the soft bake step. The baking temperature should not exceed the recommended 95°C for better pattern fidelity. The minimum time of 3 minutes is required for post-exposure baking with SU-8 3025 photoresist at 95°C, as per the manufacturer's guideline.

Finally, the photoresist patterns were developed by immersing the substrate into the SU-8 developer solution (MicroChem) for 6 min with manual agitation. This was followed by rinsing the substrate with Isopropyl Alcohol (IPA) to remove the developer solution, and rinsing with deionized water to remove IPA. The substrate was dried with a stream of nitrogen. In case the developing time was insufficient, the IPA reacted with non-polymerized residual SU-8, turning the liquid milky in color, so that contamination was easily noticed. Thus, where necessary, the substrates were further dipped into a fresh SU-8 developer for a short time (1 min) with manual agitation to obtain clean, fully developed photoresist patterns.
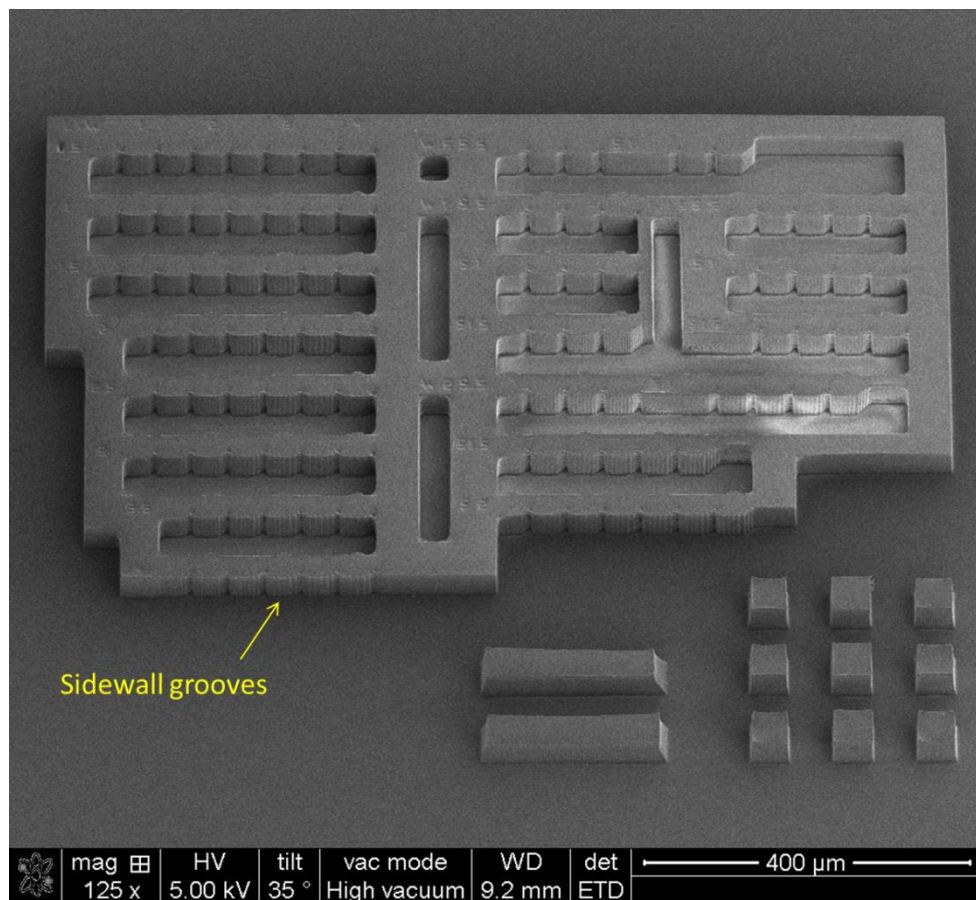
Figure 3.7 SEM image of the SU-8 test structures with sidewall grooves of different dimensions, fabricated using the optimized processing parameters

An SEM image of the test SU-8 structure fabricated with optimal processing and DLW parameters is shown in Figure 3.7. The image was acquired using the field emission SEM of the dual beam system (FEI Quanta 3D FEG). As the structures were made from a non-conductive polymeric material, prior to performing SEM imaging the sample was sputter coated with a thin layer of gold of a few nanometers to prevent the surface from charging. The resulting thickness of the SU-8 structures varied slightly around 40±2 µm at different locations on the substrate, as measured with SEM and surface profiler (Dektak stylus profiler).

3.5.3 Optimization of Direct Laser Writing Parameters

The UV dose optimization was carried out as follows. The unit in the digital mask was populated into an array on the substrate for DLW lithography, and one DLW parameter was varied from one structure to the next, while the other fabrication parameters remained unchanged. In the result, the influence of a certain parameter could be easily seen by comparing the test structures on the same substrate. The parameters for optimization were the laser intensity, number of scanning cycles, and the focus. The DWL 66+ exposure system (Heidelberg Instruments) was used in fabrication, equipped with a UV laser of 375 nm wavelength. Two standard writeheads with different characteristics were used for the test, named "HiRes" and "10 mm". The former is a high-resolution writehead, which provides a nominal minimum feature size of 300 nm, but possesses a relatively small focal length. The latter is a writehead with the focal length of 10 mm, capable of providing a nominal minimum feature size of 1 µm.

Firstly, the high-resolution writehead was tested, as its nominal resolution limit potentially allowed fabrication of the smaller microgroove features. The laser power was 70 mW, the transmission filter value was 100%. An array of 16 test units was polymerized by the scanning UV laser with different laser intensity for each unit, varied from 25% to 100% (corresponding to the laser power range from 17.5 mW to 70 mW). The result of fabrication showed that the profile of the structure was significantly distorted. The original mask pattern was configured well only at the top surface of the SU-8 layer, where the laser beam was automatically focused during exposure. However, a large area of excess polymerized SU-8 surrounded the pattern, completely failing to produce the sidewall features. This was due to a very small depth of focus of the high-

resolution writehead as compared with the thickness of the layer, which resulted in a large divergence of the beam. Hence, it was proved that the high-resolution writehead is not suitable for producing the SU-8 master structures with a vertical wall for the application.

Then, the DLW system was equipped with the "10 mm" writehead. A similar fabrication procedure was carried out with the laser intensity varied from 25% to 100% with a step of 5%. In the result, complete delamination of the structures was observed after 6 minutes of development. Delamination was observed one by one for all 16 structures, faster for those exposed at lower intensity due to the lower degree of crosslinking. This result indicated that the exposure dose was insufficient for polymerization of the SU-8.

As the scanning speed of the laser is not variable, the UV exposure could be alternatively increased by performing multiple scanning runs over the same mask pattern. The total UV dose delivered to the photoresist in this case would be multiplied by the number of laser passes. In the next test, an array of patterns was scanned by the UV laser multiple times with the full power of 70 mW; the number of cycles was varied from 2 to 9. It was observed that with a low number of laser runs (2 or 3) the total exposure dose was still insufficient for stable polymerization, as the SU-8 structures appeared partly delaminated or deformed after the development. However, with a larger number of scanning cycles (5 to 9), the SU-8 layer gained sufficient structural strength and had minimal deformation. With 8 and more scanning cycles, minor cracking was also observed in SU-8 structures around the corners and points of stress concentration. Overall, the structures had nearly vertical walls. The results showed that it is possible to perform fabrication of the SU-8 master structures of approximately 40 µm in height by DLW using the '10 mm' writehead.

The fabricated structures were inspected under an optical microscope in a tilted view in order to observe the sidewalls. Figure 3.8 compares the wall profiles of the SU-8 structures fabricated with different number of DLW cycles. A slight inclination of the wall was noticed, which varied with the total UV dose. The dashed line in Figure 3.8 is used as a guide for easy visualization, representing the angle of inclination of the wall. Thus, the wall shape gradually changed from a slight overcut at 3 laser runs, to nearly vertical profile at 6 laser runs, and to slight undercut at 9 laser runs. The profile was presumably affected by reflection of the UV beams from the substrate, and the UV absorption characteristics of the material, in agreement with [214] as discussed earlier.

The tapered profile is not acceptable as it obstructs the resolution of the fine grooves throughout the height of the wall. Therefore, 6 runs of laser scanning at 100% of intensity with the laser power of 70 mW was considered as the optimal exposure dose for fabrication of the SU-8 master mold. This result was satisfactory for the subsequent PDMS molding and application.
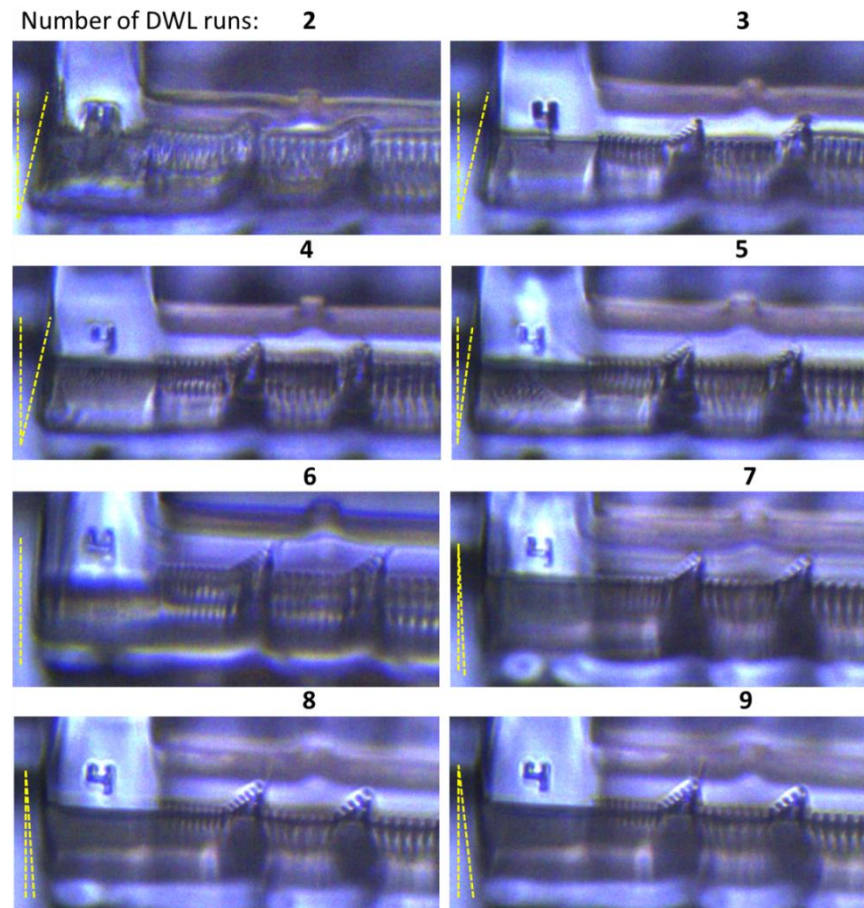
Figure 3.8 Optical microscope images of the sidewalls of the test structures fabricated by multiple cycles of laser scanning (2 to 9) using the "10 mm" writehead. The dashed lines show the inclination of the walls

Finally, the laser focus position during the scanning was subjected to optimization. When the focus setting was 0%, the laser was automatically focused on the top surface of the photoresist layer. Variation of the focus setting implies that the writehead is physically moved upwards or downwards during laser writing. The focus is indicated in percentage from -100 to +100%; the negative value moves the focus point above the initial plane, i.e. above the top surface of the photoresist layer; the positive value moves the focus below the plane. An array of 15 structures were fabricated by DWL with the focus setting varied from -70% to +70% with a step of 10%. The rest of the settings

64

were: 6 runs at 100% of intensity, 100% of the filter, and the laser power of 70 mW. The fabricated SU-8 structures were examined with a SEM (FEI Quanta 3D FEG). Prior to SEM imaging the samples were sputter coated with a thin layer of gold to prevent the surface from charging. The image of the SU-8 master structures fabricated with the default focus settings (0%) is shown in Figure 3.9a, the tilt of the substrate was 35°. The dimensions of the grooves as per the design, L and P, are indicated for each row and column of the structures. For the small features with high aspect ratio such as microgrooves on the sidewall, the quality and resolution depend significantly on the depth of focus of the lens. The best pattern fidelity was achieved near the top surface of the SU-8 structure. Towards the bottom of the structure, the microgrooves became less distinct and nearly vanished at around 25 µm from the SU-8 surface due to the beam divergence, similar to that observed in the literature [214]. The structural wall was almost flat near the substrate surface. Thus, the focus point must be manually moved downwards near the middle of the layer to achieve better quality for the microgrooves. The focus of +70% was found to be optimal in this procedure; this is shown in the SEM image in Figure 3.9b. The difference can be seen between the patterns produced with the default focus (0%) and the optimized focus (+70%). The latter resulted in symmetrical microgrooves which are well-defined throughout the whole height of the sidewall of about 40 µm.

The overall pattern quality was assessed from the SEM images. Because of the finite size of the scanning laser spot, the grooves became slightly smoothened around the corners after the UV exposure and development. Apart from the grooves, it can be seen in Figure 3.9 that the corners and deep trenches in the structure were not resolved sharply. However, it was acceptable for the intended application, where the long rectangular microbeam actuators have no sharp corners that could have critical effect for the performance. It was observed that the narrowest grooves with the period of ≤2 µm were not resolved clearly, but merged together into a flat surface. This indicated the smallest feature size that could be obtained with the developed procedure. The grooves of the period of 4 µm and larger were resolved clearly. For the length of the grooves, L = 2.5 µm was found to be the optimal parameter. With the smaller length, the grooves were slightly less distinct, whereas increasing the length beyond 2.5 µm did not further improve the resolution. In conclusion, the microgrooves with length L of 2.5 µm and period P of 4 µm were the smallest grooves suitable for the purpose of subsequent PDMS replica molding and LCE-based fabrication.
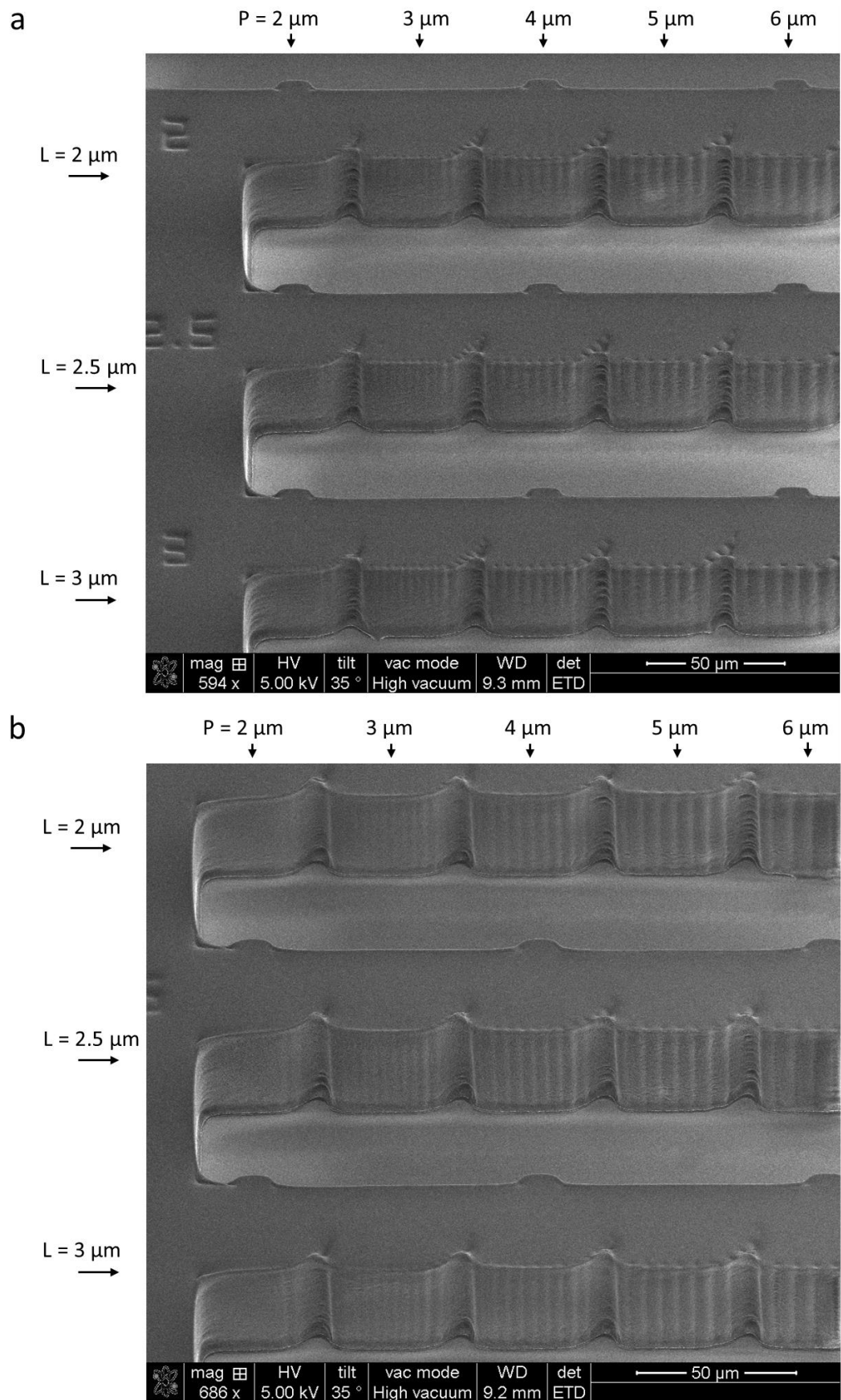
Figure 3.9 SEM images of the microgrooves on the sidewall of the SU-8 test structures fabricated by DLW , a) with automatic focus setting (0%); b) with manually adjusted focus setting (+70%)

3.5.4 Fabrication of the SU-8 Master Structures for the In-plane Microactuators and Microgrippers

The optimized process of SU-8 based fabrication was used to fabricate the master structures for the in-plane bending LCE microactuators and LCE microgrippers. Firstly, the layout of the digital mask for the master structures was designed using the KLayout software; an example is shown in Figure 3.10. Here, Figure 3.10a shows the design of the actuator microbeams with the sidewall grooves along one side. The difference in molecular alignment between the grooved side and the smooth side would induce in-plane bending of the microbeam.
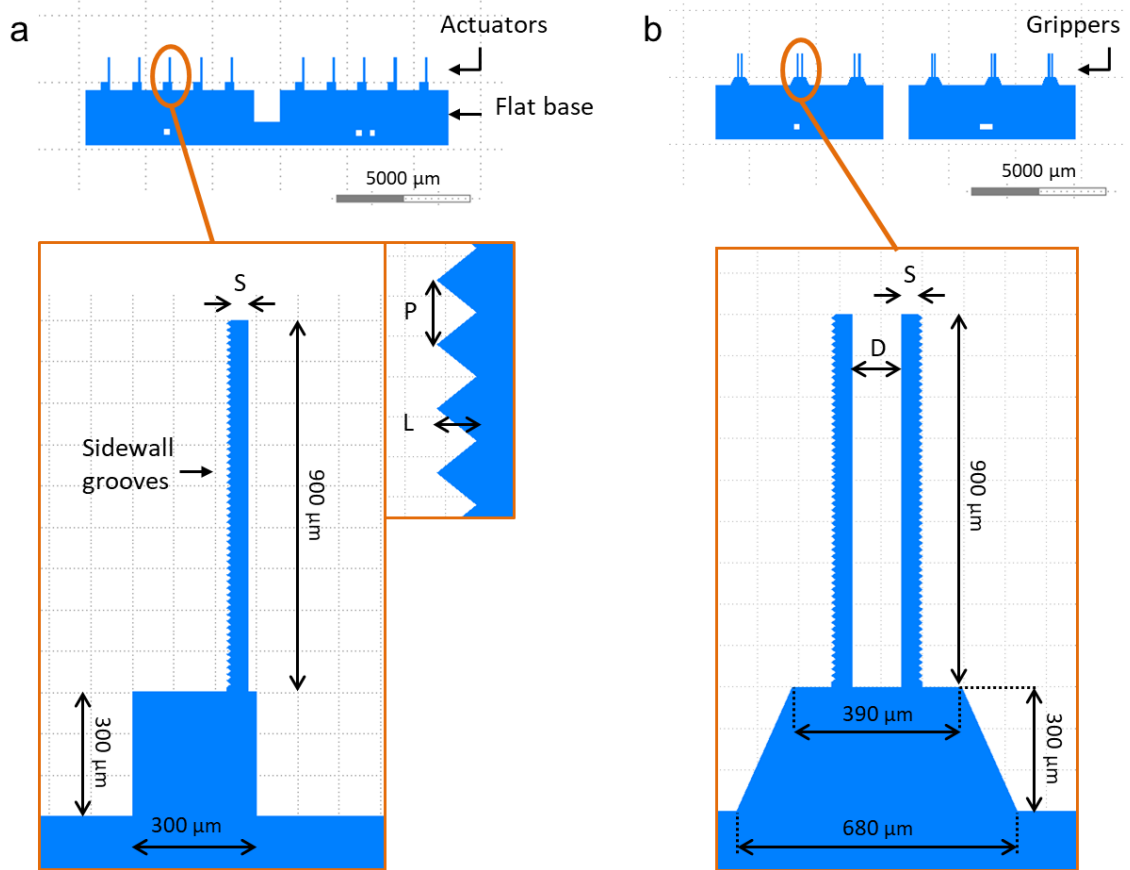
Figure 3.10 a) Design of the in-plane bending LCE microactuators, and b) design of the in-plane LCE microgrippers used in the digital mask design for fabrication of the SU-8 master structures

The thickness of all SU-8 structures was about 40 µm, the typical length of the microbeams was 900 µm. The microactuators were designed in 5 different widths, S = 20, 30 40, 50, and 60 µm, where the thinner beams are expected to exhibit larger deformation. Therefore, the cross-section of the microbeams was of rectangular or

square shape, with the thickness-to-width ratio of 2, 1.33, 1, 0.8 and 0.67 respectively. It is confirmed that the ratio of the sides was not lower than 0.4 for any beam design, which could lead to a certain imposed LC alignment due to the geometrical shape of the channel [208]. The five microbeams of different widths are placed along the edge of a common flat 'base' for easy handling of the fabricated part using tweezers without damaging the microscopic structures. The vertical grooves of triangular shape on one sidewall of each microactuator were designed in 4 different sizes, scaling up, as listed in Table 3.3, for comparison of their performances in LC alignment and actuation properties.

Table 3.3 Geometric parameters of the microgrooves used for control of the LC alignment

Groove size	Length, L [µm]	Period, P [µm]
Size 1	2.5	4
Size 2	5	8
Size 3	7.5	12
Size 4	10	16

The design of the LCE microgripper is shown in Figure 3.10b. In this example, the two microbeams with the microgrooves on the opposite sides are designed to perform thermal bending towards each other in order to grip an object. The length of the arms was 900 µm, the width of the beams, S, was varied to have the three values of 30, 40, or 50 µm. The distance between the arms, D, was also varied in different designs, which was 60, 120, or 240 µm. This could be chosen based on the size of the objects for micromanipulation; in Figure 3.10b the distance is $D = 120$ µm. Additionally, a few structures were designed without the grooves, and with the grooves on both sides. These structures could be used as a reference, because no bending is expected in such microbeams upon thermal actuation due to their symmetry.

For SU-8 fabrication, a silicon wafer of 4 inches in diameter, with a 1 µm layer of silicon oxide was used. Microactuators with alternative designs were grouped in units of the size of about 18.2×13.5 mm with the total of 40 test beams for convenience in molding. On a 4-inch wafer, 7 units were placed at once for simultaneous fabrication. The wafer surface was cleaned to remove possible dusts with a stream of nitrogen and dehydrated on a hotplate prior to fabrication. An amount of 4 ml of SU-8 3025 was used

for spin coating (the requirement of 1 ml for every inch of the diameter[37]). All SU-8 processing parameters were used as listed in Table 3.2 in the optimized process. The direct laser writing process for the full wafer was completed in 3 hours 10 minutes. The photolithography process without using a physical mask also allowed making rapid changes to the design. A photograph of the master wafer with fabricated SU-8 structures is shown in Figure 3.11. The thickness of the structures varied slightly around 40 ± 2 µm, as measured across several locations on the wafer. Two master wafers were fabricated with the structures of different designs.
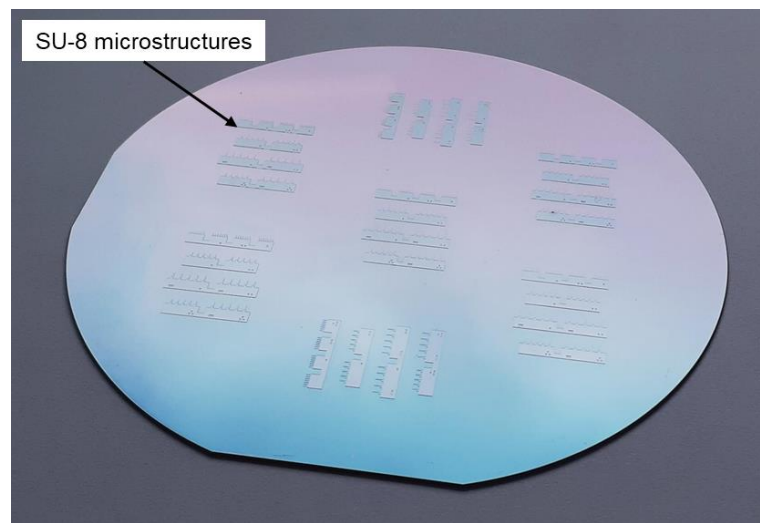
Figure 3.11 Si wafer with SU-8 master structures for fabrication of the LCE-based microactuators by micromolding

3.6 Fabrication of the Polydimethylsiloxane Molds

After the SU-8 photoresist structures were fabricated on the master wafer, the negative replica of the structures was created using the polydimethylsiloxane (PDMS) material. Afterwards, the molds would be filled with the molten LCE precursor and cured with UV light to form microstructured LCE-based actuators. Fabrication of the replica molds is described in details below.

A summary of materials required for fabrication of the molds are as follows:

- − Materials and chemicals: master wafer with fabricated SU-8 patterns, PDMS elastomer base and curing agent (Dow SYLGARD™ 184 Silicone Elastomer, purchased from Ellsworth Adhesives). For surface treatment - acetone,

photoinitiator 2,2-Dimethoxy-2-phenylacetophenone, ethanol, 2-Hydroxyethyl methacrylate (HEMA, Sigma Aldrich).

- Equipment: laboratory scales, vacuum desiccator with a vacuum pump, oven, reusable biopsy punch (inner diameter 0.75 mm, Welltech Rapid-Core). For surface treatment – hotplate, magnetic stirrer, UV LED (Thorlabs M365L2-C1). For inspection and measurements – optical microscope.
- Other tools and materials: glass Petri dishes, glass beakers, tweezers, plastic cup and spatula for mixing, razor blade, pipette, tissues
- Personal protective equipment (PPE): lab coat, protective eye glasses, nitrile gloves

The process followed the standard soft lithographic steps using PDMS [215], which are: preparation of the mixture, degassing of the mixture, deposition, degassing, thermal curing, and release. Firstly, the two components of PDMS, the resin and the curing agent, were poured into a clean plastic cup in a 10:1 weight ratio, the weight of the parts was measured using a small laboratory scale. Approximately 55 g of the PDMS mixture was required for molding for a 4-inch master wafer. The components were mixed thoroughly in a plastic cup with a clean tool. During mixing, plenty of air bubbles were introduced in the viscous mixture, which were removed next through degassing in a vacuum desiccator. For this, the cup with the mixture was placed inside the desiccator chamber, connected to a rotary pump (Picolino VTE 3, Werner Rietschle GmbH) with a rubber tube. The pump was run for about 20-30 seconds, then the mixture was left in the vacuum for degassing for about 30 minutes. A clear, fully degassed PDMS mixture obtained in the result could be used for molding.

Next, the master wafer was placed inside a glass Petri dish, and the PDMS mixture was poured to cover the wafer surface with even thickness. The wafer covered with PDMS was put into the vacuum desiccator for degassing once more to remove any air bubbles trapped in the microstructures. In the next step, curing of the PDMS material was performed in an oven at 70°C for 2 hours. Afterwards, the oven was switched off, the PDMS was allowed to cool down naturally, and it was kept at room temperature for further 24 hours before the next step. The cured PDMS was transparent and possessed the elastic properties of a flexible resin.

The PDMS layer with negative replica of the master structures was cut into individual pieces. Ample spacing between the microstructure units on the wafer allowed for easy manual cutting of the PDMS with a blade, as shown in the Figure 3.12a. The critical

step was the detaching of the PDMS replica from the substrate, which had to be performed carefully to avoid damage or delamination of the SU-8 patterns. There are several sources of demolding forces acting on the mold-to-master interface [216]. Firstly, the attractive van der Waals force becomes significant at the microscopic scale where the surface area grows rapidly as compared to the volume. Secondly, the covalent chemical and hydrogen bonding at the interface of the materials can lead to large adhesion forces, such as the bonding between the polymer chains and hydroxyl groups at the surface of a silicon or silicon oxide-coated wafer. Lastly, the lateral forces during molding can build up due to the CTE mismatch or volume shrinkage of the materials during the thermal or UV curing [216]. The effect of the listed forces may result in damage caused to the SU-8 layer, reduce the lifetime of the template, or cause faulty pattern transfer. An optional surfactant coating on the wafer surface, such as through the reaction of silanization, is usually recommended for reducing the adhesion and friction forces between the mold and the template and facilitate the removal of the cured PDMS from the substrate. However, it was demonstrated in our experiment that releasing of the PDMS replica could be performed without additional surfactant coatings with very little damage to the SU-8 layer. The PDMS structures were examined under the microscope. All the patterns and the microscopic grooves were successfully replicated in PDMS. The master wafers were used for replica molding at least 3 times by pouring new PDMS mixture onto the surface, cleaned from dust but without any additional treatment. After 3 molding cycles, less than 10% of all the thin microbeams on the two master substrates were damaged.
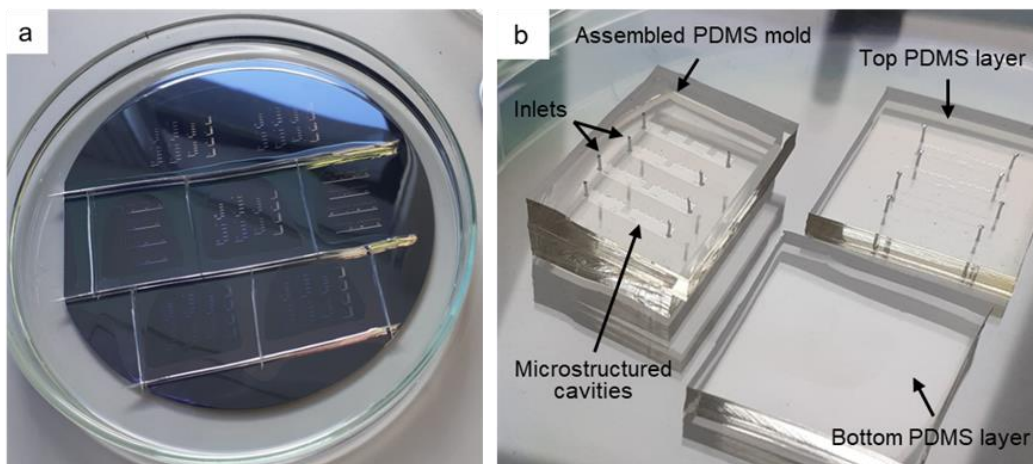
Figure 3.12 Fabrication of the PDMS molds: a) cured PDMS layer on top of the master wafer, cut into individual replica molds; b) the PDMS cell assembled from two PDMS layers for fabrication of the LCE microactuators

For fabrication of liquid crystal elastomer microactuators, the PDMS cells were assembled from two parts. The top replica layer was attached to the bottom layer with a flat surface, forming the microstructured cavities. To create the channels for filling the molten LCE into the mold, the inlet and outlet holes were manually cut through the top PDMS layer with a reusable biopsy punch tool (Welltech Rapid-Core) of 0.75 mm in diameter. Figure 3.12b shows the assembled PDMS cell, and the top and bottom layers separately. The flat bottom layer was made following similar procedures for PDMS preparation but without a master wafer. The PDMS mixture was poured into a glass Petri dish, degassed and cured, resulting in a thick resin layer with flat surface, which was subsequently cut with a blade. Approximately 30 g of the mixture was required when using a 3-inch Petri dish. Both top and bottom PDMS pieces had to be chemically treated before assembling in order to ensure successful polymerization of the LCE material inside the PDMS microchannels. The treatment modifies the properties of the surface, which affects the alignment of LC mesogens and fabrication. The influence of surface treatment of the molds was investigated. An appropriate treatment technique for the chosen application was developed, as detailed in the next section. After the treatment procedure, the two PDMS layers were attached together, with no additional adhesive required.

3.7 Surface Treatment of the PDMS Molds

Molding of the LCE is often performed in an oxygen-free environment for the best result, such as in vacuum or in a sealed chamber filled with nitrogen, because oxygen can inhibit polymerization [82], [124]. The PDMS elastomer is permeable to oxygen and moisture from the atmosphere. The presence of oxygen can scavenge free radicals in the LCE precursor, inducing degradation of the polymer at elevated temperatures, and reducing the degree of polymerization. This can lead to the formation of defects and rapid deterioration of the quality in the LCE structure. Sealing the polymer from oxygen and moisture during molding usually requires building a custom apparatus with controlled environment. However, a simple setup in the room environment was used in this work. The molding was performed on top of the hotplate for control of the temperature of the liquid LCE precursor. When using the molds with clean untreated PDMS surface, initially a problem was observed that prevented from complete LCE

polymerization. In this case, the LCE mixture filled into the mold remained in liquid state after UV curing, even after increasing the UV dose. This was attributed to the small thickness of the microstructures and exposure to oxygen. However, the following test demonstrates that the polymerization could be achieved successfully in the room environment by modifying the PDMS surface through chemical treatment.

For this purpose, a similar treatment process was investigated as described in the literature [153]. In their work, the authors developed a custom treatment procedure in order to form a thin layer of the polymerized 2-hydroxyethyl methacrylate (HEMA) covering the PDMS mold, which increased hydrophilic properties of the surface, and also modified the LC alignment from strongly homeotropic into planar alignment near the surface. 2-hydroxyethyl methacrylate (HEMA) is an acrylate monomer, its chemical structure is shown in Figure 3.13. In this process, the molds were firstly immersed into the acetone solution of a photoinitiator (30 wt %), where the molecules of the photoinitiator were trapped within the PDMS surface swollen by acetone (swelling ratio of ~1.0337). The original method subsequently uses the organic HEMA compound, which was polymerized with UV irradiation with the effect of the trapped photoinitiator, and forms a thin coating layer of poly(2-hydroxyethyl methacrylate) on the PDMS surface. Based on this method, the surface treatment of the molds was investigated.
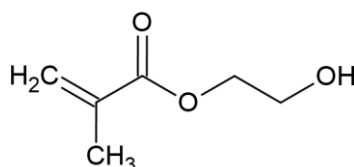
Figure 3.13 Chemical structure of the 2-hydroxyethyl methacrylate (HEMA)

Firstly, a number of tests were conducted using flat PDMS blocks treated with HEMA under different UV dosages. The liquid compound 2-hydroxyethyl methacrylate and the photoinitiator 2,2-dimethoxy-2-phenylacetophenone were purchased from Sigma Aldrich. The photoinitiator used for the treatment purpose was different from the one (1-hydroxy cyclohexyl phenyl ketone) used in the reference [153]. Both of these photoinitiators are widely used for photopolymerization of acrylates and have high solubility in acetone. The solution was prepared using 30 wt % of the photoinitiator dissolved in acetone and mixed homogeneously with magnetic stirrer at room temperature. After immersing the PDMS into the solution for 30 minutes, followed by

rinsing with acetone and drying, the PDMS blocks were put onto a flat surface. A puddle of HEMA was dispensed onto the PDMS covering the surface, and illuminated with UV light from a collimated LED (Thorlabs M365L2-C1, wavelength 365 nm, total beam power 120 mW, beam area 1960 mm^2) for various time periods. Afterwards, the PDMS surface was rinsed with ethanol and dried on a hotplate at 95°C for several minutes. The hydrophilicity of the surface increases with the increasing UV dose used for treatment. It could be confirmed by measuring the contact angle between the treated surface and a droplet of water placed onto it. The water contact angle for untreated PDMS material is usually >100° [217], which reduces significantly after applying HEMA coating.
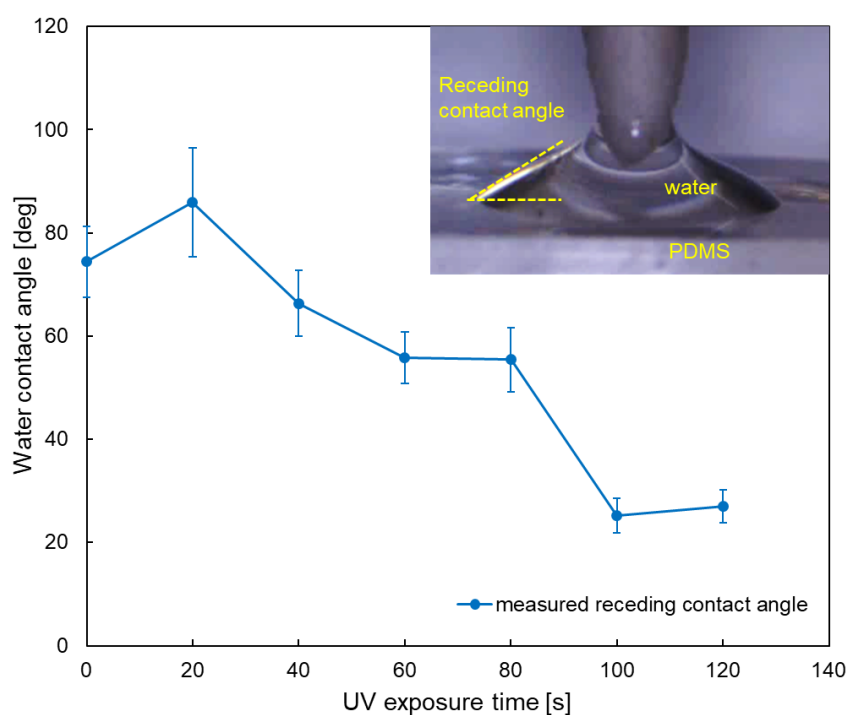
Figure 3.14 Measurements of the receding water contact angle on the flat PDMS substrates chemically treated with HEMA and various UV curing times

The measurement of the receding contact angle for a sessile drop was performed in order to record the change in hydrophilic properties of the surface. The PDMS block was placed on a flat surface; a droplet of water was placed onto the treated surface with a pipette; and the sessile droplet was observed through the side-view camera equipped in the Chronogrip robotic system. Then, the water volume was carefully absorbed with a tissue from the top. Thus, the uniform receding of the droplet was recorded with the camera, and the dynamic receding water contact angle at the edge of the droplet could

be measured using a software tool for measurement from the video frames. The measurement results are shown in Figure 3.14. The contact angle is plotted against the UV curing time. It was observed that the contact angle was gradually reducing with increasing UV exposure, reaching the minimum of approximately 25°, which corresponds well with the result reported in the literature (the minimum angle of 27° at the UV dosage of 1000 mJ/cm^2) [153]. This result proves that the polymerized HEMA coating layer has been formed on the PDMS surface.

When using the molds with treated surface, full polymerization of LCE inside the PDMS channels was achieved, which was no longer in liquid state after UV crosslinking. However, the HEMA coating tends to alter the LC alignment at the surface; and also, a small change of the surface topology may be introduced with the addition of the thin layer. Importantly, it was found that it is possible to achieve complete LCE polymerization without HEMA coating, only by treatment in the photoinitiator solution. This way the PDMS was modified only by dipping into the acetone solution of the photoinitiator 2,2-Dimethoxy-2-phenylacetophenone (30 wt %) for 30 minutes, followed by rinsing in acetone, drying in air, short UV curing (Thorlabs M365L3-C1 LED, 365 nm, ~11.8 mW/cm^2, 15 sec), and final drying on a hotplate at 95°C. Hence the PDMS surface still contained the trapped molecules of the photoinitiator, which assisted in the photo-polymerization process. Moreover, the performance of the LCE microactuators fabricated in the photoinitiator-treated molds was more effective and consistent than of those fabricated in the HEMA-treated molds. The behavior of the LCE microactuators fabricated using both methods will be described in more details and compared in Chapter 5. The photoinitiator-only treatment method is simple but sufficient to facilitate the formation of the LC network with the desired behavior upon thermal actuation.

3.8 Fabrication of LCE by Micromolding

After assembly, the PDMS molds were ready for the LCE-based fabrication. The process was started by putting the prepared PDMS molds onto the hotplate and heating them up to 80°C. The procedure should be performed in the environment with minimum exposure to the UV light, in this case by shielding the work area from the ambient light as much as possible during filling of the molds. A droplet of molten LCE was picked up

with a clean metallic spatula and placed at the inlet of the PDMS mold. The liquid started filling the microscopic cavities slowly by capillary action. A sufficient time, at least 30 minutes, must be allowed for the mixture to fill the narrowest and longest molding parts completely. It is important to ensure that no air bubbles are trapped inside the mold. Afterwards, the molds were shielded from all light during the sensitive phase transition stage, and slowly cooled down to 30°C at a rate of ~2°C/min. On cooling, when the LCE precursor reaches the phase transition temperature, the LC mesogens shift from isotropic to nematic state and obtain the prescribed orientation pattern, which is influenced by the properties of the surface and the capillary flow forces. When the system reached the temperature $T_p = 30$°C, the LCE was polymerized by illumination with UV light through the transparent PDMS molds.
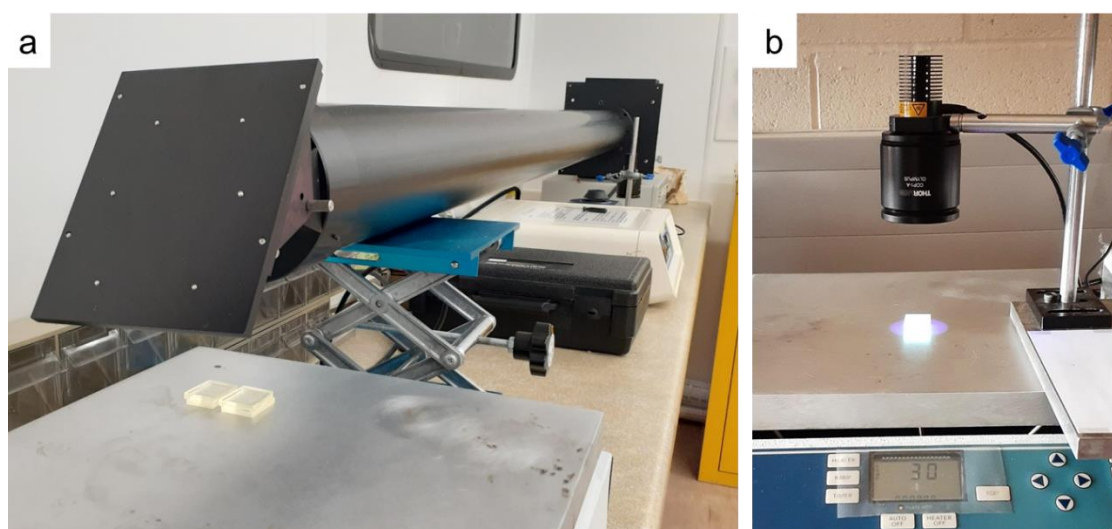
Figure 3.15 Setups for the UV-polymerization of the LCE material inside PDMS channels: a) exposure system using the Hg lamp; b) setup using the mounted UV LED

Two different sources of UV light were used in the photo-polymerization process: the Hg lamp (Ushio USH-205DP, ~365 nm, 1.58 mW/cm^2, 3 hours), or alternatively the UV LED (Thorlabs M365L3-C1 LED, 365 nm, ~11.8 mW/cm^2, 30 min). The setup of the exposure system is shown in the Figure 3.15a, which consists of the UV lamp installed inside the case, the automatically controlled shutter, and the long tube for beam collimation with the mirror directing the light downwards, onto the surface of a hotplate. The lamp provided uniform illumination, but with low intensity due to the large distance between the light source and the sample; therefore, it required a significantly long exposure time to ensure complete polymerization of the LCE

material. The large illuminated area allowed simultaneous illumination of 4 molds. The LED setup is shown in Figure 3.15b. The peak wavelength of the LED emission spectrum was 365 nm, and the bandwidth (full width at half maximum) was 9 nm. The LED with the attached collimation optics unit was mounted on a stand, and the light was directed onto the surface of a hotplate. The larger light intensity allowed reducing the exposure time significantly as compared to using the UV lamp; it potentially allows more efficient process with larger number of devices fabricated in a shorter time. Additionally, the setup using the UV LED is more compact, portable, and various characteristics such as the size of the illuminated spot, the direction of light, or the distance to the sample could be adjusted manually to the requirements of the new procedure, while the output power of the LED could be varied with a controller.

However, the light intensity provided by the LED source was found to be non-uniform across the illuminated area, with the minimum values in the center (~9.5 mW/cm^2) and the maximum near the edges of the illuminated area (~20.6 mW/cm^2). The non-uniformity could be related to some aberrations introduced by the collimation lens. The average of the values measured across multiple locations was approximately equal to the nominal LED intensity value of 11.8 mW/cm^2. To reduce the effect of the non-uniformity in the LED intensity, the molds were rotated by 180° half way through the crosslinking process. Only two molds could be exposed to the UV light simultaneously due to the small size of the illuminated spot of 5 cm in diameter. In the result of the photo-polymerization process, a solid LCE structure was formed, with no liquid residual. All measurements of the light intensity were carried out at the wavelength of 365 nm at different locations across the illuminated area using the handheld optical power meter (Newport, Model 840), through a hole of 4 mm in diameter.

The last and critical step was releasing the LCE structures from the molds. Although the LCE material possesses some degree of elasticity, the thin microbeams are still delicate and brittle. The PDMS cells were opened; then, a razor blade was used to pick up the corner of the flat base, and carefully slide underneath the structures to release them from the mold cavities. The strength and elasticity of the LCE material was sufficient to allow successful release of about 90% of the microactuators without damage. It was noticed that the LCE material with the higher content of the dye, 2 mol%, was much softer than the material with 1 mol% of the dye concentration, the structures were more flexible and could easily deform during releasing from the molds under a little force. It is the effect of the dye molecules dispersed between the polymer chains, which affects

the degree of cross-linking. This was an undesirable effect as it makes the microstructures prone to damage and deformation during fabrication and de-molding. Meanwhile, the LCE structures with 1 mol% dye concentration behaved similar to the undoped LCE structures during the release process, so the number of successfully released devices was high (~90%).

An example of the fabricated LCE microactuators and dye-doped LCE microgrippers after release from the molds is shown in Figure 3.16a. The crosslinked LCE material was off-white color, mostly transparent; the LCE containing the light-absorbing dye (Disperse Orange 3) was of dark orange color. To examine the quality of the microgrooves, the structures were inspected under the microscope equipped in the Chronogrip system (Percipio Robotics). The images of the grooves of different sizes in the SU-8 master structures (top view) and the LCE structures (side view) are compared in Figure 3.16b. In general, the patterns were successfully transferred into LCE structures by molding. It can be seen that the grooves of size 2 to 4 were clear and well defined on the sidewall of the LCE microbeams. However, the smallest grooves of size 1 were barely visible, but still present in the microbeams.
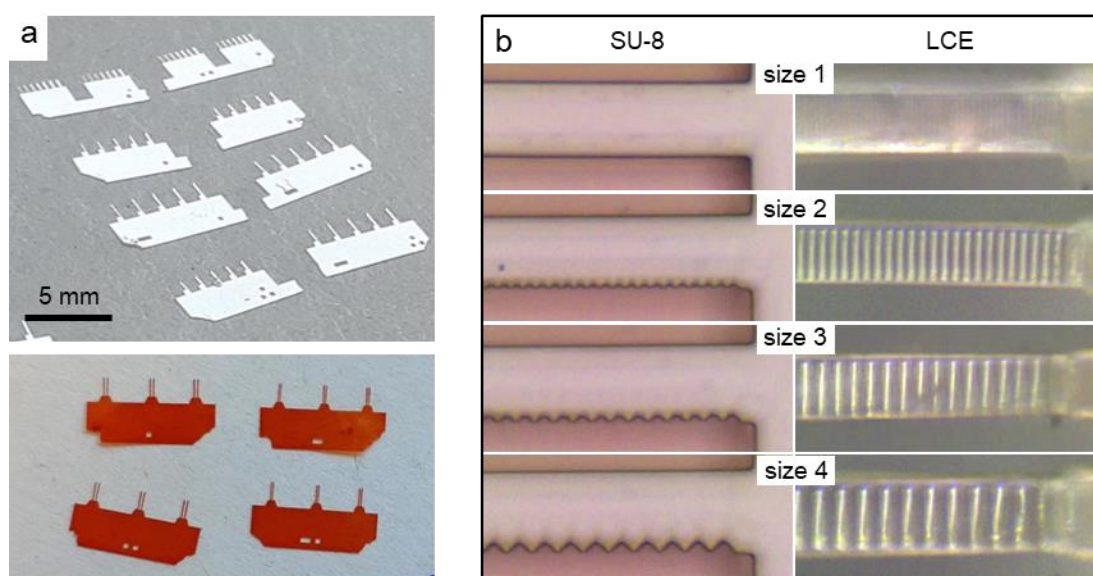
Figure 3.16 Results of the monolithic LCE-based microfabrication: a) LCE microactuators and dye-doped LCE microgrippers after releasing from the molds; b) optical microscope images of the microgrooves on the fabricated SU-8 structures (top view) and in the LCE microbeams (side view) after molding

Optionally, prior to characterization, the LCE microactuators were heated in the oven at 55°C for 15 minutes to release the internal stress accumulated during fabrication.

Otherwise, the stress release would typically occur during the first cycle of heating, and the measured behavior of the microactuators on the first cycle might differ from the behavior recorded in the subsequent cooling and heating cycles, as was previously observed in the thermal actuators in the literature [218]. It should be noted that the microbeams might be not perfectly straight at the temperature of 30°C, at which the polymerization took place, but might obtain a slight curvature after the release of residual stress, which was taken into account at the characterization stage.

The fabricated LCE microactuators successfully demonstrated reversible, repeatable actuation upon the change in the temperature. The behavior will be characterized in detail in Chapter 4, but the initial observation proved that the new method is capable of producing LCE microstructures with lateral bending operation. It is noteworthy that the microactuators fabricated inside the photoinitiator-treated molds demonstrated thermal bending in the direction away of the grooved side, whereas the microactuators fabricated inside the HEMA-treated molds showed some bending in the opposite direction, towards the grooved side. This was because different orientation of LCs was induced inside the PDMS channels chemically treated using the two different methods. The difference cannot be observed under the optical microscope, however, some details of the internal alignment of the LCE material can be seen when the sample is placed between two optical polarizers. Figure 3.17 shows the polarized-light images of several LCE microactuators of different widths fabricated using the photoinitiator-treated molds (Figure 3.17a) and HEMA-treated molds (Figure 3.17b), along with the schematic image showing the typical direction of bending respectively.

A number of local defects in the alignment of mesogens were observed; these appear as small local disturbances in the brightness pattern within the structures in Figure 3.17. Similar defects have been previously demonstrated in the literature in the LCE structures fabricated by micromolding in capillaries [134]. It was shown in the study that the number of defects are relatively low in the narrower microbeams of 20 µm in width, but becomes significant in the wider beams of 50 µm in width. This corresponds with the observations in the present work, as it can be seen in Figure 3.17 that the wider microbeams (50 µm, bottom right) seem to have more defects than the other beams. The defects would have a considerable effect on the bending behavior of the LCE microbeams, and they are the main source of scatter in the measurement of the thermal bending. Generally, the LCE microbeams have a more even color in Figure 3.17a, which were fabricated using the photoinitiator-treated molds. On the other hand, the

microbeams in Figure 3.17b, which used HEMA treatment, have a different color pattern with a characteristic sharp line in the middle along the channel. Additionally, more local defects can be noticed. It suggests that the quality of the HEMA coating was insufficient, the coverage was uneven and patchy. This is related to the fact that the actuation behavior of these microbeams is also less consistent as compared with the LCE microactuators fabricated without HEMA treatment, as will be shown in characterization.
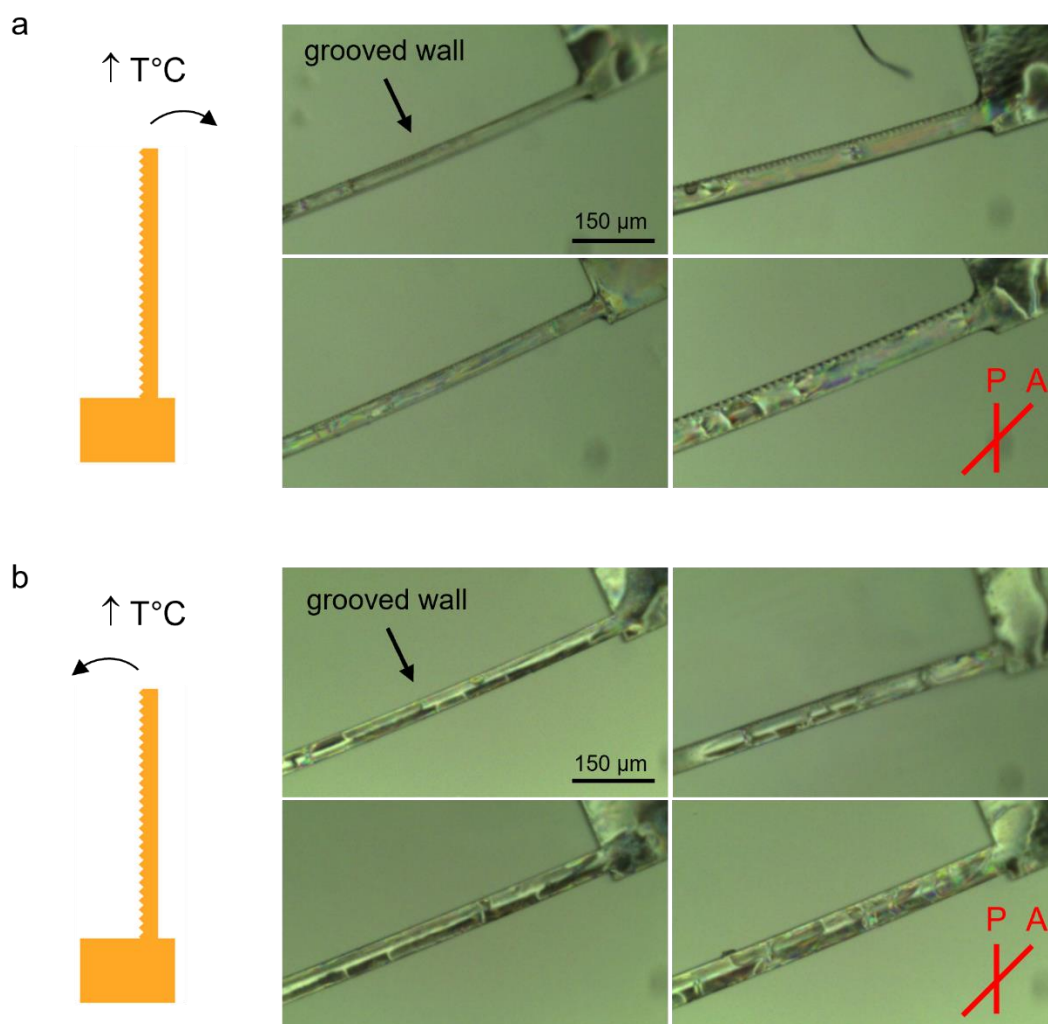
Figure 3.17 Polarized microscopy images of the LCE microactuators of various beam width, a) fabricated using the photoinitiator-treated PDMS molds, b) using the HEMA-treated PDMS molds

3.9 Summary

This chapter reported the development of the fabrication method that enables a new in-plane bending functionality in thermal and photothermal LCE microactuators. The

method is based on micromolding in PDMS channels, and uses the surfaces with patterned microgrooves for controlling the LC alignment within the channels. The key difference of the method compared to the techniques reported previously is that the microgrooves are placed on the sidewall and not on the bottom surface, which therefore allows creating a variation in the LC alignment across the width of the microbeams in lateral direction. The proposed method enables monolithic fabrication of the structures with complex geometry and in-plane functionality for easy integration of the LCE microactuators into larger MEMS or microfluidic systems without tedious microassembly steps. The fabrication process was optimized for the LCE microactuators of 40 µm in thickness. The parameters of the direct writing with the UV laser for fabrication of the SU-8 master structures were optimized. In the result, a fine resolution down to 4 µm of period of the microgrooves was achieved; well-defined features throughout the whole thickness of the structure without divergence were enabled by manual adjustment of the laser focus. The maskless fabrication provides full spatial control in patterning, reducing the error of misalignment, and enabling simultaneous fabrication of the microactuators bending in different directions, depending on the placement of the sidewall grooves. Further, it is possible that the sidewall patterning may be combined with patterning of the top and the bottom surfaces of the mold to realize 3D morphing.

Chapter 4   Modeling and Validation of Bending and Rolling Behaviors of LCE Beams

4.1 Introduction

Stimuli-responsive bending LCE films fabricated inside a glass cell attracted significant interest in the last decade for various state-of-the-art applications in actuation, including soft robotics [11], [12] and origami-like folding structures [13]–[15]. LCE actuators are capable of producing complex deformations, such as bending, curling, rolling, waving, wrinkling, or twisting [67] under thermal and photothermal actuation. However, the challenges of numerical simulation remain due to lack of an effective model, although many models based on different physical effects have been demonstrated previously in the literature for particular applications of LCE actuators (Section 2.10). This chapter presents the results of the work on investigation and comparison of the behavior of the bending LCE actuators in a large range of thicknesses, and based on the results, a model for flexible numerical simulation was developed, which is able to predict the thermal bending and curling of the LCE beams with various geometric parameters, or even the beams with non-uniform (tapered) shapes. The results of the simulation were validated based on experimental results, and also based on the previous examples of LCE actuators reported in the literature. This chapter is partly based on the results from the Publication (3).

4.2 Model Description

It has been established that the bending of flat LCE films is due to the strain difference that occurs between two surfaces with different LC alignments, which can be expressed in the following basic relationship, given by equation (4.1) [88]:

$$\gamma \approx \frac{\Delta \varepsilon l}{t} \tag{4.1}$$

where γ is the bending angle, $\Delta \varepsilon$ is strain difference, l and t are the length and thickness of the LCE beam respectively. Since $l \gg t$, the tangential angle at the end of the beam is usually assumed as

$$\gamma \approx \frac{l}{R} \tag{4.2}$$

where R is the radius or curvature. The relationship is valid for small deformations of the beam; for analysis of large deformations the numerical methods are used. The curled LCE beam is assumed to be of a perfect circular arc shape. The radius is the reciprocal of the curvature, which is more commonly used in the analysis of the bending actuation of the beams:

$$\kappa = \frac{1}{R}$$ (4.3)

where κ is the curvature. Following the above, the strain value $\Delta\varepsilon$ can therefore be shown as

$$\Delta\varepsilon = t \cdot \kappa$$ (4.4)

In case the beam is not flat in its initial state, the difference in the curvature, $\Delta\kappa$, between the two bent states would be used in equation (4.4) rather than the absolute value of κ.

A significant research effort has been put into investigation of the spontaneous strain formation in LCE materials previously in the literature, however, there are still many doubts about the relationship between the molecular arrangement and actuation [8]. It has been shown that the anisotropic volume change that leads to thermal actuation in LCE is contributed by multiple physical phenomena, primarily LC phase transition [69], and anisotropic thermal expansion [110]. For numerical modeling, the actuation properties of LCE are often approximated based on various equivalent effects for actuation. Thus, a behavioral model of the LCE actuator can be created based on the equivalent effect of thermal expansion. The LCE films used in this study were fabricated with a variation of LC alignment across the thickness of the layer, which induces a gradient of strain within the layer upon thermal actuation. Therefore, an equivalent CTE difference, $\Delta\alpha$, was introduced, which defines the difference in the CTE between the two sides of the film required to induce a certain amount of bending deformation in the LCE actuator. This value is not the actual CTE of the material, but the coefficient used to represent a collective effect of strain in response to thermal stimulus in terms of the equivalent thermal expansion. The basic relationship between the equivalent CTE and the thermally-induced strain for the analysis of bending deformation is given by equation (4.5),

$$\Delta\alpha = \frac{\Delta\varepsilon}{\Delta T}$$ (4.5)

where ΔT is the actuation temperature change.

The LCE-based bending beam problem can be treated as a special case of a thermal multimorph. The "layers" of the multimorph only differ in the thermal expansion value, while other material characteristics are the same. According to the unified theory of cantilever bimorphs [219], in the case of equal thickness and equal Young's moduli of the two components of a bimorph, the maximum curvature is given as:

$$\kappa_1 = \frac{3\Delta\alpha\Delta T}{2t} \tag{4.6}$$

In contrast to that, in the particular case where the neutral plane is assumed to be at one surface of the cantilever, and the other surface is under the strain of $\Delta\alpha\Delta T$, or in other words, when a smooth gradient of strain exists across the thickness, the estimated curvature is given as [219]:

$$\kappa_2 = \frac{\Delta\alpha\Delta T}{t} \tag{4.7}$$

The correlation between equations (4.6) and (4.7) is a factor of 1.5 of difference in the curvature value. Since the strain is distributed across the thickness of an aligned LCE film [137], [156], equation (4.7) should be used to analyze the curvature of an LCE beam assuming a smooth gradient of the equivalent CTE value across the thickness of the film. It can be seen that the relationship between the thermal strain and the curvature given with equation (4.4) directly follows from equation (4.7). Thus, in calculation, the curvature only depends on the beam dimensions and the driving term $\Delta\alpha\Delta T$, and it is independent of the Young's modulus or Poisson's ratio of the material. The equivalent effect of thermal expansion is further used in the work to compare the performance of the LCE actuators of different thicknesses, or with a different degree of LC alignment.

4.3 LCE Beam Fabrication and Measurements of the Bending Rate

For characterization of the bending behavior, thin strips were manually cut from the LCE films along the rubbing direction. The width of the strips was approximately 1 mm, and the length was between 8 mm and 23 mm, therefore, $l > w \gg t$, where l, w and t are the length, width and thickness of the strip (beam) respectively. The thickness could vary by a few microns across the area of the LCE film. The variation could have been due to non-uniform thickness of the glass cell for fabrication, or possible distortion of the shape of the flat cell under elevated temperatures. Additionally, several samples were fabricated in a tapered shape using spacers of different thicknesses at the opposite

ends of the glass cell. When the direction of taper was the same as the LC director, each beam was cut along the director to produce a tapered thickness. When the direction of taper was perpendicular to the LC director, each beam cut along the director from the same film had different thickness. Therefore, the actual thickness of each individual beam was measured under a microscope, and the measured values were used in characterization.

For measurements of the bending curvature of the LCE beams, it was important that the actuators deform freely, without friction to the surface. The bending actuation can still be observed in LCE films in air when the sample is in the vicinity of the hot surface. However, to ensure uniform, controlled heating of the samples for quantitative characterization, actuation was performed in a liquid medium: in a silicone oil (Alfa Aesar) bath in a metallic dish on top of a hotplate. The characterization of the LCE actuators was often performed in the oil bath previously in the literature [131], [220]. Silicone oil conducts the heat effectively. Each LCE beam was fixed at one end with a metal clip, immersed into silicone oil and heated on a hotplate. The actuation temperature was varied between 30°C and 80°C with ±0.1°C accuracy. Photographs of the beams under thermal actuation were taken with a digital microscope (Q-Scope QS.80200-P).

With the increase in temperature, the side of the film which was aligned with rubbed PI was rapidly shrinking along the LC director. This caused bending of the thin LCE beams towards the side with planar alignment. At the same time, it was expected that the material would experience anisotropic thermal expansion perpendicular to the LC orientation. The magnitude of shrinking along the director was significantly larger than the expansion perpendicular to the director. This behavior is shown in Figure 4.1. In the first case (Figure 4.1a) where the rubbing direction was along the beam length in the LCE actuator of 134 µm of thickness, a large curvature towards the planar aligned side was induced upon heating to 80°C. The bending was fully reversible over several actuation cycles. In the second case (Figure 4.1b) where the beam was cut perpendicularly to the rubbing direction, much smaller bending was induced by heating, in the direction away from the planar aligned side. These actuators also showed less stability over several cycles of actuation. Although, both effects of expansion and shrinking are present at the same time in both actuators, acting along perpendicular axes. The bending mode might be partially impacted by the holder type – whether the beam is free-standing or clamped from the edge. However, both the samples clamped

with a metal clip and the free-standing samples were tested in our work, and they showed similar behavior, not impacted by the holder. Therefore, it was concluded that in the LCE beams cut along the LC director (Figure 4.1a) the effect of anisotropic expansion was sufficiently weaker as compared with anisotropic shrinking in other direction, and therefore was considered negligible.
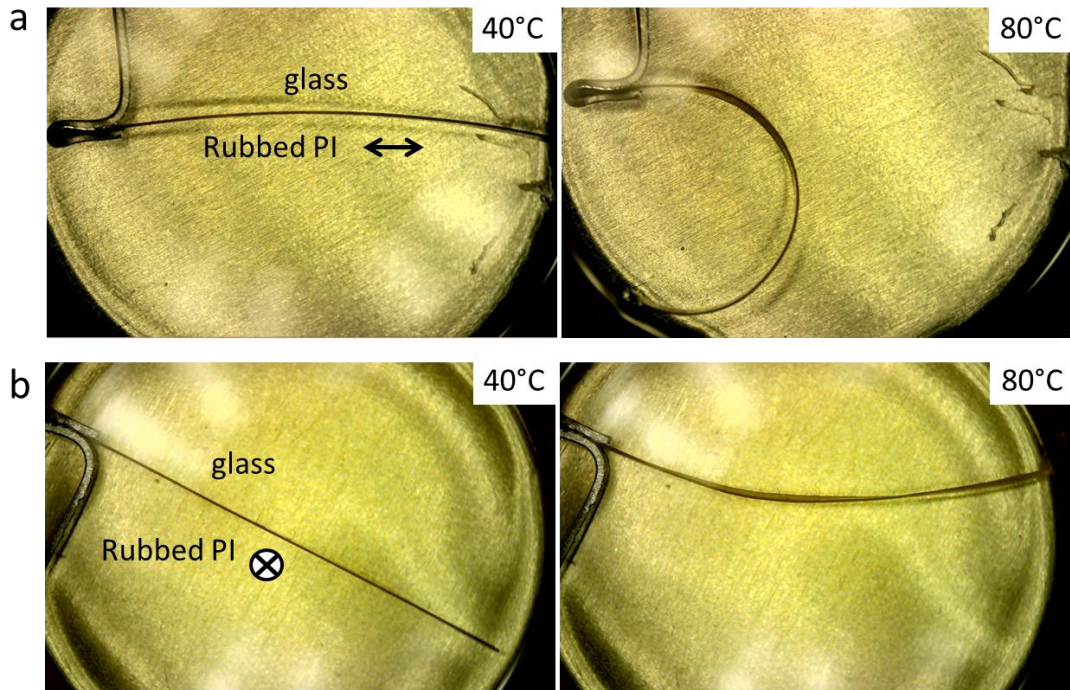
Figure 4.1 Bending behavior of the LCE actuators of 134 µm in thickness upon temperature increase a) for the beam cut along the direction of rubbing; b) for the beam cut perpendicular to the direction of rubbing

The arc-like bending of the LCE beam of 92 µm in thickness and 16 mm in length upon the increase in the actuation temperature is shown in Figure 4.2a. Each sample was subjected to 2-3 heating and cooling cycles. The radius of curvature, R, of the LCE actuator was measured from the microscope images using the built-in software tools for measurement by fitting the curved shape of the LCE beam with a circle. A similar method of measurement was used in the previous studies of LCE actuators in the literature [17]. The digital measurement tool was calibrated using a calibration sheet (Q-Scope) each time when changing the magnification. The measured values of radius were converted into the curvature, κ, which is inversely proportional to R. The curvature data was plotted against the actuation temperature, T, for four heating and cooling runs on the graph in Figure 4.2b. It can be observed that the first heating cycle differs from the

three subsequent cycles due to the release of residual stress accumulated after fabrication. Afterwards, the LCE beams exhibited stable, fully reversible bending behavior within the operating temperature range up to 80°C. The phenomenon where the first cycle of heating in thermal actuators differs from the subsequent cycles was discussed previously in the literature [218] for SU-8 based actuators, where it was also attributed to the residual stress release. The sources of such behavior in the SU-8 polymer-based thermal actuators and microgrippers have also been studied in Publication (2). It is shown that the moisture absorption from the environment also affects the actuation behavior significantly on the first heating cycle. On the other hand it was found that after the LCE actuators were additionally treated in the oven at 55°C for 15 minutes for the release of thermal stress prior to characterization, the first cycle of actuation was no longer different from the subsequent cycles.
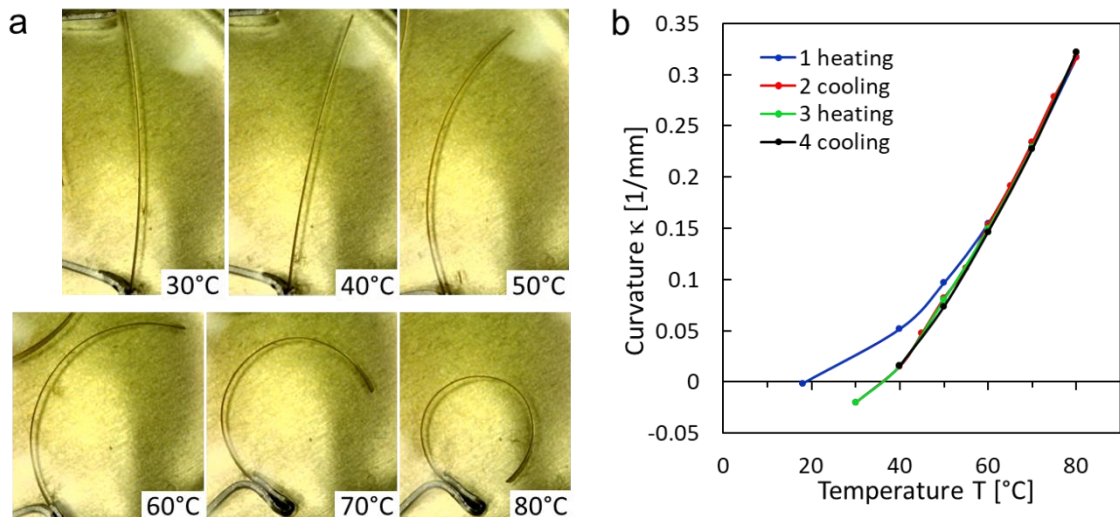
Figure 4.2 a) Microscope images of the curled shapes of the LCE actuator (thickness of 92 µm) under the temperature increase from 30°C to 80°C, b) Plot of the beam curvatures measured throughout 4 cycles of heating and cooling

Typically, the characterization of the LCE actuators in the literature has been focused on one device or a few devices with the same thickness, fabricated from a uniform LCE film. Thus, the efficiency of the particular alignment method for the actuation behavior of LCE structures of different thicknesses is unknown. Several studies in the literature previously stated that the LC alignment induced by a rubbed surface can only propagate to a limited thickness of about 100 µm, and therefore, the actuation performance of the LCE films would deteriorate rapidly with the increase in thickness beyond 100 µm

87

[115]. However, a direct comparison of the bending rate of the LCE actuators in a large range of thicknesses has not been demonstrated before. Therefore, in the thesis work, it was important to characterize a large number of LCE film samples fabricated in the same process in order to observe the trend and to develop a more universal approach for modeling of the actuation behavior.

The thermal bending rate, $\Delta\kappa/\Delta T$, for the LCE actuators was calculated between the two actuated states at 40°C and 80°C ($\Delta T = 40$°C) on the cooling cycle. Using the $\Delta\kappa/\Delta T$ data the behavior can be compared for various thicknesses of the actuators. The plot in Figure 4.3a shows the values of thermal bending for the LCE beams fabricated in the range of thicknesses from 12 µm to 194 µm. The data points of different colors refer to different batches of fabrication, meaning that the data presented with the points of one color was collected from the LCE beams that were cut from the same LCE film. It is evident that the actuators with a smaller thickness exhibit rapidly increasing bending rates. Further, the bending effect could be expressed in terms of the equivalent thermal expansion effect; the values of $\Delta\kappa/\Delta T$ were used to calculate the equivalent CTE, $\Delta\alpha$, following equation (4.7). The plot of the equivalent thermal expansion values is shown in Figure 4.3b.

It was observed that for the LCE samples of different thicknesses up to ~134 µm, the equivalent CTE tends to approach a similar average value. The average $\Delta\alpha$ was 649 ppm/°C (calculated excluding one point at 124 µm with a large offset possibly due to a fabrication problem), shown in Figure 4.3b with a yellow line. Up to the thickness of ~134 µm, the curve of average approximates the actual measurement data of the bending rate in Figure 4.3a very well. The deviation from the average value may be due to slight non-uniformity of the internal LC alignment pattern or non-uniform beam thickness. Another source of error is associated with the measurement method of fitting the arc shape of the LCE beam with a perfect circle, while the actual curvature of the beam may be not perfect due to the aforementioned factors. It was also shown that for the beams of larger thicknesses (140-194 µm, indicated with hollow circles in Figure 4.3) the equivalent $\Delta\alpha$ value is significantly lower. This is due to the limited thickness of the layer to which the alignment of LC can propagate from the surface [115]. It is important to note that the value of $\Delta\alpha = 649$ ppm/°C was related to the particular LCE recipe and particular fabrication process used in this work. For other fabrication conditions, the average $\Delta\alpha$ can be derived in the same way from the measurements of

the beam curvature. The equivalent CTE will be further used to create a finite element model for numerical simulation of the bending and rolling behavior in LCE actuators.
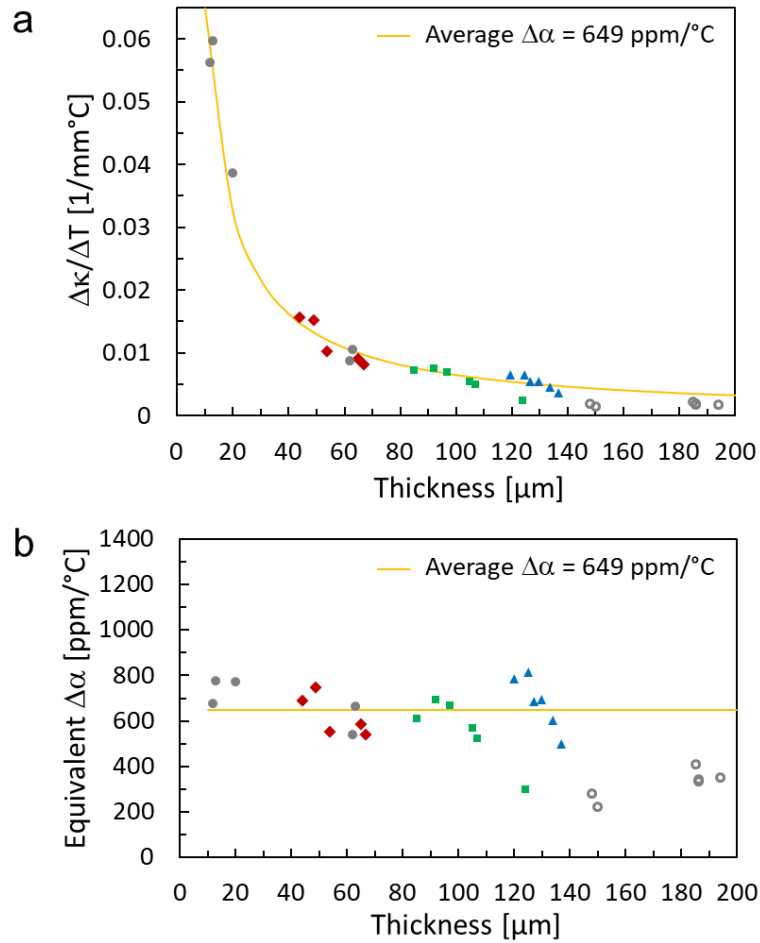
Figure 4.3 a) Measurements of the thermal bending rate, $\Delta\kappa/\Delta T$, for LCE actuators of various thicknesses; b) calculated equivalent coefficient of thermal expansion, $\Delta\alpha$, used in analysis

4.4 Model Validation

This section describes the development of the model for numerical simulation of the bending and rolling behaviors of LCE beams based on the gradient of the equivalent thermal expansion. In the FEM model for simulation, the LCE beam is built in a layered structure, where the layers are assigned with the CTE values linearly decreasing from one surface to the opposite surface. Thus, the gradient of thermal expansion causes out-of-plane bending under the influence of an elevated temperature. Although the actual physics behind the formation of strain in LCE is complex, as characterized with the order parameters [66], [103], it will be shown that a simplified behavioral model based

on the equivalent thermal expansion effect is able to provide sufficient level of accuracy in prediction of the resultant bending and curling characteristics. In contrast to the FEM models of the LCE-based actuators demonstrated previously in the literature (Section 2.10), which were typically demonstrated for actuators of a certain thickness for a particular application, the aim of this work was to develop a more flexible model that would be able to predict the bending behavior of the actuators in a wide range of thicknesses, and also of the actuators with non-uniform and tapered thickness.

4.4.1 Finite Element Simulation Setup

A 2D finite element model of the LCE beam was created in COMSOL Multiphysics using the 'Structural Mechanics' module and the 'Thermal Stress' multiphysics interface. It couples two physics interfaces, 'Solid Mechanics' and 'Heat Transfer in Solids', and creates the 'Thermal Expansion' multiphysics, in order to simulate the thermal strains in the structures according to equation (4.5). The stationary study was performed to find a steady-state response of the actuator to the thermal stimulus. The rectangular actuator was built on a 2D plane, the length of the beam was along the Y axis, the thickness of the LCE layer was along the X axis. The values were set with variable parameters for length and thickness of the beam, and the third dimension (width) was omitted. In this case, the 'plane stress' approximation was used for modeling, as the width of the LCE beams was sufficiently small compared with the length [221]. 'Plane stress' approximation implies that the stresses in the third dimension are neglected, in which case:

$$\sigma_{zx} = \sigma_{zy} = \sigma_{zz} = 0 \,,$$

$$\varepsilon_{zx} = \varepsilon_{zy} = 0, \ \varepsilon_{zz} \neq 0 \qquad\qquad (4.8)$$

where σ_{zx} and σ_{zy} are the shear stresses, σ_{zz} is the normal stress, ε_{zx} and ε_{zy} are the shear strains, and ε_{zz} is the normal strain in the structure represented with a 2D model on the XY-plane, and Z is the axis perpendicular to the XY-plane. This approximation is typically used in the case where the third dimension of the structure is small compared with the other dimensions. The LCE was modeled as a nearly incompressible material with Young's modulus of $E = 1$ MPa and Poisson's ratio of $v \approx 0.5$, the same values as those used for modeling of the similar LCE material composition previously in the

literature [78]. However, in the model based on the thermal expansion, the choice of *E* and *v* has negligible effect on the amount of bending [219], [222], which was confirmed by simulation. The standard model for polyimide from the COMSOL materials library was used as a basis to create the custom LCE material, therefore, the other material properties used in simulation were those of a polyimide material, which were: density of 1300 kg/m^3, thermal conductivity of 0.15 W/(m*K), and heat capacity at constant pressure of 1100 J/(kg*K). These parameters are not available from the literature for the LCE of the particular chemical composition used in the work. However, these values are not critical, because in a stationary model with a fixed temperature load the result of modeling does not depend on these properties.

The key material property which defines the actuation behavior of the structure is the coefficient of thermal expansion. The model of the beam was built of multiple layers across the thickness of the beam, where *n* is the total number of layers, and *i* = 1, 2,…, *n* is the *i*th layer, as shown in Figure 4.4. The CTE of the *n*th layer (at the surface of the LCE film planar aligned with the rubbed PI) was assigned with the value α_n = 1 ppm/°C as it had to be a non-zero value for FEM analysis. The CTE of the layer at the opposite surface of the film (*i* =1) had the maximum value, therefore $\alpha_1 = \alpha_{max} = \Delta\alpha + \alpha_n = 650$ ppm/°C, according to the average equivalent CTE, $\Delta\alpha$, defined in the fabrication process. Hence, for the intermediate layers, the CTE value was gradually decreasing from one boundary of the beam to the opposite boundary, as given with equation (4.9):

$$\alpha_i = \alpha_{max} \times (n - i)/(n - 1),\qquad\qquad(4.9)$$

where α_i is the CTE of the *i*th layer. Therefore, the CTE of material layers in the model varied in the range from 1 to 650 ppm/°C, and this gradient would give rise to the bending deformation. The rest of the material properties were the same for each LCE layer. It must be noted that the values of α_i are not the actual coefficients of thermal expansion of the real material, but the values used for the purpose of modeling of the bending behavior; where only the increment in CTE between the layers is important, and not the actual value. Thus, the current model investigates the curvature of the beam, while disregarding the global contraction/expansion component. It was confirmed in simulation that when α_n had a value different from 1 ppm/°C, the effect on the total curvature was negligibly small.

In setting up the boundary conditions for simulation, for the Solid Mechanics interface, the Linear Elastic Material model was used for the entire LCE structure. The "fixed" boundary condition was set at the short edge of the beam (Figure 4.4), where the LCE

actuator was held at one end with a clip. In the Heat Transfer in Solids interface, a fixed temperature load, T, was set at the outer boundaries of the structure, as the device was heated through the surrounding medium. In the Thermal Expansion multiphysics interface, the strain reference temperature was defined, T_0, at which the beam shows zero bending. T and T_0 were variable parameters. A mapped mesh with rectangular elements was created for the structure with a distribution of 200 elements along the long axis of the beam. In the settings for the stationary study, the option 'Include geometric nonlinearity' was selected, which enables the physics of large deformations to be deployed for calculation of the large curvature of the beam. This is applied when the magnitude of displacement is large so that it may affect the response of the structure. Simulation of the actuation behavior of the beam was performed using the 'auxiliary sweep' function, which allowed obtaining multiple results at once within the chosen range of temperatures with the defined step size. Through performing auxiliary sweep, the solver algorithm was using the solution from the previous temperature point for calculating the solution in the next point. It is an efficient approach in simulation of large deformations, as the solution gradually 'builds up', which substantially reduces the computation time required for the algorithm to find multiple solutions for a range of input values.
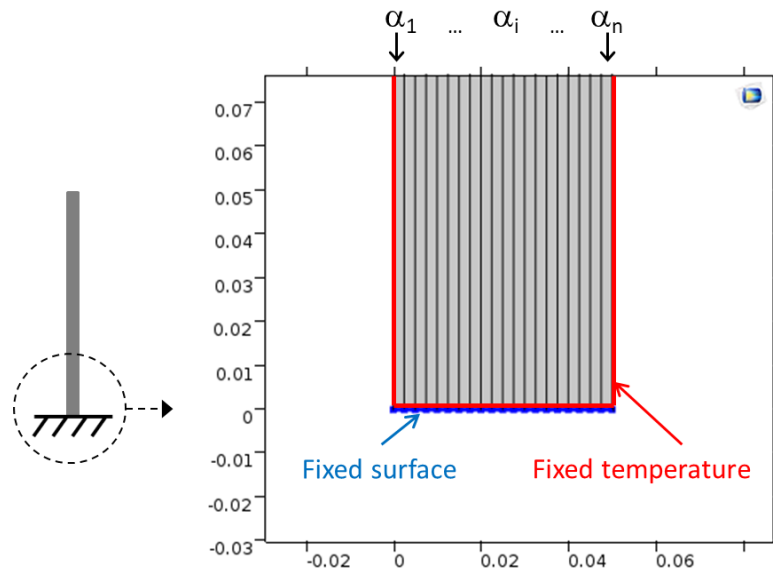
Figure 4.4 Design and boundary conditions of the multilayered 2D model of a bending LCE actuator

For the initial test, the FEM simulation was performed for the beam of 50 μm of thickness and 10 mm of length; it was assumed that there were no residual stresses, and

the strain reference temperature T_0 is 30°C (temperature of polymerization), where the beam is perfectly flat ($\kappa = 0$). Figure 4.5 shows the results of the simulation and analysis. The curvature values were derived from the coordinates of the three points in the beam, as the actuators obtain arc-like deformation at elevated temperatures. Since α_{max} has a constant value, therefore, there is a nearly linear relationship between the curvature and the temperature. The simulation was performed with a different number of layers, n. The results follow the trend as expected that in the case of a two-layer model ($n = 2$), the curvature is close to the analytical result for a bimorph as given by equation (4.6), indicated with a black solid line in Figure 4.5. As the number of layers increases ($n = 4, 8, 12$), the model produces a smoother strain gradient, and the results approach to that of the analytical prediction from equation (4.7), as indicated with a red solid line. The slight non-linearity of the simulation curve may be attributed to the specific mechanics of large deformations, whereas the simple relationships given by equations (4.6) and (4.7) are suitable for moderate deformation level.
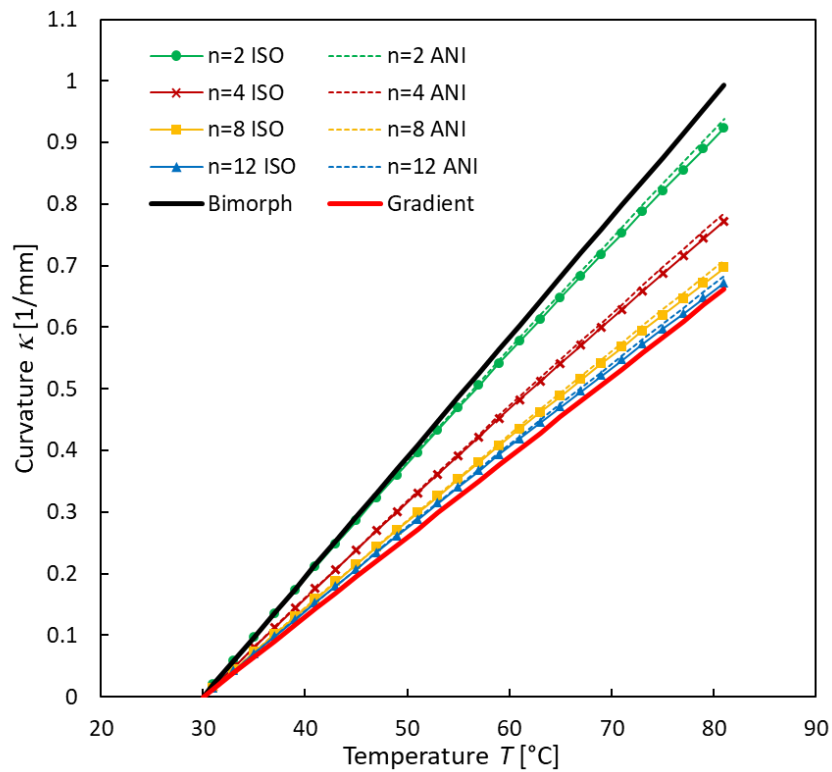
Figure 4.5 Comparison of the results of FEM simulation using a layered model (n - number of layers) with a gradient of thermal expansion across the thickness of the actuator beam (thickness 50 µm, length 10 mm). The solid lines with symbols represent simulation results using isotropic CTE properties; the dotted lines - anisotropic CTE properties. The linear behaviors for the beams from equations (4.6) and (4.7) are also shown

Next, the results were compared for the models which use an isotropic or anisotropic CTE parameter. For this, the CTE was defined in the Thermal Expansion multiphysics for each layer separately in the following tensor form:

$$\begin{pmatrix} 0 & 0 & 0 \\ 0 & \alpha_i & 0 \\ 0 & 0 & 0 \end{pmatrix}, \qquad (4.10)$$

so that the thermal expansion/shrinking acts only along the long axis of the beam, Y axis (the PI rubbing direction). It was discussed that the thermal expansion of the nematic LCE material has a strongly anisotropic character. In the previous studies in the literature [128], [180], anisotropic thermal expansion has been commonly used for modeling of the LCE actuators. However, as shown in Figure 4.5, the difference in results between the models with isotropic (solid lines) and anisotropic (dashed lines) coefficients is small, only within 1.7%. The 12-layer model already provides an efficient estimation of deformation of the beam in comparison with the theoretical prediction. However, certain limitations are associated with using an anisotropic model with larger number of layers. Firstly, the computational complexity and time for anisotropic simulation increased rapidly with the number of layers. For n≥12, the time of simulation from several minutes increases twice with each new added layer; for n≥17, a computational problem occurred which prevented simulations with larger number of layers from completing. Secondly, anisotropic CTE tensors had to be manually specified with new entry for each layer in the model, which is potentially much less efficient for the purpose of rapid development and optimization for applications. Whereas, by using isotropic thermal expansion in the model, the number of layers could be increased to 20 easily, which gives better agreement with the analytical model. Therefore the subsequent simulations were performed using 20 layers with isotropic CTE for prediction of bending and curling behaviors of the LCE beams.

The nearly linear model with a constant CTE was hereby used to optimize the solver settings and verify that the result of modeling agrees with the theoretical prediction of bending deformation based on the relationship described by equation (4.7). In practice, the CTE of the LCE materials, like other polymers, varies significantly with temperature. Therefore, a temperature-dependent CTE was introduced in the model, leading to the nonlinear actuation behavior, which is discussed in the next subsection.

4.4.2 Nonlinear Simulation of the Bending LCE Actuators

Three fabricated LCE beams of 44 µm, 92 µm, and 134 µm of thicknesses were selected for the following detailed analysis, because the actual values of $\Delta\alpha$ of these samples were close to the average value of 649 ppm/°C. The results of linear analysis using equation (4.7) (solid blue line) were compared with the measurement data (filled circles) as shown in Figure 4.6a, Figure 4.6b and Figure 4.6c for the three actuators respectively. The actual measured reference temperatures for T_0 for each sample in the flat state were used in the analysis, which were 40°C, 35°C and 32°C for the three actuators respectively. These temperatures were different from the polymerization temperature of 30°C due to the effect of residual stresses after fabrication. The values $\Delta\varepsilon$ in Figure 4.6 indicate a strain difference between the opposite sides of the beam which causes arc-like bending, calculated using equation (4.4). For the samples of 44 µm, 92 µm, and 134 µm of thicknesses, the values of $\Delta\varepsilon$ at the maximum actuation temperature of 80°C were 0.0275, 0.0291 and 0.0290 respectively. The three graphs demonstrate that with approximately the same strain difference $\Delta\varepsilon$ in the material, the resulting curvature was smaller as the thickness was increasing. However, it is evident that the linear analytical model does not provide a good level of accuracy in prediction of the actual bending behavior of the beam, which is nonlinear. In practice, CTE is a temperature-dependent property. Therefore, a temperature-dependent α_{max} is introduced in equation (4.11) [218], [223]:

$$\alpha_{max}(T) = \alpha_{max}(T_{ref})[1 + \theta(T - T_{ref})] , \qquad\qquad (4.11)$$

where T_{ref} is the reference temperature for the value of CTE, and θ is the first order temperature constant. In Section 3.3, it was shown that the equivalent CTE was derived from the measurements taken at the actuation temperature of 80°C. Therefore, the following values were used for analysis: T_{ref} = 80°C and α_{max}(80°C) = 650 ppm/°C. The coefficient, θ, was then determined by fitting the measurements data with a curve through the least squares method for 7 different samples; the average value was found to be θ = 0.00742°C^{-1}, and this was used in further modeling. The value of α_{max} as a function of temperature is shown in Figure 4.6d. The results of nonlinear analysis for the beams are presented in the Figure 4.6a-c (solid red curve). It can be seen that the nonlinear curve based on the temperature-dependent equivalent CTE predicts the behavior of the beams of different thicknesses with good accuracy.
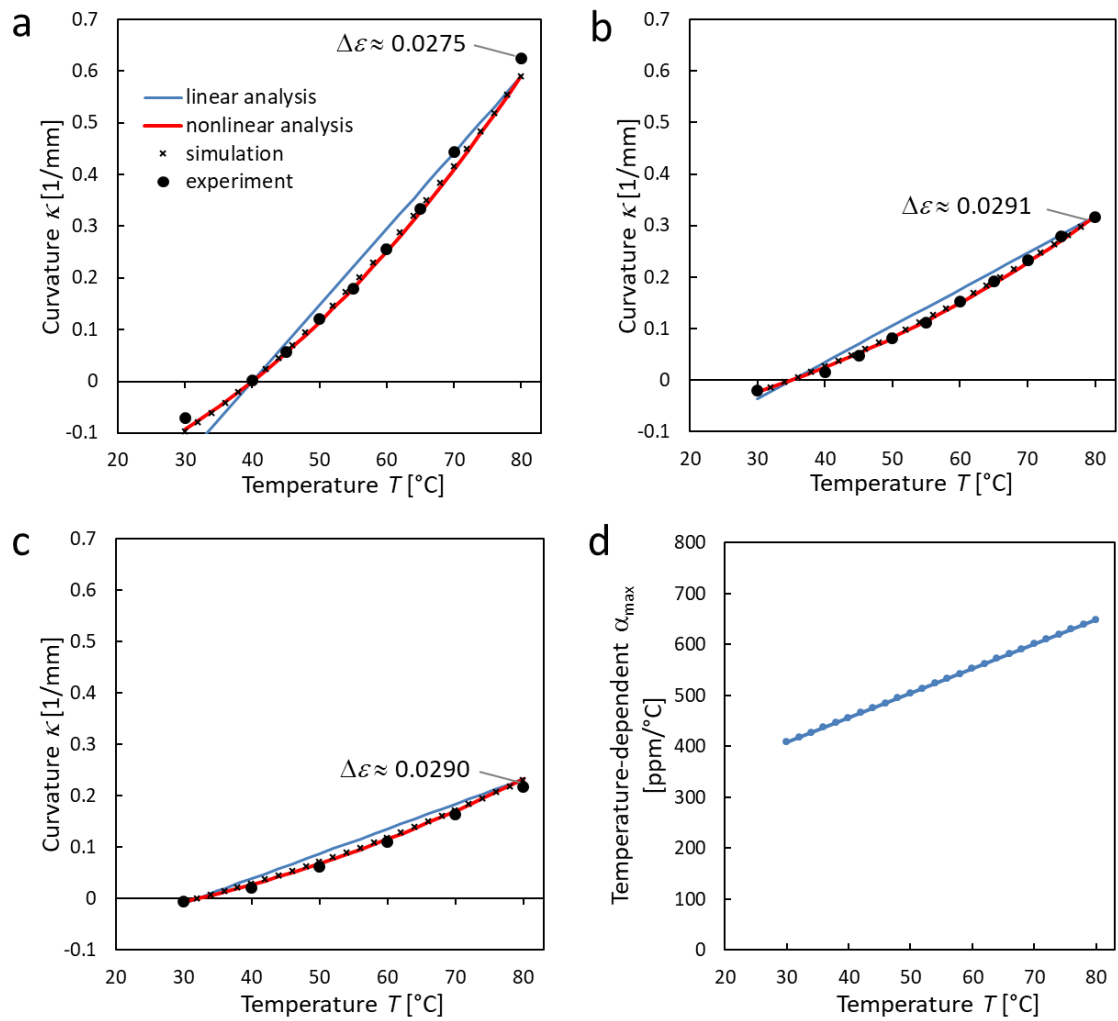
Figure 4.6 Analytical and numerical results and experimental measurements of the beam curvature demonstrating a nonlinear bending behavior of the LCE beams with the thickness a) 44 µm; b) 92 µm; c) 134 µm; d) the plot of α_{max} as a function of temperature

To perform numerical simulation in COMSOL, the parameter α_{max} was set with an analytical expression of the argument T based on equation (4.11). The results of simulation are also presented in Figure 4.6a-c (cross marks). The radius of curvature was calculated from the coordinates of three points along the length of the bending beam. It can be seen that the nonlinear FEM model matches closely with the results of nonlinear theoretical analysis, and can accurately predict the behavior of the LCE beams of various thicknesses under thermal actuation. The example in Figure 4.7 shows the bending shapes of the LCE beam, as obtained in simulation, upon actuation within the range from 30°C to 80°C. The thickness of the beam was 92 µm, the length was 16 mm, the strain reference temperature $T_0 = 35$°C. The radius of curvature at 80°C was 3.16 mm in the result of simulation. The bending behavior of the model agrees well with the

96

actual behavior of the actuator observed under the microscope as was shown in Figure 4.2.
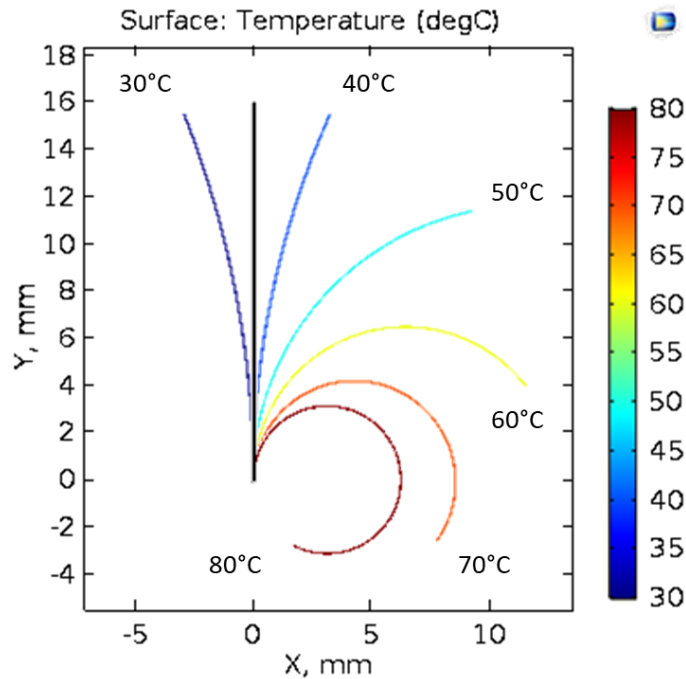
Figure 4.7 Deformation shapes of the LCE beam obtained by FEM simulation for a beam model of uniform thickness of 92 µm and length of 16 mm

When designing and making analytical prediction for new functional LCE structures, the average $\Delta\alpha$ value rather than the exact measured value should be used for the beams of thicknesses less than ~134 µm. The actual equivalent CTE values for the samples may scatter due to non-uniformities in fabrication, while the average value describes the general trend in the behavior. Therefore, it was important to characterize a number of test samples rather than one in order to observe the trend. Below is an example of using the proposed FEM model to predict the behavior of the LCE beams, in which case the actual $\Delta\alpha$ deviated more significantly from the average. Two fabricated LCE actuators with the thicknesses of 49 µm and 67 µm have demonstrated the thermal actuation with the equivalent CTE values of 745 ppm/°C and 537 ppm/°C, respectively. The measurement data for the bending curvature are presented in Figure 4.8a and Figure 4.8b. The numerical simulation was performed using the same FEM model based on equation (4.11) assuming the average value $\alpha_{max}(80°C) = 650$ ppm/°C. It can be observed from Figure 4.8 that the discrepancy between the simulation and

measurements becomes noticeable only at high actuation temperatures (~70°C). When the actual CTE for the sample is larger than the average (Figure 4.8a), the simulation under-predicts the actual magnitude of deformation. When the actual CTE is smaller than the average (Figure 4.8b), the simulation over-predicts the deformation. However, the model is still able to provide reasonable prediction of the bending behavior using the average equivalent CTE for the material. Although using the actual $\Delta\alpha$ value in each individual case would provide more accurate agreement with the experiment, it is better to use the average $\Delta\alpha$ when designing new actuators of thicknesses less than ~134 µm, because the average value is more representative of the material behavior than the individual values.
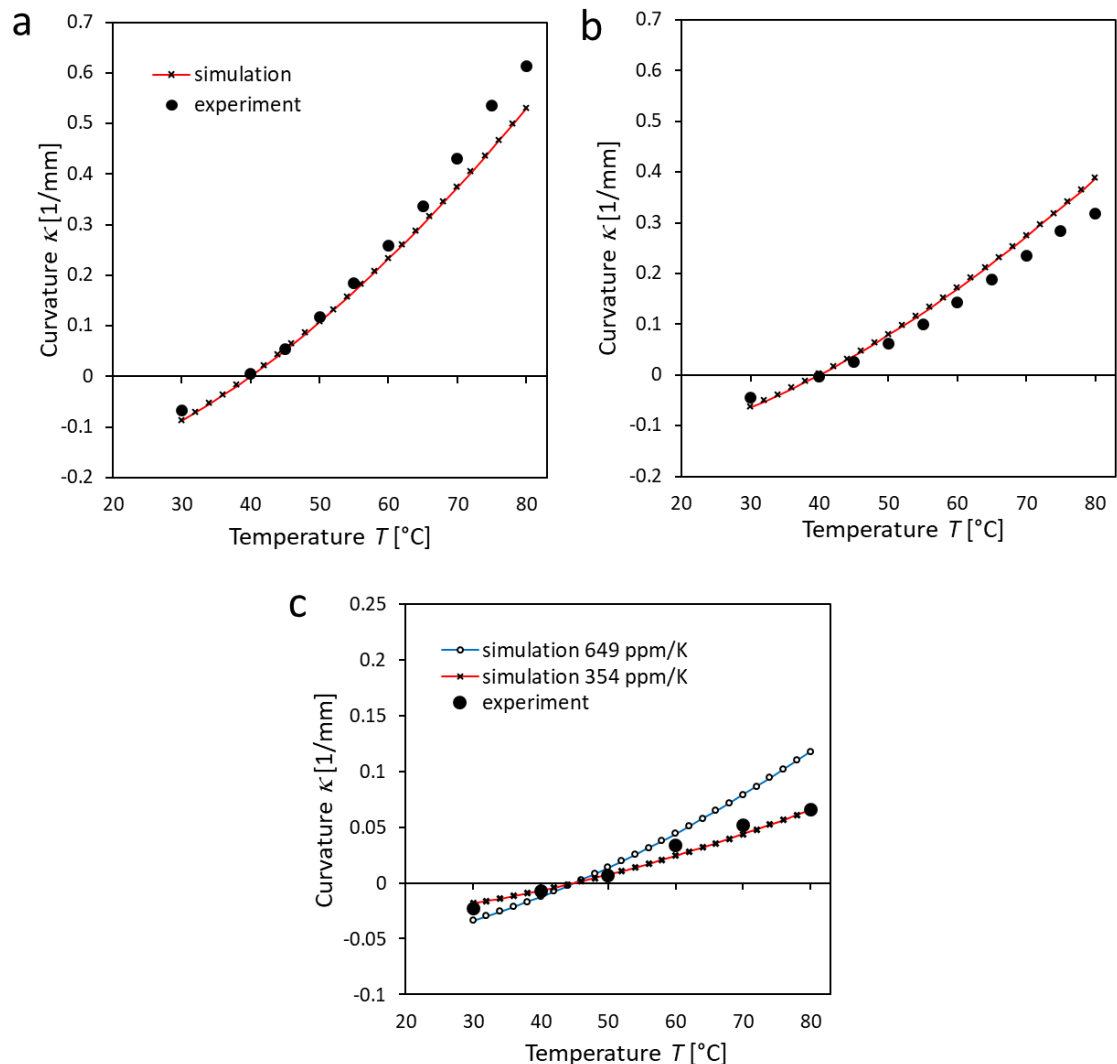
Figure 4.8 Results of simulation and experimental measurements of the curvature of LCE beams of the thickness of a) 49 µm; and b) 67 µm, simulations performed using the average value, $\Delta\alpha = 649$ ppm/°C; c) beam thickness 194 µm, simulations performed using average $\Delta\alpha$ and actual $\Delta\alpha$ (354 ppm/°C) values

On the other hand, surface aligned LCE actuators with thicknesses larger than ~134 μm cannot be modeled using the average CTE, as the LC alignment from the surface cannot propagate effectively into thicker films. In this case, the individual equivalent $\Delta\alpha$ value must be used for numerical simulation. The measured bending curvatures of the LCE actuator of 194 μm in thickness are demonstrated in Figure 4.8c, along with the results of modeling. It can be seen that the simulation based on the average $\Delta\alpha$ value of 649 ppm/°C is not suitable for estimation of the actuation behavior, whereas, the model using the actual $\Delta\alpha$ value of 354 ppm/°C for the particular beam can predict the curvature with good accuracy.

4.4.3 Numerical Simulation of the LCE Actuators of Tapered Shape

The proposed FEM modeling approach can be applied not only to the LCE beams with uniform thickness, but also to some actuators with a more complex geometry, such as beams with tapered thickness variation. A LCE-based actuator of tapered shape have been fabricated and modeled by numerical simulation previously in the literature [182]. The thickness of the splay-aligned LCE actuator varied linearly from 50 μm to 20 μm. The model provided good prediction of the rolled shape of the beam under thermal actuation up to 65°C, however, the simulation started to deviate significantly from the experimental results at higher temperatures. As compared with the 3-layer model in the literature, the proposed multi-layer numerical model may be able to provide a more accurate agreement with the experiment for curling LCE actuators of tapered shape.

The tapered LCE films were fabricated by using different spacers at the opposite ends of the glass cell for fabrication. The direction of the taper was the same as the direction of rubbing, so that the LCE beams cut from the film along the LC director were in a tapered shape. The beam shown in Figure 4.9 had a thickness of 63 μm at the fixed end, decreasing linearly to 12 μm at the free end. The length of the beam was 22.5 mm. The beam was fixed with a metal clip at the thicker end and immersed in the oil bath for characterization. The film was initially flat at $T_0 = 38.7$°C. Upon actuation with the temperatures of 50°C, 60°C and 70°C, the tapered LCE beam curled into a roll shape, with a smaller radius of curvature at the thinner end of the beam, as expected from the equation (4.7). The FEM model of a tapered beam was built using tapered polygonal elements rather than rectangles for each of the 20 layers. The other parameters and the

boundary conditions in the model were similar to those described previously in Section 3.4.1. The thicker end of the actuator (63 µm of thickness) had the fixed edge. The temperature-dependent equivalent CTE was set up with an analytic function based on equation (4.11), where $\alpha_{max}(80°C) = 650$ ppm/°C. The results of simulation are shown in Figure 4.9, under the same actuation temperatures as for the test beam shown in the microscopic images. It can be seen that the numerical simulation provided very good prediction of the beam deformation across the actuating temperature range. Therefore, it was experimentally validated that the proposed FEM approach is effective for modeling of the LCE-based beams of various shapes and thicknesses. Due to the complex mode of deformation, the behavior of the beams with non-uniform shape may be extremely challenging to calculate with analytical methods. In this case, finite element modeling becomes a key technique capable of predicting the behavior of the LCE actuators. As compared with the model of a tapered beam from the literature [182], the new model provided good accuracy in prediction of the LCE behavior at low actuation temperatures as well as higher temperatures up to 80°C.
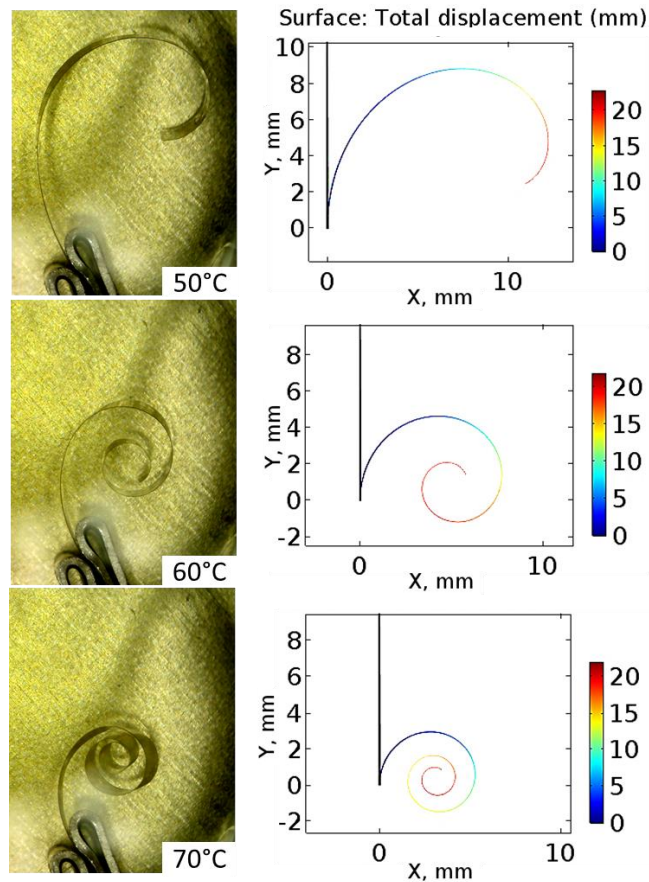
Figure 4.9 Microscopic images and FEM simulation of rolling behavior of the LCE beam with tapered thickness (63 µm to 12 µm at each end respectively) and length of 22.5 mm under thermal actuation

100

4.4.4 Numerical Simulation of Bending Beams based on Different LCE Material Systems

The calculated equivalent CTE value is specific to the chemical composition of the LCE material and the alignment method used in fabrication. For instance, it has been demonstrated in the literature that the crosslinker ratio has a major influence on the total deformation produced by the LCE actuators [17], [224]. Different coating layers induce the LC alignment with different order parameters. Therefore, the derived value of $\Delta\alpha =$ 649 ppm/°C corresponds to the particular LCE recipe and particular fabrication process used in this work. For another combination, the appropriate $\Delta\alpha$ can be determined in the same way merely from the measurements of the curvature of the beam. One of the key advantages of this approach is that it does not require measurement of the actual strain, which is more challenging in terms of procedure and calibration [225]. It will be shown that the proposed modeling method can be used effectively with different LCE material systems. The behavior of the LCE actuators demonstrated previously in literature [17], [187] could be recreated in the numerical model based on the developed simulation method, using the actual parameters as available in the reference.

The work by Shahsavan et al [17] on thermally active LCN cantilevers for bio-inspired application was used as the basis for analysis and simulation. In their work, the LCE mixture was prepared using two monomer components: the M1 is 4-(6-Acryloxy-hex-1-yloxy)phenyl 4-(hexyloxy)benzoate, and the M2 is 1,4-Bis[4-(6-acryloyloxyhexyloxy) benzoyloxy]-2-methylbenzene. Four material systems with different ratios of the crosslinker M2 of 12%, 25%, 50%, and 75% were used to fabricate LCE cantilevers with the thickness of 188 µm. Splayed alignment of LCE film was created using two polymer-coated glass slides: one for planar alignment, and one for homeotropic alignment. Therefore, both the chemical composition of the LCE material and the alignment method used by Shahsavan et al. in their work were different from those used in the thesis work. Following the developed method of numerical simulation, a multi-layered FEM model was built for these actuators. The parameters used for modeling are listed in Table 4.1. The values of the thermal bending rate, $d\kappa/dT$, were obtained from the reference [17]. These values were used to calculate the equivalent CTE, $\Delta\alpha$. The approximate values of the strain reference temperature, T_0, was extracted from the plot provided in [17], at the point where the measurement curve intersects the temperature axis (zero curvature). The reference temperature for calculation of the nonlinear CTE,

T_{ref}, was assumed to be the boundary of the actuation temperature range, which could also be extracted from the same plot. Thus, all necessary boundary conditions and parameters for modeling are already known from the previous work in [73].
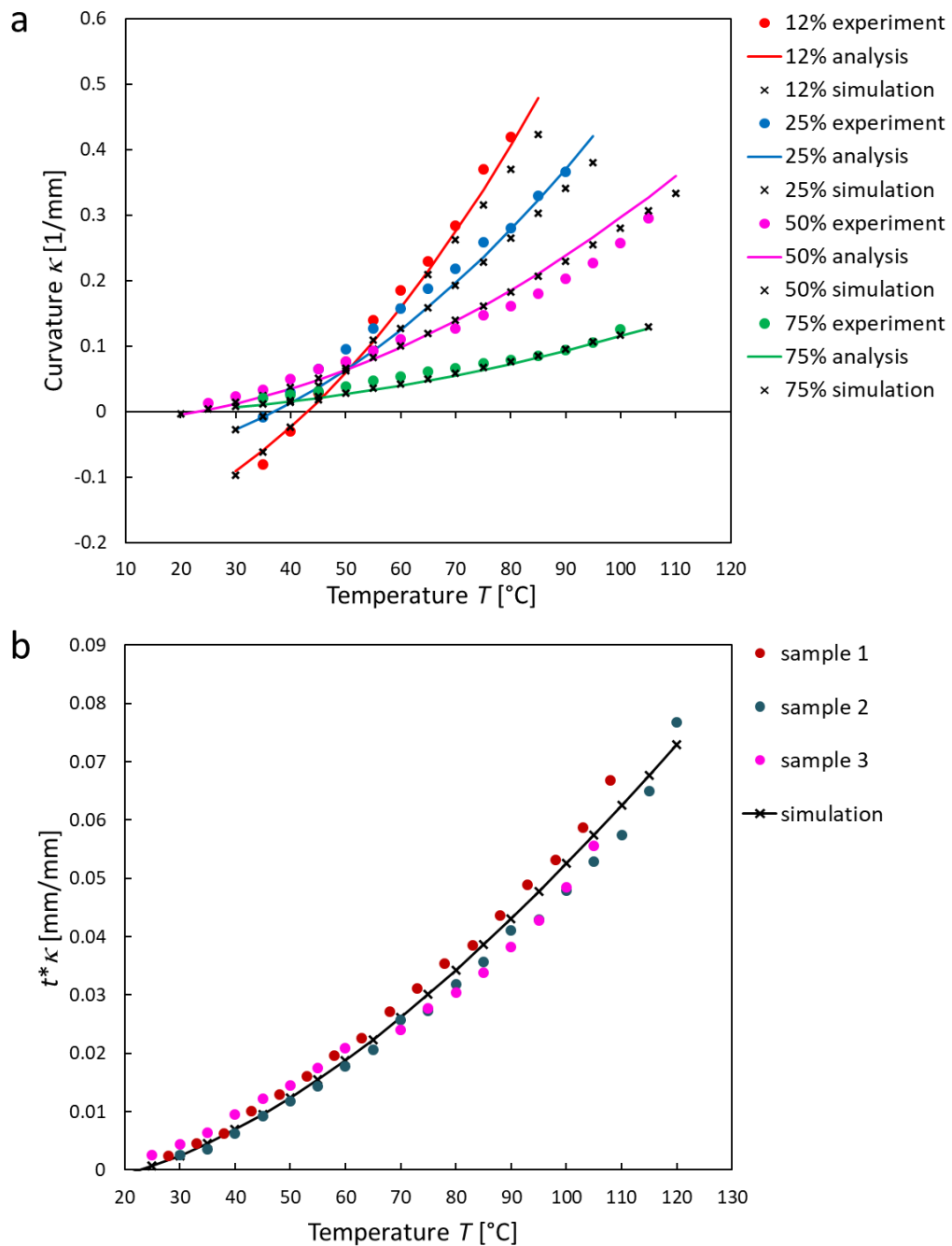
Figure 4.10 a) Comparison of simulation results with measurement data for LCE cantilever actuators with various LCE cross-linker content, based on experimental data reported in [17]; b) Comparison of simulation results with measurement data for LCE cantilever actuators with 50% cross-linker content, based on experimental data reported in [187]

Table 4.1 Parameters used for modeling and simulation of the bending behavior of LCE actuators with various LCE material composition. Based on experimental data reported in [17]

LCE system	Thermal bending rate, $d\kappa/dT$	Equivalent CTE, $\Delta\alpha$	Strain reference temperature, T_0	T_{ref}
12% M2	0.011 (mm°C)$^{-1}$	2068 ppm/°C	43°C	80°C
25% M2	0.007 (mm°C)$^{-1}$	1316 ppm/°C	37°C	90°C
50% M2	0.004 (mm°C)$^{-1}$	752 ppm/°C	23°C	105°C
75% M2	0.0015 (mm°C)$^{-1}$	282 ppm/°C	20°C	100°C

Figure 4.10a compares the results of the nonlinear analysis (solid lines) and FEM simulation (cross marks) with the measured results in [73] (filled circles). It can be seen that the model demonstrated reasonably good prediction of the bending behavior of the LCE cantilevers with different amounts of the crosslinker content. Additionally, the same material with 50% weight ratio of M2 was used in the work by Neufeld et al [187], therefore, the characterization data from 3 samples was also used to validate our model as shown in Figure 4.10b. The plot shows the values of the curvature normalized to the film thickness of 188 µm, $t^*\kappa$, as a function of temperature T (the measurements were taken on the cooling cycle). It can be seen that the results of simulation based on the developed modeling method match well with the reported experimental data within the given temperature range. Therefore, the proposed modeling approach can be used effectively to predict the behavior of the actuators based on various LCE material systems.

4.5 Characterization and Simulation for Photothermal LCE Actuators

In principle, the bending LCE beams can be actuated in air by thermal irradiation, such as near the hotplate surface. The main drawback of this approach is the requirement to have a source of heat in the vicinity of the LCE actuator. Actuation by thermal irradiation is poorly controlled and unreliable. On the other hand, untethered controlled operation in air can be provided by photothermal actuation. By incorporating the light-absorbing dye into the LCE matrix, the LCE material can be made responsive to light stimuli. The LC elastomers doped with photothermal agents have been widely used in previous research in the literature for photothermal actuation [226], due to the

advantages of remote operation, untethered operation without wire connection for supply of electrical signals, no additional integrated metal heater layers. In this work, the actuation properties of LCE material doped with 1 mol% and 2 mol% concentration of the dye were studied. The dye-doped LCE films were successfully fabricated with various thicknesses. For characterization of the actuation behavior, thin strips of the LCE film were cut along the rubbing direction.

The commercially available dye Disperse Orange 3 used in this work has its main light absorption peak at the wavelength region of 440-446 nm; therefore, photothermal actuation was performed using a blue-light LED (Thorlabs M455L4-C1) with the wavelength of 455 nm and the bandwidth (full width at half maximum) of 18 nm. The LCE beam was suspended in air, one end of the beam was fixed with tweezers, the side aligned with the rubbed PI facing upwards, as shown in Figure 4.11. The LED light was focused in a smaller spot of about 8 mm in diameter, illuminating the LCE beam from the top. The LED was driven with a current of 0.7 A, the intensity of light could be manually controlled with the LED driver. The maximum intensity from the LED was 239 mW/cm^2. All the light intensity values were measured using a handheld power meter through the circular hole of 4 mm in diameter.
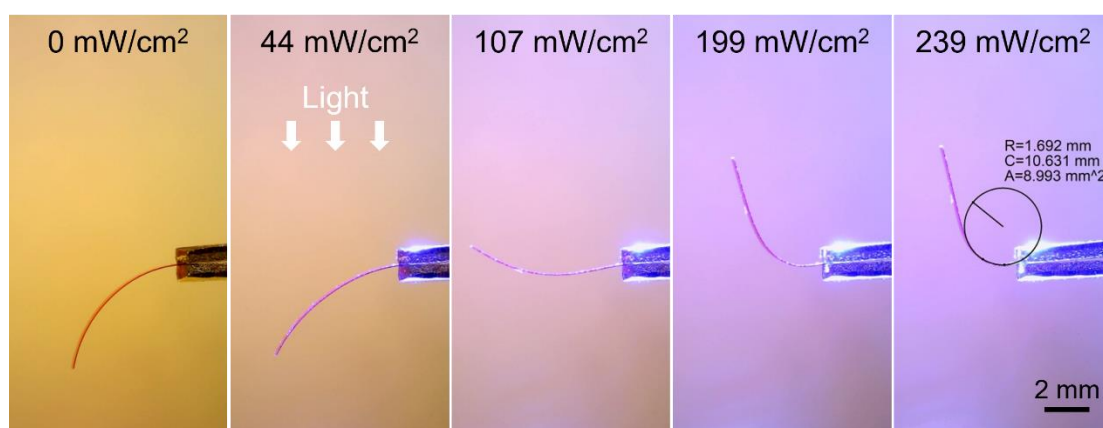
Figure 4.11 Photothermal actuation of the LCE film (50 µm of thickness) doped with the light absorbing dye (2 mol%) using the light of 455 nm of wavelength and various intensities up to 239 mW/cm^2

Figure 4.11 shows the deflection of the LCE beam of 50 µm of thickness, 8 mm of length, with 2 mol% dye concentration, which bent upwards, towards the side with planar alignment upon photothermal actuation with different stimuli. The bending was recorded with a digital microscope, and the curvature was measured using the built-in

measurement tools by fitting the curled shape with a circle, as shown in the example. It can be seen in Figure 4.11 that under high light intensity, the radius of curvature is small at the illuminated area; however, the free end of the beam curls upwards and remains straight, because of the low angle between the beam surface and the direction of light. In order to obtain a full arc-shape bending of the beam, another light source could be used to illuminate the sample from the side, thus avoiding the shadowing effect.

Besides photothermal actuation, the dye-doped LCE beams also demonstrated common thermal actuation. The beams curled in the vicinity of the hot surface of a hotplate in air. The beams showed bending and curling behavior in the oil medium similar to that of the undoped LCE actuators. Therefore, thermal actuation upon uniform heating in oil was recorded following the same method used before. Comparison of the thermal and photothermal actuation performance is shown in Figure 4.12 for the LCE material with 1 mol% dye concentration. Five samples of different thicknesses, t, were investigated: 43 µm, 62 µm, 73 µm, 92 µm, and 114 µm of thickness. The values of curvature induced by thermal stimuli (diamond shape marks) are plotted against the actuation temperature (bottom horizontal axis). A numerical model was built using this data. The simulation was based on the equivalent CTE values calculated for each individual sample, which were: 487, 419, 468, 466, and 479 ppm/°C for the beams of five different thicknesses, respectively. Thus, it was confirmed that the equivalent CTE was approximately similar over a large range of beam thicknesses; however, the average value was lower than that for the undoped LCE, due to the change in the material composition, and hence, its properties. The results of simulation are shown in Figure 4.12, the red curves, which closely match the experimental results. The curvatures of the beam induced by photothermal stimuli (solid blue curve with filled circles) are plotted against the light intensity (top horizontal axis). Since the photothermally induced temperature in the structure was not measured, the direct comparison of the performance cannot be made, however, it can be expected that the actuation response should be similar. Therefore, in the plots shown in Figure 4.12, the photothermal curves were matched to the thermal curves using the least squares method (same fitting coefficient was used in all five plots). The initial state of the beam at zero light intensity corresponded to the temperature of the environment of 22°C. This was to demonstrate that deformations induced by two different actuation methods in the same beam were overall comparable, as can be seen in Figure 4.12.
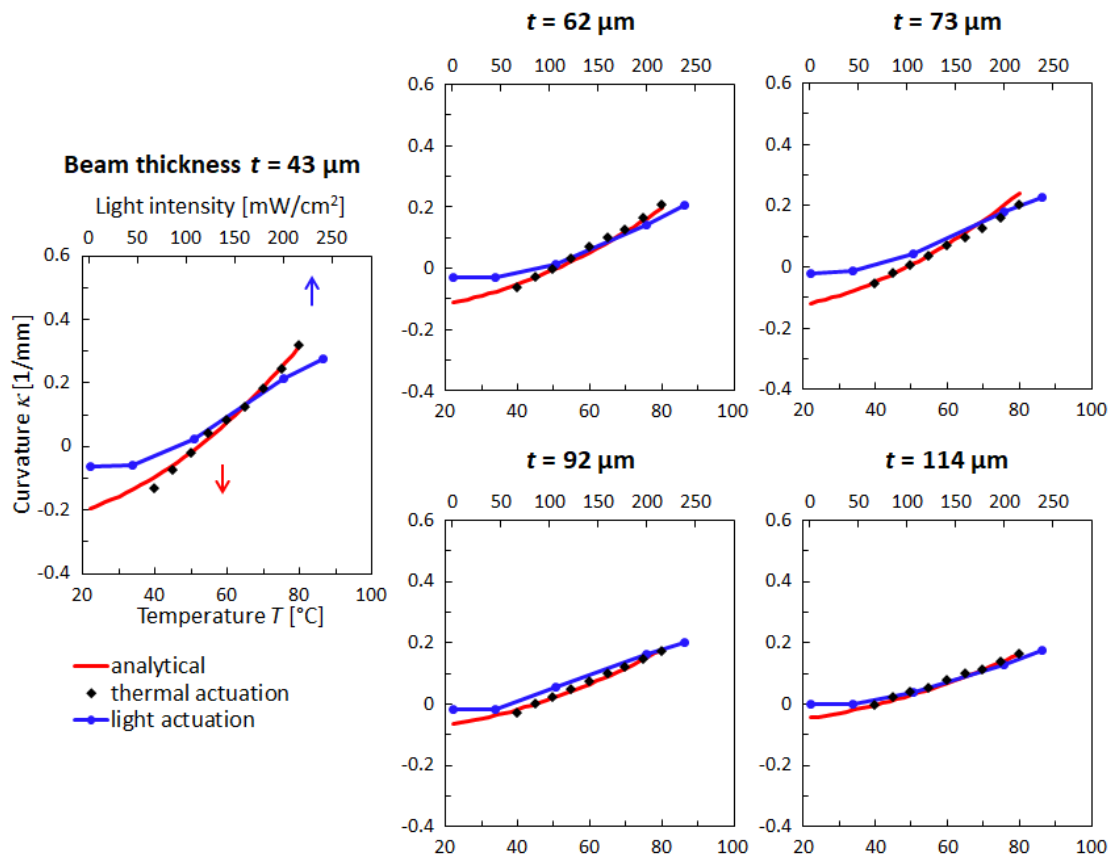
Figure 4.12 Measurements of the beam curvature for the LCE actuators doped with 1 mol% of the light-absorbing dye under thermal actuation between 40-80°C and light actuation with various light intensities

Figure 4.13 shows the results of thermal and photothermal actuation in the LCE beams with 2 mol% dye concentration of five different thicknesses: 44 µm, 50 µm, 65 µm, 70 µm, and 77 µm. The calculated equivalent CTE values used in thermomechanical simulation were: 600, 894, 570, 715, and 803 ppm/°C respectively. Similarly, the photothermal and thermal curves were matched using the least squares method, but the fitting coefficient was slightly different from that for the LCE samples with 1 mol% dye concentration; the environment temperature was 22.7°C in the initial state.

It can be seen that overall, larger curvatures were induced in the LCE films with higher dye concentration under the same light intensities. This is primarily due to the higher light absorption of the LCE material with 2 mol% dye. To confirm this, measurements of the transmitted light intensity were performed. Several pieces of the dye-doped LCE films were fixed on the flat glass slide, which was then placed over the sensor of the power meter, so that one film could completely cover the 4 mm opening. The transmitted power was measured and compared through the bare glass, and through the two LCE films of approximately the same thickness. For the first set of samples, the

106

results showed that for the measured power of 15.25 mW, the power transmitted through the LCE film with 1 mol% dye was 2.20 mW (14%), and through the LCE film with 2 mol% dye was 0.20 mW (1.3%). For the second set of samples of a different thickness, for the measured power of 1.45 mW, the power transmitted through the LCE film with 1 mol% dye was 0.47 mW (32%), and through the LCE film with 2 mol% dye was 0.05 mW (3.4%). It is evident that the films with higher dye concentration absorb more light, and thus generate more heating effect in actuation.
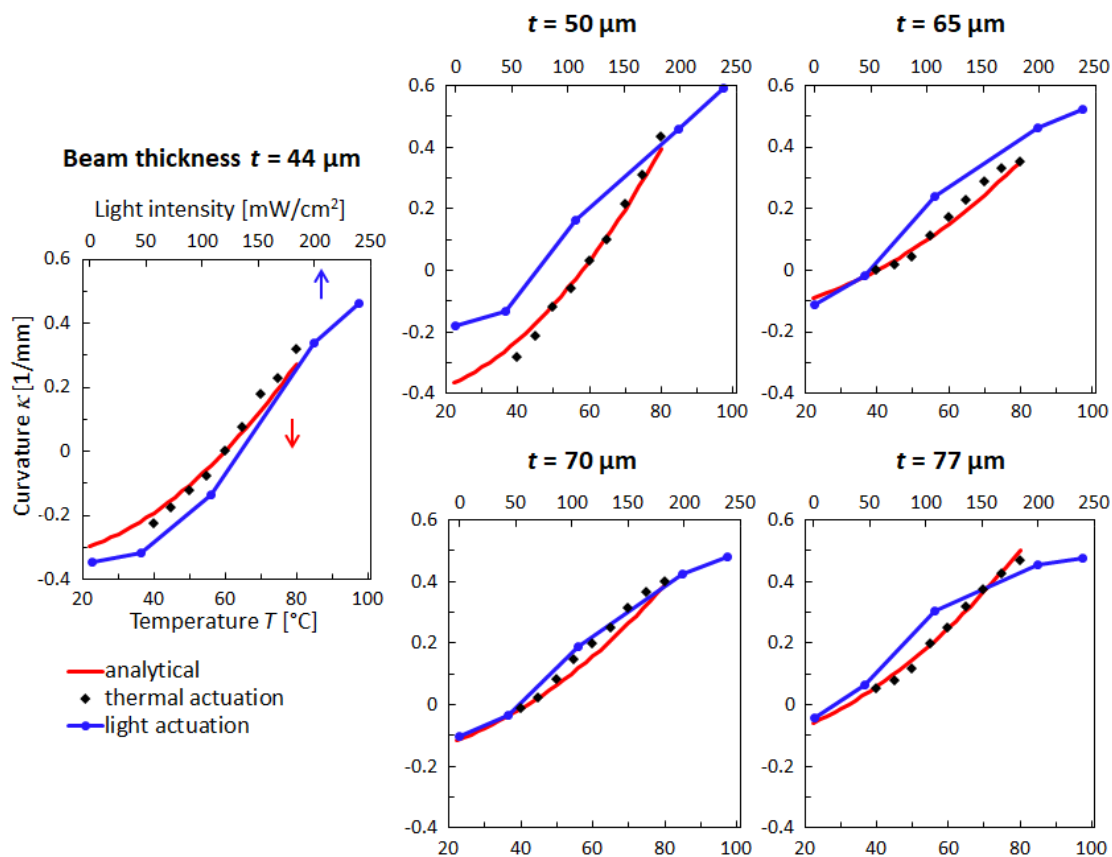
Figure 4.13 Measurements of the beam curvature for the LCE actuators doped with 2 mol% of the light-absorbing dye under thermal actuation between 40-80°C and light actuation with various light intensities

Some other factors also played a significant role in the performance of the photothermal actuators. For instance, it was observed that the LCE with 2 mol% of dye was more flexible, possibly due to the effect of the dye molecules incorporated between the elastomer chains, which could change the elastic properties of the material and the efficiency of crosslinking. This also could explain the difference in the calculated equivalent CTE values. Additionally, light illumination from one side creates a gradient of light absorption across the thickness of the LCE layer, and hence, a gradient of

temperature distribution. This is a common effect observed in photothermal actuators [226]. This could lead to different actuation effects arising between the two sides of the film. Whereas, on thermal actuation in oil, the beams were heated uniformly. The differences between the thermal and photothermal curves in Figure 4.12 and Figure 4.13 can therefore be connected significantly with the non-uniform heating effect. Finally, the effect of gravity acting on the long free-standing beam during actuation in air could have had a small contribution to the performance of the actuators, but the effect is expected to be small, as the LCE beams had sufficient structural rigidity to preserve their shape in the non-actuated state. Nevertheless, the results showed that the LCE actuators doped with the light-absorbing dye demonstrate effective actuation by various stimuli (heat, light) and in various media (air, liquid) with similar performance. Numerical simulation using equivalent thermal expansion effect based on the measured data has been used to provide good prediction of the bending behaviors of the dye-doped actuators over a large range of thicknesses for designing new actuators and new applications.

4.6 Summary

This chapter has covered the analysis of the bending behavior of the LCE actuators produced from a flat LCE film uniformly aligned at one side using the rubbed PI layer. It has been shown that the LCE beams demonstrate large reversible bending under thermal actuation in liquid medium and in air. Additionally, LCE actuators doped with the light-absorbing dye with concentration of 1 mol% and 2 mol% showed effective photothermal actuation. A simple model for numerical simulation was developed for prediction of the bending and curling behaviors of thermal LCE actuators. The model is based on the equivalent thermal expansion effect arising from the strain change in LCE structures under elevated temperatures. Using a layered structure, the gradient of strain across the thickness of the material was represented using the corresponding equivalent CTE across the thickness of the beam. For a given material composition and alignment method, the temperature-dependent CTE can be measured and represented in a first order relationship which is used for numerical simulation. It was found experimentally that in a large range of thicknesses (12-134 µm) of the LCE beams the equivalent CTE tend to approach a similar value. It has been shown that the model can be used to make

a good prediction of the bending and curling behaviors of LCE beams. With the growing interest towards functional materials with advanced characteristics in research and applications, the simple and computationally efficient model can be used to design new LCE actuators for practical applications.

Chapter 5   Measurements and Characterization of Lateral Bending LCE Microbeams

5.1 Introduction

This chapter discusses a series of experiments to characterize the performance of the LCE microactuators fabricated by the new micromolding technique. In the long and narrow microbeams fabricated from LCE by micromolding, the difference in the topologies of the opposite sidewalls was used to modify the alignment of the LC mesogens. Since the volume expansion and shrinkage in nematic LCE materials under elevated temperatures is highly anisotropic, depending on the LC order, the gradual variation of alignment across the beam thickness can induce in-plane bending deformation. The microgrooves of different sizes may induce different alignment effect, which would determine the displacement behavior. The quantitative analysis would help determine the optimal geometry of the microbeams to achieve controllable and efficient thermal actuation. Moreover, the variations in the treatment and crosslinking processes during fabrication would be investigated for their effect on the actuator performance and reliability. It will be shown that the results of thermal actuation can be used to create a simulation model which is able to predict the actual behavior of the microbeams with precision as described in Chapter 4. This chapter is partly based on the results from the Publication (4).

5.2 Investigation of the Alignment of Mesogens in the LCE Actuators

In the liquid crystal elastomer-based actuators, the actuation properties are determined by the internal molecular arrangement. The difference in orientation of the LC mesogens between two surfaces with alignment properties gives rise to anisotropic strains at elevated temperatures; thus, the deformation is controlled by programming the LC director during fabrication. Several methods are usually used to examine the alignment of LC mesogens in the material. Firstly, the X-ray scattering technique can be used to determine the nematic liquid crystalline orientation [111]. The anisotropy of the material can be detected by the presence of the diffraction peaks, which indicate the orientation of the LC director and even allow to measure the average distance between

the mesogens. Secondly, another widely used technique to investigate the alignment in LCE is polarized optical microscopy (POM). Linearly polarized light can be used to determine the unidirectional or twisted LC orientation in the material due to the ability of liquid crystals to alter the polarization of the light passing through the material [24]. This method is flexible, it allows observing large or small areas of the sample, freely rotate the sample or the polarizers to obtain more information. Finally, a fractured cross-section of the LCE sample can be investigated with SEM, and the cracks on the fractured surfaces could indicate the LC alignment [137]. In this method, an LCE sample is fractured or microtomed at cryogenic temperature [106], or at room temperature [227], and the thin cracks that appear on the fractured surface can indirectly indicate to the internal molecular alignment [137]. In this section, the alignment of LC mesogens is investigated for the LCE films fabricated using the glass cells and the LCE microbeams fabricated by micromolding.

5.2.1 LC Alignment in the Flat LCE Films

The LCE films were fabricated inside cells as described in Chapter 4, where one surface was a uniformly rubbed PI film, and the other surface was bare glass. It is known that the PI surface forces the LC mesogens to align along the rubbing direction planar to the surface. It is expected that the untreated glass surface would typically induce nearly homeotropic orientation of the LC mesogens at the surface [142].

The internal alignment of LCE in the fabricated films was investigated through SEM. Since the fabricated LCE films were brittle enough to be fractured with little elastic deformation, the sample preparation was performed at room temperature. Several samples were fractured both along and perpendicular to the rubbing direction of the PI layer to better inspect the alignment pattern. Prior to SEM imaging the samples were sputter coated with gold from two sides for 90 seconds each side (Automatic sputter coater, Agar Scientific) to prevent the charging effect in the polymer layer. SEM imaging was performed using the electron beam lithography system (Raith PIONEER), electron high tension voltage of 5 kV. Figure 5.1 shows the SEM images of the cross-section of two LCE films fractured along the rubbing direction. It is indicated in the image which surface was aligned to the untreated glass, and which one was aligned to the rubbed PI, with the direction of rubbing indicated with an arrow.
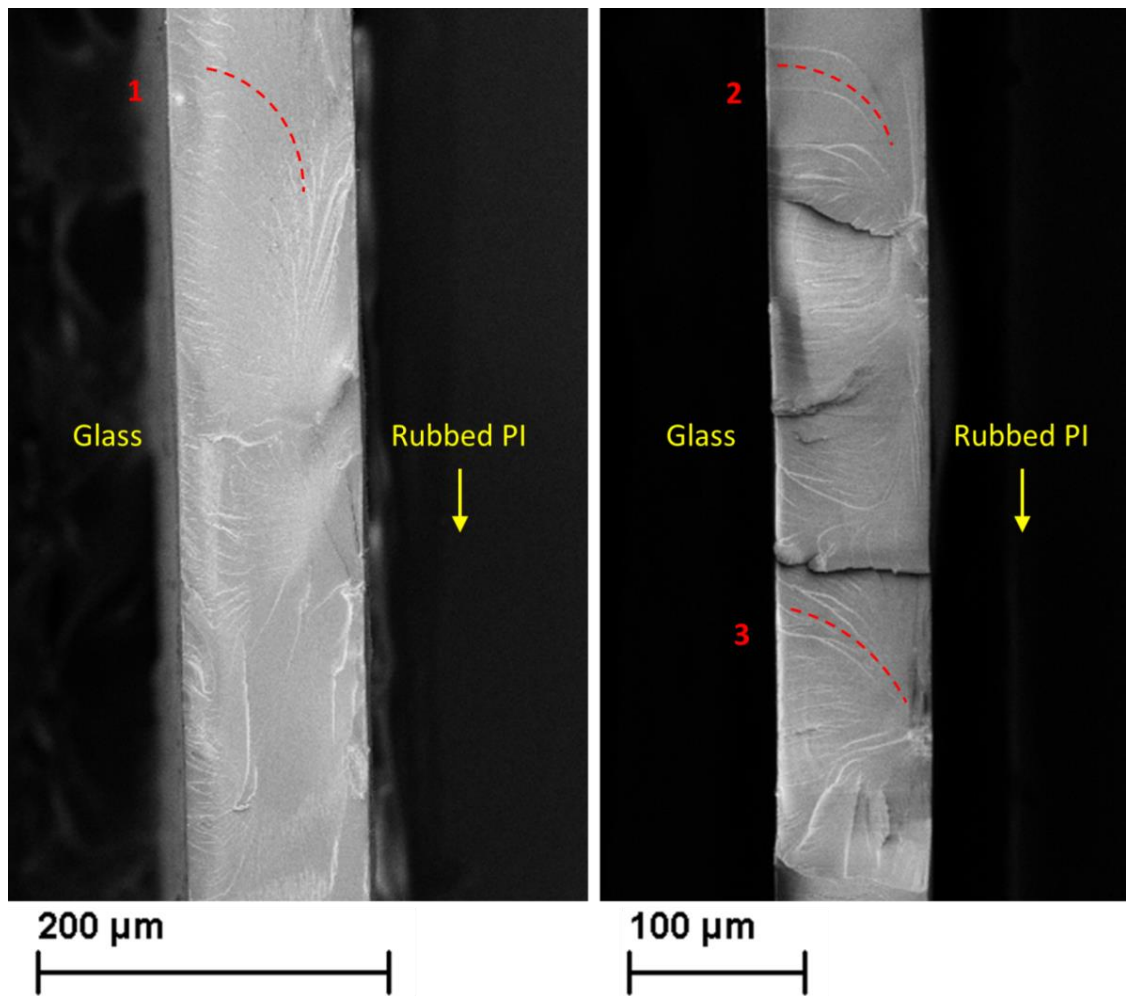
Figure 5.1 SEM images of the fractured cross-sections of the LCE films demonstrating variation in the directions of cracks between two surfaces with different LC alignment

Although the inspected surfaces had an irregular topology as a consequence of the mechanical impact during fracturing, some fracture lines can still be observed in Figure 5.1, in the form of thin cracks of bright color. It can be observed that the cracks tend to be nearly perpendicular to the surface aligned to the glass. This can indicate that a nearly homeotropic alignment of LC mesogens was induced by the untreated glass. Whereas, it could be seen that the direction of the cracks is more parallel to the surface near the rubbed PI layer, which promotes the planar LC alignment. The variation of the fracture lines' direction across the layer is more clearly shown in the highlighted regions 1, 2 and 3 in Figure 5.1, the dashed lines as used as a guide for the eye. Generally, the observations matched with the expected alignment pattern in the LCE films. However, some defects were present near the rubbed surface as could be noticed in Figure 5.1. Some of the defects may have been introduced during fracturing, while other local defects may also be a consequence of slight non-uniformities of the surface of the PI

layer, which interfered with the LC alignment pattern. The quality of the alignment could possibly be improved further by using a thin uniform spin-coated layer of polyimide with less roughness instead of the hard PI film used in this case.
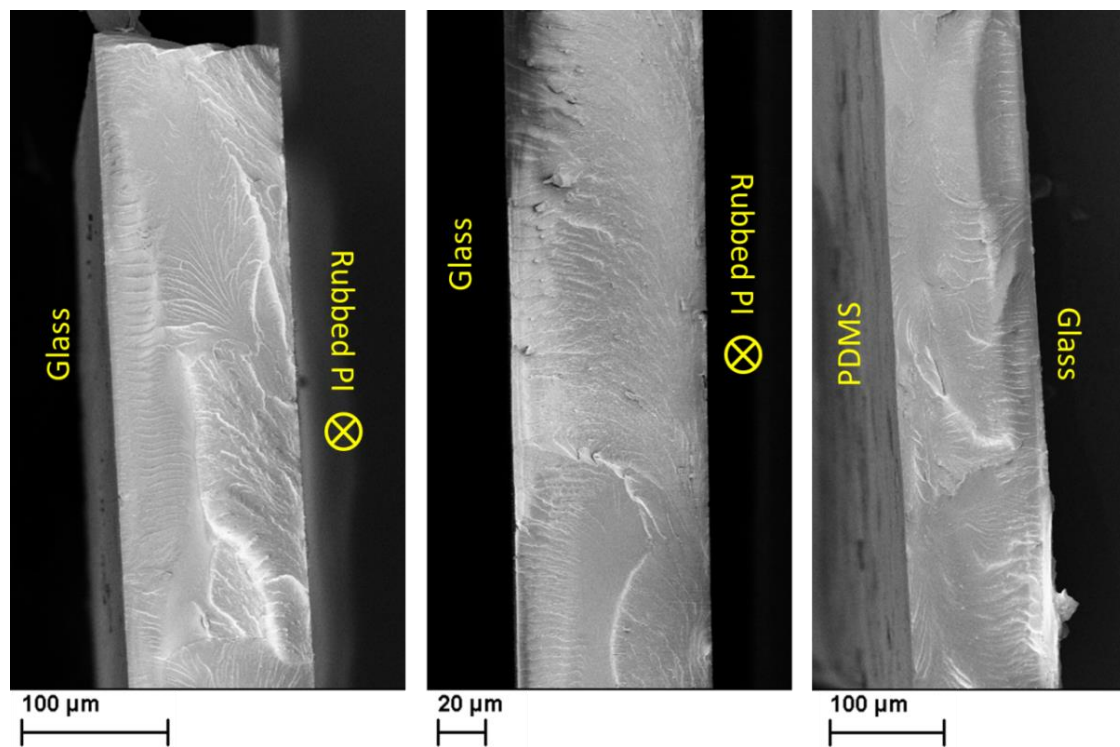
Figure 5.2 SEM images of the fractured cross-sections of the LCE films demonstrating a nearly homeotropic orientation of cracks near the surface aligned with untreated flat glass

Overall, a common tendency was noticed that the cracks were always oriented nearly homeotropic to the surface aligned with the untreated glass. This can be seen from the SEM images of the fractured LCE films with the direction of rubbing perpendicular to the cross-section surface in Figure 5.2. In comparison with the glass side, the fracture lines were much less clear at the rubbed PI side, and the topology was rather non-uniform. In addition, the image on the right side in Figure 5.2 shows an example of the LCE film fabricated using an untreated glass at one side, and a flat PDMS layer at the other side. The fracture was more irregular at the side aligned with PDMS. Whereas, the clear thin crack lines can still be seen oriented nearly homeotropic to the surface of the glass substrate, which shows that the tendency is preserved even with other variations in the fabrication process.

5.2.2 LC Alignment in Microactuators Fabricated by Micromolding

It is known that the alignment of LC mesogens promoted near the surface during fabrication depends on both the surface chemistry and the surface topology [142]. On one hand, the microgrooved surfaces possess the ability to induce unidirectional orientation of nematic LCs along the grooves; the general trend is that the deeper and narrower grooves provide a stronger alignment effect. On the other hand, the PDMS surface with low anchoring energy is able to impact the LC orientation even in the presence of strong magnetic alignment fields, as was demonstrated in [153]. This is a significant factor for fabrication using microstructured molds, where the surface effects grow rapidly at microscale as compared to the volume effects. Additionally, there are multiple factors affecting the LC alignment inside the molding channels of a particular shape, such as the geometry and the aspect ratio of the channels, or the liquid's shear flow forces acting during molding. Therefore, the actual internal orientation of LCs formed in the result of fabrication by micromolding was investigated separately.

The traditional methods used to examine the LC alignment have certain limiting factors, which make it challenging to determine the LC alignment in the narrow asymmetric LCE microbeams produced in the microchannels. Thus, X-ray scattering technique is suitable for investigating LCE samples with monodomain orientation, rather than microstructures with locally varying LC pattern. The POM method is effective in characterization of the LCE with complex alignment patterns on a 2D plane. However, for the structures fabricated inside the microchannels, the alignment pattern is not 2-dimensional, but rather 3-dimensional due to the effect of the four surrounding walls. The SEM method for inspecting the cross-section plane of the microbeams could provide some new, however, very limited information, because the microbeams were designed to have a variation of LC orientation in the substrate plane, not in the cross-section plane. In this work, the LC alignment in the LCE microbeams was investigated using polarization microscopy and SEM observation of the fractured surfaces.

The LCE microbeams fabricated inside the PDMS mold with the surfaces treated with a photoinitiator solution typically demonstrated stable, reversible thermal bending in the direction away from the grooved side, as shown in Figure 5.3a. The image demonstrates the curvature of the microbeam induced on heating to 70°C; the length of the microbeam was 900 μm. The lateral bending actuation observed in the test is determined by the internal alignment of LCs, which is schematically shown in Figure

5.3a. The conclusion on the LC orientation is justified based on the results of polarized light microscope inspection shown in the following.

The samples were inspected under the microscope (Chronogrip system, Percipio Robotics) in a simple custom setup using two dichroic film polarizers for visible light (Thorlabs). The LCE microbeam was placed onto a clean glass slide, one film polarizers was placed below, and another one (analyzer) was placed above the sample. The setup was illuminated from the bottom side with unpolarized white light. The sample and the top analyzer film were free to rotate during the test. The images of the microactuator were taken in the parallel and crossed polarizers settings. Different areas on the image vary in brightness due to the liquid crystalline structures passing through a portion of light with certain polarization depending on the LC director. Although a large number of microactuators were inspected, in some cases it was challenging to directly determine the particular mesogenic orientation from the images. The defects introduced during the fabrication by capillary micromolding caused color variation in the POM image, which interfere with the local analysis. Also, as opposed to the truly 2-dimensional LC patterns typically used in LCE films and easily determined by POM method, the microbeams fabricated by micromolding have a more complex 3-dimensional pattern, as was mentioned previously. In the end, it was still possible to outline the general trend after analyzing a number of samples.

Figure 5.3b demonstrates a good example of the trend. The images of an LCE microbeam were obtained under parallel and crossed polarizers, when the long axis of the microbeam was directed in parallel with the polarizer, or rotated at 45° to the polarizer. The change of the brightness in the image could be interpreted as that the LC mesogens were oriented along the microbeam in the part of the beam near the flat wall. This is similar to the alignment of mesogens along the channels observed previously in the literature for the long LCE microwires fabricated by micromolding in the channels with flat surfaces [134]. The microwires therefore demonstrated longitudinal contraction in the reference. In comparison to that, we observed that in the vicinity of the grooved wall, the LC orientation was disturbed, as can be seen in Figure 5.3b, the brightness differs from that in the rest of the structure. This suggests that the orientation of the mesogens is more random in the vicinity of the grooved wall. Therefore, competing anisotropic shrinking/expansion effects arise in two parts of the LCE microbeam. The part with a higher degree of LC order (the flat wall side) exhibits shrinking along the

beam with increasing temperature, which explains the bending actuation towards the flat side of the microbeam.
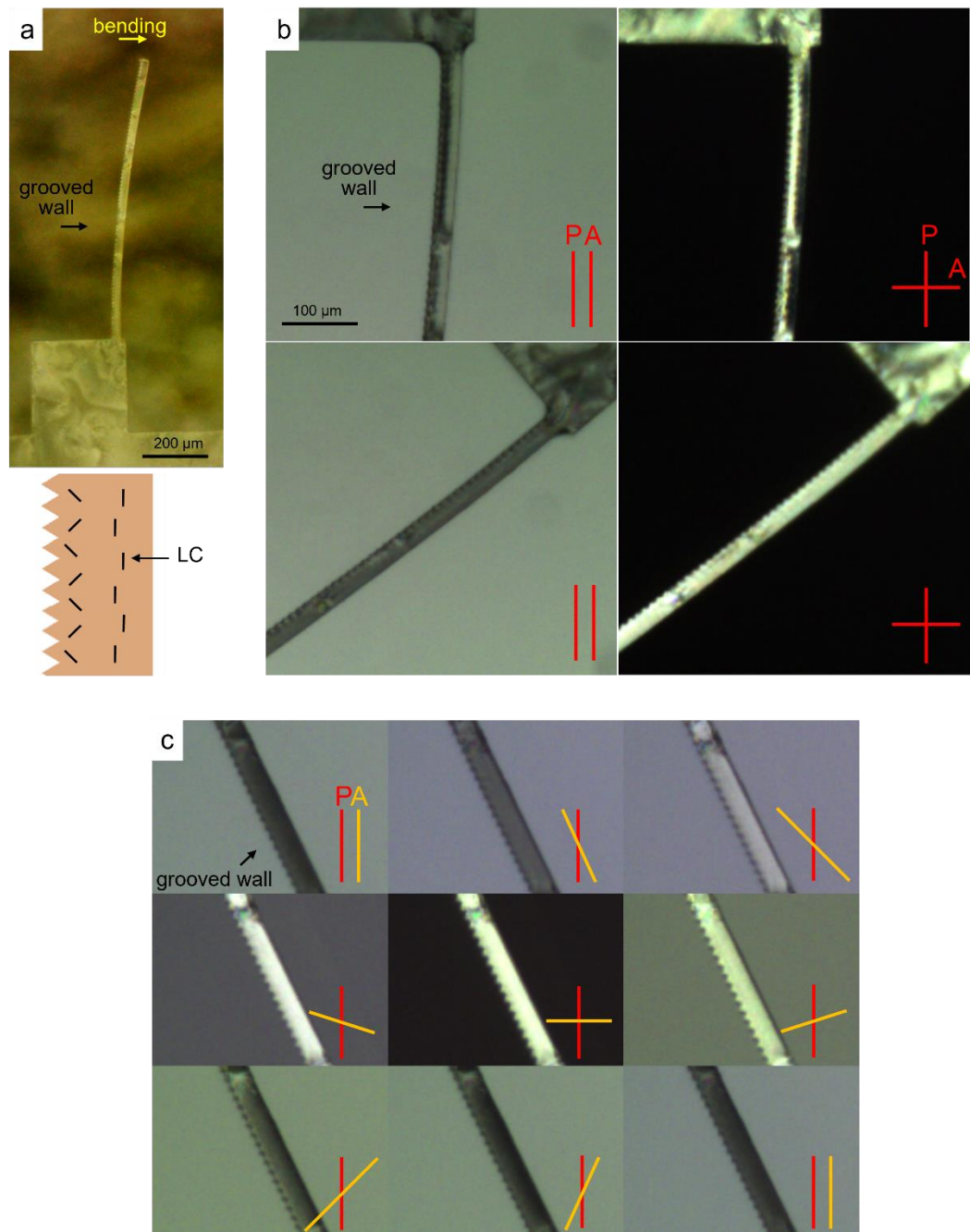
Figure 5.3 LCE microactuator fabricated using the photoinitiator-treated molds: a) Optical microscope image of the microbeam in actuated state and the schematic image of the internal LC alignment; b) POM image of the LCE microactuator; c) POM image of the LCE microactuator under freely rotated analyzer

More evidence is given in Figure 5.3c. The images were taken with the bottom polarizer in the same direction, while the top analyzer was freely rotated with a step of about $\pi/8$. The direction of the long axis of the microbeam was slightly rotated with respect to the

polarizer in order to break the symmetry and to observe the variation in brightness easily under different rotations of the analyzer. The intensity of light transmitted through the analyzer is described with the Malus's law as follows:

$$I_{tr} = I_0 cos^2\theta \, , \tag{5.1}$$

where I_{tr} is the transmitted light intensity, I_0 is the incident light intensity, and θ is the angle between the direction of polarization of incident light and the transmission axis of the analyzer. If the nematic LCE material plays the role of the third polarizer placed between the two polarizers in the setup, therefore, the orientation of the LC director could be confirmed from the relationship in equation (5.1). From the brightness patterns observed in the Figure 5.3c, a gradient in color across the microbeam width can be noticed at certain positions, which demonstrates the difference in alignment between the flat and the grooved sides of the microbeam.

In the next test, the cross-sections of several microbeams were inspected with SEM. For this purpose, the microbeams were fractured at room temperature by placing the beams between two glass slides, such that a portion of the beam extended beyond the edge of the slide, which then was manually snapped off with help of a razor blade. The LCE microbeams could not be cut, as the material would deform under the pressure of the blade. The problem of deformation during fracturing caused by the elasticity of the material is usually eliminated by bringing the sample to cryogenic temperatures firstly, by dipping in the liquid nitrogen. However, for the microscopic beam-shape structures investigated in this project, it could be extremely challenging to bring the sample to cryogenic temperatures without damaging it; therefore, the test was performed using samples as fractured at room temperature. Prior to SEM imaging the samples were sputter coated with gold on both sides for 90 seconds each side (Automatic sputter coater, Agar Scientific) to prevent the surface from charging. The samples were fixed on a substrate with the fractured cross-section of the microbeams facing upwards. SEM imaging was performed using the electron beam lithography system (Raith PIONEER).

Two examples of the fractured LCE microactuators of the width of 40 μm and 50 μm are shown in Figure 5.4a and Figure 5.4b, respectively. Fracture lines could be observed on the surfaces. Since the shape of the fractured surface was uneven, the appearance of the fracture lines varied significantly across several samples. Due to this factor the actual LC alignment on the plane was unclear from the SEM images. Nevertheless, one common feature was noticed: the facture lines change direction sharply and randomly near the grooved wall (the region directly below the indication arrows in the Figure).

This may indicate a sharp change in LC orientation near the corrugated surface, which matches with the previous observations.
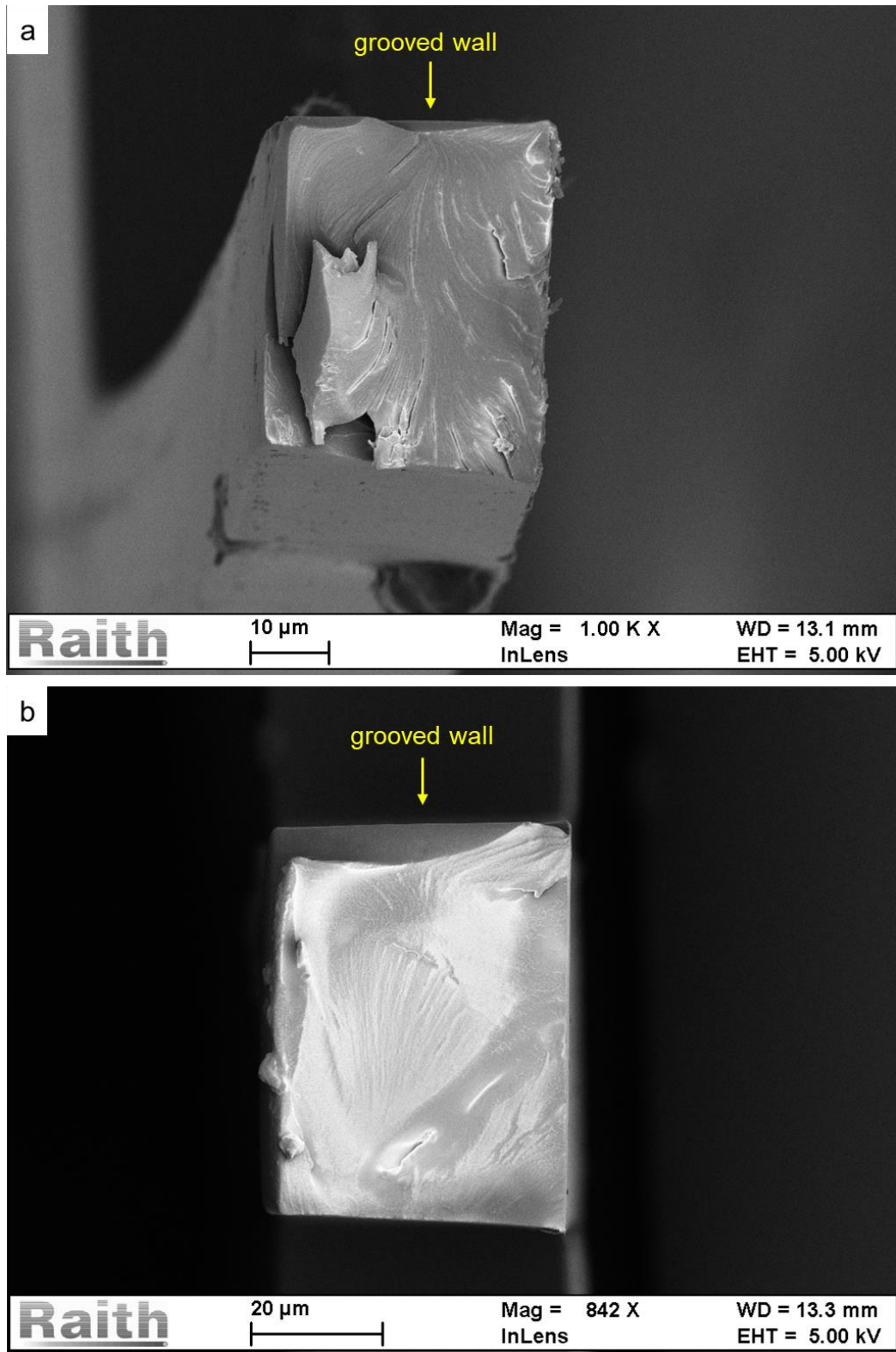
Figure 5.4 SEM images of the fractured cross-section of the LCE microactuator fabricated using the photoinitiator-treated molds: a) beam width 40 µm; b) beam width 50 µm

Overall, the analysis using POM and SEM methods showed that the LC mesogens tend to align along the microbeam, when the actuators have been fabricated inside the narrow PDMS channels treated with a photoinitiator. This alignment effect could be caused by the shear flow of the molten LCE in the channel as well as by the tendency of adjusting the LC alignment with the symmetry of the confined channels [134]. The alignment was disturbed and randomized in the vicinity of the corrugated sidewall, which created a gradient in the LC order necessary to achieve lateral bending. Evidently, the planar alignment effect of the microgrooves was less significant in comparison with the effects of the channel geometry and the surface chemistry. In the result, it was demonstrated that the corrugated PDMS surface was able to modify the LC orientation, even though the pattern was different from that typically observed near the grooved surfaces (usually PI, PVA or epoxy-based) for planar alignment of LCs. The difference in the LC order gives rise to a different amount of anisotropic expansion/contraction in two part of the microactuator, which results in the reversible bending deformation away from the grooved sidewall.

5.2.3 LC Alignment in Microactuators Fabricated Using the HEMA-Treated Molds

A number of LCE microactuators were fabricated inside the PDMS molds with the surfaces treated with HEMA. Notably, these microactuators generally demonstrated a different behavior from those investigated in the previous section. The majority of the LCE microactuators from the HEMA-treated molds were bending in the opposite direction, towards the grooved side, and exhibited less repeatability in actuation as well as smaller curvature, as shown in the example in Figure 5.5a. The image demonstrates the small bending of the microbeam upon heating to 70°C; the length of the microactuator was 900 µm. A large amount of defects could be observed in the polarized-light images, which may have originated from non-uniform coverage of the PDMS surface with the thin HEMA layer. This factor could significantly interfere with the LC alignment mechanism. Figure 5.5b shows the polarized-light image of the LCE microactuator fabricated inside a mold pretreated with HEMA. The results obtained from the POM analysis are significantly different from the result for the microactuators fabricated without HEMA treatment. It was found that the microbeams, which bend in

the direction opposite to expected, typically have a similar prominent "line" along the microbeam in its middle part, clearly visible on the POM images. This feature indicates a sharp change in the LC director in the middle of the LCE microbeam.

A number of images were taken under the freely rotating analyzer, following the same method described previously. This result is shown in Figure 5.5c. Taking into account of the relationship given with the Malus's law, the LC pattern is more complex and it may be interpreted as shown in the schematic drawing in Figure 5.5a. The pattern of brightness observed in the POM images indicates that the mesogens are directed along the channel in the middle part, but the tilt increases further away from the center. It can also be seen in Figure 5.5b that the LC orientation in the vicinity of the corrugated wall is slightly disturbed, similar to that observed in the previous section. Consequently, the difference in the degree of LC order between the two sides of the microbeam causes the beam to bend sideways upon heating. But since the overall pattern of LC mesogens was different from that in the previous experiment, the combination of the anisotropic expansion effects was different, resulting in the deformation in the opposite direction. In addition to that, a significant number of defects in the alignment of LC inside the microbeam could be seen in the POM images.

Several microbeams were fractured in order to be examined under SEM. The procedure and the equipment used were similar to that stated in the previous section. Two examples of the fractured cross-section are given in Figure 5.6a and Figure 5.6b, the microbeams had the widths of 40 µm and 60 µm, respectively. Due to the irregular topology of the cross-section surface, it was hard to directly determine the actual LC orientation from the images. However, importantly, the fractured edge obtained a particular shape for the LCE microbeams fabricated in the HEMA-treated molds. This can be seen from the photographs taken under the optical microscope (the insets in Figure 5.6), the features are highlighted with dashed arrows. The shape of the fracture resembles the arcs converging in the middle of the channel, which could have been caused upon fracturing due to the structural properties of the material according to the internal alignment of the molecules. The fractures with a prominent pointed feature in the middle correspond with the observations by the POM method.

Overall, using HEMA for treatment of the molds in fabrication of the LCE structures significantly altered the alignment of LC mesogens in the channels. Such microactuators possess a prominent feature clearly visible using polarized light, which is a sharp change of the LC director in the middle of the microbeams. Consequently,

these microactuators demonstrate a different thermal bending behavior in the direction opposite to that expected, towards the grooved side. It was observed from the POM images that the amount of various defects in the pattern was generally larger in these structures, as compared with the microbeams fabricated without HEMA. It indicates that the quality of the HEMA coating may be insufficient to produce a reliable LC alignment mechanism.
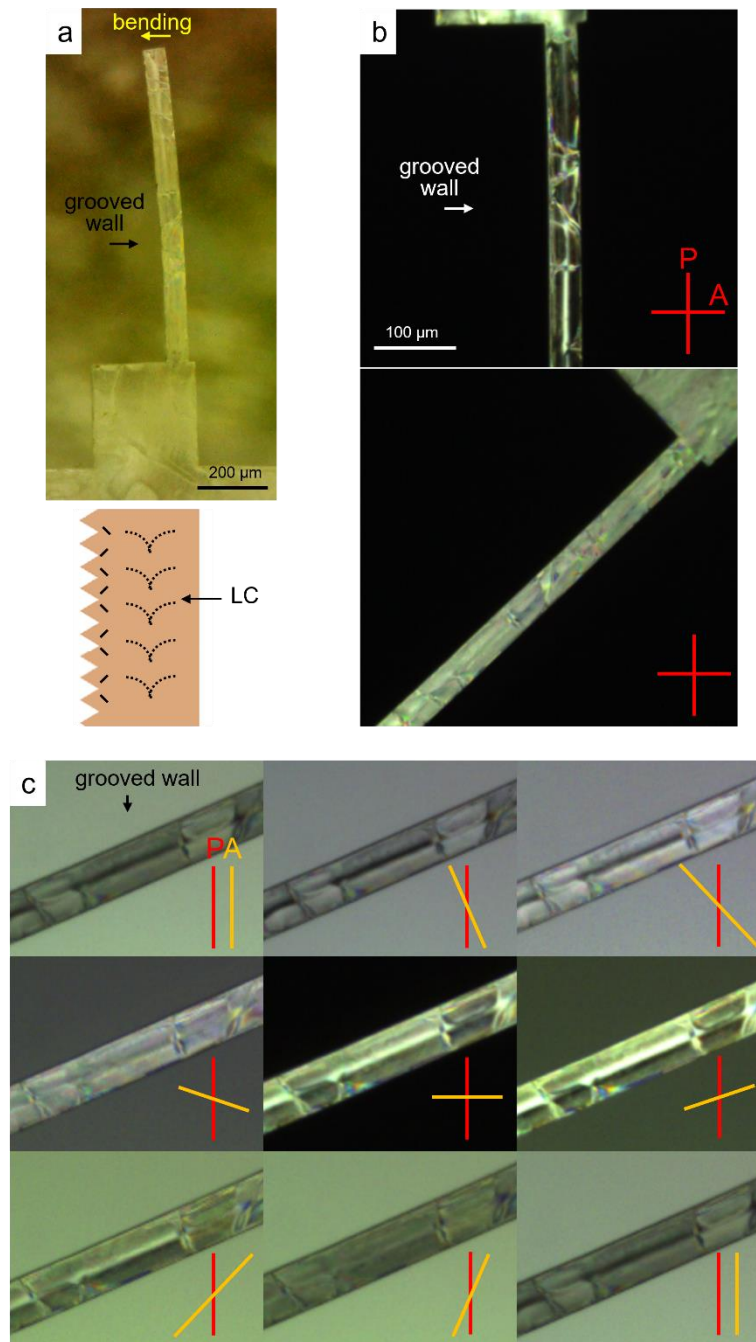
Figure 5.5 LCE microactuator fabricated using the HEMA-treated molds: a) Optical microscope image of the microbeam in actuated state and the schematic image of the internal LC alignment; b) POM image of the LCE microactuator; c) POM image of the LCE microactuator under freely rotated analyzer
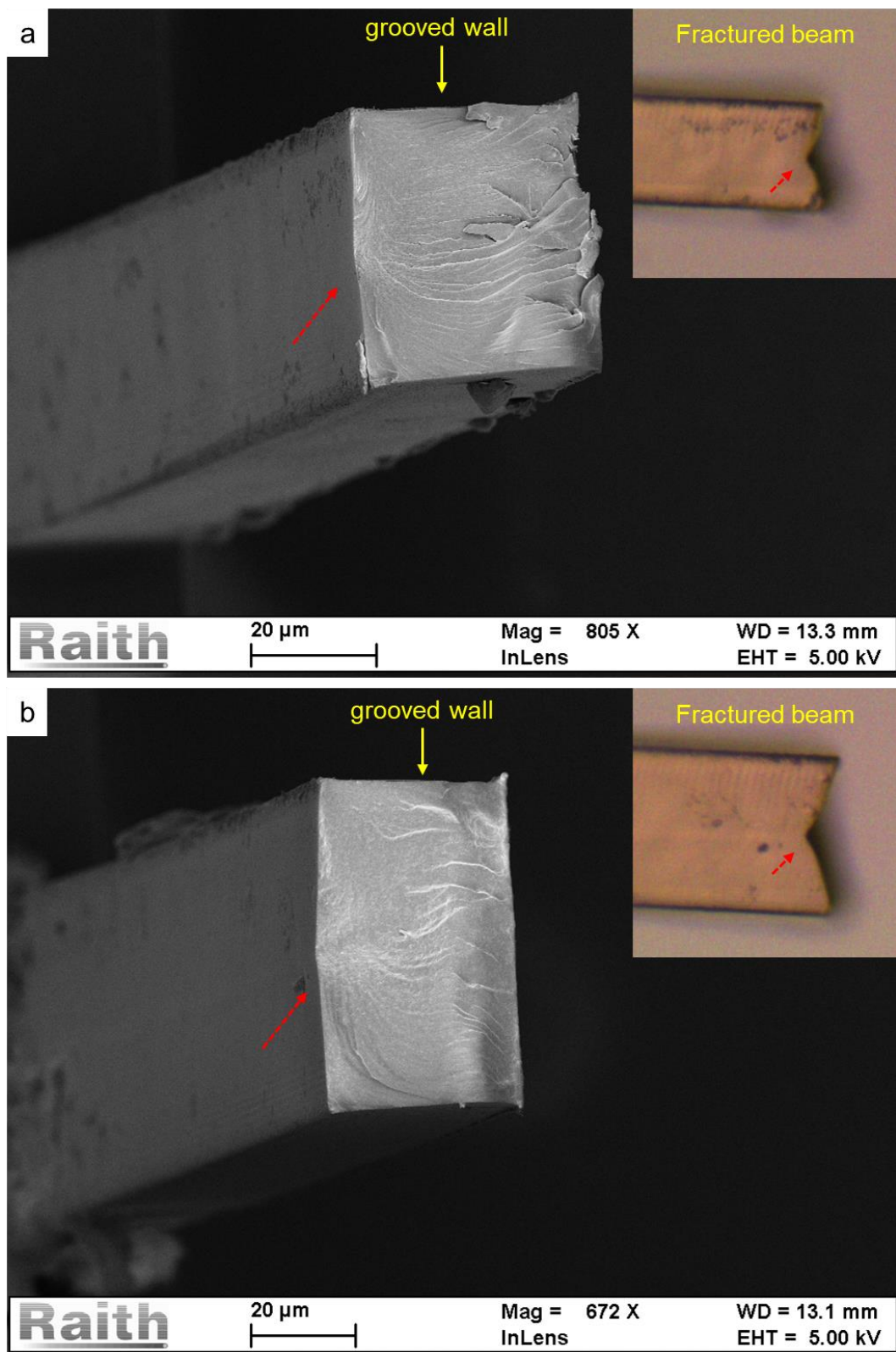
Figure 5.6 SEM images of the fractured cross-section of the LCE microactuator fabricated using the HEMA-treated molds: a) beam width 40 µm; b) beam width 60 µm

5.3 Analysis of the Bending Behavior of the LCE based Microactuators

The characterization of the bending behavior of the LCE microbeams was performed in a liquid medium (silicone oil) to provide controlled and uniform heating for the microstructures. For this, the LCE microbeams were placed onto a glass slide covered with a small amount of silicone oil, to prevent stiction or friction between the actuators and the glass during the test. The slide was placed onto the hotplate, and the temperature was varied between 40°C and 70°C. Each microactuator was subjected to 3 cycles of heating and cooling. The microactuators showed fully reversible, repeatable in-plane thermal bending. An example is shown in Figure 5.7; the actuator has the length of 900 µm, the width S of 20 µm, and the sidewall grooves of size 3; the microbeam was fabricated using the PDMS mold treated with the photoinitiator. Arc-like bending can be seen in the microactuator upon heating from 40°C to 70°C in the direction away from the grooved side, which is more clearly shown on the combined image. Upon cooling, the microactuator returns to the initial shape. The change of the shape of the microactuators was recorded with a digital microscope (Q-scope) and analyzed from the images using the built-in software tool for measurement (Q-focus) by fitting a circle in order to obtain the curvature of the microbeam. Prior to measurements, the tool was calibrated for a particular magnification setting using the calibration sheet with the distance marks provided with the microscope. The curvature, κ, was calculated using equation (4.3). For each actuation cycle between the two states, at 40°C and at 70°C, the magnitude of thermal bending was recorded as $\Delta\kappa/\Delta T$, where $\Delta\kappa$ is the difference in the beam curvature between the two states, and ΔT is the difference in the temperature, which was $\Delta T = 30$°C. Since the microbeams might obtain a small initial curvature due to the release of the residual stress after fabrication, the microbeams could be not perfectly flat at the temperature at which the LCE material was polymerized ($T_\mathrm{p} = 30$°C). However, by using the differential value $\Delta\kappa/\Delta T$ between the two actuated states, the possible deviation associated with the different amount of residual stress in every microbeam was eliminated from the analysis. In the example of the microactuator shown in Figure 5.7, the radius of the fitted arc was measured as -19.26 mm at 40°C, and 3.93 mm at 70°C (negative or positive sign indicates the bending direction towards or away from the grooved side, respectively). Thus, the magnitude of bending as demonstrated in Figure 5.7 was $\Delta\kappa/\Delta T = 0.0102$ (mm°C)$^{-1}$.

The actuation performance was examined for a large number of samples with various beam widths and groove sizes. The behavior was compared for the microbeams fabricated using the photoinitiator-treated PDMS molds, the HEMA-treated PDMS molds, and also separately for the microbeams polymerized either using the UV lamp with low intensity light or using the UV LED with higher intensity. The results are presented and discussed in the following sections.
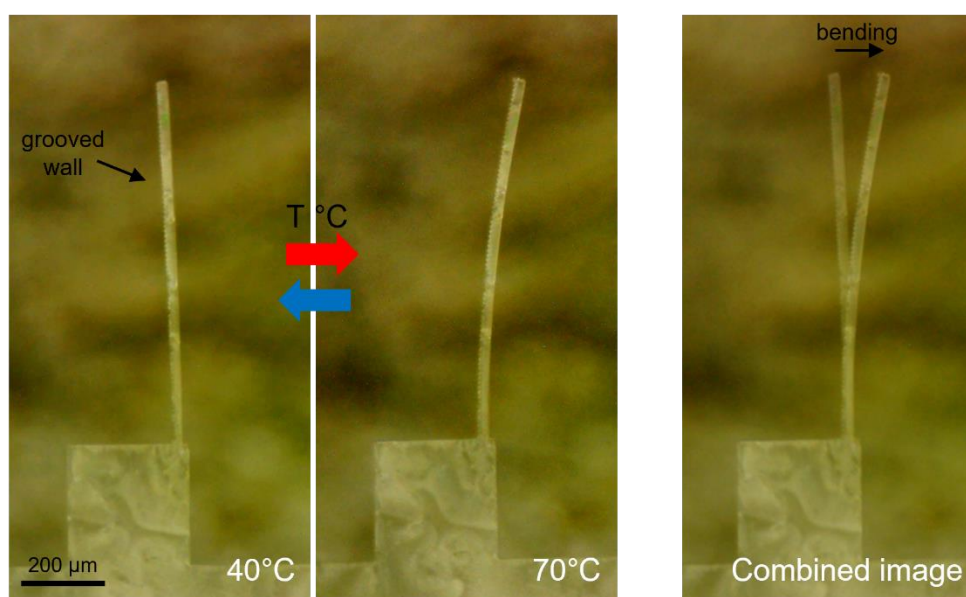
Figure 5.7 Microscope image of the in-plane bending LCE microactuator (length 900 µm, width 20 µm, groove size 3) under thermal actuation from 40°C to 70°C

5.3.1 Bending Performance of the LCE Microactuators Fabricated Using the Photoinitiator-Treated Molds

This section contains the results and discussion of the bending performance of the LCE-based microactuators, which were fabricated using the photoinitiator-treated molds, and the LCE material was polymerized using the Hg lamp (~365 nm, 1.58 mW/cm^2, 3 hours).

The results of measurements of the thermal bending of the microbeams are shown in the Figure 5.8. The plots of the $\Delta\kappa/\Delta T$ values as the beam width, S, are shown in Figure 5.8 for the grooves of size 1, 2, 3 and 4, respectively. Each data point is the average of the results from 3 temperature cycles for the same LCE microbeam: cooling, heating and cooling between 40°C and 70°C. The plots using average values provide better comparison of the bending behavior between the microbeams. There was no indication

of degradation in the actuation performance between the first cycle and the last cycle. Several microbeams were characterized for each beam width and groove size combination, as given in Figure 5.8. It can be seen that the smallest grooves (size 1) did not provide sufficient effect for the alignment of LC mesogens, as the microbeams have shown nearly random bending behavior with the average value close to zero (Figure 5.8a). This indicates that the topography of the surface with the relatively shallow grooves was not sufficient to overcome other alignment factors including the chemical properties of the surface and the confined geometry of the molding channels. On the other hand, the larger grooves (size 2-4) were able to modify the LC orientation pattern and induce prominent in-plane actuation in the microbeams.
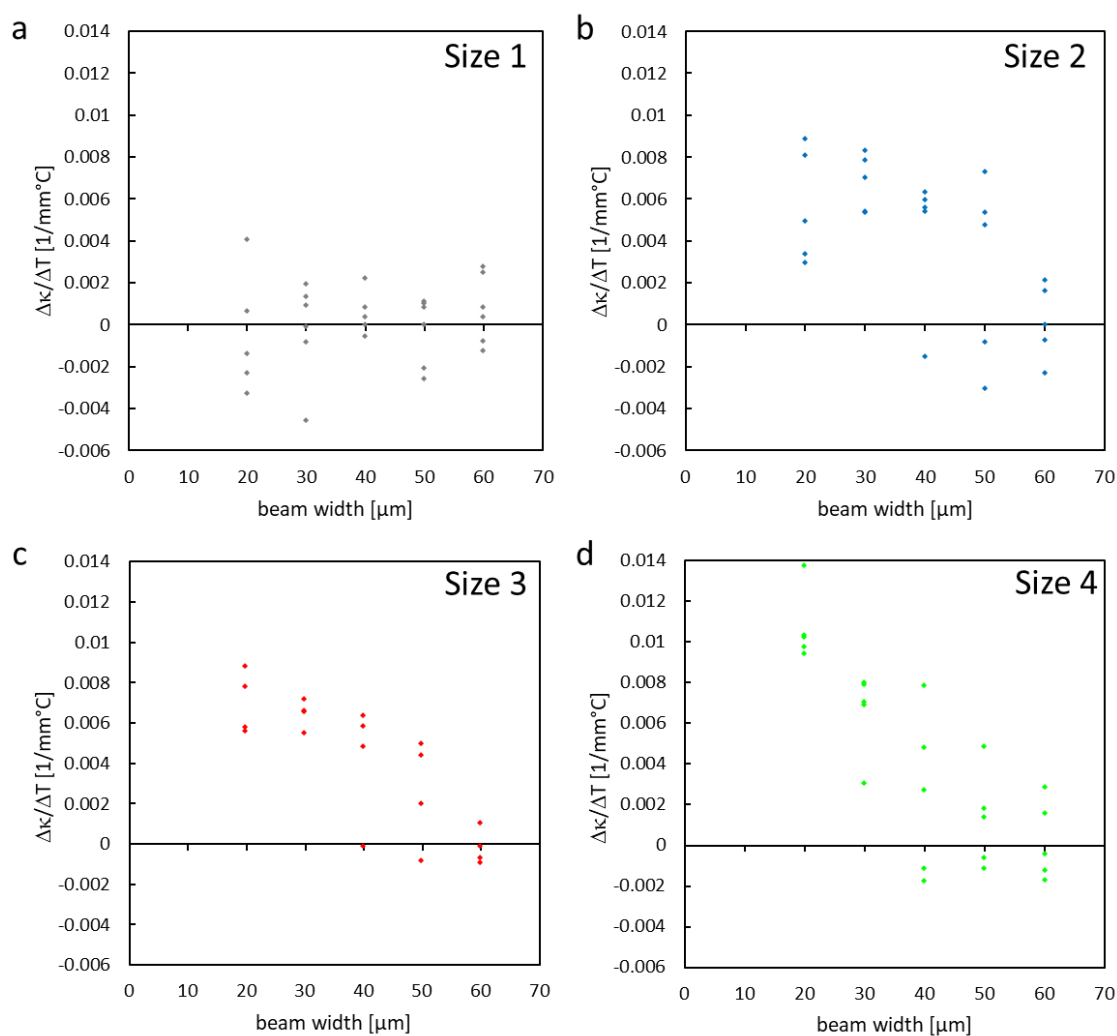
Figure 5.8 Experimental measurements of the bending rate, $\Delta\kappa/\Delta T$, under the temperature cycling from 40°C to 70°C in the LCE microbeams fabricated using the photoinitiator-treated molds, a) with the grooves of size 1; b) size 2; c) size 3; and d) size 4

A clear trend in the bending behavior of the LCE microactuators can be seen in Figure 5.8b to Figure 5.8d. The positive values of $\Delta\kappa/\Delta T$ indicate the bending direction away from the grooved sidewall. The microbeams with the smaller width show larger deflection under the thermal stimulus, due to lower stiffness of the narrower microbeams. The spread in measurements may be attributed to the small defects and variations in the LC alignment pattern between the samples. A number of microactuators (25% of the total number) exhibited nearly-zero deflection or small deflection in the opposite direction towards the grooved side, marked with the negative $\Delta\kappa/\Delta T$ values, which is due to the non-uniformity in the fabrication process. It was reported previously that the LC alignment mechanism is more effective for the smaller widths of the channel, whereas the defects become significant in the channels of 50 µm or larger [134]. This is also the case in the current work, as the LCE microbeams of 40 µm in width and smaller have shown very few instances of negative deflection, meanwhile the microbeams of 50 and 60 µm in width have shown relatively low thermal response and the increased negative deformation.

An important observation was that the amount of deformation was approximately similar for the microactuators with the grooves of size 2, 3 and 4. This indicated that all three configurations can be used effectively to produce in-plane thermal actuation in LCE microbeams; however, the difference in the size of the grooves may have relatively little effect on the total amount of deformation upon actuation, as long as the grooves are of sufficient size to influence the alignment of LC mesogens. However, a small number of microactuators exhibited failure in actuation with nearly zero or negative deflection, their behavior differs significantly from the average trend as could be seen in Figure 5.8. Generally, the microactuators of 40 µm in width tend to show a fairly controllable, repeatable bending, except for only a few microbeams with negative bending due to irregularity in fabrication. The arc-like bending deformation arises from the difference in the strain between the parts of the microbeam with different internal LC alignment. From the measurements of the curvature, the strain difference induced at a certain actuation temperature can be calculated using equation (4.4) using the beam width S, and the difference in the beam curvature between two actuated states $\Delta\kappa$ (the difference in the actuation temperatures of $\Delta T = 30°C$ in this case).

It was noticed that the difference in the strain, $\Delta\varepsilon$, upon actuation varied with the widths of the microbeam. For instance, as can be seen in Figure 5.8c, the microbeams with the sidewall grooves of size 3 have demonstrated good performance with a relatively small

scatter, which is therefore a good example of the controlled thermal actuation. The average values of the bending rate were 0.0070 (mm°C)$^{-1}$, 0.0065 (mm°C)$^{-1}$, 0.0057 (mm°C)$^{-1}$, 0.0038 (mm°C)$^{-1}$ and 0.0010 (mm°C)$^{-1}$ for the microbeams of the width of 20, 30, 40, 50, and 60 µm respectively. As the width of the beam increased, the total bending curvature for the same temperature stimulus decreased. Meanwhile, the calculated average strain difference in the microbeams were 0.42%, 0.58%, 0.68%, 0.57%, and 0.18% respectively. Thus, the largest average bending was achieved in the narrowest microbeams of 20 µm in width, while the largest strain difference was achieved in the microbeams of 40 µm in width. The thickness of all microbeams for testing was 40 µm. Therefore, the analysis has shown that the largest strain difference occurred when the ratio of the sides in the beam cross-section was close to 1. This ratio can be used for efficient design and performance of the LCE-based microactuators. Large strain indicates an efficient conversion of the thermal stimulus into the bending deformation.

5.3.2 Bending Performance of the LCE Microactuators Fabricated Using the HEMA-Treated Molds

This section contains the results and discussion of the bending performance of the LCE-based microactuators, which were fabricated using the HEMA-treated molds, and the LCE material was polymerized using the Hg lamp (~365 nm, 1.58 mW/cm^2, 3 hours). The treatment procedure using 2-Hydroxyethyl methacrylate (HEMA) was introduced in order to improve polymerization of the LCE inside PDMS channels during molding. However, the hydrophilic HEMA coating changed the properties of the PDMS surface, and therefore altered the alignment of LC mesogens inside the microchannels. It was found that with the increase in the actuation temperature, these actuators usually exhibit bending deformation in the opposite direction, towards the grooved side, in contrast to the microbeams fabricated without HEMA treatment. Therefore, a number of LCE microactuators fabricated using HEMA-coated molds were tested in order to compare their actuation performance with the results of microactuators fabricated using the photoinitiator-treated molds as described in section 5.3.1.

The results of measurements of the bending curvature are shown in Figure 5.9. Each data point is the average of the results from 3 temperature cycles for the same LCE

microbeam (cooling, heating and cooling). A large number of thermal microactuators exhibited deflection towards the grooved side of the microbeam, as indicated by the negative $\Delta\kappa/\Delta T$ values. The actuators with the smallest grooves (size 1) in Figure 5.9a showed nearly random behavior, similar to that observed in the previous section, which was because the effect of the smallest grooves was insufficient to modify the alignment of LC mesogens and induce significant macroscopic deformation. For the microactuators with the sidewall grooves of size 2, 3 and 4, it can be seen from Figure 5.9b, Figure 5.9c, and Figure 5.9d that with the addition of the HEMA coating, there is no clear trend in in the actuation behavior of the LCE microbeams. The majority of the microactuators demonstrated a nearly random amount of bending in the negative direction, without noticeable relation to the width of the microbeam.

Figure 5.9 Experimental measurements of the bending rate, $\Delta\kappa/\Delta T$, under the temperature cycling from 40°C to 70°C in the LCE microbeams fabricated using the HEMA-treated molds, a) with the grooves of size 1; b) size 2; c) size 3; and d) size 4

The lack of repeatability in the magnitude of bending may be attributed to significant non-uniformities in the treatment process. The large amount of defects could be observed in the microbeams fabricated using the HEMA-treated molds. The presence of many defects indicates that the HEMA coating layer on the microstructured PDMS mold was highly non-uniform, which interfered with the alignment of LCs and resulted in the unstable behavior of the microactuators. Also, it could be noticed that only a small number of microactuators demonstrated thermal bending in the positive direction (away from the grooved side) with the amount of deformation which increased as the width of the microbeam reduced. After inspection by POM, it was found that the microbeams which bend in the positive direction mostly had a consistent internal LC alignment similar to the actuators fabricated without HEMA treatment, with relatively few irregularities and without the characteristic bright line in the middle of the channel. It is possible that the PDMS surface inside the microchannels for molding in this case was not sufficiently covered with HEMA due to non-uniformity in the treatment process. Such significant defects in the HEMA coating could have appeared due to several reasons. Trapping of the air bubbles in the narrow channels during treatment with liquid chemicals could lead to poor quality, patched coverage of the PDMS surface with HEMA. Possible contamination of the PDMS surface or the treatment solution could also affect the quality of the coating layer, since the dust particles and other contaminants may be introduced from the surrounding atmosphere during the test.

5.3.3 Bending Performance of the LCE Microactuators Polymerized Using the UV LED

This section contains the results and discussion of the bending performance of the LCE-based microactuators, which were fabricated using the photoinitiator-treated molds, and the LCE material was polymerized using the UV LED source (365 nm, ~11.8 mW/cm^2, 30 min).

In comparison with the previous test in Section 5.3.1 where the Hg lamp was used as a source of UV light in fabrication of the LCE microactuators, in this test a UV LED was used instead. The LED provided higher light intensity, and therefore, allowed reducing the duration of exposure to only 30 minutes to ensure thorough cross-linking of the LCE

material in the mold. However, not only the difference in the light intensity, but also the difference in the emission light spectrum, and most importantly, the substantially non-uniform distribution of the light intensity across the illuminated spot when using the LED could become a critical point in the process. As was shown in Section 3.8, the light intensity had the minimum value near the center (~9.5 mW/cm^2) and the maximum values near the edges of the illuminated area (~20.6 mW/cm^2); the average value was approximately equal to the nominal LED intensity (11.8 mW/cm^2). The molds were rotated during the UV exposure to help reducing the spatial non-uniformity; nevertheless, the effect of using the alternative UV source on the performance of the LCE microactuators had to be additionally investigated. The measurements of the beam curvature were performed upon thermal actuation from 40°C to 70°C; the results are shown in Figure 5.10. Each data point is the average of the results from 3 temperature cycles for the same LCE microbeam (cooling, heating and cooling).

It can be seen that the microactuators with the smallest grooves of size 1 demonstrated nearly zero or random bending under the thermal stimulus, similar to the results for the microactuators fabricated using the UV lamp. The microbeams with the grooves of size 2-4 demonstrated fully reversible bending in the direction away from the grooved side, with only a small number of the microactuators, about 12% of the total number, which showed small bending in the negative direction presumably due to non-uniformity in fabrication. The measurement data shows that generally the microbeams with a smaller width exhibit larger bending curvatures due to more flexibility. However, in comparison with the previous results for the microbeams fabricated using the UV lamp and using the photoinitiator-treated molds in Figure 5.8, a much larger scatter in the data for each beam width can be seen in Figure 5.10. Generally, a larger number of defects were observed via polarized microscopy in the microactuators fabricated using the UV LED, which is a direct reason of a large scatter in the data.

It was shown in the Section 5.3.1 that the optimal geometry of a LCE microactuator which provided the most consistent result was: the width of 40 µm, and the groove size 3. Comparing the performance of the microactuators with the same geometry, the standard deviation of the curvature $\Delta\kappa/\Delta T$ for the microactuators fabricated using the UV lamp (Figure 5.8c) was about 20% of the average curvature value, whereas the standard deviation for the actuators fabricated using the UV LED (Figure 5.10c) was much higher, about 63% of the average curvature value. Overall, significant deviation in the performance is not acceptable for using such LCE microactuators in practical

applications, based on the current polymerization procedure using the UV LED. The procedure using the UV lamp provides better uniformity of the LCE fabrication, and hence, more controllable actuation of the bending microbeams.
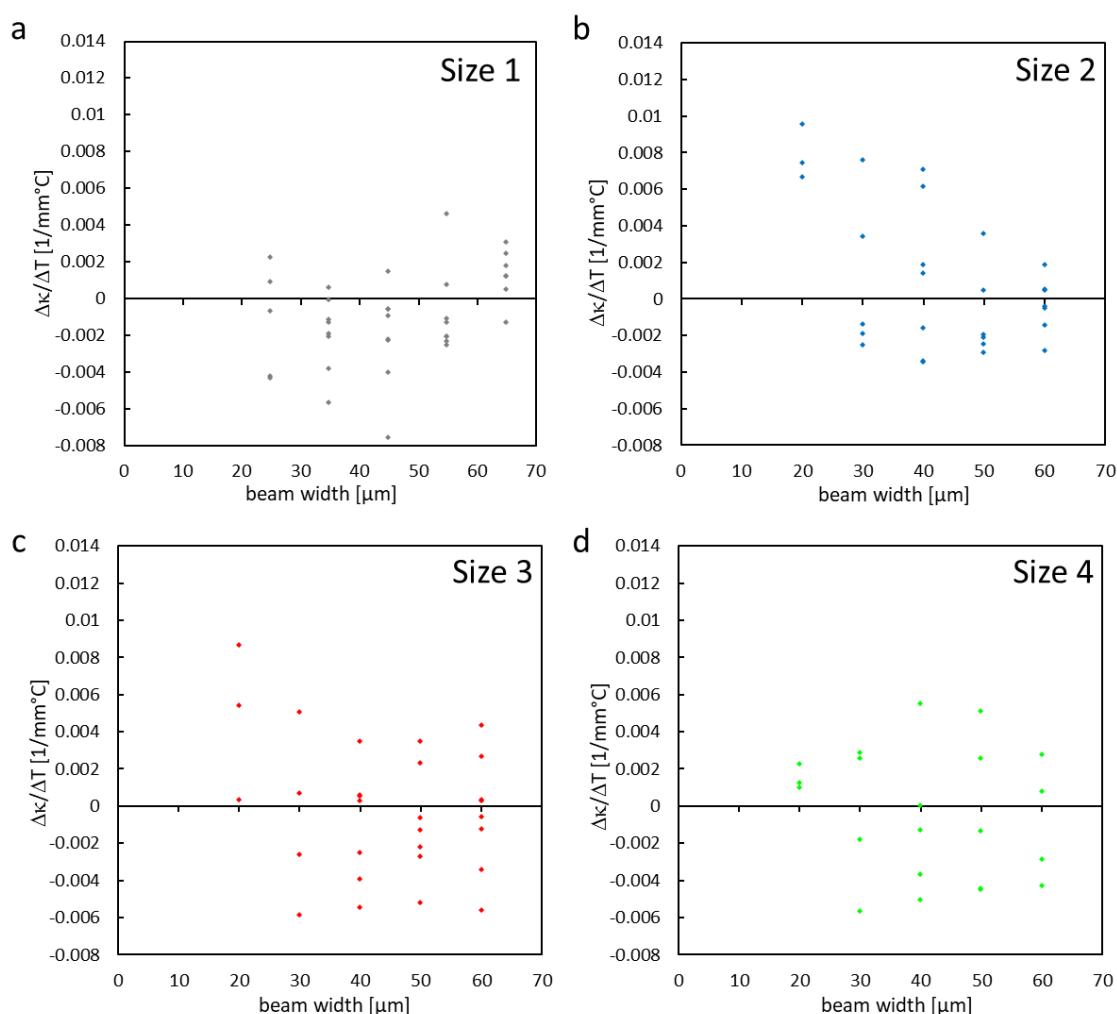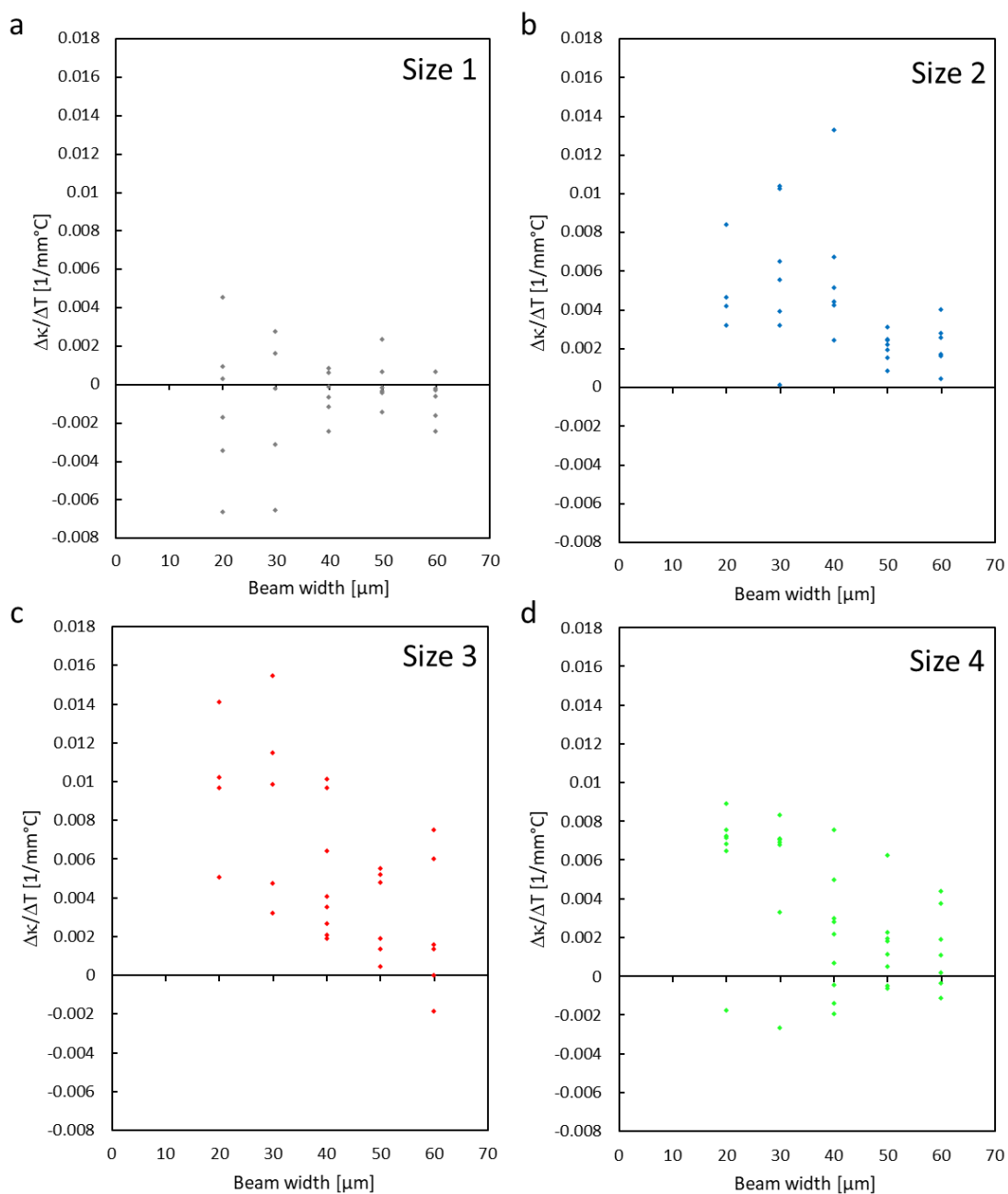

Figure 5.10 Experimental measurements of the bending rate, $\Delta\kappa/\Delta T$, under the temperature cycling from 40°C to 70°C in the LCE microbeams fabricated using the UV LED, a) with the grooves of size 1; b) size 2; c) size 3; and d) size 4

5.3.4 Thermal Actuation of the Symmetric LCE Microbeams with Flat and Grooved Walls

In order to prove that the asymmetric LCE alignment was due to the effect of the microgrooves, a number of microbeams were fabricated, which had grooves on both sidewalls or no grooves at all in symmetric LCE microbeams. It was expected that without any topological difference between the opposite sidewalls, the microbeams would exhibit no lateral bending upon temperature increase to 70°C. In the result, some of the microbeams showed nearly zero bending as expected, but also a number of microbeams showed random bending behavior, or even zigzag bending along LCE microbeams in some cases. This was attributed to the local variations and defects in the LC alignment. Thus, it justified that the thermal bending in all LCE microbeams fabricated by micromolding was mainly due to the internal anisotropic LC order, rather than the possible mechanical effects (such as stress release) of the surfaces with different topology.
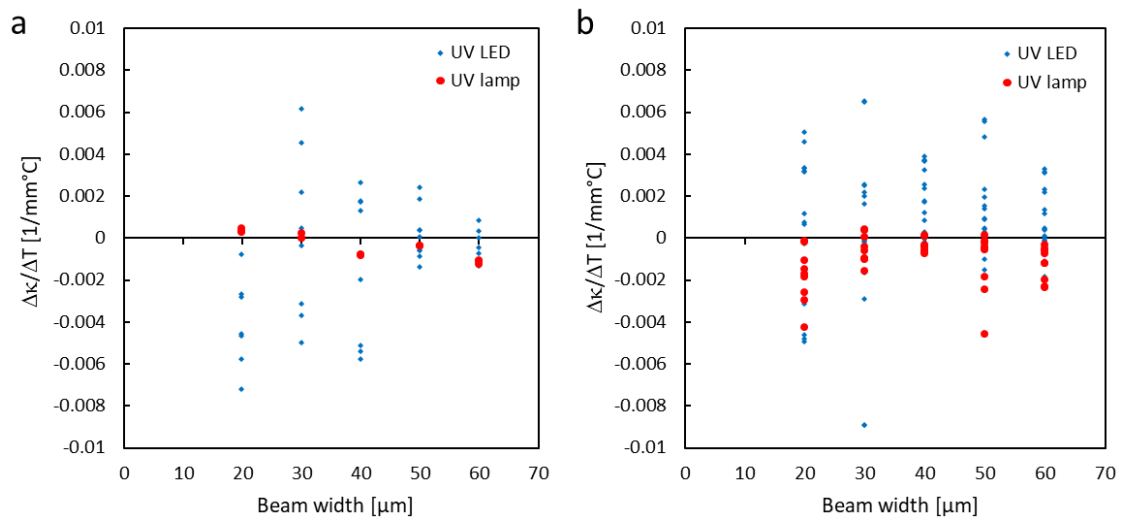
Figure 5.11 Experimental measurements of the bending rate, $\Delta\kappa/\Delta T$, under the temperature increase from 40°C to 70°C in the symmetric LCE microbeams, a) without microgrooves; b) with microgrooves on both sidewalls

The measurements of the curvature, $\Delta\kappa/\Delta T$, upon thermal actuation in symmetric microbeams with flat walls (no grooves) and with microgrooves on both sidewalls are given in Figure 5.11a and Figure 5.11b, respectively. The data points of different color demonstrate the results for the LCE microbeams fabricated using the Hg lamp in

comparison to those fabricated using the UV LED. The difference in the effect of the two UV sources is evident in the results. It can be seen that the thermal bending of the microbeams fabricated using the Hg lamp tend to be close to zero, with little scatter. Meanwhile, the microbeams fabricated using the UV LED demonstrated a more random bending behavior with a large scatter in both lateral directions. It was discussed in the Section 3.8 that these LCE structures tend to have more impurities in the LC alignment, which explains the large variations in the actuation behavior observed in Figure 5.11 below. Since the large scatter was observed even for the symmetric LCE microbeams, this explains the scatter observed in Figure 5.10 in the previous section for the microactuators with lateral bending.

5.3.5 Discussion

Overall, the reversible lateral bending actuation within the temperature range from 40°C to 70°C was demonstrated in the LCE microbeams fabricated by micromolding using the photoinitiator-treated molds. It was observed that the LCE microactuators of 30-40 µm in width with the grooves of sizes 2 and 3 have shown more controlled, consistent results in fabrication as well as actuation performance. The microactuators of 40 µm in width have also demonstrated largest calculated strain difference, which suggests that it is the optimal parameter for the given structural thickness of 40 µm. The microactuators with these parameters provide the average magnitude of curvature $\Delta\kappa/\Delta T$ close to 0.006 $(\text{mm}°\text{C})^{-1}$. On the other hand, microactuators with the smaller width have more flexibility and, hence, exhibit even larger curvatures, which can be used in the applications that require large bending displacements, while the actuation force is less important. The design of the microactuators can be adjusted to a particular application. The value of the curvature does not depend on the length of the microbeam, but larger total displacements can be provided by increasing the length, though it must be taken into account that the LCE microbeams are brittle, and longer microbeams may be more prone to damage during fabrication and operation. The micromolding method combined with the surface treatment method using the photoinitiator solution showed good results in producing the LCE microactuators with the desired in-plane bending behavior.

A combination of factors during the surface treatment procedure for the PDMS molds using HEMA significantly affected the performance of the thermal LCE microactuators.

Significant irregularities in the bending behavior of the actuators were observed. Optimization of the treatment process using HEMA could not achieve sufficient stability of the performance of the LCE microactuators, which was likely due to a complex topography of the PDMS surface subjected to treatment. Therefore, the microactuators fabricated using the HEMA-treated molds were not further used for the intended application. Comparing the performance and stability of the two actuator groups, the conclusion is that the surface treatment method for the PDMS molds using only the photoinitiator produced better and more consistent results in achieving the desired in-plane actuation of the LCE microbeams.

The effect of using different UV sources in fabrication was also investigated. Analysis of actuation of the symmetric microbeams with grooves on both sides or no grooves at all was useful in clarifying the random actuation effects arising from irregularities in the fabricated structures. The conclusion is that using the Hg lamp for LCE polymerization in the current fabrication process seems to be a more reliable method. In this case the bending microactuators demonstrate a relatively more stable performance, while the symmetric microbeams exhibit very little lateral deformation as expected. Using the UV LED in fabrication induces more random inhomogeneities in the LCE structure, and hence, some instability in the actuation performance.

5.4 Finite Element Modeling of the In-plane Bending LCE Microactuators

Based on the results of characterization, a 2D finite element model of the microactuators was built using COMSOL Multiphysics software. The same method of simulation was applied as that for the LCE bending films described in the Chapter 4. The method is based on utilizing the equivalent effect of thermal expansion in a multi-layer model through assigning the CTE values, which gradually increase from one LCE layer to the next. The LCE was modeled as a nearly incompressible material with the Young's modulus of $E = 1$ MPa and the Poisson's ratio of $v \approx 0.5$. The rectangular 2D shape of the microbeam was composed of 20 layers, the total length of the microbeam was 900 µm, and the total width was set with a parameter, varying from 20 µm to 60 µm. An array of triangular groove features of different sizes was placed along the whole length of the microbeam on the surface of left side of the beam as shown in Figure 5.12a. A fixed constraint was put onto the bottom short edge of the microbeam. Each layer was

assigned a CTE value, α_i, according to equation (4.9); where the leftmost layer including the grooves ($i = 1$) had the maximum value (α_1). The rightmost layer ($n = 20$) was assigned the CTE of 1 ppm°C^{-1} as it had to be a non-zero value for the analysis. Equivalent CTE values, α_{eq}, for the microbeams of different widths were calculated from the experimental measurements of the curvature, $\Delta\kappa/\Delta T$, according to equation (4.7). For this purpose, the combined data from the fabricated microactuators with the groove sizes 2, 3 and 4 with the positive curvature $\Delta\kappa/\Delta T$ was analyzed, because these microactuators demonstrated repeatable, controlled actuation. The calculated average equivalent CTE, α_{eq}, are shown on the graph in Figure 5.12b.

The values of α_{eq} are listed below:

- For the beam width of 20 µm – 156 ppm°C^{-1};
- For the beam width of 30 µm – 198 ppm°C^{-1};
- For the beam width of 40 µm – 222 ppm°C^{-1};
- For the beam width of 50 µm – 203 ppm°C^{-1};
- For the beam width of 60 µm – 118 ppm°C^{-1}.
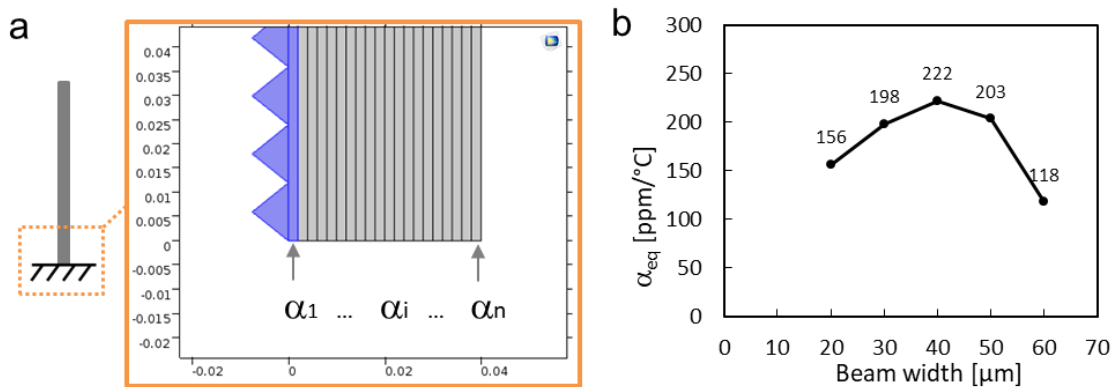
Figure 5.12 Finite Element Modeling of the in-plane bending LCE microactuators: a) the layered model of the microbeam with the equivalent CTE values, α_i, assigned to each layer; b) the calculated average equivalent CTE values, α_{eq}, for the LCE microbeams of different widths used for simulation

The values above are about a factor of 3 smaller than the equivalent CTE for the out-of-plane bending actuators fabricated from the flat LCE films, described in Chapter 4. This difference is not surprising because the rubbed polyimide layers used in the fabrication of the LCE films inside the glass cells possess strong alignment properties, which lead to large out-of-plane bending in the actuated LCE films. The alignment capability of the patterned PDMS surfaces was less strong, due to both the lower surface energy and the

3D geometries in the molding process. Additionally, as was discussed previously, the LC orientation inside the confined channels for micromolding is influenced by 4 surrounding walls, which leads to the formation of complex three-dimensional LC patterns, as opposed to the more uniform patterns inside the planar glass cells, influenced by only two surfaces. Also, the calculated α_{eq} values for the microstructured actuators were not constant for different widths of the microbeam. This is possibly due to the alignment mechanism which becomes less efficient with the increasing channel width [134]. This was unlike the α_{eq} for the flat film actuators in the Section 4.3, which was found to be similar across a very wide range of film thicknesses that allowed using an average value for modeling. For more precise result of modeling that matches well with the behavior of the fabricated microactuators, the actual value of α_{eq} for each different beam width, and not the average value, should be used in the model of the grooved microactuator. It was found that the highest α_{eq} of about 222 ppm°C^{-1} was obtained for the beam width of 40 µm (the microbeams with a square cross-section shape), thus providing the most efficient conversion of the thermal stimulus into the bending deformation.
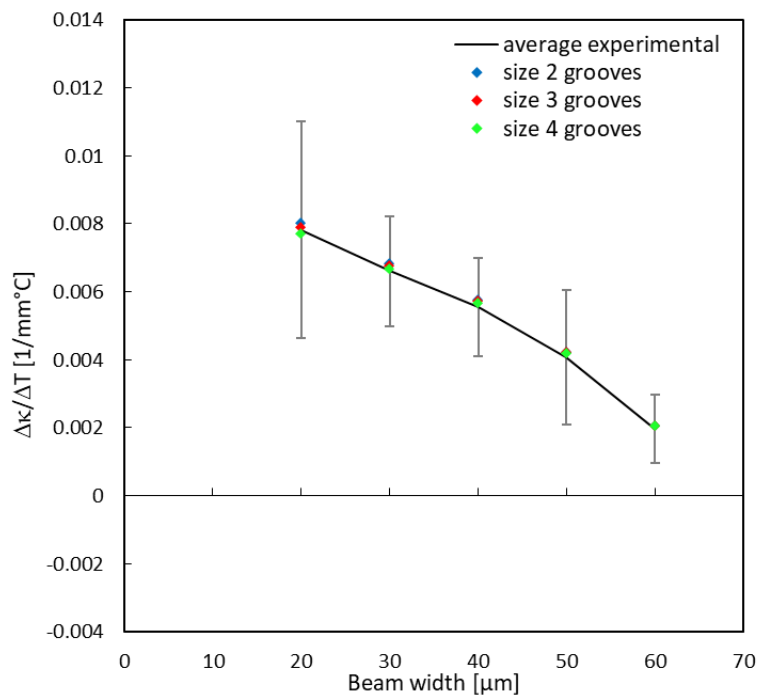
Figure 5.13 Results of the thermal bending rate, $\Delta\kappa/\Delta T$, obtained in simulation for the microbeams with different groove sizes, compared with the average experimental measurements

The strain reference temperature in the model was set conditionally at 40°C, where the microbeam had zero bending; the deformation was modeled at 70°C (30°C increase). The results of modeling are shown in Figure 5.13. The graph shows the curvature, $\Delta\kappa/\Delta T$, demonstrated by the models of the microbeams with different groove sizes; the curvature was calculated from the displacement data extracted from the model. These results agreed well with the average curvature obtained experimentally. The amount of deformation exhibited by the microbeam depends mainly on the CTE value and the strain induced through the equivalent thermal expansion effect in the model. Similarly to what was observed for the fabricated microbeams with different grooves, the size of the grooves had a very small effect on the total beam deflection when all other parameters of the model were the same. For the microbeams of 20 µm of width, the difference in the curvature, $\Delta\kappa/\Delta T$, was less than 3.8% between the microbeams with the grooves of size 2 and the grooves of size 4 with the two times larger period and length. The difference may be related to the stress concentration at the groove notches on bending of the microbeam. For instance, the effect of different depths and periods of the scribed grooves on the substrates has been studied in the literature for enhancement of bending and flexibility of the polymer films for flexible device applications [228]. However, the resulting effect of the grooves of different sizes was very small in our model.

Additionally, when all the layers were assigned the same CTE value in the simulation, as if the LCE alignment was homogeneous, it allowed observing whether any lateral deformation arises, which can only be due to different topology of the two sidewalls. This model with a homogeneous CTE parameter demonstrated only a negligible amount of lateral displacement, in the order of 0.3 µm, which proved that the mechanical effect of the surfaces with different topology on actuation is negligibly small.

Figure 5.14 shows a comparison of the arc-like bending shape of the microbeams with the grooves of size 3, the beam length of 900 µm, and five different widths S of 20, 30, 40, 50 and 60 µm. The values of the lateral tip displacement in the X axis, δ_x, extracted from the model were 95 µm, 82 µm, 69 µm, 51 µm and 25 µm for each beam width S respectively, induced as the temperature is increased by 30°C. Overall, it can be seen that the results of simulation show an excellent representation of the actual bending behavior of the LCE microactuators, observed under a microscope. Therefore, the model can be used to design LCE based in-plane microactuators for practical applications.
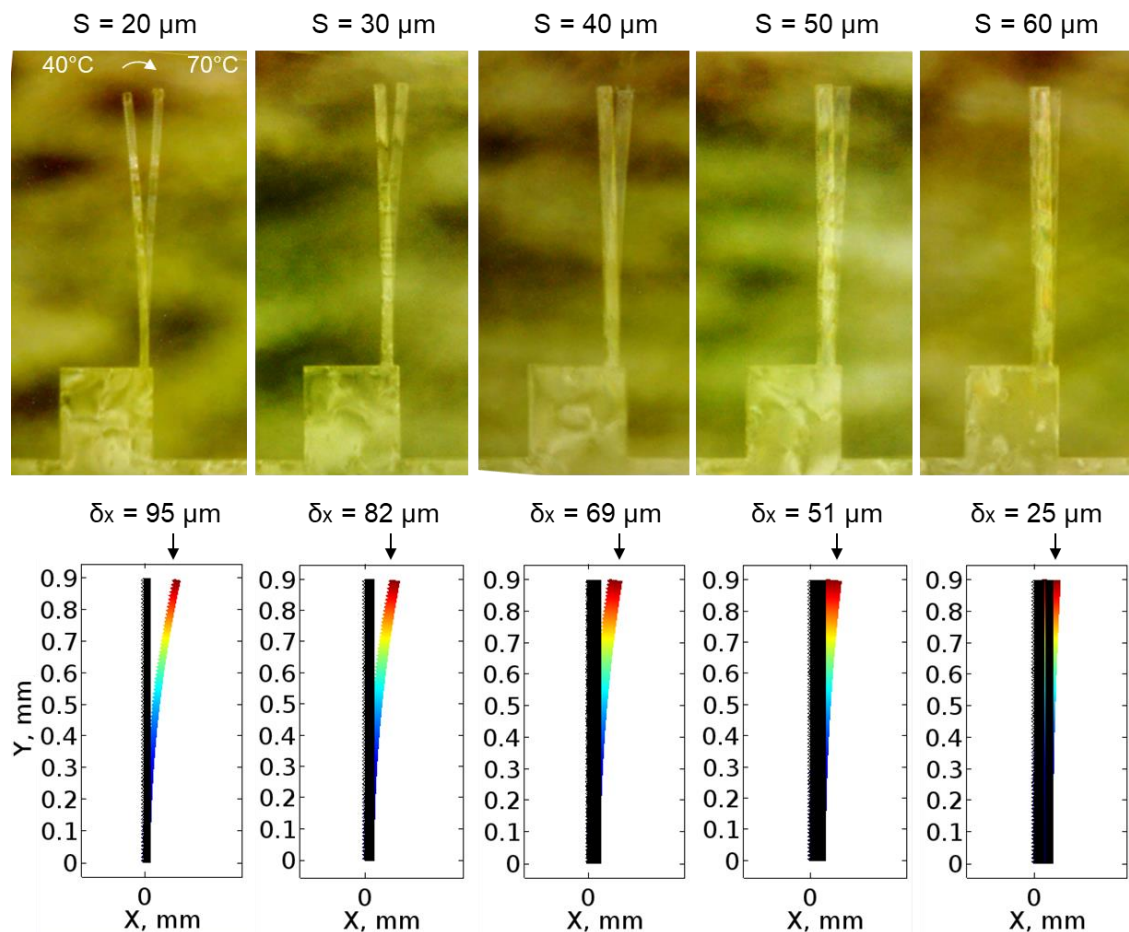
Figure 5.14 Comparison of the bending of the LCE microactuators recorded under the microscope (combined images) and modeled by a finite element method for the microactuators of five different widths S, where δ_x is the lateral tip displacement

5.5 Investigation of the Glass Transition Temperature of the LCE Materials with Different Dye Concentration

It is important to understand the relationship between the material structure, properties and the performance for designing and using the actuators for applications. The LCE-based actuators commonly operate in the nematic region or around the nematic-isotropic transition region. Generally, it is stated that the glass transition temperature of liquid crystal elastomers is low, often below the room temperature, which is one of the unique properties that distinguish the stimuli-responsive LCE from non-crosslinked liquid crystal polymers (LCP) with their high glass transition temperatures (>200°C) and high stiffness [105]. The low glass transition temperature, T_g, makes liquid crystal elastomer

based actuators very efficient for a wide range of practical applications. Therefore, it is highly important to experimentally measure the T_g of the new LCE material systems. The glass and phase transition properties can be investigated using the differential scanning calorimetry (DSC) method. In DSC measurements, the sample for characterisation is encapsulated in a crucible, the sample and a reference are heated and cooled together in a controlled environment. The heat flow to the sample is measured in comparison to the heat flow to the reference, and the change in the amount of heat transferred to the sample indicates different thermal events, such as glass transition, phase transition, melting and crystallization. The measurements of the T_g can be used to determine the glass transition behaviour in the LCE material that occurs at the temperature below the intended working temperature range for the actuators. The T_g for the LCE doped with dye for photothermal actuation in a biomimetic device was investigated in the literature [88], the LC components used for preparing the elastomer in the literature were same as the ones used in the thesis work. However, only the DSC measurements for the LCE with 2 mol% dye concentration has been reported in the literature. Thus, the impact of different dye concentrations on the glass transition properties of the LCE network was unknown. In our work, three different compositions were used – undoped LCE, doped with 1 mol% and 2 mol% of the light-absorbing dye.

The characterization by differential scanning calorimetry was carried out using a DSC2500 (TA Instruments) instrument equipped with a refrigerated cooling system RCS90 (TA Instruments); the measurements were carried out at School of Physics and Astronomy, University of Edinburgh. The DSC instrument was calibrated using the Indium calibration standard. Four samples of LCE materials were prepared from the previously fabricated LCE films, cut to the size of the crucible (each sample of 2-3 mg of weight), sealed in the crucibles and loaded onto the DSC system together with the empty reference crucible. Two undoped LCE film samples, LCE_1 and LCE_2, were taken from different fabrication batches, however, with the same chemical composition, in order to confirm whether the glass transition properties were similar. Sample LCE_3 was the LCE film doped with 1 mol% of the light-absorbing dye, and sample LCE_4 was doped with 2 mol% of the dye. The measurements of the heat flow were performed firstly on heating the sample from -20°C to 100°C at a rate of 5°C/min, then on cooling from 100°C to -20°C at the same rate of 5°C/min. The resulting DSC curves are shown in Figure 5.15. At the start of the experiment, a common endothermic start-up event was observed in the form of a sharp large baseline change during the first minutes of the

heating cycle. This usually occurs due to the difference in the heat capacity and the weight of the crucible with a sample and the empty reference crucible. The weight of an empty crucible was about 52 mg on average, thus the difference in weight to the loaded crucible was about 5%, which leads to the faster heating rates on the first minutes of the heating cycle. Similarly, in the first minutes of the cooling cycle, a sharp large exothermic start-up event could be observed. The glass transition phenomenon could be observed by a step in the baseline on the graph, indicating the change in the material properties, such as the specific heat capacity. The DSC curves were analyzed using the built-in software for analysis (TRIOS, TA Instruments). The glass transition temperature, T_g, was determined automatically at the midpoint (half height) of the transition step, the values are given in Table 5.1. The transition temperatures differ slightly between the heating and cooling cycle due to small thermal hysteresis effect.
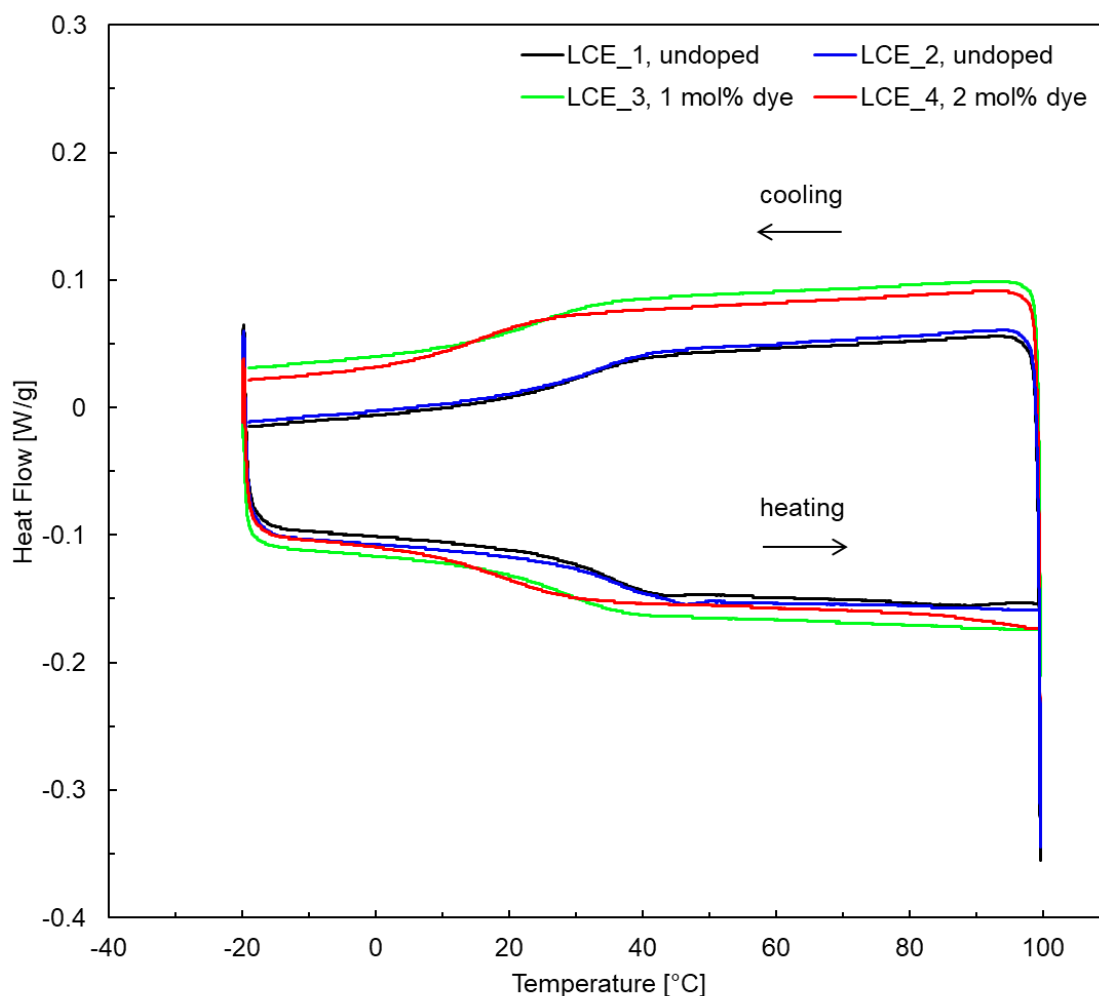
Figure 5.15 Differential scanning calorimetry curves of the polymerized LCE films without the dye, and with 1 mol% and 2 mol% of the light absorbing dye. Heating and cooling rate 5°C/min.

Table 5.1 The glass transition temperature of the undoped and dye-doped polymerized LCE films, as analyzed from the DSC curves on heating and cooling

LCE sample	T_g on the heating cycle [°C]	T_g on the cooling cycle [°C]
LCE_1, undoped	32.91	31.13
LCE_2, undoped	34.60	30.35
LCE_3, 1 mol% dye	27.01	23.19
LCE_4, 2 mol% dye	18.91	15.62

It can be seen in Figure 5.15 that the DSC curves for the two undoped LCE films from different fabrication batches are very similar, regardless of the different thermal history of the samples, such as heating, cooling and long storage of the fabricated films prior to the experiment. The glass transition temperature for the undoped LCE was slightly above 30°C in the result of measurements (31.1°C for LCE_1 on the cooling curve). It can be seen that the T_g of the material doped with 1 mol% dye is significantly lower (23.2°C on cooling). For the LCE doped with 2 mol% of the dye, the T_g is below the room temperature (15.6°C on cooling). This corresponds to the measurements reported in the literature for the LCE doped with 2 mol% dye (Disperse Red 1 dye as opposed to the Disperse Orange 3 dye used in this study) [88]. Therefore, it is evident that the glass-to-nematic transition occurs at lower temperatures with the increasing dye concentration. It indicates that the doped LCE can be used effectively for actuation in biomedical and life science applications, with biological samples such as living cells or tissues, where the temperature of the system must not exceed 40°C. No change in the properties was observed for the LCE material samples within the working temperature range of the actuators from 40°C to 80°C. Therefore, the results of DSC measurements confirmed that during characterization of the bending behavior of the actuators within the intended temperature range, all doped and undoped LCE materials remained in the nematic state.

5.6 Summary

The results of the characterization work by thermal cycling between 40°C and 70°C showed that the fabricated LCE microactuators with the sidewall microgrooves for controlling the alignment of LC mesogens were capable of performing reversible,

repeatable in-plane thermal bending. It was found that for achieving the controlled lateral bending actuation, the optimal fabrication conditions were: photo-polymerization of LCE using the Hg lamp with uniform illumination, and the treatment of the molds with a photoinitiator solution. Analysis of the bending curvature showed that the optimal width of the LCE microactuator is 40 µm, with the beam thickness of about 40 µm and groove size 3, which provides a more consistent result in actuation as well as in fabrication, and the largest calculated strain difference between the two sides of the microbeam which leads to the in-plane deformation. The microbeams with the smaller width (20 or 30 µm) can provide larger total bending curvatures; however, the calculated strain difference which causes the in-plane deformation may be smaller.

Chapter 6   Thermal and Photothermal LCE Microgrippers

6.1 Introduction

To demonstrate the lateral bending LCE microactuators for practical applications, the new micromolding method was used to fabricate planar LCE microgrippers based on the design shown in Figure 3.10b, where two microbeams are placed next to each other with a separation, and the geometry of the microgrooves for LC alignment is mirrored. The treatment process with the acetone solution of the photoinitiator was used in fabrication of the PDMS molds. When the microgrooves are placed on the outer sidewalls of the two beams, thermal bending of the arms occurs in the direction towards each other; and therefore, the microgripper has a normally-open property for operation. When the microgrooves are placed on the inner walls of the two beams, the arms bend away from each other, and this microgripper design provides normally-closed operation behavior. The LCE microgrippers made of the LCE precursor without adding any chemical dye can be actuated by a thermal stimulus, for example, in air in the vicinity of a hot object by thermal irradiation, or in a liquid by heating the medium. However, for most practical applications for pick-and-place of the micro-objects, remote actuation mechanism is highly desired, such as by using the light stimulus. For this purpose, the chemical dye of 1 mol% and 2 mol% concentrations was incorporated into the LCE material to realize the microgrippers for flexible, remote photothermal actuation. The fabrication and performance of the LCE microgrippers are described in this chapter. The micromanipulation procedure was demonstrated using the in-plane photothermal LCE microgripper using a microscopic glass bead as the object. This chapter is partly based on the results from the Publication (4).

6.2 Thermal Actuation of the LCE Microgrippers

In the initial experiment, a number of LCE microgrippers were fabricated from the same undoped LCE precursor as the bending beams in the previous section, without the chemical dye. Thermal actuation was tested by placing the microgrippers onto the glass slide, covered with a small amount of silicone oil. The structures were heated on the hotplate, and the bending of the arms was recorded with the digital microscope.

Figure 6.1 shows examples of actuation of the normally-open, in-plane LCE grippers upon the temperature increase from 40°C to 80°C. All grippers had the thickness of 40 µm defined in the fabrication process, and the typical length of 900 µm. The gripper shown inn Figure 6.1a had the beam width, *S*, of 40 µm, and the nominal distance between the arms, *D*, of 120 µm. The distance *D* is defined in the design of the digital mask, but it should be noted that the actual distance between the tips in the non-actuated gripper may differ due to the thermal stress release after fabrication. The gripper on Figure 6.1b was: *S* = 50 µm, and *D* = 60 µm. It can be seen that both microgrippers are fully closed at the actuation temperature of about 80°C. The closing movement of the gripper tips was fully reversible upon cooling back to the initial temperature of 40°C.
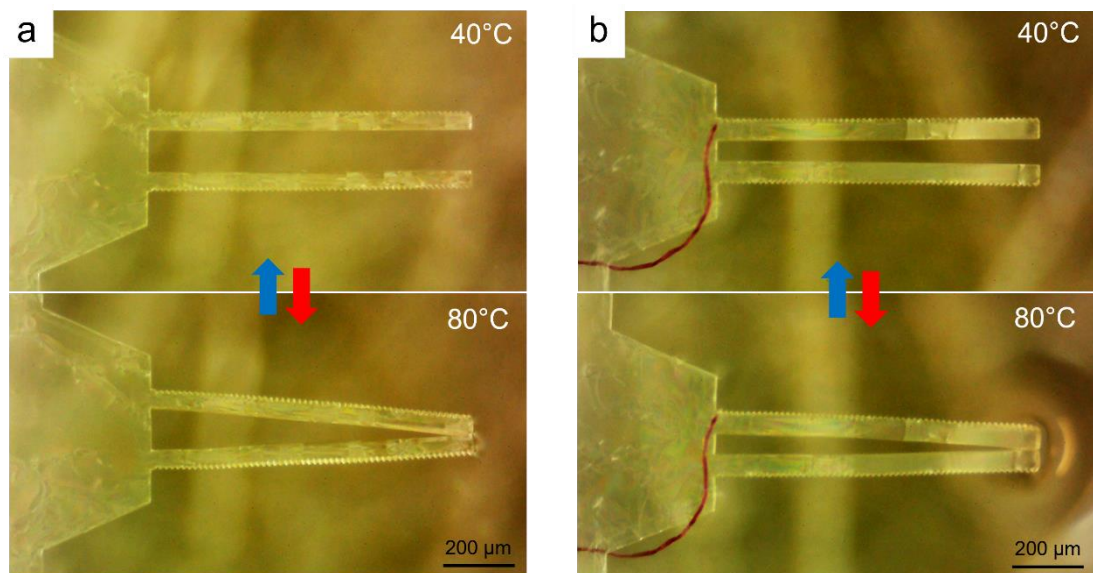
Figure 6.1 Reversible closing movement of the tips in the thermally-actuated in-plane LCE microgrippers, with the arm length of 900 µm, a) *S* = 40 µm, *D* = 120 µm; b) *S* = 50 µm, *D* = 60 µm

The thermal in-plane LCE microgripper in principle can be used for picking objects in a liquid medium, however, the actuation process is very slow when heating is performed on the hotplate. Also, since micromanipulation in a liquid medium is performed mostly in the life science applications, such as manipulation of bio-cells in a physiological solution, global heating of the environment to high temperatures is prohibited in this case. The thermal microgripper demonstrated in this study is used to prove the concept that the planar LCE-based microgrippers can be realized successfully with the micromolding method and they can perform reversible, repeatable in-plane gripping action.

6.3 Photothermal Actuation of the LCE Microgrippers

To enable photothermal actuation of the LCE microgrippers, the light-absorbing azo-dye Disperse Orange 3 was mixed into the LCE precursor in two different concentrations: 2 mol% or 1 mol%. A number of microgrippers were successfully fabricated by micromolding. To perform photothermal actuation, the microgripper was mounted on the edge of a glass slide, so that the arms were suspended in the air. The grippers were placed under the microscope equipped in the Chronogrip system for recording the bending of arms. The light from the blue-light LED (Thorlabs M455L4-C1, 455 nm) was focused in a small area of about 8 mm in diameter by adjusting the optical lens attached to the mounted LED; the distance between the lens and the illuminated sample in this case was about 17 cm. The light was directed at the LCE microgripper under the objective of the microscope. The illuminated spot was still much larger than the LCE microactuators, therefore, the actuation was performed by flood exposure, unlike in some other LCE-based microrobotic systems reported in the literature, which require spatially selective light exposure for in-plane movement [81], [189], [201]. The light intensity was regulated with the LED driver; the maximum intensity provided by the LED was 239 mW/cm^2 at the wavelength of 455 nm. This value was measured with the handheld power meter through the 4 mm hole in the non-transparent film cover on the optical sensor.

The results of the photothermal actuation of the LCE microgrippers doped with 2 mol% of the light-absorbing dye are shown in Figure 6.2. Figure 6.2a shows an LCE microgripper with the beam width, S, of 40 µm, and the nominal distance between the arms, D, of 120 µm. Figure 6.2b shows an LCE microgripper with $S = 40$ µm, and $D = 60$ µm. The length of arms was 900 µm for all microgrippers. These are the same gripper designs as those shown in the previous section in Figure 6.1, therefore, the thermal and photothermal response could be compared. It can be seen from Figure 6.2a and b that in the non-actuated state, the gripper arms have a curvature after release of the residual stress after fabrication. The measurements of the distance between the gripper tips shown in Figure 6.2 were performed using the built-in metrology tools of the robotic system. The resolution of the camera was 1.67 µm/pixel, the objective with magnification of 5x was used; therefore, the software tool for metrology was calibrated using the value 1.67/5 = 0.334 µm/pixel. Upon illumination with blue light, gripper arms bent towards each other, and restored to the initial shape when the light was

switched off. The gripping stroke (total displacement of the gripper tips) was 64 µm for the arm width of 40 µm in Figure 6.2a, and 32 µm for the arm width of 50 µm in Figure 6.2b. The displacement was repeatable over several cycles of actuation under the same light exposure conditions. The maximum displacement in the microstructures usually was reached in only about 2-3 seconds due to the fast photothermal conversion mechanism. This is comparable or slightly faster than actuation by resistive heating in SU-8 photoresist-based microgrippers (Publication (2)), and faster than the actuation by resistive heating in LCE structures of several millimeters in size with integrated heaters [163].
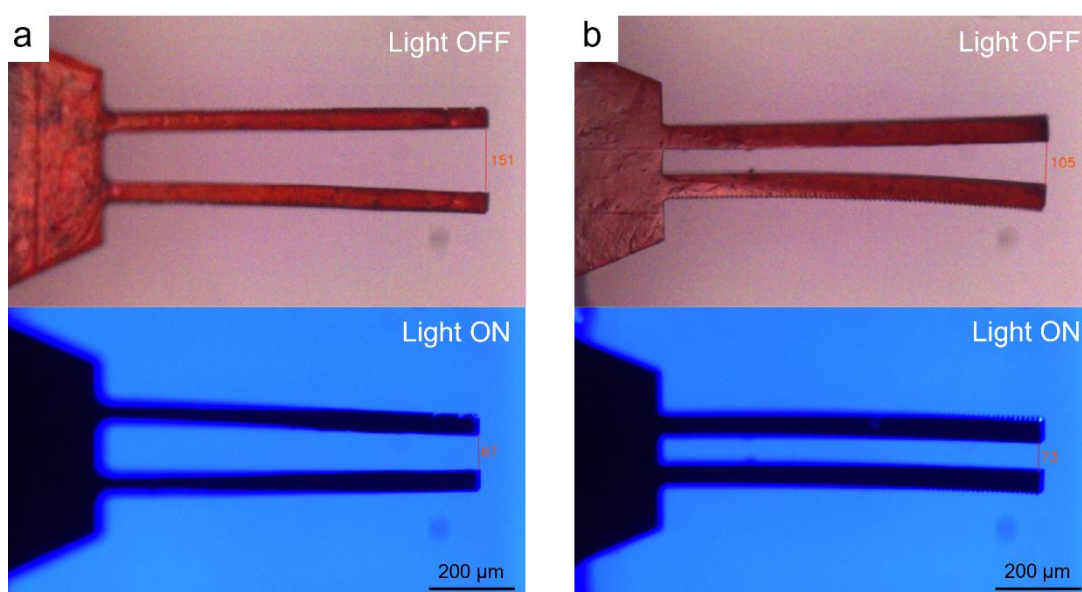
Figure 6.2 Reversible closing movement of the tips in the photothermally-actuated in-plane LCE microgrippers with 2 mol% light-absorbing dye concentration, the arm length of 900 µm, a) $S = 40$ µm, $D = 120$ µm; b) $S = 50$ µm, $D = 60$ µm

The photothermal actuation of the LCE microgrippers doped with 1 mol% dye concentration was also tested; the results are shown in Figure 6.3. Three microgrippers are compared, with the arm widths S of 30, 40 and 50 µm, and the distance between the arms of $D = 60$ µm. The grippers were actuated with the light intensity of 239 mW/cm^2. The distances were measured from the images. The LCE microgrippers with the dye concentration of 1 mol% showed the following performance characteristics:

– Test 1: the gripping strokes were 58, 35 and 27 µm for the grippers with the arm width of 30, 40 and 50 µm, respectively (Figure 6.3);

– Test 2: the gripping strokes were 42, 23 and 12 µm for the grippers with the arm width of 30, 40 and 50 µm, respectively.
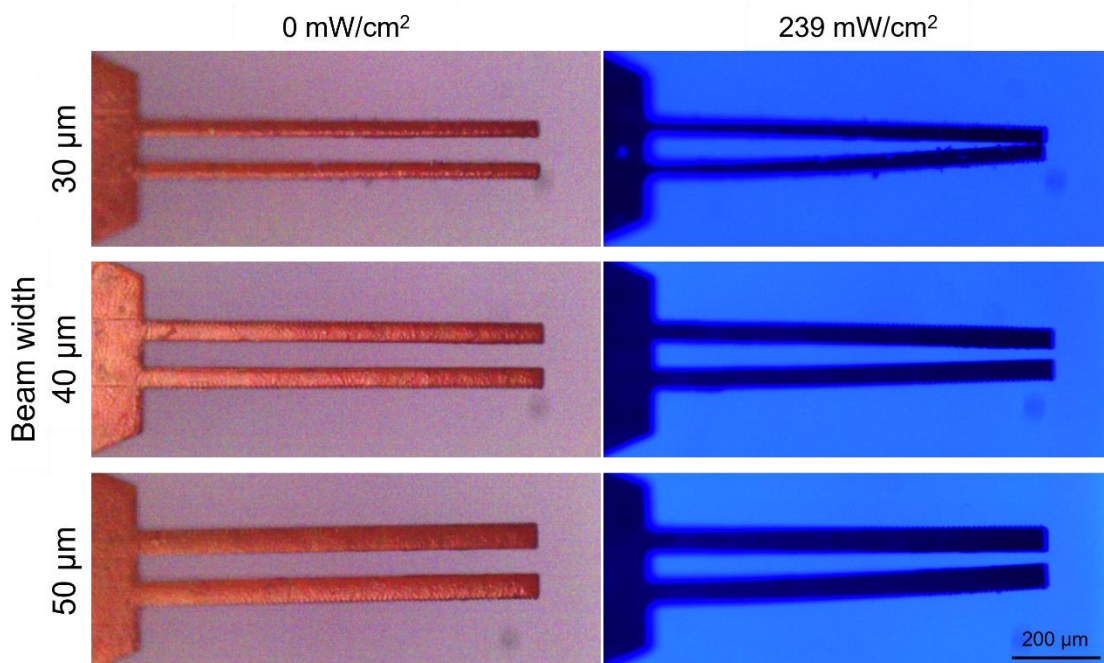
Figure 6.3 Photothermal actuation of the in-plane LCE microgrippers with 1 mol% dye concentration under the light of 239 mW/cm^2 intensity

The difference between the two test conditions was that the LED setup had to be disassembled, and then readjusted again, and thus, the position of the light spot may have been slightly different in the two cases. Considering the non-uniformity of the illumination across the light spot, as was observed previously, the actual light intensity delivered to the LCE structure in the second test may have been lower. It explains the difference in the results between the two tests. The difference is not the effect of structural decay, because the measurements were also repeated after a few days in both setups, and the displacement of the gripper tips was repeatable if the setup was unchanged. In general, it is evident that the thinner beams exhibit larger deflections. Full closure of the tips was achieved for the gripper with the smallest arm width of 30 µm under the light stimulus. Some parasitic out-of-plane displacement of the gripper tips, comparable to the amount of in-plane displacement, was also noticed in the microgrippers with 1 mol% dye upon light exposure.

For comparison of the performance of the LCE structures with different dye concentrations, the displacements were measured for microgrippers with the identical

designs, actuated under the same light exposure conditions. Therefore, the difference in the gripping stroke is associated only with the difference in the dye doping, hence, the difference in the light absorption. The comparison is given below for the microgrippers of 3 designs:

- 2 mol% dye: recorded gripping strokes of 64 µm ($S = 40$ µm), 32 µm ($S = 50$ µm), and 57 µm ($S = 50$ µm);
- 1 mol% dye: recorded gripping strokes of 35 µm ($S = 40$ µm), 12 µm ($S = 50$ µm), and 27 µm ($S = 50$ µm), respectively.

The microgrippers with 2 mol% of the dye showed photothermally induced bending displacements which was on average a factor of 2.2 larger than that in case of the dye concentration of 1 mol%. Therefore, in general, larger gripping strokes can be realized by using higher dye doping in the LCE material for more light absorption. However, at the same time as mentioned above, the higher dye content also changes the mechanical and elastic properties of the material, the crosslinking density, which may cause undesirable deformation. It was noticed that the grippers form LCE material with 1 mol% of the dye (Figure 6.3) generally had a well-defined shape with more straight arms, with only a very little deflection due to the stress release after fabrication, whereas the arms of the grippers with 2 mol% of the dye show a significant curvature in the non-actuated state (Figure 6.2). Nevertheless, the microgrippers based on both doped LCE materials could be operated successfully. Multiple cycles of actuation have shown that in both cases the amount of deflection was repeatable under the same light stimulus. The largest gripping stroke demonstrated in this experiment was 64 µm for the microgripper with the arm width of 40 µm and doped with 2 mol% of the dye.

6.4 Parasitic Out-of-plane Displacement

An important observation was that during photothermal actuation, the parasitic out-of-plane displacement of the gripper tips occurs simultaneously with the in-plane displacement. This can be seen from Figure 6.4, which shows a side view of the LCE gripper with the arm width of 50 µm, doped with 2 mol% of the dye, actuated by light from one side. The position of the camera was unchanged, when two images of the same beam were taken before actuation and during actuation, and the images were combined to observe the change of the shape. The image on the left shows the beam

bending towards the illuminated side, where the illuminated side was in contact with the bottom PDMS layer with a planar surface during fabrication. The out-of-plane displacement of the tip was 80 µm. Then, the LCE structure was flipped upside down. The image on the right shows the beam bending away from the illuminated side, where the illuminated side was the one adjacent to the top surface of the channels of the PDMS mold during fabrication. In this case, the out-of-plane displacement was smaller, 57 µm.
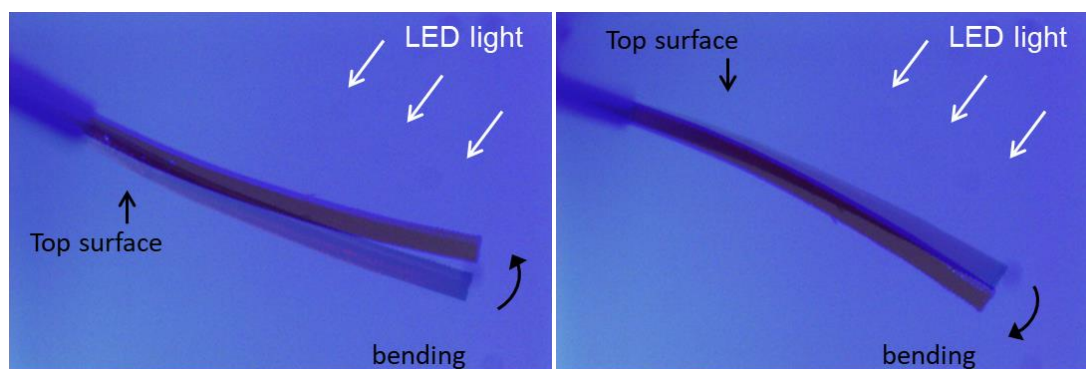
Figure 6.4 Combined images showing the out-of-plane bending of the LCE microgripper tip (side view) under one-sided light illumination. Dye concentration 2 mol%

The source of the parasitic out-of-plane displacement may come from two different effects. First source is the gradient of light absorption within the LCE layer, this effect is commonly observed in the literature for light-actuated structures [226]. Light penetration into the LCE is limited with the thickness of the layer due to the absorption of light by the dye incorporated into the material. Therefore, light is attenuated, and an emerging gradient of the absorbed light causes a gradient in the photo-generated heating effect throughout the thickness of the layer. In the result, the illuminated side exhibits larger actuation, and the beams tend to bend in the out-of-plane direction. However, this effect is not the only source of the parasitic displacement, otherwise the same amount of bending in the same direction would have been observed by illuminating the LCE structure from either of the two sides. Another effect contributing to the out-of-plane deflection could have been a small difference in LC alignment between the top and the bottom surface of the beams. This effect could be eliminated with further development and optimization of the fabrication process.

6.5 Numerical Simulation for LCE Microgrippers

Finite element simulation of the microgripper was performed based on the method described in Section 5.4 for in-plane bending LCE microbeams. Instead of a single beam, the gripper model had two beams with 20-layer structure attached to the common base, as shown in Figure 6.5. 'Fixed' mechanical constraint was put on the bottom edge of the base, the other constraints were similar to those used in Section 5.4. The equivalent thermal expansion value was assigned to each layer, where the boundary layers facing towards the inner side (flat side) has the smallest value, and the values gradually increased towards the outer layers of the beams (microgrooved side). The flat base has no directional LCE alignment, therefore, it was assigned with a homogeneous CTE value, α_{eq}. The CTE values α_{eq} used in the model were the average values derived from the measurements of the beam bending rate in Section 5.4. Therefore, for the beam width of 40 µm, $\alpha_{eq} = 222$ ppm$°C^{-1}$; for the beam width of 50 µm, $\alpha_{eq} = 203$ ppm$°C^{-1}$. The strain reference temperature for modeling was 40°C, where the arms of the grippers were straight with no bending.
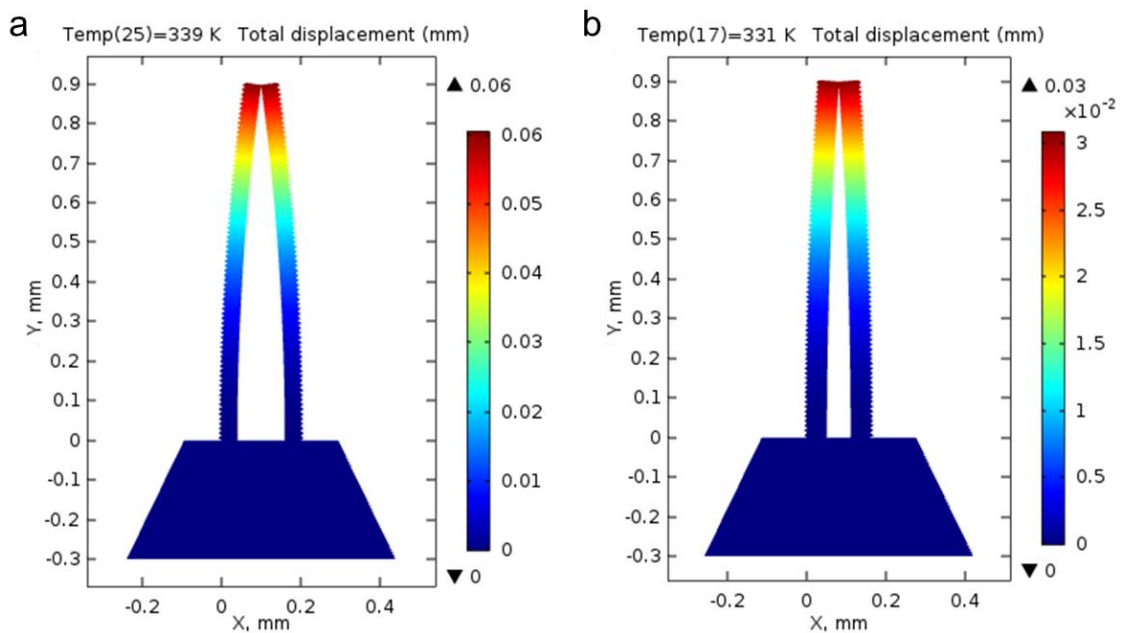
Figure 6.5 Finite element simulation of the LCE microgrippers a) with $S = 40$ µm, $D = 120$ µm, full tip closing at the temperature $T = 66°C$; b) with $S = 50$ µm, $D = 60$ µm, full tip closing at $T = 58°C$

Figure 6.5a shows the microgripper model with the beam width of $S = 40$ µm and the distance between the arms of $D = 120$ µm; Figure 6.5b shows the microgripper model

with $S = 50$ µm and $D = 60$ µm. The model shows tip displacement towards each other upon temperature increase. Thus, the numerical model is a good representation of the gripping movement of the arms, which was observed in the experiment in the LCE microgrippers upon thermal actuation, such as in Figure 6.1 for the same gripper designs. The results of simulation have shown that using the average values of equivalent CTE, α_{eq}, calculated from the experimental data, it is possible to achieve the full closing of the gripper tips upon the temperature increase to 66°C and 58°C as shown in Figure 6.5a and Figure 6.5b for the two gripper designs, respectively. In characterization, however, the fabricated microgrippers showed full tip closing at a slightly higher temperature, between 70°C and 80°C (Figure 6.1). This can be associated with slight deviation of the actual value of α_{eq} from the average value used in simulation, and also with deviation of the actual strain reference temperature from the value used in simulation, which was 40°C. The results demonstrated that the finite element method based on the gradient of thermal expansion can be used to model beam bending in various directions in the same device, depending on how the gradient of CTE is assigned within the structure. The actuator beams and parts with predesigned LCE alignment can be built with a multi-layer structure, where the distribution of properties can be spatially controlled with the design of the model, whereas polydomain LCE parts can be built with a homogeneous structure.

6.6 Manipulation of Micro-objects Using LCE Microgrippers

To demonstrate pick-and-place function of a micro-object using the in-plane LCE microgrippers, a microgripper was mounted onto a robotic manipulation system (Chronogrip, Percipio Robotics), the setup is shown in Figure 6.6. The LCE microgripper with the arm width of 40 µm, arm length of 900 µm, and doped with 2 mol% of the light-absorbing dye was firstly attached on the edge of a small glass chip using a tape. The chip was attached to a microscope glass slide, which then was mounted onto the robotic manipulator arm. The arm has 3 degrees of freedom (XYZ): in forward direction, lateral direction, and vertical direction. The movement of the arm was precisely controlled with a joystick, and the speed of movement could be controlled with the built-in software of the manipulation system. The objects used for micromanipulation were the microscopic glass beads of ~100 µm in diameter. Glass

beads were placed onto a piece of paper on the surface of the hexapod platform. The movement of the platform can also be controlled with the joystick and the speed could be set in the software. The robotic platform can also perform movement in 3 directions (forward, lateral and vertical movement). The LED light was directed under the objective of the microscope, so that the microgripper could be photothermally actuated while it was within the field of view of the microscope.
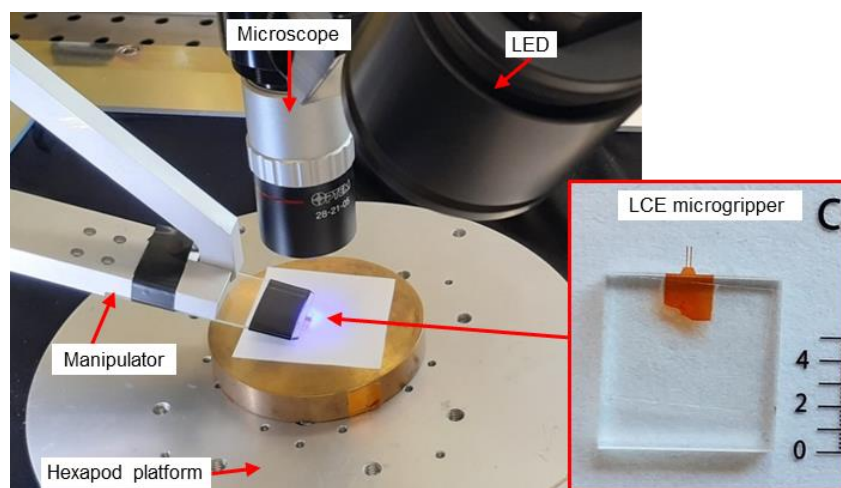
Figure 6.6 Setup for manipulation of the micro-objects using the in-plane LCE microgrippers. The unit of the scale bar for the LCE microgrippers is mm.

An example of the pick-and-place operation on a micro-glass bead is shown in Figure 6.7. Firstly, the gripper tips were brought into the position to capture the glass bead by robotic positioning. When the LED was turned on with the light intensity of 239 mW/cm^2, the tips were closed to grip the glass bead securely. By robotic adjustment of the gripper position in Z direction it was possible to compensate for the parasitic out-of-plane displacement of the tips under the light irradiation from the top LED. Then, the LCE microgripper and hence the glass bead was lifted and transported to a new position. The glass bead was released by switching off the blue light. Due to the fast photo-thermal actuation, which only takes a couple of seconds, the whole manipulation process could be completed in about one minute; the time marks of the process recorded on a video are shown in Figure 6.7. The diameter of the glass bead was 97 µm. It can be seen in Figure 6.7a, step 6, that there was an undesirable effect of stiction of the glass bead to one of the LCE arms during releasing. This common phenomenon is associated with the surface adhesion force between the object and the gripper, which has a strong effect at microscale, overcoming the gravitation force. However, a number of passive

and active release methods have been proposed previously in the literature to solve the stiction problem [229], such as modification of the tip shape to reduce the contact area. In Figure 6.7b, the glass bead was picked up using the microgripper and placed onto a sticky tape. It can be seen that in this case the object was firmly attached to the sticky surface after releasing, and the gripper tips were easily moved away.
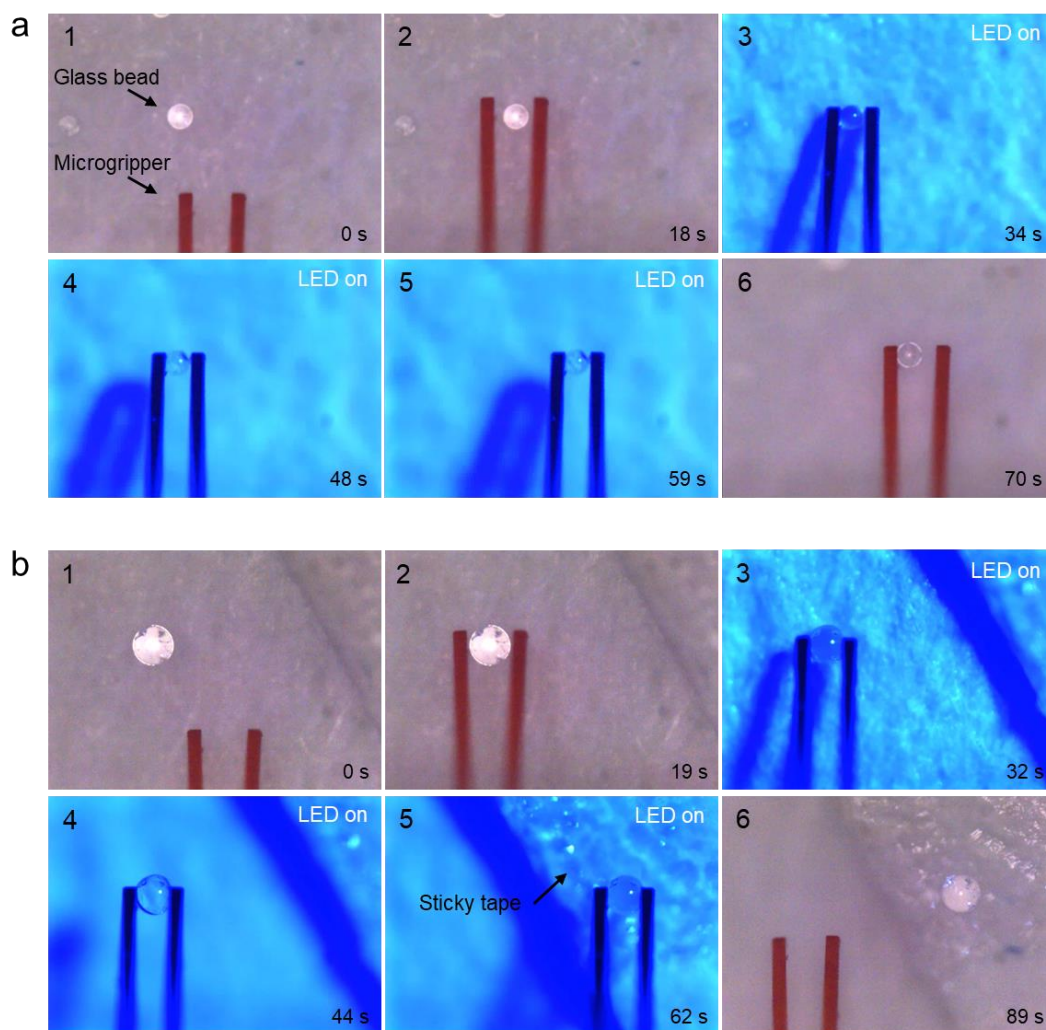
Figure 6.7 Demonstration of manipulation of the micro-glass beads using the photothermal in-plane LCE microgrippers, a) gripping and transporting the glass bead; b) placing the glass bead onto a sticky surface. The sequence of the micromanipulation is shown: 1 – start; 2 – positioning the microgripper tips to capture the object; 3 – griping the object by photothermal actuation; 4 – lifting the object from the surface; 5 – transporting the object; 6 – releasing the object by removing the light stimulus. The time marks refer to the video of the manual operation recorded in real time

These results demonstrate that the in-plane LCE microgrippers can be used to perform manipulation of the micro-objects. A single microgripper could successfully perform multiple cycles of pick-and-place operations for objects of various sizes without

significant degradation in the performance. Remote photothermal actuation allows easy integration of the LCE gripper in the larger robotic system, hence, easy replacement of the end-effector while using the same actuation source. Remote actuation also potentially allows more flexible movement and possibility to use the gripper for micromanipulation in the areas with difficult access. Relatively fast closing and opening of the tips makes the LCE microgripper an easy-to-use instrument for manual operation.

6.7 Comparison of the Performance of LCE Microgrippers Systems

In this section, the photothermal in-plane LCE microgripper demonstrated in this work is compared with some existing gripper systems in terms of the actuation stimulus value, footprint and the size of objects demonstrated in manipulation. The comparison includes various LCE-based gripper systems, responsive to photothermal, thermal or electrothermal stimuli, multimaterial grippers with integrated LCE actuators, and some untethered photothermal SU-8 based microgrippers for in-plane actuation. The comparison is shown in Table 6.1.

Table 6.1 Comparison of the photothermal LCE microgripper with existing gripper systems

Gripper system	Material	Actuation	Stimulus	Arm length	Actuator size	Size of objects in manipulation
[93][1]	LCE	Photothermal	51 mW	0.1 mm	$0.2 : 0.02 : 0.02$ mm^3	0.02-0.06 mm
[19][1]	LCE	Photothermal	≥40 mW	2-5 mm	$4\text{-}10 : 1 : 0.02$ mm^3	2 mm
[193][1]	LCE	Photothermal	150 mW/cm^2	≤7 mm	up to $25 : 14 : 0.05$ mm^3	-
[194][1]	LCE	Photothermal	3 W/cm^2	5 mm	$5 : 1 : 0.05$ mm^3	2 mm
[131][1]	LCE	Thermal	70 °C	~15 mm	thickness ~1 mm	~10 mm
[132][1]	LCE /polymers /conductive ink	Electrothermal	1.5 A	30 mm	thickness 0.5 mm	40 mm
[170][2]	LCE / Si / Au	Electrothermal	3.5 V	20 mm	$16 : 4 : 0.03$ mm^3	≤2.7 mm
[230][2]	SU-8 / Cr / Au	Photothermal	53.3 mW (spot size 0.3 mm)	~0.5 mm	thickness 0.05 mm	0.12 mm
[231][2]	SU-8 / ink	Photothermal	50 mW (spot size 0.075 mm)	0.92 mm	thickness 0.05 mm	0.02-0.05 mm
Current work[2]	LCE	Photothermal	239 mW/cm^2	0.9 mm	$0.9 : 0.04 : 0.04$ mm^3	~0.1 mm

[1] Out-of-plane actuation; [2] In-plane actuation

A number of LCE-based grippers demonstrated in the literature [19], [193], [194] are fabricated from the splay-aligned LCE film and operated by out-of-plane bending of the LCE film under photothermal or thermal stimuli. Hence, all devices required further assembly in order to be used for pick-and-place of the objects. The 3D printed LCE grippers have only been used for manipulation of centimeter scale objects. Also, the photothermal in-plane LCE microgripper was compared with more traditional in-plane microgripper structures based on SU-8. It has been shown that the working temperature range of the LCE grippers was from the room temperature up to 80°C, whereas, the SU-8 systems often have to exceed 100°C in operation due to the much lower CTE of SU-8 compared to LCE. To realize photothermal actuation in SU-8 microgrippers, the structure must have a light-absorbing element, such as in the two examples in Table 6.1, it can be an integrated metal layer, or a light-absorbing ink [230], [231]. These photothermal SU-8 microgrippers are capable of manipulation of the objects of few tens of microns in size. However, in comparison with our in-plane LCE microgrippers, the SU-8 microgrippers used a focused laser light to provide sufficiently high light intensity and hence temperature for actuation. Meanwhile, the demonstrated in-plane LCE microgrippers used flood exposure with relatively much lower intensity to achieve similar gripping displacements with ease of operation. As compared with the simple structure of the LCE gripper, the SU-8 based grippers usually also require more complex structures for effective amplification of the displacement.

6.8 Summary

The demonstrated LCE microgripper is the first example of a photothermally-actuated LCE gripper system with in-plane operation produced by the monolithic fabrication method described in Chapter 3. It is intended for applications in manipulation of sub-millimeter size objects, such as for assembly of the MEMS systems, or in bio-cell manipulation. The microgripper does not require assembly of the actuator parts, in contrast to the common out-of-plane LCE grippers. It is capable of providing the gripping strokes similar and larger than those in more traditional planar microgrippers based on SU-8, but with the advantage of using non-localized light exposure with much lower intensity and within relatively low actuation temperatures range. The in-plane photothermal LCE microgripper was used to perform successful pick-and-place of

microscopic glass beads, using the visible-light LED (455 nm) for remote actuation with the light intensity of 239 mW/cm^2 and using robotic manipulation. The method allows monolithic fabrication of LCE-based microgrippers for micromanipulation and microassembly applications in life sciences and in manufacture of microsystems, and potentially a useful route towards realization of gripping and cargo transportation functionality in microrobotics.

Chapter 7   Conclusions and Future Work

7.1 Conclusions

Liquid crystal elastomer based actuators are a recently emerged and rapidly growing technology, which holds a vast potential for many practical applications. The work described in this thesis focused on developing the new actuation modes, fabrication and modeling techniques for LCE actuators in the applications for micromanipulation.

Firstly, a detailed literature review was conducted to study the recent progress in the field. It was identified that LCE materials have favorable properties for implementing stimuli-responsive actuators and microgrippers with relatively low temperature operation and programmable bending, with possibility of remote actuation using light, they can be operated both in air and liquid medium, and they show flexibility and biocompatibility, which is crucial for operations with the biological samples. A lot of work has already been presented in the literature for LCE-based robots and soft gripper structures, mostly inspired by the motion strategies in various living organisms. However, a lack of effective technique for monolithic fabrication and LC alignment was a significant challenge for realization of the LCE structures with lateral bending, such as a traditional planar microgripper with two bending arms for manipulation of the objects in the size range of tens to hundreds of microns.

The challenges were addressed in this work; in the result, a new combination of techniques was developed that enabled the new lateral bending functionality in LCE microbeams upon thermal and photothermal actuation. This was achieved by LCE micromolding, where one sidewall of the molding channel was patterned with vertical microgrooves. The novelty of this work was that the micropatterned surface was used to create an in-plane alignment gradient across the width of the LCE structure, as opposed to the common out-of-plane LCE actuators and films using horizontally patterned surfaces. This approach provides flexibility and full spatial control over the areas for LC alignment since the microgroove patterns are integrated in the mask layout for photolithography and in the PDMS structures for molding. The monolithic LCE devices with in-plane operation can also be easily integrated into larger systems for practical applications. Therefore, the simultaneous alignment and fabrication using PDMS molds ensures the assembly-free fabrication of LCE microgrippers, which was not achievable previously with the surface alignment techniques for out-of-plane bending in LCEs.

The sequence of steps for fabrication was developed and the parameters were optimized. The master structures for subsequent molding were fabricated by direct laser writing in SU-8 photoresist, achieving the groove size as small as 4 µm by careful optimization of the scanning parameters; the grooves were well defined on the structural walls across the whole thickness of 40 µm. The microactuator structures were successfully replicated using PDMS molds, and finally, fabricated in LCE material, with minimal loss or damage to the structures due to demolding forces. It was shown that the LCE microactuators with the sidewall microgrooves were capable of reversible, repeatable lateral bending at elevated temperatures. The average bending rate of 0.0057 $(mm°C)^{-1}$ was recorded for the microactuator with the optimal geometry providing the largest strain: the width of 40 µm, the thickness of 40 µm; and the bending rate of 0.007 $(mm°C)^{-1}$ was recorded for the narrowest microactuators of 20 µm of width. Analysis of the bending rate and investigation of the internal LC alignment in the microactuators have shown that the method of surface treatment used for the PDMS molds has a significant impact on the actuation behavior of the LCE beams. It was shown that treatment with the acetone solution of photoinitiator is a simple and sufficient surface treatment method to achieve the desired LC alignment for lateral bending. The treatment was also required to ensure complete polymerization of the LCE material inside the PDMS mold, without the need for additional custom setup providing oxygen-free environment for the micromolding procedure.

A novel planar LCE microgripper with a simple structure has been demonstrated, which is operated by lateral bending of the two gripper arms. It is capable of untethered photothermal actuation using a light-absorbing dye dispersed in the material, and therefore, can be used as a replaceable or disposable end-effector for the robotic manipulation system. The microgripper with the arm width of 40 µm, length of 900 µm, doped with 2 mol% of the dye showed a gripping stroke of 64 µm under the light intensity of 239 mW/cm^2. This is several times more efficient than the thermal and photothermal SU-8 microgrippers, which usually require much larger actuation temperature or light intensity from a focused laser, and only capable of delivering smaller gripping strokes. The LCE microgripper was used to perform precise and repeated pick-and-place operations using the glass micro-beads of about 100 µm in diameter, whereas most of the existing LCE-based grippers have been demonstrated for manipulation of the larger objects of a few millimeters in diameter.

Finally, a computationally-efficient method for finite element simulation of the bending behaviors of LCE actuators was developed and experimentally verified. The model is based on the gradient of the temperature-dependent equivalent CTE parameter in a multi-layered structure. It has been shown that the same model is suitable for predicting the bending behavior of the LCE beams in a wide range of thicknesses (12-134 µm) with good accuracy. Flexibility of the model is valuable for designing new actuators, for comparing and performing optimization of the structure in various applications, whereas the models demonstrated previously in the literature mostly focused on a single structural design for a particular application. The simulation method can be applied to actuators with a variable thickness along the beam, such as the tapered actuators which show rolling deformation, as demonstrated in the thesis. The method was used successfully for simulation of the actuation behavior of the lateral bending LCE beams and microgrippers.

7.2 Future Work

The research presented in this thesis covered various aspects, such as design, fabrication, simulation, material characterization, device characterization, as well as demonstration of application in micromanipulation. Further research on the topic can be carried out in the following areas: a) in-depth study of multi-cycled actuation, hysteresis effect, lifetime, fatigue and reliability of the LCE microactuators; b) study of the effect of microactuator thicknesses other than 40 µm; c) dynamic measurements of the thermal and photothermal actuation to determine the response time of the microactuators; measurements of the gripping force of the LCE microgrippers; d) further optimization of the molding and surface treatment processes in order to eliminate parasitic out-of-plane bending, to increase the yield of functional devices with minimum alignment defects, and to improve repeatability; e) improvement of the resolution of the microgrooves may be possible, such as by using X-ray lithography or other fabrication methods. Furthermore, the new lateral bending LCE microbeams can be demonstrated for various other applications besides object transportation, such as in microrobotics for locomotion function in the walking and swimming microrobots by propulsion using the microbeams attached to the robot body; also in the lab-on-a-chip systems for fluid manipulation and active mixing, or in photo-actuated microswitches.

References

[1] D. Jang, J. Jeong, H. Song, and S. K. Chung, "Targeted drug delivery technology using untethered microrobots: a review," *J. Micromechanics Microengineering*, vol. 29, no. 5, p. 53002, 2019.

[2] M. Sitti *et al.*, "Biomedical Applications of Untethered Mobile Milli/Microrobots," *Proc. IEEE*, vol. 103, no. 2, pp. 205–224, 2015.

[3] D. Ditter, P. Blümler, B. Klöckner, J. Hilgert, and R. Zentel, "Microfluidic Synthesis of Liquid Crystalline Elastomer Particle Transport Systems which Can Be Remote-Controlled Magnetically," *Adv. Funct. Mater.*, vol. 29, no. 29, p. 1902454, Jul. 2019.

[4] L. Hines, K. Petersen, G. Z. Lum, and M. Sitti, "Soft actuators for small-scale robotics," *Adv. Mater.*, vol. 29, no. 13, p. 1603483, 2017.

[5] K. Wouters and R. Puers, "Diffusing and swelling in SU-8: insight in material properties and processing," *J. Micromechanics Microengineering*, vol. 20, no. 9, p. 95013, 2010.

[6] L. Ionov, "Polymeric actuators," *Langmuir*, vol. 31, no. 18, pp. 5015–5024, 2014.

[7] Y. Wu *et al.*, "Insect-scale fast moving and ultrarobust soft robot," *Sci. Robot.*, vol. 4, no. 32, p. eaax1594, 2019.

[8] D. Sun *et al.*, "Toward Application of Liquid Crystalline Elastomer for Smart Robotics: State of the Art and Challenges," *Polymers* , vol. 13, no. 11. 2021.

[9] C. Yoon, "Advances in biomimetic stimuli responsive soft grippers," *Nano Converg.*, vol. 6, no. 1, pp. 1–14, 2019.

[10] S. Palagi and P. Fischer, "Bioinspired microrobots," *Nat. Rev. Mater.*, vol. 3, no. 6, pp. 113–124, 2018.

[11] S. Chen *et al.*, "Soft crawling robots: design, actuation, and locomotion," *Adv. Mater. Technol.*, vol. 5, no. 2, p. 1900837, 2020.

[12] H. Zeng, P. Wasylczyk, D. S. Wiersma, and A. Priimagi, "Light Robots: Bridging the Gap between Microrobotics and Photomechanics in Soft Materials," *Adv. Mater.*, vol. 30, no. 24, p. 1703554, Jun. 2018.

[13] K. Fuchi *et al.*, "Topology optimization for the design of folding liquid crystal elastomer actuators," *Soft Matter*, vol. 11, no. 37, pp. 7288–7295, 2015.

[14] C. Yuan *et al.*, "3D printed reversible shape changing soft actuators assisted by

liquid crystal elastomers," *Soft Matter*, vol. 13, no. 33, pp. 5558–5568, 2017.

[15]   M. K. McBride *et al.*, "A readily programmable, fully reversible shape-switching material," *Sci. Adv.*, vol. 4, no. 8, p. eaat4634, 2018.

[16]   H. Shahsavan, L. Yu, A. Jákli, and B. Zhao, "Smart biomimetic micro/nanostructures based on liquid crystal elastomers and networks," *Soft Matter*, vol. 13, no. 44, pp. 8006–8022, 2017.

[17]   H. Shahsavan, S. M. Salili, A. Jákli, and B. Zhao, "Thermally Active Liquid Crystal Network Gripper Mimicking the Self-Peeling of Gecko Toe Pads," *Adv. Mater.*, vol. 29, no. 3, p. 1604021, Jan. 2017.

[18]   H. Shahsavan *et al.*, "Bioinspired underwater locomotion of light-driven liquid crystal gels," *Proc. Natl. Acad. Sci.*, vol. 117, no. 10, pp. 5125–5133, 2020.

[19]   O. M. Wani, H. Zeng, and A. Priimagi, "A light-driven artificial flytrap," *Nat. Commun.*, vol. 8, no. 1, p. 15546, 2017.

[20]   H. Shahsavan, S. M. Salili, A. Jákli, and B. Zhao, "Smart Muscle-Driven Self-Cleaning of Biomimetic Microstructures from Liquid Crystal Elastomers," *Adv. Mater.*, vol. 27, no. 43, pp. 6828–6833, Nov. 2015.

[21]   E. Kizilkan, J. Strueben, A. Staubitz, and S. N. Gorb, "Bioinspired photocontrollable microstructured transport device," *Sci. Robot*, vol. 2, no. 2, 2017.

[22]   S. Schuhladen, F. Preller, R. Rix, S. Petsch, R. Zentel, and H. Zappe, "Iris-Like Tunable Aperture Employing Liquid-Crystal Elastomers," *Adv. Mater.*, vol. 26, no. 42, pp. 7247–7251, Nov. 2014.

[23]   T. H. Ware, M. E. McConney, J. J. Wie, V. P. Tondiglia, and T. J. White, "Voxelated liquid crystal elastomers," *Science (80-.).*, vol. 347, no. 6225, pp. 982–984, Feb. 2015.

[24]   H. Zeng, P. Wasylczyk, G. Cerretti, D. Martella, C. Parmeggiani, and D. S. Wiersma, "Alignment engineering in liquid crystalline elastomers: Free-form microstructures with multiple functionalities," *Appl. Phys. Lett.*, vol. 106, no. 11, p. 111902, Mar. 2015.

[25]   A. Kotikian, R. L. Truby, J. W. Boley, T. J. White, and J. A. Lewis, "3D Printing of Liquid Crystal Elastomeric Actuators with Spatially Programed Nematic Order," *Adv. Mater.*, vol. 30, no. 10, p. 1706164, Mar. 2018.

[26]   M. Verotti, A. Dochshanov, and N. P. Belfiore, "A comprehensive survey on microgrippers design: mechanical structure," *J. Mech. Des.*, vol. 139, no. 6, p.

060801, 2017.

[27]   K. N. Andersen *et al.*, "Electrothermal microgrippers for pick-and-place operations," *Microelectron. Eng.*, vol. 85, pp. 1128–1130, May 2008.

[28]   K. S. Colinjivadi, J.-B. Lee, and R. Draper, "Viable cell handling with high aspect ratio polymer chopstick gripper mounted on a nano precision manipulator," *Microsyst. Technol.*, vol. 14, pp. 1627–1633, Aug. 2008.

[29]   R. Zhang, J. Chu, H. Wang, and Z. Chen, "A multipurpose electrothermal microgripper for biological micro-manipulation," *Microsyst. Technol.*, vol. 19, no. 1, pp. 89–97, Jan. 2013.

[30]   K. Kim, X. Liu, Y. Zhang, J. Cheng, X. Y. Wu, and Y. Sun, "Mechanical characterization of polymeric microcapsules using a force-feedback MEMS microgripper," in *2008 30th Annual International Conference of the IEEE Engineering in Medicine and Biology Society*, 2008, pp. 1845–1848.

[31]   S. Yang and Q. Xu, "A review on actuation and sensing techniques for MEMS-based microgrippers," *J. Micro-Bio Robot.*, vol. 13, pp. 1–14, May 2017.

[32]   A. Dochshanov, M. Verotti, and N. P. Belfiore, "A comprehensive survey on microgrippers design: operational strategy," *J. Mech. Des.*, vol. 139, no. 7, p. 070801, 2017.

[33]   MicroChem, "SU-8 2000 Permanent Epoxy Negative Photoresist. Technical Data Sheet." .

[34]   L. Ionov, "Hydrogel-based actuators: possibilities and limitations," *Mater. Today*, vol. 17, no. 10, pp. 494–503, 2014.

[35]   J. W. L. Zhou, H.-Y. Chan, T. K. H. To, K. W. C. Lai, and W. J. Li, "Polymer MEMS actuators for underwater micromanipulation," *IEEE/ASME Trans. Mechatronics*, vol. 9, no. 2, pp. 334–342, 2004.

[36]   A. Azam, K. E. Laflin, M. Jamal, R. Fernandes, and D. H. Gracias, "Self-folding micropatterned polymeric containers," *Biomed. Microdevices*, vol. 13, no. 1, pp. 51–58, 2011.

[37]   MicroChem, "SU-8 3000 Permanent Epoxy Negative Photoresist. Technical Data Sheet." .

[38]   T. A. Anhøj, "Fabrication of High Aspect Ratio SU-8 Structures for Integrated Spectrometers," Technical University of Denmark, 2007.

[39]   M. Sangermano *et al.*, "Enhancement of electrical and thermal conductivity of Su-8 photocrosslinked coatings containing graphene," *Prog. Org. Coatings*, vol.

86, pp. 143–146, 2015.

[40] M. Sharif *et al.*, "The effect of graphene oxide on UV curing kinetics and properties of SU8 nanocomposites," *Polym. Int.*, vol. 66, no. 3, pp. 405–417, 2017.

[41] F. Mohammadzadeh Honarvar, B. Pourabbas, M. Salami Hosseini, M. Kharazi, and H. Erfan-Niya, "Molecular dynamics simulation: The effect of graphene on the mechanical properties of epoxy based photoresist: SU8," *Sci. Iran.*, vol. 25, no. 3, pp. 1879–1890, 2018.

[42] B. Xue and Y. Zou, "Homogeneous transfer of graphene oxide into photoresist: Fabrication of high surface area three-dimensional micro-arrays by modified photolithography," *Compos. Sci. Technol.*, vol. 157, pp. 78–85, 2018.

[43] Y. Xia and G. M. Whitesides, "Soft lithography," *Annu. Rev. Mater. Sci.*, vol. 28, no. 1, pp. 153–184, 1998.

[44] M. Al Zandi, C. Wang, R.-C. Voicu, and R. Muller, "Testing and characterisation of electrothermal microgrippers with embedded microheaters," in *2016 Symposium on Design, Test, Integration and Packaging of MEMS/MOEMS (DTIP)*, 2016, pp. 1–5.

[45] M. Deubel, G. von Freymann, M. Wegener, S. Pereira, K. Busch, and C. M. Soukoulis, "Direct laser writing of three-dimensional photonic-crystal templates for telecommunications," *Nat. Mater.*, vol. 3, no. 7, pp. 444–447, 2004.

[46] N. Chronis and L. P. Lee, "Electrothermally activated SU-8 microgripper for single cell manipulation in solution," *J. Microelectromechanical Syst.*, vol. 14, no. 4, pp. 857–863, 2005.

[47] N. Chronis and L. P. Lee, "Polymer MEMS-based microgripper for single cell manipulation," in *17th IEEE International Conference on Micro Electro Mechanical Systems (MEMS2004)*, 2004, pp. 17–20.

[48] B. Solano and D. Wood, "Design and testing of a polymeric microgripper for cell manipulation," *Microelectron. Eng.*, vol. 84, pp. 1219–1222, May 2007.

[49] R. Voicu, R. Muller, and L. Eftime, "Design optimization for an electro-thermally actuated polymeric microgripper," in *Design, Test, Integration and Packaging of MEMS/MOEMS, 2008. MEMS/MOEMS 2008. Symposium on*, 2008, pp. 182–186.

[50] R. Voicu, R. Müller, L. Eftime, and C. Tibeica, "Design study for an electro-thermally actuator for micromanipulation," *Rom. J. Inf. Sci. Technol*, vol. 12, no.

3, pp. 402–409, 2009.

[51]   R. Voicu and R. Muller, "New electro-thermally actuated micromanipulator with optimized design and FEM simulations analyses," in *Design, Test, Integration and Packaging of MEMS/MOEMS (DTIP), 2013 Symposium on*, 2013, pp. 1–6.

[52]   M. H. M. Al-Zandi, C. Wang, R. Voicu, and R. Muller, "Measurement and characterisation of displacement and temperature of polymer based electrothermal microgrippers," *Microsyst. Technol.*, vol. 24, no. 1, pp. 379–387, 2018.

[53]   S. Iamoni and A. Somà, "Design of an electro-thermally actuated cell microgripper," *Microsyst. Technol.*, vol. 20, no. 4–5, pp. 869–877, 2014.

[54]   A. Somà, S. Iamoni, R. Voicu, R. Müller, M. H. M. Al-Zandi, and C. Wang, "Design and experimental testing of an electro-thermal microgripper for cell manipulation," *Microsyst. Technol.*, vol. 24, no. 2, pp. 1053–1060, 2017.

[55]   N.-T. Nguyen, S.-S. Ho, and C. L.-N. Low, "A polymeric microgripper with integrated thermal actuators," *J. Micromechanics Microengineering*, vol. 14, no. 7, pp. 969–974, 2004.

[56]   J. Chu, R. Zhang, and Z. Chen, "A novel SU-8 electrothermal microgripper based on the type synthesis of the kinematic chain method and the stiffness matrix method," *J. Micromechanics Microengineering*, vol. 21, no. 5, p. 054030, 2011.

[57]   R. C. Voicu, C. Tibeica, R. Mueller, A. Dinescu, M. Pustan, and C. Birleanu, "SU-8 Microgrippers based on V-shaped Electrothermal Actuators with Implanted Heaters," *Rom. J. Inf. Sci. Technol.*, vol. 19, no. 3, pp. 269–281, 2016.

[58]   R. C. Voicu, C. Tibeica, R. Müller, and A. Dinescu, "An SU-8 micro-tweezer based on the chevron electro-thermal actuators with a large in-plane displacement," in *Semiconductor Conference (CAS), 2017 International*, 2017, pp. 105–108.

[59]   R. C. Voicu, C. Tibeica, M. Al-Zandi, A. Potekhina, and C. Wang, "V-shaped and Z-shaped SU-8 Micro-Tweezers with In-plane Displacement for Micromanipulation," in *2019 International Conference on Manipulation, Automation and Robotics at Small Scales (MARSS)*, 2019.

[60]   R.-C. Voicu, "Design, numerical simulation and experimental investigation of an SU-8 microgripper based on the cascaded V-shaped electrothermal actuators," *J. Phys. Conf. Ser.*, vol. 757, no. 1, p. 012015, 2016.

[61]   R. E. Mackay, H. R. Le, and R. P. Keatch, "Design optimisation and fabrication

of SU-8 based electro-thermal micro-grippers," *J. Micro-Nano Mechatronics*, vol. 6, no. 1, pp. 13–22, 2011.

[62] R.-C. Voicu, M. Al Zandi, R. Müller, and C. Wang, "Nonlinear numerical analysis and experimental testing for an electrothermal SU-8 microgripper with reduced out-of-plane displacement," *J. Phys. Conf. Ser.*, vol. 922, no. 1, p. 012006, 2017.

[63] J. K. Luo *et al.*, "Modelling and fabrication of low operation temperature microcages with a polymer/metal/DLC trilayer structure," *Sensors Actuators A Phys.*, vol. 132, no. 1, pp. 346–353, 2006.

[64] Z. Zhang, Y. Yu, X. Liu, and X. Zhang, "A comparison model of V-and Z-shaped electrothermal microactuators," in *Mechatronics and Automation (ICMA), 2015 IEEE International Conference on*, 2015, pp. 1025–1030.

[65] C. Ohm, M. Brehmer, and R. Zentel, "Liquid Crystalline Elastomers as Actuators and Sensors," *Adv. Mater.*, vol. 22, no. 31, pp. 3366–3387, Aug. 2010.

[66] M. Warner and E. M. Terentjev, *Liquid crystal elastomers*, vol. 120. Oxford university press, 2007.

[67] F. Ge and Y. Zhao, "Microstructured Actuation of Liquid Crystal Polymer Networks," *Adv. Funct. Mater.*, vol. 30, no. 2, p. 1901890, Jan. 2020.

[68] H. Yang, G. Ye, X. Wang, and P. Keller, "Micron-sized liquid crystalline elastomer actuators," *Soft Matter*, vol. 7, no. 3, pp. 815–823, 2011.

[69] T. J. White and D. J. Broer, "Programmable and adaptive mechanics with liquid crystal polymer networks and elastomers," *Nat. Mater.*, vol. 14, no. 11, pp. 1087–1098, 2015.

[70] G. Babakhanova and O. D. Lavrentovich, "The Techniques of Surface Alignment of Liquid Crystals," in *Modern Problems of the Physics of Liquid Systems*, 2019, pp. 165–197.

[71] J. Zhao, L. Zhang, and J. Hu, "Varied Alignment Methods and Versatile Actuations for Liquid Crystal Elastomers: A Review," *Adv. Intell. Syst.*, vol. n/a, no. n/a, p. 2100065, Nov. 2021.

[72] T. H. Ware, J. S. Biggins, A. F. Shick, M. Warner, and T. J. White, "Localized soft elasticity in liquid crystal elastomers," *Nat. Commun.*, vol. 7, no. 1, p. 10781, 2016.

[73] D. Mistry and H. F. Gleeson, "Toward Programmed Complex Stress-Induced Mechanical Deformations of Liquid Crystal Elastomers," *Crystals*, vol. 10, no. 4,

p. 315, 2020.

[74] C. Ohm, M. Brehmer, and R. Zentel, "Applications of Liquid Crystalline Elastomers BT - Liquid Crystal Elastomers: Materials and Applications," W. H. de Jeu, Ed. Berlin, Heidelberg: Springer Berlin Heidelberg, 2012, pp. 49–93.

[75] S. W. Ula, N. A. Traugutt, R. H. Volpe, R. R. Patel, K. Yu, and C. M. Yakacki, "Liquid crystal elastomers: an introduction and review of emerging technologies," *Liq. Cryst. Rev.*, vol. 6, no. 1, pp. 78–107, Jan. 2018.

[76] J. Naciri, A. Srinivasan, H. Jeon, N. Nikolov, P. Keller, and B. R. Ratna, "Nematic Elastomer Fiber Actuator," *Macromolecules*, vol. 36, no. 22, pp. 8499–8505, Nov. 2003.

[77] H. Zeng, O. M. Wani, P. Wasylczyk, and A. Priimagi, "Light-Driven, Caterpillar-Inspired Miniature Inching Robot," *Macromol. Rapid Commun.*, vol. 39, no. 1, p. 1700224, Jan. 2018.

[78] M. Rogóż, H. Zeng, C. Xuan, D. S. Wiersma, and P. Wasylczyk, "Light-Driven Soft Robot Mimics Caterpillar Locomotion in Natural Scale," *Adv. Opt. Mater.*, vol. 4, no. 11, pp. 1689–1694, Nov. 2016.

[79] H. Zeng, P. Wasylczyk, C. Parmeggiani, D. Martella, M. Burresi, and D. S. Wiersma, "Light-Fueled Microscopic Walkers," *Adv. Mater.*, vol. 27, no. 26, pp. 3883–3887, Jul. 2015.

[80] M. Camacho-Lopez, H. Finkelmann, P. Palffy-Muhoray, and M. Shelley, "Fast liquid-crystal elastomer swims into the dark," *Nat. Mater.*, vol. 3, no. 5, pp. 307–310, 2004.

[81] S. Palagi *et al.*, "Structured light enables biomimetic swimming and versatile locomotion of photoresponsive soft microrobots," *Nat. Mater.*, vol. 15, p. 647, Feb. 2016.

[82] H. Yang *et al.*, "Micron-Sized Main-Chain Liquid Crystalline Elastomer Actuators with Ultralarge Amplitude Contractions," *J. Am. Chem. Soc.*, vol. 131, no. 41, pp. 15000–15004, Oct. 2009.

[83] J. Cui *et al.*, "Bioinspired Actuated Adhesive Patterns of Liquid Crystalline Elastomers," *Adv. Mater.*, vol. 24, no. 34, pp. 4601–4604, Sep. 2012.

[84] Z. L. Wu *et al.*, "Microstructured Nematic Liquid Crystalline Elastomer Surfaces with Switchable Wetting Properties," *Adv. Funct. Mater.*, vol. 23, no. 24, pp. 3070–3076, Jun. 2013.

[85] D. Liu and D. J. Broer, "Light controlled friction at a liquid crystal polymer

coating with switchable patterning," *Soft Matter*, vol. 10, no. 40, pp. 7952–7958, 2014.

[86] D. Liu, C. W. M. Bastiaansen, J. M. J. den Toonder, and D. J. Broer, "Photo-Switchable Surface Topologies in Chiral Nematic Coatings," *Angew. Chemie Int. Ed.*, vol. 51, no. 4, pp. 892–896, Jan. 2012.

[87] C. J. Camargo *et al.*, "Batch fabrication of optical actuators using nanotube–elastomer composites towards refreshable Braille displays," *J. micromechanics microengineering*, vol. 22, no. 7, p. 75009, 2012.

[88] H. Zeng, O. M. Wani, P. Wasylczyk, R. Kaczmarek, and A. Priimagi, "Self-Regulating Iris Based on Light-Actuated Liquid Crystal Elastomer," *Adv. Mater.*, vol. 29, no. 30, p. 1701814, Aug. 2017.

[89] M. López-Valdeolivas, D. Liu, D. J. Broer, and C. Sánchez-Somolinos, "4D Printed Actuators with Soft-Robotic Functions," *Macromol. Rapid Commun.*, vol. 39, no. 5, p. 1700710, Mar. 2018.

[90] M.-H. Li and P. Keller, "Artificial muscles based on liquid crystal elastomers," *Philos. Trans. R. Soc. A Math. Phys. Eng. Sci.*, vol. 364, no. 1847, pp. 2763–2777, 2006.

[91] A. Sánchez-Ferrer *et al.*, "Liquid-Crystalline Elastomer Microvalve for Microfluidics," *Adv. Mater.*, vol. 23, no. 39, pp. 4526–4530, Oct. 2011.

[92] E.-K. Fleischmann, H.-L. Liang, N. Kapernaum, F. Giesselmann, J. Lagerwall, and R. Zentel, "One-piece micropumps from liquid crystalline core-shell particles," *Nat. Commun.*, vol. 3, no. 1, p. 1178, 2012.

[93] D. Martella, S. Nocentini, D. Nuzhdin, C. Parmeggiani, and D. S. Wiersma, "Photonic Microhand with Autonomous Action," *Adv. Mater.*, vol. 29, no. 42, p. 1704047, Nov. 2017.

[94] C. Ohm, C. Serra, and R. Zentel, "A Continuous Flow Synthesis of Micrometer-Sized Actuators from Liquid Crystalline Elastomers," *Adv. Mater.*, vol. 21, no. 47, pp. 4859–4862, Dec. 2009.

[95] S. Haseloh, C. Ohm, F. Smallwood, and R. Zentel, "Nanosized Shape-Changing Colloids from Liquid Crystalline Elastomers," *Macromol. Rapid Commun.*, vol. 32, no. 1, pp. 88–93, Jan. 2011.

[96] C. Ohm *et al.*, "Preparation of actuating fibres of oriented main-chain liquid crystalline elastomers by a wetspinning process," *Soft Matter*, vol. 7, no. 8, pp. 3730–3734, 2011.

[97] M. Yamada *et al.*, "Photomobile Polymer Materials: Towards Light-Driven Plastic Motors," *Angew. Chemie Int. Ed.*, vol. 47, no. 27, pp. 4986–4988, Jun. 2008.

[98] V. Gimenez-Pinto, F. Ye, B. Mbanga, J. V Selinger, and R. L. B. Selinger, "Modeling out-of-plane actuation in thin-film nematic polymer networks: From chiral ribbons to auto-origami boxes via twist and topology," *Sci. Rep.*, vol. 7, no. 1, pp. 1–7, 2017.

[99] W. Kaufhold, H. Finkelmann, and H. R. Brand, "Nematic elastomers, 1. Effect of the spacer length on the mechanical coupling between network anisotropy and nematic order," *Die Makromol. Chemie Macromol. Chem. Phys.*, vol. 192, no. 11, pp. 2555–2579, 1991.

[100] M. O. Saed, R. H. Volpe, N. A. Traugutt, R. Visvanathan, N. A. Clark, and C. M. Yakacki, "High strain actuation liquid crystal elastomers via modulation of mesophase structure," *Soft Matter*, vol. 13, no. 41, pp. 7537–7547, 2017.

[101] Y. Lee, S. Choi, B.-G. Kang, and S. Ahn, "Effect of Isomeric Amine Chain Extenders and Crosslink Density on the Properties of Liquid Crystal Elastomers," *Materials (Basel).*, vol. 13, p. 3094, Jul. 2020.

[102] H. Wermter and H. Finkelmann, "Liquid crystalline elastomers as artificial muscles," *e-Polymers*, vol. 1, no. 1, 2001.

[103] D. Mistry, S. D. Connell, S. L. Mickthwaite, P. B. Morgan, J. H. Clamp, and H. F. Gleeson, "Coincident molecular auxeticity and negative order parameter in a liquid crystal elastomer," *Nat. Commun.*, vol. 9, no. 1, pp. 1–9, 2018.

[104] D. Mistry, P. B. Morgan, J. H. Clamp, and H. F. Gleeson, "New insights into the nature of semi-soft elasticity and 'mechanical-Fréedericksz transitions' in liquid crystal elastomers," *Soft Matter*, vol. 14, no. 8, pp. 1301–1310, 2018.

[105] T. J. White, "Photomechanical effects in liquid crystalline polymer networks and elastomers," *J. Polym. Sci. Part B Polym. Phys.*, vol. 56, no. 9, pp. 695–705, May 2018.

[106] M. T. Brannum, A. M. Steele, M. C. Venetos, L. T. J. Korley, G. E. Wnek, and T. J. White, "Light Control with Liquid Crystalline Elastomers," *Adv. Opt. Mater.*, vol. 7, no. 6, p. 1801683, Mar. 2019.

[107] Z. Pei, Y. Yang, Q. Chen, E. M. Terentjev, Y. Wei, and Y. Ji, "Mouldable liquid-crystalline elastomer actuators with exchangeable covalent bonds," *Nat. Mater.*, vol. 13, no. 1, pp. 36–41, 2014.

[108] D. Liu and D. J. Broer, "Self-assembled Dynamic 3D Fingerprints in Liquid-Crystal Coatings Towards Controllable Friction and Adhesion," *Angew. Chemie Int. Ed.*, vol. 53, no. 18, pp. 4542–4546, Apr. 2014.

[109] F. Greco *et al.*, "Liquid single crystal elastomer/conducting polymer bilayer composite actuator: modelling and experiments," *Soft Matter*, vol. 9, no. 47, pp. 11405–11416, 2013.

[110] G. N. Mol, K. D. Harris, C. W. M. Bastiaansen, and D. J. Broer, "Thermo-mechanical responses of liquid-crystal networks with a splayed molecular organization," *Adv. Funct. Mater.*, vol. 15, no. 7, pp. 1155–1159, 2005.

[111] S. Dey, "Elasticity of main chain liquid crystal elastomers and its relationship to liquid crystal microstructure," Kent State University, Kent State University, 2013.

[112] I. Kundler and H. Finkelmann, "Strain-induced director reorientation in nematic liquid single crystal elastomers," *Macromol. Rapid Commun.*, vol. 16, no. 9, pp. 679–686, Sep. 1995.

[113] C. M. Yakacki, M. Saed, D. P. Nair, T. Gong, S. M. Reed, and C. N. Bowman, "Tailorable and programmable liquid-crystalline elastomers using a two-stage thiol–acrylate reaction," *RSC Adv.*, vol. 5, no. 25, pp. 18997–19001, 2015.

[114] Z. Wang, W. Fan, Q. He, Y. Wang, X. Liang, and S. Cai, "A simple and robust way towards reversible mechanochromism: Using liquid crystal elastomer as a mask," *Extrem. Mech. Lett.*, vol. 11, pp. 42–48, 2017.

[115] R. S. Kularatne, H. Kim, J. M. Boothby, and T. H. Ware, "Liquid crystal elastomer actuators: Synthesis, alignment, and applications," *J. Polym. Sci. Part B Polym. Phys.*, vol. 55, no. 5, pp. 395–411, Mar. 2017.

[116] M. Chambers, H. Finkelmann, M. Remskar, A. Sanchez-Ferrer, B. Zalar, and S. Zumer, "Liquid Crystal Elastomer-Nanoparticle Systems for Actuation," *J. Mater. Chem.*, vol. 19, pp. 1524–1531, Mar. 2009.

[117] R. Wei, Y. He, X. Wang, and P. Keller, "Photoluminescent Nematic Liquid Crystalline Elastomer with a Thermomechanical Emission Variation Function," *Macromol. Rapid Commun.*, vol. 35, no. 18, pp. 1571–1577, Sep. 2014.

[118] B. Ni, H. Chen, M. Zhang, P. Keller, M. Tatoulian, and M.-H. Li, "Thermo-mechanical and photo-luminescence properties of micro-actuators made of liquid crystal elastomers with cyano-oligo(p-phenylene vinylene) crosslinking bridges," *Mater. Chem. Front.*, vol. 3, no. 11, pp. 2499–2506, 2019.

[119] L. Qin, X. Liu, and Y. Yu, "Soft Actuators of Liquid Crystal Polymers Fueled by Light from Ultraviolet to Near Infrared," *Adv. Opt. Mater.*, vol. 9, no. 7, p. 2001743, Apr. 2021.

[120] Z. Li *et al.*, "Polydopamine nanoparticles doped in liquid crystal elastomers for producing dynamic 3D structures," *J. Mater. Chem. A*, vol. 5, no. 14, pp. 6740–6746, 2017.

[121] H. Tian, Z. Wang, Y. Chen, J. Shao, T. Gao, and S. Cai, "Polydopamine-Coated Main-Chain Liquid Crystal Elastomer as Optically Driven Artificial Muscle," *ACS Appl. Mater. Interfaces*, vol. 10, no. 9, pp. 8307–8316, Mar. 2018.

[122] C. Ohm, M. Brehmer, and R. Zentel, "Applications of liquid crystalline elastomers," in *Liquid Crystal Elastomers: materials and applications*, Springer, 2012, pp. 49–93.

[123] H. Finkelmann, H.-J. Kock, and G. Rehage, "Investigations on liquid crystalline polysiloxanes 3. Liquid crystalline elastomers — a new type of liquid crystalline material," *Die Makromol. Chemie, Rapid Commun.*, vol. 2, no. 4, pp. 317–322, Jun. 1981.

[124] H. Zhao *et al.*, "High-Fidelity Replica Molding of Glassy Liquid Crystalline Polymer Microstructures," *ACS Appl. Mater. Interfaces*, vol. 8, no. 12, pp. 8110–8117, Mar. 2016.

[125] H. Aharoni, Y. Xia, X. Zhang, R. D. Kamien, and S. Yang, "Universal inverse design of surfaces with thin nematic elastomer sheets," *Proc. Natl. Acad. Sci.*, vol. 115, no. 28, p. 7206 LP-7211, Jul. 2018.

[126] Y. Cheng, H. Lu, X. Lee, H. Zeng, and A. Priimagi, "Kirigami-Based Light-Induced Shape-Morphing and Locomotion," *Adv. Mater.*, vol. 32, no. 7, p. 1906233, 2020.

[127] A. Otuka *et al.*, "Three-dimensional structures fabricated after laser-induced free radical generation in azoaromatic compounds," *Opt. Mater. Express*, vol. 10, p. 1792, Aug. 2020.

[128] T. A. Kent, M. J. Ford, E. J. Markvicka, and C. Majidi, "Soft actuators using liquid crystal elastomers with encapsulated liquid metal Joule heaters," *Multifunct. Mater.*, vol. 3, no. 2, p. 25003, 2020.

[129] T. Yoshino, M. Kondo, J. Mamiya, M. Kinoshita, Y. Yu, and T. Ikeda, "Three-Dimensional Photomobility of Crosslinked Azobenzene Liquid-Crystalline Polymer Fibers," *Adv. Mater.*, vol. 22, no. 12, pp. 1361–1363, Mar. 2010.

[130] M. Barnes and R. Verduzco, "Direct shape programming of liquid crystal elastomers," *Soft Matter*, vol. 15, no. 5, pp. 870–879, 2019.

[131] M. O. Saed *et al.*, "Molecularly-Engineered, 4D-Printed Liquid Crystal Elastomer Actuators," *Adv. Funct. Mater.*, vol. 29, no. 3, p. 1806412, Jan. 2019.

[132] D. J. Roach, X. Kuang, C. Yuan, K. Chen, and H. J. Qi, "Novel ink for ambient condition printing of liquid crystal elastomers for 4D printing," *Smart Mater. Struct.*, vol. 27, no. 12, p. 125011, 2018.

[133] T. Hessberger *et al.*, "Co-flow microfluidic synthesis of liquid crystalline actuating Janus particles," *J. Mater. Chem. C*, vol. 4, no. 37, pp. 8778–8786, 2016.

[134] R. Wei, Y. He, X. Wang, and P. Keller, "Nematic Liquid Crystalline Elastomer Grating and Microwire Fabricated by Micro-Molding in Capillaries," *Macromol. Rapid Commun.*, vol. 34, no. 4, pp. 330–334, Feb. 2013.

[135] Y. Sawa *et al.*, "Shape selection of twist-nematic-elastomer ribbons," *Proc. Natl. Acad. Sci.*, vol. 108, no. 16, p. 6364 LP-6368, Apr. 2011.

[136] Y. Liu, B. Xu, S. Sun, J. Wei, L. Wu, and Y. Yu, "Humidity- and Photo-Induced Mechanical Actuation of Cross-Linked Liquid Crystal Polymers," *Adv. Mater.*, vol. 29, no. 9, p. 1604792, Mar. 2017.

[137] C. L. Van Oosten, C. W. M. Bastiaansen, and D. J. Broer, "Printed artificial cilia from liquid-crystal network actuators modularly driven by light," *Nat. Mater.*, vol. 8, no. 8, p. 677, 2009.

[138] L. Liu *et al.*, "Single-layer dual-phase nematic elastomer films with bending, accordion-folding, curling and buckling motions," *Chem. Commun.*, vol. 53, no. 11, pp. 1844–1847, 2017.

[139] H.-H. Yoon, D.-Y. Kim, K.-U. Jeong, and S. Ahn, "Surface Aligned Main-Chain Liquid Crystalline Elastomers: Tailored Properties by the Choice of Amine Chain Extenders," *Macromolecules*, vol. 51, no. 3, pp. 1141–1149, Feb. 2018.

[140] W. Wang, X. Sun, W. Wu, H. Peng, and Y. Yu, "Photoinduced Deformation of Crosslinked Liquid-Crystalline Polymer Film Oriented by a Highly Aligned Carbon Nanotube Sheet," *Angew. Chemie*, vol. 124, no. 19, pp. 4722–4725, May 2012.

[141] C. H. Lee, H. Yoshida, Y. Miura, A. Fujii, and M. Ozaki, "Local liquid crystal alignment on patterned micrograting structures photofabricated by two photon excitation direct laser writing," *Appl. Phys. Lett.*, vol. 93, no. 17, p. 173509, Oct.

2008.

[142] Y. Xia, G. Cedillo-Servin, R. D. Kamien, and S. Yang, "Guided Folding of Nematic Liquid Crystal Elastomer Sheets into 3D via Patterned 1D Microchannels," *Adv. Mater.*, vol. 28, no. 43, pp. 9637–9643, Nov. 2016.

[143] W. Zheng and M.-C. Lee, "Attainment of Planarly Aligned Liquid Crystal Using Vertical Alignment Polymer Walls," *Mol. Cryst. Liq. Cryst.*, vol. 553, no. 1, pp. 28–35, Feb. 2012.

[144] L. T. de Haan, C. Sánchez-Somolinos, C. M. W. Bastiaansen, A. P. H. J. Schenning, and D. J. Broer, "Engineering of Complex Order and the Macroscopic Deformation of Liquid Crystal Polymer Networks," *Angew. Chemie Int. Ed.*, vol. 51, no. 50, pp. 12469–12472, Dec. 2012.

[145] L. T. de Haan *et al.*, "Accordion-like Actuators of Multiple 3D Patterned Liquid Crystal Polymer Films," *Adv. Funct. Mater.*, vol. 24, no. 9, pp. 1251–1258, Mar. 2014.

[146] D. Ditter *et al.*, "MEMS analogous micro-patterning of thermotropic nematic liquid crystalline elastomer films using a fluorinated photoresist and a hard mask process," *J. Mater. Chem. C*, vol. 5, no. 47, pp. 12635–12644, 2017.

[147] Q. Qian, J. Chen, M.-H. Li, P. Keller, and D. He, "Direct preparation of nematic liquid crystalline elastomer actuators by electron beam irradiation polymerization," *J. Mater. Chem.*, vol. 22, no. 11, pp. 4669–4674, 2012.

[148] S. Varghese, S. Narayanankutty, C. W. M. Bastiaansen, G. P. Crawford, and D. J. Broer, "Patterned Alignment of Liquid Crystals by μ-Rubbing," *Adv. Mater.*, vol. 16, no. 18, pp. 1600–1605, Sep. 2004.

[149] O. Yaroshchuk and Y. Reznikov, "Photoalignment of liquid crystals: basics and current trends," *J. Mater. Chem.*, vol. 22, no. 2, pp. 286–300, 2012.

[150] R. Lin and J. A. Rogers, "Molecular-Scale Soft Imprint Lithography for Alignment Layers in Liquid Crystal Devices," *Nano Lett.*, vol. 7, no. 6, pp. 1613–1621, Jun. 2007.

[151] J.-Y. Chun and D.-S. Seo, "Soft Imprinting Lithography for Multi-Domain Alignment Layers in Liquid Crystal Devices," *Jpn. J. Appl. Phys.*, vol. 49, no. 4R, p. 40210, 2010.

[152] D. W. Berreman, "Solid Surface Shape and the Alignment of an Adjacent Nematic Liquid Crystal," *Phys. Rev. Lett.*, vol. 28, no. 26, pp. 1683–1686, Jun. 1972.

[153] Y. Xia *et al.*, "Better Actuation Through Chemistry: Using Surface Coatings to Create Uniform Director Fields in Nematic Liquid Crystal Elastomers," *ACS Appl. Mater. Interfaces*, vol. 8, no. 19, pp. 12466–12472, May 2016.

[154] T. Seki, S. Nagano, and M. Hara, "Versatility of photoalignment techniques: From nematics to a wide range of functional materials," *Polymer (Guildf).*, vol. 54, no. 22, pp. 6053–6072, 2013.

[155] N. Koshida and S. Kikui, "Magnetic field assisted alignment of nematic liquid crystal on a polymeric surface," *Appl. Phys. Lett.*, vol. 40, no. 6, pp. 541–542, Mar. 1982.

[156] P.-G. De Gennes and J. Prost, *The physics of liquid crystals*, vol. 83. Oxford university press, 1993.

[157] A. Onuki, "Liquid crystals in electric field," *J. Phys. Soc. Japan*, vol. 73, no. 3, pp. 511–514, 2004.

[158] A. L. Elias, K. D. Harris, C. W. M. Bastiaansen, D. J. Broer, and M. J. Brett, "Photopatterned liquid crystalline polymers for microactuators," *J. Mater. Chem.*, vol. 16, no. 28, pp. 2903–2912, 2006.

[159] E. Sungur *et al.*, "External stimulus driven variable-step grating in a nematic elastomer," *Opt. Express*, vol. 15, no. 11, pp. 6784–6789, 2007.

[160] H. Zeng *et al.*, "High-Resolution 3D Direct Laser Writing for Liquid-Crystalline Elastomer Microstructures," *Adv. Mater.*, vol. 26, no. 15, pp. 2319–2322, Apr. 2014.

[161] D. Martella *et al.*, "Light activated non-reciprocal motion in liquid crystalline networks by designed microactuator architecture," *RSC Adv.*, vol. 7, no. 32, pp. 19940–19947, 2017.

[162] Z. Yan, X. Ji, W. Wu, J. Wei, and Y. Yu, "Light-Switchable Behavior of a Microarray of Azobenzene Liquid Crystal Polymer Induced by Photodeformation," *Macromol. Rapid Commun.*, vol. 33, no. 16, pp. 1362–1367, Aug. 2012.

[163] S. Petsch *et al.*, "A thermotropic liquid crystal elastomer micro-actuator with integrated deformable micro-heater," in *2014 IEEE 27th International Conference on Micro Electro Mechanical Systems (MEMS)*, 2014, pp. 905–908.

[164] Z. Yang, G. A. Herd, S. M. Clarke, A. R. Tajbakhsh, E. M. Terentjev, and W. T. S. Huck, "Thermal and UV Shape Shifting of Surface Topography," *J. Am. Chem. Soc.*, vol. 128, no. 4, pp. 1074–1075, Feb. 2006.

[165] C. Sánchez, F. Verbakel, M. J. Escuti, C. W. M. Bastiaansen, and D. J. Broer, "Printing of Monolithic Polymeric Microstructures Using Reactive Mesogens," *Adv. Mater.*, vol. 20, no. 1, pp. 74–78, Jan. 2008.

[166] A. L. Elias, M. J. Brett, K. D. Harris, C. W. M. Bastiaansen, and D. J. Broer, "Three Techniques for Micropatterning Liquid Crystalline Polymers," *Mol. Cryst. Liq. Cryst.*, vol. 477, no. 1, p. 137/[631]-151/[645], Dec. 2007.

[167] D. B. Weibel, W. R. DiLuzio, and G. M. Whitesides, "Microfabrication meets microbiology," *Nat. Rev. Microbiol.*, vol. 5, no. 3, pp. 209–218, 2007.

[168] C. R. Martin and I. A. Aksay, "Microchannel molding: A soft lithography-inspired approach to micrometer-scale patterning," *J. Mater. Res.*, vol. 20, no. 8, pp. 1995–2003, 2005.

[169] Y. Shang, J. Wang, T. Ikeda, and L. Jiang, "Bio-inspired liquid crystal actuator materials," *J. Mater. Chem. C*, vol. 7, no. 12, pp. 3413–3428, 2019.

[170] A. Sánchez-Ferrer, T. Fischl, M. Stubenrauch, H. Wurmus, M. Hoffmann, and H. Finkelmann, "Photo-Crosslinked Side-Chain Liquid-Crystalline Elastomers for Microsystems," *Macromol. Chem. Phys.*, vol. 210, no. 20, pp. 1671–1677, Oct. 2009.

[171] C. M. Spillmann, J. Naciri, B. D. Martin, W. Farahat, H. Herr, and B. R. Ratna, "Stacking nematic elastomers for artificial muscle applications," *Sensors Actuators A Phys.*, vol. 133, no. 2, pp. 500–505, 2007.

[172] N. Torras, M. Duque, C. J. Camargo, J. Esteve, and A. Sánchez-Ferrer, "Heat-controlled micropillar array device for microsystems technology," *Soft Matter*, vol. 13, no. 40, pp. 7264–7272, 2017.

[173] C. Li, Y. Liu, X. Huang, and H. Jiang, "Direct Sun-Driven Artificial Heliotropism for Solar Energy Harvesting Based on a Photo-Thermomechanical Liquid-Crystal Elastomer Nanocomposite," *Adv. Funct. Mater.*, vol. 22, no. 24, pp. 5166–5174, Dec. 2012.

[174] Y. Yu, M. Nakano, and T. Ikeda, "Directed bending of a polymer film by light," *Nature*, vol. 425, no. 6954, p. 145, 2003.

[175] J. M. Boothby, H. Kim, and T. H. Ware, "Shape changes in chemoresponsive liquid crystal elastomers," *Sensors Actuators B Chem.*, vol. 240, pp. 511–518, 2017.

[176] S. S. Roy, W. Lehmann, E. Gebhard, C. Tolksdorf, R. Zentel, and F. Kremer, "Inverse Piezoelectric and Electrostrictive Response in Freely Suspended FLC

Elastomer Film as Detected by Interferometric Measurements," *Mol. Cryst. Liq. Cryst.*, vol. 375, no. 1, pp. 253–268, Jan. 2002.

[177] T. Guin *et al.*, "Tunable Electromechanical Liquid Crystal Elastomer Actuators," *Adv. Intell. Syst.*, vol. 2, no. 7, p. 2000022, Jul. 2020.

[178] H. E. Fowler, P. Rothemund, C. Keplinger, and T. J. White, "Liquid Crystal Elastomers with Enhanced Directional Actuation to Electric Fields," *Adv. Mater.*, vol. 33, no. 43, p. 2103806, Oct. 2021.

[179] C. Wang *et al.*, "Soft ultrathin electronics innervated adaptive fully soft robots," *Adv. Mater.*, vol. 30, no. 13, p. 1706695, 2018.

[180] Y. Cui *et al.*, "A simple analytical thermo-mechanical model for liquid crystal elastomer bilayer structures," *AIP Adv.*, vol. 8, no. 2, p. 25215, 2018.

[181] M. P. Da Cunha *et al.*, "A self-sustained soft actuator able to rock and roll," *Chem. Commun.*, vol. 55, no. 74, pp. 11029–11032, 2019.

[182] J. A. H. P. Sol, A. R. Peeketi, N. Vyas, A. P. H. J. Schenning, R. K. Annabattula, and M. G. Debije, "Butterfly proboscis-inspired tight rolling tapered soft actuators," *Chem. Commun.*, vol. 55, no. 12, pp. 1726–1729, 2019.

[183] A. Persano, J. Iannacci, P. Siciliano, and F. Quaranta, "Out-of-plane deformation and pull-in voltage of cantilevers with residual stress gradient: Experiment and modelling," *Microsyst. Technol.*, vol. 25, no. 9, pp. 3581–3588, 2019.

[184] T. B. Asafa, "Studies on the Residual Stress and Strain Gradients in Poly-SiGe Nanocantilevers," *FUOYE J. Eng. Technol.*, vol. 4, no. 1, 2019.

[185] M. M. Okyar, "Cantilever beam microactuators with electrothermal and electrostatic drive," 1998.

[186] N. An, M. Li, and J. Zhou, "Instability of liquid crystal elastomers," *Smart Mater. Struct.*, vol. 25, no. 1, p. 15016, 2015.

[187] R. A. E. Neufeld, H. Shahsavan, B. Zhao, and N. M. Abukhdeir, "Simulation-based design of thermally-driven actuators using liquid crystal elastomers," *Liq. Cryst.*, vol. 45, no. 7, pp. 1010–1022, 2018.

[188] M. Rogóż, K. Dradrach, C. Xuan, and P. Wasylczyk, "A Millimeter-Scale Snail Robot Based on a Light-Powered Liquid Crystal Elastomer Continuous Actuator," *Macromol. Rapid Commun.*, vol. 40, no. 16, p. 1900279, 2019.

[189] K. Dradrach *et al.*, "Traveling Wave Rotary Micromotor Based on a Photomechanical Response in Liquid Crystal Polymer Networks," *ACS Appl. Mater. Interfaces*, vol. 12, no. 7, pp. 8681–8686, 2020.

[190] A. Konya, V. Gimenez-Pinto, and R. L. B. Selinger, "Modeling defects, shape evolution, and programmed auto-origami in liquid crystal elastomers," *Front. Mater.*, vol. 3, p. 24, 2016.

[191] B. L. Mbanga, F. Ye, J. V Selinger, and R. L. B. Selinger, "Modeling elastic instabilities in nematic elastomers," *Phys. Rev. E*, vol. 82, no. 5, p. 51701, 2010.

[192] A. Kirillova and L. Ionov, "Shape-changing polymers for biomedical applications," *J. Mater. Chem. B*, vol. 7, no. 10, pp. 1597–1624, 2019.

[193] O. M. Wani, H. Zeng, P. Wasylczyk, and A. Priimagi, "Programming Photoresponse in Liquid Crystal Polymer Actuators with Laser Projector," *Adv. Opt. Mater.*, vol. 6, no. 1, p. 1700949, Jan. 2018.

[194] M. Lahikainen, H. Zeng, and A. Priimagi, "Reconfigurable photoactuator through synergistic use of photochemical and photothermal effects," *Nat. Commun.*, vol. 9, no. 1, p. 4148, 2018.

[195] M. Pilz da Cunha, S. Ambergen, M. G. Debije, E. F. G. A. Homburg, J. M. J. den Toonder, and A. P. H. J. Schenning, "A Soft Transporter Robot Fueled by Light," *Adv. Sci.*, vol. 7, no. 5, p. 1902842, Mar. 2020.

[196] S. Nocentini, C. Parmeggiani, D. Martella, and D. S. Wiersma, "Optically Driven Soft Micro Robotics," *Adv. Opt. Mater.*, vol. 6, no. 14, p. 1800207, Jul. 2018.

[197] Z. Jiang, Y. Xiao, X. Tong, and Y. Zhao, "Selective decrosslinking in liquid crystal polymer actuators for optical reconfiguration of origami and light-fueled locomotion," *Angew. Chemie*, vol. 131, no. 16, pp. 5386–5391, 2019.

[198] R. R. Kohlmeyer and J. Chen, "Wavelength-Selective, IR Light-Driven Hinges Based on Liquid Crystalline Elastomer Composites," *Angew. Chemie Int. Ed.*, vol. 52, no. 35, pp. 9234–9237, Aug. 2013.

[199] M. Yamada *et al.*, "Photomobile polymer materials—various three-dimensional movements," *J. Mater. Chem.*, vol. 19, no. 1, pp. 60–62, 2009.

[200] Y.-Y. Xiao, Z.-C. Jiang, X. Tong, and Y. Zhao, "Biomimetic Locomotion of Electrically Powered 'Janus' Soft Robots Using a Liquid Crystal Polymer," *Adv. Mater.*, vol. 31, no. 36, p. 1903452, Sep. 2019.

[201] F. Ge, R. Yang, X. Tong, F. Camerel, and Y. Zhao, "A Multifunctional Dye-doped Liquid Crystal Polymer Actuator: Light-Guided Transportation, Turning in Locomotion, and Autonomous Motion," *Angew. Chemie*, vol. 130, no. 36, pp. 11932–11937, 2018.

[202] B. Zuo, M. Wang, B.-P. Lin, and H. Yang, "Visible and infrared three-

wavelength modulated multi-directional actuators," *Nat. Commun.*, vol. 10, no. 1, p. 4539, 2019.

[203] Y.-Y. Xiao, Z.-C. Jiang, J.-B. Hou, and Y. Zhao, "Desynchronized liquid crystalline network actuators with deformation reversal capability," *Nat. Commun.*, vol. 12, no. 1, p. 624, 2021.

[204] W. Hilber, "Stimulus-active polymer actuators for next-generation microfluidic devices," *Appl. Phys. A*, vol. 122, no. 8, p. 751, 2016.

[205] J. M. J. den Toonder and P. R. Onck, "Microfluidic manipulation with artificial/bioinspired cilia," *Trends Biotechnol.*, vol. 31, no. 2, pp. 85–91, 2013.

[206] L. Fang, H. Zhang, Z. Li, Y. Zhang, Y. Zhang, and H. Zhang, "Synthesis of Reactive Azobenzene Main-Chain Liquid Crystalline Polymers via Michael Addition Polymerization and Photomechanical Effects of Their Supramolecular Hydrogen-Bonded Fibers," *Macromolecules*, vol. 46, no. 19, pp. 7650–7660, Oct. 2013.

[207] A. H. Gelebart, M. Mc Bride, A. P. H. J. Schenning, C. N. Bowman, and D. J. Broer, "Photoresponsive Fiber Array: Toward Mimicking the Collective Motion of Cilia for Transport Applications," *Adv. Funct. Mater.*, vol. 26, no. 29, pp. 5322–5327, Aug. 2016.

[208] W. Zheng and Y.-T. Hu, "Alignment of Liquid Crystal Confined in Polydimethylsiloxane Channels," *Mol. Cryst. Liq. Cryst.*, vol. 615, no. 1, pp. 1–8, Jul. 2015.

[209] D. Byun, J. Kim, H. S. Ko, and H. C. Park, "Direct measurement of slip flows in superhydrophobic microchannels with transverse grooves," *Phys. Fluids*, vol. 20, no. 11, p. 113601, Nov. 2008.

[210] H. C. Ko, A. J. Baca, and J. A. Rogers, "Bulk Quantities of Single-Crystal Silicon Micro-/Nanoribbons Generated from Bulk Wafers," *Nano Lett.*, vol. 6, no. 10, pp. 2318–2324, Oct. 2006.

[211] S. Achenbach, G. Wells, M. Jacobs, B. Moazed, S. Iyer, and J. Hanson, "Polymer-based X-ray masks patterned by direct laser writing," *Rev. Sci. Instrum.*, vol. 89, no. 11, p. 115001, 2018.

[212] G. Kostovski, A. Mitchell, A. Holland, and M. Austin, "Sidewall corrugation lithography: Bulk fabrication of ordered nanowires, nanoribbons, and nanorings," *Appl. Phys. Lett.*, vol. 92, no. 22, p. 223109, Jun. 2008.

[213] S. Achenbach, S. Hengsbach, J. Schulz, and J. Mohr, "Optimization of laser

writer-based UV lithography with high magnification optics to pattern X-ray lithography mask templates," *Microsyst. Technol.*, vol. 25, no. 8, pp. 2975–2983, 2019.

[214] E. Rabe, S. Kopetz, and A. Neyer, "The generation of mould patterns for multimode optical waveguide components by direct laser writing of SU-8 at 364 nm," *J. Micromechanics Microengineering*, vol. 17, no. 8, pp. 1664–1670, 2007.

[215] Dow, "SYLGARD^{TM} 184 Silicone Elastomer. Technical Data Sheet." .

[216] M. Li, Y. Chen, W. Luo, and X. Cheng, "Interfacial Interactions during Demolding in Nanoimprint Lithography," *Micromachines* , vol. 12, no. 4. 2021.

[217] A. Mata, A. J. Fleischman, and S. Roy, "Characterization of Polydimethylsiloxane (PDMS) Properties for Biomedical Micro/Nanosystems," *Biomed. Microdevices*, vol. 7, no. 4, pp. 281–293, 2005.

[218] L. R. Viannie, G. R. Jayanth, V. Radhakrishna, and K. Rajanna, "Fabrication and Nonlinear Thermomechanical Analysis of SU8 Thermal Actuator," *J. Microelectromechanical Syst.*, vol. 25, no. 1, pp. 125–133, 2016.

[219] G. A. Gehring, M. D. Cooke, I. S. Gregory, W. J. Karl, and R. Watts, "Cantilever unified theory and optimization for sensors and actuators," *Smart Mater. Struct.*, vol. 9, no. 6, p. 918, 2000.

[220] Y. Sawa, K. Urayama, T. Takigawa, A. DeSimone, and L. Teresi, "Thermally Driven Giant Bending of Liquid Crystal Elastomer Films with Hybrid Alignment," *Macromolecules*, vol. 43, no. 9, pp. 4362–4369, May 2010.

[221] J. R. Barber, "Plane strain and plane stress," in *Elasticity*, Springer, 2010, pp. 37–44.

[222] V. Iannotti, G. Ausanio, C. Hison, and L. Lanotte, "10Modeling of cantilever deflection for sensors and actuators: Role of Poisson's ratio for a unified theory," *J. Appl. Phys.*, vol. 97, no. 10, p. 104516, 2005.

[223] J. C. Asseko Ondo, E. J. J. Blampain, G. N'Tchayi Mbourou, S. Mc Murtry, S. Hage-Ali, and O. Elmazria, "FEM Modeling of the Temperature Influence on the Performance of SAW Sensors Operating at GigaHertz Frequency Range and at High Temperature Up to 500° C," *Sensors*, vol. 20, no. 15, p. 4166, 2020.

[224] J. J. Wie, K. M. Lee, T. H. Ware, and T. J. White, "Twists and turns in glassy, liquid crystalline polymer networks," *Macromolecules*, vol. 48, no. 4, pp. 1087–1092, 2015.

[225] N. Akamatsu *et al.*, "Facile strain analysis of largely bending films by a surface-

labelled grating method," *Sci. Rep.*, vol. 4, no. 1, pp. 1–6, 2014.

[226] L. Dong and Y. Zhao, "Photothermally driven liquid crystal polymer actuators," *Mater. Chem. Front.*, vol. 2, no. 11, pp. 1932–1943, 2018.

[227] Y. Xia, F. Serra, R. D. Kamien, K. J. Stebe, and S. Yang, "Direct mapping of local director field of nematic liquid crystals at the nanoscale," *Proc. Natl. Acad. Sci.*, vol. 112, no. 50, pp. 15291–15296, Dec. 2015.

[228] D. W. Heo, M. G. Kang, H. Lee, and S. Y. Kim, "Stress/strain and curvature analysis of laser-scribed polyethylene terephthalate films with multiple grooves using finite element method," *Adv. Mech. Eng.*, vol. 10, no. 8, p. 1687814018793236, Aug. 2018.

[229] G. Fantoni and M. Porta, "A critical review of releasing strategies in microparts handling," in *International Precision Assembly Seminar*, 2008, pp. 223–234.

[230] B. Ahmad, H. Chambon, P. Tissier, and A. Bolopion, "Laser Actuated Microgripper Using Optimized Chevron-Shaped Actuator," *Micromachines*, vol. 12, no. 12, p. 1487, 2021.

[231] C. Elbuken, L. Gui, C. L. Ren, M. Yavuz, and M. B. Khamesee, "Design and analysis of a polymeric photo-thermal microactuator," *Sensors Actuators A Phys.*, vol. 147, no. 1, pp. 292–299, 2008.